CFIRE

Impact of Overweight Vehicles (with Heavy Axle Loads) on Bridge Deck Deterioration

CFIRE 04-06
March 2012

National Center for Freight & Infrastructure Research & Education
Department of Civil and Environmental Engineering
College of Engineering
University of Wisconsin–Madison

Authors:
Zhibin Lin, Jian Zhao, and Habib Tabatabai
University of Wisconsin – Milwaukee

Principal Investigator:
Jian Zhao
Department of Civil Engineering and Mechanics
University of Wisconsin – Milwaukee

Technical Report Documentation Page

1. Report No.	2. Government Accession No.	3. Recipient's Catalog No.
CFIRE 04-06		

4. Title and Subtitle	5. Report Date
Impact of Overweight Vehicles (with Heavy Axle Loads) on Bridge Deck Deterioration	**March 2012**
	6. Performing Organization Code
7. Author(s)	8. Performing Organization Report No.
Zhibin Lin, Jian Zhao, and Habib Tabatabai	
9. Performing Organization Name and Address	10. Work Unit No. (TRAIS)
National Center for Freight and Infrastructure Research and Education **University of Wisconsin Madison** **1415 Engineering Drive, 2205 EH** **Madison, WI 53706**	11. Contract or Grant No. **248K091**
12. Sponsoring Agency Name and Address	13. Type of Report and Period Covered
Research and Innovative Technology Administration **United States Department of Transportation** **1200 New Jersey Avenue, SE** **Washington, DC 20590**	**Final Report (10/01/2010-03/31/2012)**
	14. Sponsoring Agency Code

15. Supplementary Notes

Project completed for USDOT's RITA by CFIRE and UW-Milwaukee

16. Abstract

Bridge deck slabs develop compressive stresses from global flexural deformation and locally from high-level wheel loads when it is subjected to overweight trucks. This study quantified the impact of overweight vehicles with heavy axle loads on bridge decks using laboratory tests and numerical simulations.

The laboratory tests focused on evaluating the impact of combined mechanical stresses and freeze-thaw cycles on the durability of air-entrained concrete. Concrete cylinders, after being cured in saturated limewater for 28 days, were subjected to various levels of compressive loads and then exposed to 300 freeze-thaw (F/T) cycles. Rapid chloride ion penetrability tests were conducted to evaluate the chloride permeability of the concrete samples. The laboratory test results indicated that the mechanical loading combined with freeze-thaw cycles significantly increased the permeability of air-entrained concrete and may accelerate the deterioration of concrete elements such as bridge decks. The observed permeability increase was due to the fact that higher compressive loads caused more extensive microcracks in concrete, and the damaged concrete further degrades under freeze-thaw cycles, which may have further opened and interconnected the microcracks.

Bridge deck analyses were conducted to investigate stress distributions and stress levels in typical concrete bridge decks subjected to high axle loads. The numerical analyses using the idealized bridge models indicated that the normal stress in bridge decks in the transverse direction can be significantly affected by the thickness of bridge deck, the girder spacing, and the magnitude of the wheel loads. The analyses results also indicated that the normal stresses in the longitudinal direction may be calculated as the summation of the stresses due to global bending of the bridge superstructure under the truck loads, which can estimated using typical design/rating procedures and the stress elevations near the wheel loads. The proposed equations may be used, in addition to the typical design/rating calculations, to capture the adverse stresses in bridge decks subjected to overweight trucks.

17. Key Words	18. Distribution Statement
Overweight vehicle; microcracking; freeze-thaw; permeability; durability; concrete; bridge deck	**No restrictions. This report is available through the Transportation Research Information Services of the National Transportation Library**.

19. Security Classif. (of report)	20. Security Classif. (of this page)	21. No. of pages	22. Price
Unclassified	**Unclassified**	**220**	**-0-**

Form DOT F 1700.7 (8-72) Reproduction of completed page authorized

Impact of Overweight Vehicles (with Heavy Axle Loads) on Bridge Deck Deterioration

Final Report

Prepared by:

Zhibin Lin
Jian Zhao
Habib Tabatabai

Department of Civil Engineering and Mechanics
University of Wisconsin-Milwaukee

March 2012

Disclaimers

This research was funded by the National Center for Freight and Infrastructure Research and Education. The contents of this report reflect the views of the authors, who are responsible for the facts and the accuracy of the information presented herein. This document is disseminated under the sponsorship of the Department of Transportation, University Transportation Centers Program, in the interest of information exchange. The U.S. Government assumes no liability for the contents or use thereof. The contents do not necessarily reflect the official views of the National Center for Freight and Infrastructure Research and Education, the University of Wisconsin, the Wisconsin Department of Transportation, or the USDOT's RITA at the time of publication.

Acknowledgments

The authors would like to thank the CFIRE Director, Dr. Teresa Adams for her support to the project. We also thank the CFIRE project committee members for their valuable guidance and support during the course of conducting the research. Specially, Mr. Travis McDaniel from Wisconsin Department of Transportation (WisDOT) provided guidance for the bridge analysis.

We are grateful to Ismael Flores Vivian (Research Associate), Cem Gogtas (PhD student), Morteza Janbaz and Guillermo Puerta Falla (graduate students) at the University of Wisconsin at Milwaukee (UWM) for their help during the research. We also thank Professor Hani Titi (UWM) during rapid chloride permeability tests and Professor Rani El-Hajjar (UWM) during the optical microscope observations.

This page has been intentionally left blank.

EXECUTIVE SUMMARY

Overweight vehicles can have heavy axle loads. The heavy axle loads, combined with a large gross weight may create micro-cracks in the concrete, and the accumulation of such damage along with environmental attacks can accelerate the deterioration of bridge decks. This study quantified the impact of overweight vehicles with heavy axle loads on bridge decks using laboratory tests and numerical simulations.

The laboratory tests focused on evaluating the impact of combined mechanical stresses and freeze-thaw cycles on the durability of air-entrained concrete. Eight groups of three 100×200 mm (4×8 in.) cylinders were cast using air-entrain concrete, which is widely used for bridge construction in Wisconsin. After being cured in saturated limewater for 28 days, the concrete cylinders were subjected to predefined compressive loads, equal to 40 though 80 percent of the measured compressive strength. The cylinders were then exposed to 300 freeze-thaw (F/T) cycles following a procedure similar to that described in ASTM C666. Concrete durability is closely related to its water and chloride permeability. Rather than measuring the dynamic moduli and weight losses, rapid chloride ion penetrability (RCIP) tests (ASTM C1202) were conducted to evaluate the chloride permeability of the concrete samples. Two 50-mm (2-in.) thick samples were sliced from each cylinder for the rapid chloride permeability tests. All RCIP tests were conducted within a week at roughly 120 days to minimize the impact of age to the test results. Samples sliced from cylinders without being subjected to loads and F/T cycles were also tested to provide reference performance.

The laboratory test results indicated that the mechanical loading combined with freeze-thaw cycles significantly increased the permeability of air-entrained concrete and may accelerate the deterioration of concrete elements such as bridge decks. The reference samples made of air-entrained concrete allowed very small amount of passing charges, indicating that the concrete used in the study can be classified as high performance concrete for northern States in US according to the high performance concrete (HPC) Lead State Team established by Federal Highway Administration (FHWA) in 1996. However, the chloride permeability of concrete samples increased significantly with an increase in the applied compressive loads. The highest increase in the total passing charge was 55 percent when compared with the samples from unloaded cylinders but subjected to F/T cycles. This increase became over 93 percent when the results are compared with the reference samples. The observed permeability increase was due to the fact that higher compressive loads caused more extensive microcracks in concrete. In addition, the initially damaged concrete further degrades under freeze-thaw cycles, which may have further opened and interconnected the microcracks.

The explanation for the test results was confirmed by the scanning electronic microscopic images of the loaded and unloaded specimens. The images of concrete parallel to the applied compressive load revealed the through-thickness microcracks that were responsible for the observed increase in chloride permeability in loaded specimens. The amount of microcracks as well as air voids was indirectly measured using water absorption values. A strong relationship was identified between the chloride permeability and the water absorption, which outlined a new test method that can be used to evaluate the durability of concrete in the field.

Concrete in bridge decks under a vehicular load is subjected to complex stresses. The actual complex stress states were not simulated in the laboratory tests on concrete permeability in this study. Instead, the bridge deck analyses were conducted to investigate stress distributions

and stress levels in typical concrete bridge decks subjected to high axle loads. The numerical analyses focused on compressive stresses in both longitudinal and transverse directions and the resulted minimum principal stress developed on top of concrete deck slab. Deck slabs develop compressive stresses from global flexural deformation and locally from high-level wheel loads when it is subjected to overweight trucks. Linear elastic analysis was first conducted for a sample bridge documented in WisDOT Bridge Manual as a design example and the simulated stresses were compared with the calculated stress during the design process to validate the modeling technique used in the study. Instead of modeling bridges with numerous geometric configurations including bridge type, span length, girder spacing, deck thickness, the majority of the bridge deck analyses were conducted on idealized bridge models. The idealized bridge models contained a segment of multi-girder bridges near the wheel loads. In addition to the wheel loads that simulated the high axle weights, the bridge segments were subjected to initial longitudinal stresses ranging from 10 percent of the concrete compressive strength in tension to 40 percent of concrete compressive strength in compression. These initial longitudinal stresses were used to simulate the global flexural stresses in the deck slab of a variety of bridges subjected to many types of loads. The numerical analyses were then used to capture the true stress that included the global bending stresses and the local stress concentrations.

The numerical analyses using the idealized bridge models indicated that the normal stress in bridge decks in the transverse direction can be significantly affected by the thickness of bridge deck, the girder spacing, and the magnitude of the wheel loads. The analyses results also indicated that the normal stresses in the longitudinal direction may be calculated as the summation of the stresses due to global bending of the bridge superstructure under the truck loads, which can estimated using typical design/rating procedures and the stress elevations near the wheel loads. The local stress increase in the longitudinal direction is about 80 percent of the transverse stress based on the limited number of analyses. In addition, the stress contours indicated that the normal stresses in the longitudinal and transverse directions are not highly coupled such that the minimum principle stress in the bridge decks is very close to the longitudinal stresses.

The analyses showed that the AASHTO design truck can cause low level stresses and therefore might not cause much internal damage to the bridge deck. Note that this conclusion did not include the impact of repeated loading. Meanwhile the overweight trucks may cause more than 50 percent increase in the minimum principal stress on the top of a deck slab. Specifically the local stress increase can be higher than $0.20f'_c$ when the thickness of deck is 7 in. In addition, the overweight truck also causes higher bending moments in bridge superstructure, thus leading to higher longitudinal normal stresses. The combined stresses in can be higher than $0.4f'_c$, which will cause internal micro-cracks in concrete as shown in the laboratory tests in this study. Empirical equations were proposed to capture the transverse stresses and the stress elevation in the longitudinal direction. The proposed equations can be used, in addition to the typical design/rating calculations, to capture the adverse stresses in bridge decks subjected to overweight trucks.

Table of Contents

List of Figures

List of Tables

Nomenclature

A	=	Empirical constant
b	=	Equivalent width of bridge deck
ΔE	=	Activation energy of the reaction process
I_o	=	Electric current (amperes) at initial stage
$I_{i*\Delta t}$	=	Electric current (amperes) at $i*\Delta t$ min
k_b	=	Boltzmann's constant
L	=	Span length of a bridge
n	=	No. of interval over 6-hour period (n=360/Δ t)
P	=	Applied one axle load
Q	=	Total charge passed, in coulombs
R	=	Resistivity of the sample
t	=	Thickness of deck slab
Δt	=	Interval (min) used to record current
S	=	Girder spacing length
S_1, S_2, S_3	=	First, second, and third principal stresses
T	=	Absolute temperature
$\sigma(T)$	=	Conductivity of the sample (1/R)
σ_x, σ_y, σ_z	=	Transversal stress, stress along vertical and longitudinal stresses
σ_{z0}	=	Initial longitudinal stress

Chapter 1. Introduction

1.1 Introduction

The service life of concrete bridges can be affected by material selection, construction process, environmental attacks, and traffic loading. The deterioration of well-constructed concrete bridges is mainly caused by traffic loads, especially heavy trucks and various environmental attacks (AASHTO, 2008; Tabatabai et al., 2011). The environmental attacks on bridges in cold climates include chloride penetration and the subsequent corrosion of steel reinforcement; freeze-thaw (F/T) cycles on concrete in saturated or near-saturated conditions; and scaling of concrete exposed to deicing salts (Mirza, 2006). Much research has been conducted to understand the mechanism of various environmental attacks, and technologies have been developed for durable concrete construction, including proper selection of raw materials, optimal mixture design, and adequate curing processes (ACI 201.2R-1). Meanwhile bridge decks constructed with laboratory-proven durable concrete often do not perform as expected, and multiple repairs and replacements are needed within their service life (Cady and Weyers, 1984; Elzafraney and Soroushian, 2005; Nagi, 2007).

Such undesired performance may be attributed to the conditions of the field concrete, which are different from that of the concrete samples in laboratories (Cady and Weyers, 1984; CEB, 1992). For example, concrete in the field is subjected repeated traffic loads. The strength requirements of traffic loads have been well satisfied in various design checks and bridge rating practices; however, the stresses in bridge components (i.e., bridge decks) and the resulting impact on bridge durability cannot be overlooked, especially when the bridge is subjected to overweight vehicles, as illustrated in Figure 1.1. The vehicle caused large, visible deflection in the steel girder bridge, indicating an elevated level of bending moments and internal stresses, in both tension and compression, in the bridge deck. Heavy trucks are usually allowed to operate on highways with a permit. For example, a previous study of trucks on Wisconsin highways using weigh-in-motion (WIM) records in 2007 indicated that 1.3 million out of 6 million recorded trucks weighed more than the legal limit, thereby requiring a permit for their operations. In addition, many overweight trucks can have high axle loads as shown in Figure 1.2 for Axle No. 3 in this group of overweight vehicles. Thousands of the trucks have an axle load beyond 40 kips and hundreds of them have an axle load beyond 50 kips. In addition, some vehicles have a axle load up to 74 kips (Zhao and Tabatabai, 2010).

Concrete in the field such as a bridge deck develops cracks due to drying shrinkage, temperature gradients, and mechanical loading, which are not present in the laboratory specimens used for evaluating the durability of concrete material. These cracks, usually caused by tensile stresses, are visible on the surface of bridge decks, causing concerns to bridge maintenance engineers (Cady and Weyers, 1984; Cao et al., 1996; Wan et al., 2010). This is because the surface cracks allow moisture and aggressive chemicals, such as chloride ions, to infiltrate the protective layer, leading to corrosion and the deterioration of concrete. However, it is recognized that such cracks contribute to an earlier onset of corrosion of reinforcement rather than significantly shortening the life of concrete bridge decks (Kostem, 1978).

Meanwhile, researchers have found that concrete bridge decks with a higher traffic volume have a higher deterioration rate (Nowak et al., 2000; Tabatabai et al., 2011). This

indicates that the durability of field concrete may be affected by truck-induced stresses in concrete. Rather than visible major cracks on deck surfaces, such stresses may cause internal microcracks, which increase the porosity and permeability of concrete (Elzafraney and Soroushian, 2005; CEB, 1992). Microcracks in concrete may also be caused by freeze-thaw cycles (Alexander, 1999). For example, Figure 1.3 shows the temperature variation on the deck of Hoan bridge in Milwaukee, WI, in solid black lines for the year 2007. When exposed to freezing temperature, free water in voids of saturated concrete creates internal hydraulic pressure. Concrete with poor freeze-thaw resistances thus develops microcracks in concrete, and such cracks near a surface lead to spalling and eventually the decomposition of concrete.

Laboratory tests have been used to explore and verify the means to improve the freeze-thaw resistance of concrete (Powers, 1949; Powers and Helmuth, 1953; Philleo, 1983). The impact of freeze-thaw cycles on concrete has been evaluated in laboratories by checking the weight loss and reduction in the dynamic modulus of concrete (ASTM C666, 2003). Air-entraining admixtures have been used to stabilize and to help distribute the air voids in concrete, which alleviates the internal disruptive pressure and thus improves the freeze-thaw resistance of concrete (Pigeon and Pleau, 1994).

The expected durability of air-entrained concrete may diminish in the field because both compressive stresses and freeze-thaw actions can cause microcracks in concrete. Such combined actions may accelerate concrete deterioration. For example, tests of samples taken from a 25 year old highway pavement indicated that the water permeability of the concrete subjected to traffic was much higher than that of the concrete without traffic loading (Yang et al., 2005). Micrographs of the samples revealed that more microcracks existed in concrete subjected to combined actions.

Structural loads from overweight vehicles have been considered in bridge design and rating processes, which mostly minimize the possibility of structural failure. This project examined the impact of vehicle induced stresses, along with freeze-thaw cycles, on the permeability of air-entrained concrete. Specifically, the focus was on compressive stresses since the impact of the various tensile stresses has been studied extensively in the literature.

1.2 Objectives

The goal of this project is to investigate impact of combined mechanical loading and environmental attacks on the durability of bridge decks. The objectives of the project were:

1) To determine the stress levels in concrete bridge decks from overweight vehicles;
2) To evaluate the impact of mechanical stresses and freeze-thaw cycles on concrete durability by measuring chloride permeability; and
3) To provide empirical relationships between overweight vehicles with high axle loads and the stresses in typical bridge decks.

1.3 Report Organization

This report is organized as follows. The laboratory tests and microcracks analysis of air-entrained concrete are presented in Chapter 2 through Chapter 4. Specifically, a review of existing studies and experimental tests on permeability of concrete with stress-induced cracks is

provided in Chapter 2. The experimental program of this study is described in details in Chapter 3, and the microcrack analyses are documented in Chapter 4. The micrographs provided evidences for the observed chloride permeability test results in Chapter 3. The bridge deck analyses are presented in Chapters 5 and 6. A series of subjects were identified for future studies in Chapter 7 in addition to summary and main conclusions.

Figure 1.1: Overweight vehicle on a bridge (Foley, 2007)

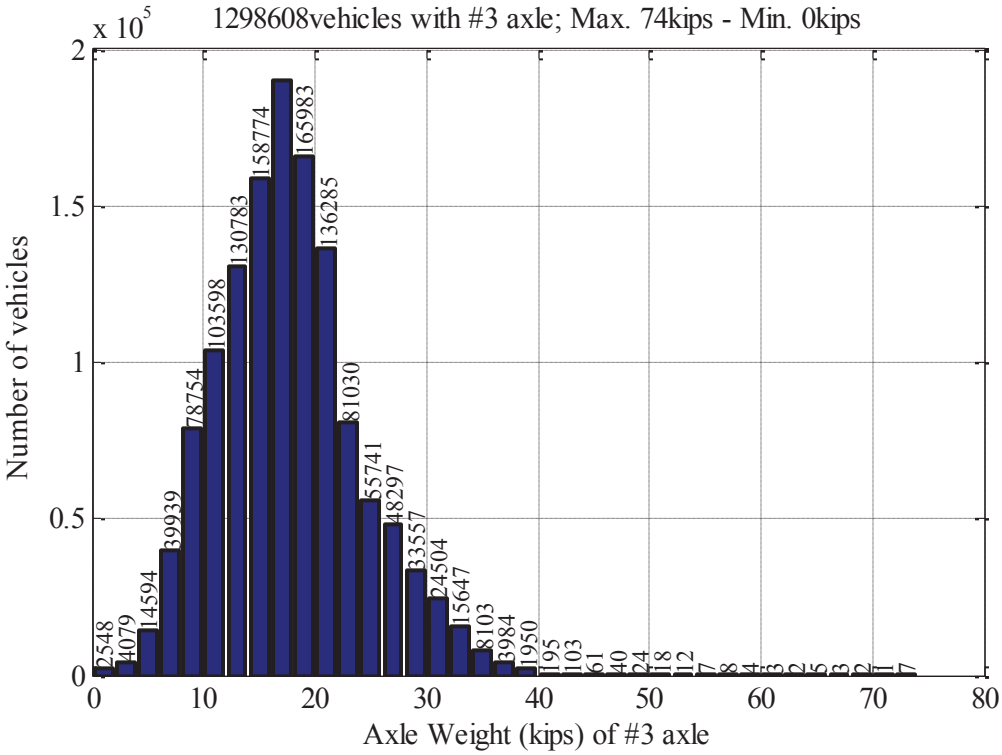

Figure 1.2: Distribution of the weight of No.3 axle

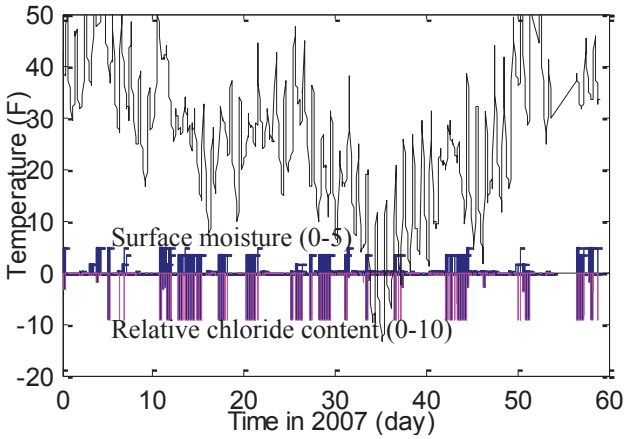

Figure 1.3: Temperature variation over times on bridge deck
(Data from Wisconsin Traffic Operations and Safety Lab.)

This page has been intentionally left blank.

Chapter 2. Literature Review

2.1 Introduction

The country's 590,000 bridges are critical for the US economy in transporting natural resources, agricultural products, and industrial goods. Mainly constructed in the 1950s and 1960s, US bridges are 45 years old today on average (AASHTO, 2008; Reid, 2008), with 50 percent of all bridges over 35 years old. According to data from the Federal Highway Administration (FHWA, 2008), it would cost $140 billion in 2006 to repair all deficient bridges (FHWA, 2006). The actual cost would increase due to inflation and soaring construction costs over time since the immediate total repair is not practical. To avoid the similar situations in the future, the new bridges are expected to have an increased service life (e.g., 100 years or 150 years for major connections in urban areas) (Freyermuth, 2001; Hook, 2003) compared with the old bridges (i.e., 50~75 years) (AASHTO, 2010). Bridge design has primarily focused on strength and stability while the new challenge of longer service life places additional requirements to bridge design: engineers need to equally consider concrete durability in the design (Mays, 1992; Sarja and Vesikari, 1996; ACI Committee 201, 2001; Gjørv, 2010).

The mechanical properties and durability of concrete can be affected by its component phases, including aggregate, cement matrix, interfacial transition zone between the aggregates and cement paste, and pore structures in the cement matrix. The onset and the rate of deck deterioration are closely related to the mechanism of mass transport processes in concrete. The permeability characteristics of concrete are affected by not only its porosity and the degree of saturation (Basheer et al., 1997; Shoukry et al., 2011), but also by mechanical loads (Oh, 1991; Laman and Ashbaugh, 2000) and other environmental attacks (Mays, 1992; Sarja and Vesikari, 1996). A brief review on concrete durability is provided below.

2.2 Literature Review

2.2.1 Durability of Concrete

Durability of concrete, as defined in ACI Committee 201 (2001), refers to its ability to resist weathering action (e.g., freeze-thaw cycling, leaching), chemical attack (e.g., acids, carbon dioxide, chlorides and sulfates), abrasion, or other processes of deterioration while maintaining its desired engineering properties. The durability of concrete affects the performance and service life of concrete structures, as schematically shown in Figure 2.1. Meanwhile, concrete durability is affected by structural design, material selection, casting and compaction, and curing conditions as illustrated in Figure 2.2 (CEB, 1992; Mays, 1992; Sarja and Vesikari, 1996). These influential factors determine or alter the microstructure of concrete. It is generally believed that that the pore structure dictates the moisture transport mechanism of concrete, which in turn impacts the deterioration of concrete. Concrete deteriorates when aggressive chemicals, carried by water through the pores in cement matrix, get inside concrete (CEB, 1992; Kropp and Hilsdorf, 2005; Mehta and Monteiro, 2006). Specifically, the chloride ions and moisture may destroy a protective film of steel reinforcement, leading to its corrosion (Mehta and Gerwick, 1982).

Therefore, the permeability of the concrete is a key factor that governs the rate of deterioration and thus influences the durability of concrete.

The permeability of concrete can be affected by the microcracks in the concrete due to temperature gradients, structural loading, and freeze-thaw actions, as illustrated in Figure 2.3. As a result, the structural loading and freeze-thaw cycles may be coupled with the processes of chemical deterioration (Mehta and Monteiro, 2006). In addition, temperature, the distribution and width of microcracks/cracks, and environmental conditions, affect the substance flowing and thus affect the permeability of concrete.

2.2.2 Permeability of Concrete

The hydration of cement is associated with the development of a pore system in concrete at nanoscopic, microscopic, and macroscopic levels, as illustrated in Figure 2.4. In addition, air bubbles with diameters of about 50-200 μm can be introduced in the cement paste by air-entraining admixtures, as summarized by Whiting and Stark (1983) and Lamond and Pielert (2006). Capillary pores (size varying from 30 nm to 30 μm) and macro-pores (size from 30 μm to 1 mm), influences the moisture transport in concrete and is thus associated with the durability of concrete (CEB, 1992; Mehta and Monteiro, 2006).

Besides pore systems, freeze-thaw cycles and structural loading may cause microcracks in concrete. The fluid transport of the concrete is also associated with microcracks (Oh, 1991; Laman and Ashbaugh, 2000) because microcracks interconnect the pores into passageways that may facilitate the transport of liquids (CEB, 1992). The permeability of concrete may be reduced by the use of supplementary cementitious materials, such as fly ash, ground granulated blast-furnace slag, and silica fume, in concrete mixtures (Mays, 1992; Sarja and Vesikari, 1996; Sengul, 2005; Gjørv, 2009). For example, chloride permeability of concrete with fly ash, as measured in Rapid Chloride Ions Permeability (RCIP) tests (ASTM C1202), indicated that the charge passed through the concrete samples can be greatly reduced with an increase in the quantity of fly ash in the mixture as shown in Figure 2.5 (Sengul, 2005).

2.2.3 Chloride Permeability Tests

Ingress of dissolved chloride (and sulfate) ions into concrete can be accounted for by unsteady- or steady-state diffusion, and the diffusion is more effective in saturated pores (Wilkinson, 2000; Bertolini et al., 2004). ASTM standard tests such as the chloride ion permeability ponding test, chloride diffusion test, and rapid chloride ion permeability tests are usually used to determine the diffusion rate for chloride ions, as summarized by Lane (2009).

-Salt Ponding Test: this standard test (ASTM C1543) is often used to determine the penetration of chloride ions into concrete. In a salt ponding test, the test specimen is conditioned under moist curing for 14 days followed by another 14 days of drying with a 50 percent relative humidity. A dike is then casted around the top edges of the test specimen to contain a 3% by mass sodium chloride (NaCl) solution while the lateral surfaces of the specimen are coated using epoxy to avoid leaking and evaporation. A typical ponding test is conducted at room temperature about 23 °C (73 °F) and at 50% relative humidity for a minimum of 90 days. Longer test periods are usually used for high performance concretes with low permeability. After the completion of the ponding process, samples (13-mm (0.5-in.) thick discs) are extracted through the depth of the

specimen for chloride content analysis. The chloride content of each disc indicating the amount of chloride migrated into the concrete is determined in accordance with ASTM C1152 (2004a).

-Chloride Diffusion Test: This standard test (ASTM C1556) is used for determining the apparent chloride diffusion coefficient of concrete. A test specimen usually has a 75 mm (3 in.) diameter and is 75 mm (3 in.) long. The specimen is first coated with epoxy leaving one polished surface that is expected to be exposed to salt solution and then conditioned in lime-saturated water for 6 days before being immersed in 15 percent by mass sodium chloride (NaCl) solution. The specimen remains immersed in the salt solution for at least 35 days. Cores are taken from the specimen for chloride content analysis. The chloride content in the cored samples is measured at an increment of 1 to 2 mm (0.04 to 0.08 in.). The measured chloride content as a function of depth from the exposed surface are used to calculate the apparent chloride diffusion coefficient in accordance with ASTM C 1152 (2004a).

-Rapid Chloride Permeability Test: This standard test (ASTM C1202) for rapid chloride ions permeability (RCIP) is usually used in laboratories to evaluate resistance of concrete to chloride penetration. The RCIP test was originally developed by Whiting (1981) to provide a fast means of evaluating the chloride permeability of concrete, the results of which are expected to be equivalent to the 90-day ponding tests as mentioned above (ASTM C 1543; Shi, 2003). Chloride ions, carrying negative charges, move through the pores and microcracks in concrete under a 60-volt potential. The total charge passed through the specimen (in coulombs) within six hours is used to reflect the concrete permeability as shown in ASTM C1202. The basic procedures of RCIP test consist of conditioning samples and monitoring the amount of electric current. Specifically, test samples with a 101.6-mm (4-in.) diameter and a 50.8-mm (2-in.) thickness with sides coated with epoxy are placed in a vacuum desiccator under no more than 1 mm Hg for three hours for conditioning purposes. De-aerated water is used in the conditioning chamber and also in making NaOH and NaCl solution. After the three hours, de-aerated water is filled into the vacuum desiccator till totally covering the specimens and then the vacuum is maintained for an additional hour. After this additional hour, the vacuum pump is turned off and the vacuum desiccator is opened to atmospheric pressure. The test specimens within de-aerated water are saturated for 18 hours (± 2 hours). The test specimens are then placed in RCIP test cells. The negative terminal is attached to the end cap containing sodium chloride and the positive terminal is attached to the end cap containing sodium hydroxide. A potential of 60 volts is then applied to each specimen for six hours. Also, the temperature is monitored with a probe inserted in the NaCl reservoir. A data acquisition system connected to PC screen is used to automatically measure the total coulombs passed through each specimen during a six–hour period.

In an RCIP test, the amount of electric current passing through the test specimen under a 60-volt potential is measured during a 6-hour period. The change of charge passed through a test sample, dQ, is a function of the electric current, I, under time, dt:

$$dQ = Idt. \tag{2.1}$$

Thus, the total charge passed is derived by integration of the electric current over the time,

$$Q = \int Idt. \tag{2.2}$$

Specifically, ASTM C1202 stipulates that total charge passed in RCIP test is approximately determined by summing up the area of the electric current curve over a 6-hour period

$$Q = \frac{60\Delta t}{2}(I_0 + I_{360} + 2\sum_{i=1}^{n-1} I_{i*\Delta t}), \quad (2.3)$$

where,

Q = Total charge passed, in coulombs;
Δt = Interval (min) used to record current;
n = No. of interval over 6-hour period (n=360/Δ t);
I_o = Electric current (amperes) at initial stage;
$I_{i*\Delta t}$ = Electric current (amperes) at i*Δt min.

A higher passing charge (in coulombs) in an RCIP test indicates test sample may have higher permeability and lower durability. In addition, the electric current heats up the test specimen, and the elevated temperature in turn affects the electric current through the sample. The conductivity of the sample, $\sigma(T)$, is a function of its temperature, T according to Whittington et al. (1981) and Liu and Beaudoin (2000),

$$\sigma(T) = \mathrm{A} * exp(-T\Delta E/k_b), \quad (2.4)$$

where,

$\sigma(T)$ = Conductivity of the sample (1/R);

R = Resistivity of the sample;

A = Empirical constant;

ΔE = Activation energy of the reaction process;

T = Absolute temperature;

k_b = Boltzmann's constant.

Eq. (2.4) indicates that the conductivity of the test sample increases with an increase in its temperature. Therefore, the measured current needs to be modified according to the measured sample temperature. With the electric current passing through the test sample, the temperature of the sample may rise due to the effect of Joule heating (Julio-Betancourt and Hooton, 2004; Benz, 2007).

$$J = VIt, \quad (2.5)$$

where,

J = the heat (joules);
V = the potential (volts).

Various methods have been proposed to eliminate the Joule heating effects on the measured passing charge (Julio-Betancourt and Hooton, 2004) in a RCIP tests. This includes the use of low voltage (McGrath and Hooton, 1999; Liu and Beaudoin, 1999) in the tests. In addition, the test time may be reduced. For example, the charge passed can be measured within 30 minutes rather than 6 hours (McGrath, 1996; McGrath and Hooton, 1999). The latter method is used to correct the total charge passed due to Joule heating, that is,

$$Q_c = 12Q_{30}, \quad (2.6)$$

where,

Q_c = Corrected charge passed (in coulombs);
Q_{30} = charge passed over the first 30 minutes (in coulombs).

This method, based on Eq. (2.6), was used in this study to adjust the charge passed to minimize the temperature effect.

In summary, both salt ponding test (ASTM C1543) and Chloride diffusion test (ASTM C1556) are used to determine the chloride diffusion characteristics in concrete. On the other hand, without complex chloride content analysis, RCIP test offers an indirect but effective way to evaluate the chloride permeability of concrete. Also, the RCIP test results are found to correlate well with that of 90-day salt ponding tests (McGrath and Hooton, 1999, Shi, 2003).

2.2.4 Water Permeability Tests

Water in capillary pores attributes to the majority of free water in concrete (CEB, 1992), which can be critical for the freeze-thaw resistance of concrete (Bertolini et al., 2004). The property of concrete to absorb free water by capillary action is defined as sorptivity (Wilson et al., 1999) and the water absorption process has been described by the nonlinear diffusion equation (Hall, 1989; Martys and Ferraris, 1997; Lockington et al., 1999). Water absorption tests are also used to evaluate the permeability of concrete (Lockington et al., 1999, and Wilson et al., 1999; Wang et al., 1997; Martys and Ferraris, 1997). The standard tests include the water permeation test stipulated by Corps of Engineers Standards (CRD-C 163-92, 1992) and the capillary sorption test by ASTM C 1584 (2010).

-Water Permeation: This test is used to measure the water permeation of concrete based on a steady-state flow condition through a cylindrical concrete specimen placed in a triaxial cell. The cylindrical specimen with a diameter within 20 to 100 mm (0.79 to 3.94 in.) and a length of 280 mm (1.1 in.) is vacuum saturated in deionized water under the pressure of at most 1 mm Hg for at least 72 hours. The conditioned specimen is then placed into the triaxial cell with deionized water. A compressed nitrogen gas provides the confining radial pressure, and a gas-over-water accumulator is used to maintain the hydraulic pressure drop along the length. The volume flow rate is measured to obtain permeability of the specimen using Darcy's law (Cemica, 1995).

-Water Sorptivity: This standard test (ASTM C 1584) is for measuring the rate of water absorption through concrete. The test specimens with a 50-mm (2-in.) depth and a 100-mm (4-in.) diameter are first conditioned in an oven for three days at a temperature of 50 °C (122 °F) and a relative humidity of 80%. The bottom surface of the test specimen is indulged into the water about 1 to 3 mm (0.04 to 0.12 in.) while the rest sides of the specimen are sealed with epoxy to avoid evaporative effects. After 8 days, the change in the sample mass over time is used to calculate the rates of water sorption of the concrete (ASTM C1584).

In general, pressured water absorption tests are used to determine water permeation through pore system while the near-surface sorptivity test (ASTM C 1585) are used for determining the absorption rate of water into the capillary pore system of concrete. Other water absorption tests have been proposed in the literature (Kermani, 1991; Wang et al., 1997; Hearn, 1999; Yang et al., 2005; Banthia et al., 2005; Hoseini et al., 2009), which will be reviewed in more details in the Section 2.2.7.

2.2.5 Influence of Freeze-Thaw Action on Permeability of Concrete

When the capillary pores are filled with water in saturated or near-saturated concrete, and the temperature is below the freezing point, the transformation of ice crystals from liquid water in those small capillary pores, as illustrated in Figure 2.6a, may generate hydraulic pressure that

damages the capillary walls (CEB, 1992; Mehta and Monteiro, 2006). The high pore pressure may lead to microcracks/cracks, which facilitate the moisture transport in concrete.

Air entraining admixtures have been shown effective in reducing the pressure buildup by providing an effective escape boundary using evenly distributed air bubbles, as shown in Figure 2.6b (Powers, 1949; Powers and Helmuth, 1953; Powers, 1975; Whiting 1983; Lamond and Pielert, 2006). Air-entraining agents can stabilize air bubble distribution in cement paste (Powers, 1975; Whiting, 1983). When ice is formed in a capillary pore, some of ice crystals can expand with less restraint near the air bubbles, leading to a reduced hydraulic pore pressure (Powers, 1975; Mehta and Monteiro, 2006). In addition, the growth of ice crystals in the air voids is accompanied by water diffusion from the capillary pores to air voids due to osmotic transport (Powers, 1975; Mehta and Monteiro, 2006), thus reducing the hydraulic pressure in the cement paste.

Extensive laboratory tests have showed that the air void system needs to have proper sizes, volumes, and spacing factors in order to provide effective protection against frost damage (Powers, 1949; Powers and Helmuth, 1953; Powers, 1975). Specifically, an air void system with a spacing factor of 0.01 in. (0.25 mm) or less have been shown effective (Powers, 1949). In addition, the size of the air voids should be within the range of 50-200 μm, and the total air content should be from 5 to 8 percent for durable concrete (ASTM C260).

ASTM standard test (ASTM C666) is widely used in the laboratory to evaluate frost resistance of concrete. The standard specimens (either prisms or cylinders) with a dimension of a width/diameter within 3 in. (75 mm) to 5 in. (125 mm), and a length within 11 in. (275 mm) to 16 in. (405 mm) are stipulated. Each freeze/thaw (F/T) cycle starts from lowering temperature of specimens from 40 °F to 0 °F (4 to –18 °C) and then to raising the temperature from 0 °F to 40 °F (–18 to 4 °C) within 2 to 5 hours. The frost resistance of concrete during rapid freezing and thawing test is determined using ASTM standardized tests C215 through relative dynamic modulus of elasticity (RDM). The dynamic modulus of elasticity of specimens is estimated form the transverse vibration frequency (ASTM C215). Failure due to frost damage is defined when the value of RDM is below 60 percent after 300 cycles, in accordance with ASTM C666 Procedure A. Another alternative measurement of frost resistance of concrete after F/T cycles is length change of specimen (ASTM C490). The change of the specimen length is determined by measuring the effective gage length between the innermost ends of the gage studs before and after cycles.

2.2.6 Bridge Deck Performance

Bridge deck deterioration is a continuous process that is affected by bridge design, material selection, construction, environmental attacks, and traffic loading. The environmental attacks on bridge decks may include freeze/thaw (F/T) actions on concrete exposed to freezing temperature in saturated or near-saturated conditions; scaling of concrete exposed to deicing salts; and chloride penetration and the resulting corrosion of steel reinforcements. The environmental exposures (such as temperature variation and the moisture content of concrete) that concrete bridge decks are subjected to differ from that in laboratory tests. For example, Figure 1.3 shows the temperature variation on the deck of Hoan bridge in Milwaukee, WI, in solid black lines for the year 2007. The low temperature of most possible freeze-thaw (F/T) cycles is higher than 0°F. The temperature variations on the deck surface at the end of January may not qualify as an F/T cycle because the high temperatures are below 20°F. In addition, the

rate of temperature variation is very low compared with that in laboratory tests (Pigeon et al., 1985; ASTM C 666, 2003). Thus, if subjected to less severe environmental attacks, the deck made of durable concrete is not expected to deteriorate over the design life of most bridges (e.g., 50~75 years).

However, concrete bridge decks often need multiple repairs and even deck replacement within its design life (Cady and Weyers, 1984; Elzafraney and Soroushian, 2005). Daily truck traffic might cause fatigue-related damage to bridge decks (Oh, 1999; Laman and Ashbaugh, 2000; Boothby and Laman, 1999). Laboratory studies have indicated the possibility of damaging bridge decks by repeated mechanical loading; however, field studies of similar bridges subjected to different loading have failed to show significant damage due to increased vehicle loading. Meanwhile, some research has reported insignificant influence of mechanical loads on bridge deck deterioration (James et al., 1987). Other researchers have suggested that very little of the concrete damage should be assigned to mechanical loading caused by daily truck traffic (Beeby, 1978). Note that most of these studies on deck deterioration by truck loading have focused on vehicles with legal weights and the damage has been represented by the visible cracks on deck surfaces.

The stresses in bridge decks can be significantly increased when a bridge is loaded by overweight vehicles, as illustrated in Figure 1.1. The overweight vehicle caused large, visible deflection in the steel girder bridge, indicating an elevated level of bending moments and internal stresses, in both tension and compression, in the bridge deck. In addition, some studies have indicated that axle weights are more important indicators of deck damage than gross vehicle weights (Laman and Ashbaugh, 2000; Boothby and Laman, 1999). With these loads, the compressive stresses can be high enough to cause internal damage (i.e., micro-cracking) to the bridge deck. The micro-cracking in concrete may increase the permeability of the concrete and accelerate the deterioration of bridge decks. Thus, the stress-induced microcracks play an essential role in permeability of concrete and reviewed as detailed in the following section.

2.2.7 Influence of Stress-Induced Damages on Permeability of Concrete

The effects of mechanical stress-induced macrocracks on the transport properties of concrete have been studied much as summarized by Hoseini et al. (2009). Most existing studies focused on the effects of cracks resulted from shrinkage, tensile loading, and bending moments (Yang et al., 2005, Wang et al., 1997; Aldea et al., 1999; Aldea et al., 1999; Rapoport et al., 2002; Yang et al., 2006; Kim et al., 2010). Wang et al. (1997) investigated the water transport properties of concrete with cracks created by controlled splitting tensile forces. The cracked samples were first conditioned following the procedures for rapid chloride permeability tests (AASHTO T277). The water transport of cracked concrete in the study, as shown in Figure 2.7, was measured based on a concept developed by Ludirdja et al. (1989), in which water was forced through the preformed cracks under a low water pressure head. The drop in water pressure head was monitored for 20 to 50 days, and the results were explained using Darcy's law (Cemica, 1995). The tests showed that water flow through a tensile splitting crack was negligible when the crack opening was less than 50 microns while the water flow increased sharply when the crack was in the range of 50 to 200 microns. Shah and his group (Aldea et al., 1999; Aldea et al., 1999; Rapoport et al., 2002) further studied the water permeability of several types of concrete, including high-strength and fiber-reinforced concrete with tensile splitting cracks. It was suggested a crack width of 100 microns be used as a permeability threshold for concrete, under

which the water permeability of concrete was negligibly affected. It should be noted that smaller cracks that did not allow water flow may still facilitate chloride ingression as shown later in this study.

Rather than using tensile splitting tests, Yang et al. (2005, 2006) investigated the effects of tension cracks on the permeability of concrete. The direct tension was applied to concrete samples with closed-loop control, and the crack levels were monitored using acoustic emission technique. Water permeability test was used similar to a low-pressure ponding absorption test developed by Bentz et al. (2001). The sides of the sample sliced from a preloaded cylinders were coated with epoxy and then conditioned in an environmental room with a controlled temperature of 23 ºC (73.4 ºF) and a relative humidity of 50 percent for 14 days. A ponding dyke was cast on the top of each sample, and approximately 15 mm (0.6 in.) deep water was added. The mass change of the sample was recorded at certain time intervals. The study showed that the water absorption increased substantially when concrete was subjected to approximately 90% of peak tensile capacity. In addition, image analyses showed that the increase in the water absorption was mainly due to a major crack caused by the direct tensile loading.

The permeability of concrete after being subjected to direct tensile loading was also evaluated by Kim et al. (2010) using chloride penetration test in accordance with NT BUILD 492 (1999). This test, as illustrated in Figure 2.8, allowed the determination of the chloride diffusion coefficient from the measured chloride penetration depths. The preconditioned samples were placed on an oblique surface of a plastic stand in a reservoir. One side of the samples was filled with a 0.3 percent normal solution of sodium hydroxide and the rest surface was exposed to a 10 percent sodium chloride solution. The negative terminal was attached to the end electrode containing sodium chloride and the positive terminal was attached to the end electrode containing sodium hydroxide. A potential of 15 volts was then applied for 24 hours. The chloride penetration depth was observed and recorded by splitting samples into half and spraying with silver nitrate solution on the splitting surface. The tests indicated that chloride permeability increased more than ten percent when tensile load was 30 percent of the tensile capacity. In addition, and the observed chloride penetration was significantly affected by the localized damage to concrete caused by direct tension.

Unlike the common views on the impact of tensile loading on the concrete permeability, different opinions exist on the influences of compressive loading. Hearn (1999) investigated the water transport properties of cracked concrete under various levels of compressive loading. The compression test setup is shown in Figure 2.9. samples were sliced from preloaded concrete cylinders and conditioned in accordance with AASTHO T277 procedure (AASHTO T277). The samples were then placed in a permeameter cell filled with water. A low hydraulic pressure was applied, as illustrated in Figure 2.10, and the water flow was recorded for about 20 hours. Hearn indicated that mechanical loading did not affect the water permeability of concrete till up to 80 percent of the concrete compressive capacity. Meanwhile, Kermani (1991) examined the water permeability of concrete using a high-pressure water permeability test, as illustrated in Figure 2.11. Similar to Hearn's tests, the concrete samples were sliced from cylinders after being subjected to different levels of compressive loading. The samples were placed into a steel cylinder and their top surfaces were exposed to pressurized water. Rather than the low pressure caused by the self weight of water in Hearn's tests, a hydrostatic pressure of 10.5 MPa (1523 psi) was applied using a hydraulic pump. The high water pressure facilitated water through the microcracks. As a result, the measured water permeability increased dramatically when the

compressive loading was above 40 percent of the concrete compressive capacity. Similarly to Kermani (1991), Banthia et al. (2005) proposed a test setup, as illustrated in Figure 2.12, to determine the water absorption in the presence of mechanically compression loading. Unlike a traditional solid cylinder, the proposed test specimen was a 200-mm long hollow cylinder with a 50 mm inner diameter and 100 mm outer diameter. The inner hollow core was intentionally designed to collect water permeated through the 25 mm thick concrete cylinder outer wall under a pressure of 1.0 MPa. During this period of water transport processes, compression loading, as shown in Figure 2.12, was placed on the top of the cylinder. The test results showed that the permeability of concrete can be significantly increased when the applied stress is above 40 percent of the compression strength.

In addition to water permeability tests, the effects of compressive loading on concrete permeability have also been investigated using rapid chloride permeability tests. Samaha and Hover (1992) measured chloride penetration through samples from concrete cylinders subjected to various levels of compressive loading. Chloride permeability of concrete is determined by standardized RCIP tests (ASTM C1202). The test results indicated that the charge passed did not significantly increase until the compressive load level was above 75 percent of the load capacity. Similar observations were made by Saito and Ishimori (1995) in their study of normal weight concrete subjected to static and repeated compressive loads. Chloride permeability in concrete, measured by using RCIP tests (ASTM C 1202), was little affected by the monotonic load level even up to 100 percent and by the repeated load up to 60 percent of the load capacity. It was concluded that mechanical loading had insignificant influence on concrete permeability, which is against the field observation described above in Chapter 1.

The discrepancy of these findings indicates that levels of compressive loads may not necessarily reflect the resulted internal damage in concrete due to the heterogeneous nature of concrete materials and the variations in the applied loads. Such damage can be represented by microcracks, especially those connected into passageways for chimerical ions. In addition, the combined effects of mechanical loading and environmental attacks on the permeability and durability of concrete have not been fully understood.

Table 2.1: RCIP test results for quality control (ASTM C 1202)

Charge passed (coulombs)	Chloride ion penetrability
> 4000	High
2,000-4,000	Moderate
1,000-2,000	Low
100-1,000	Very low
< 100	Negligible

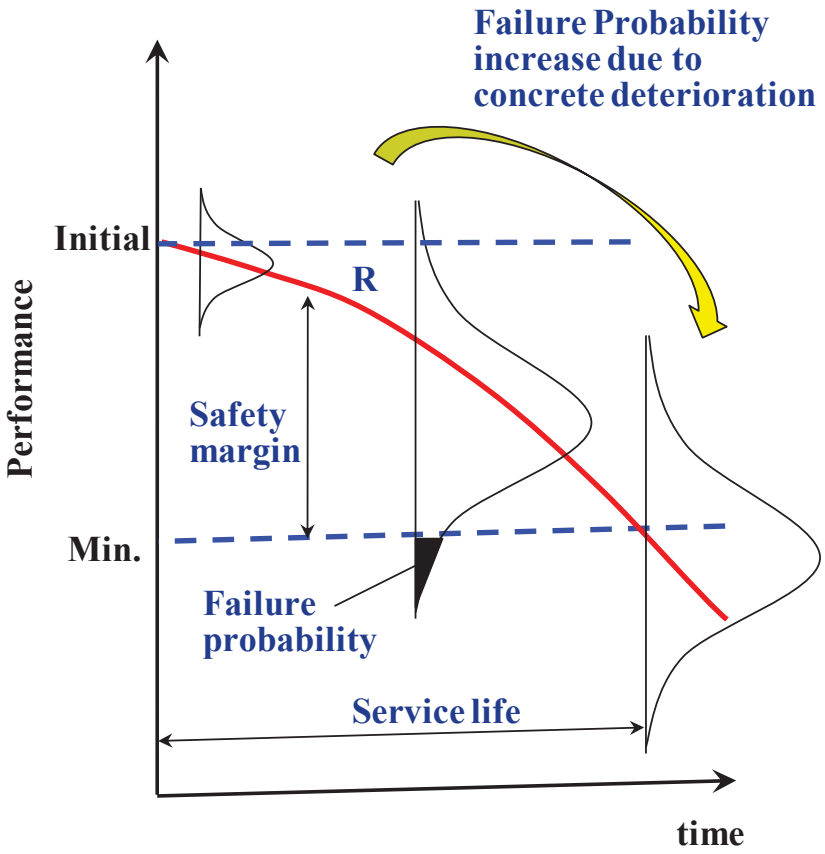

Figure 2.1: Concrete performance vs. service life (Sarja and Vesikari, 1996 and CEB, 1992)

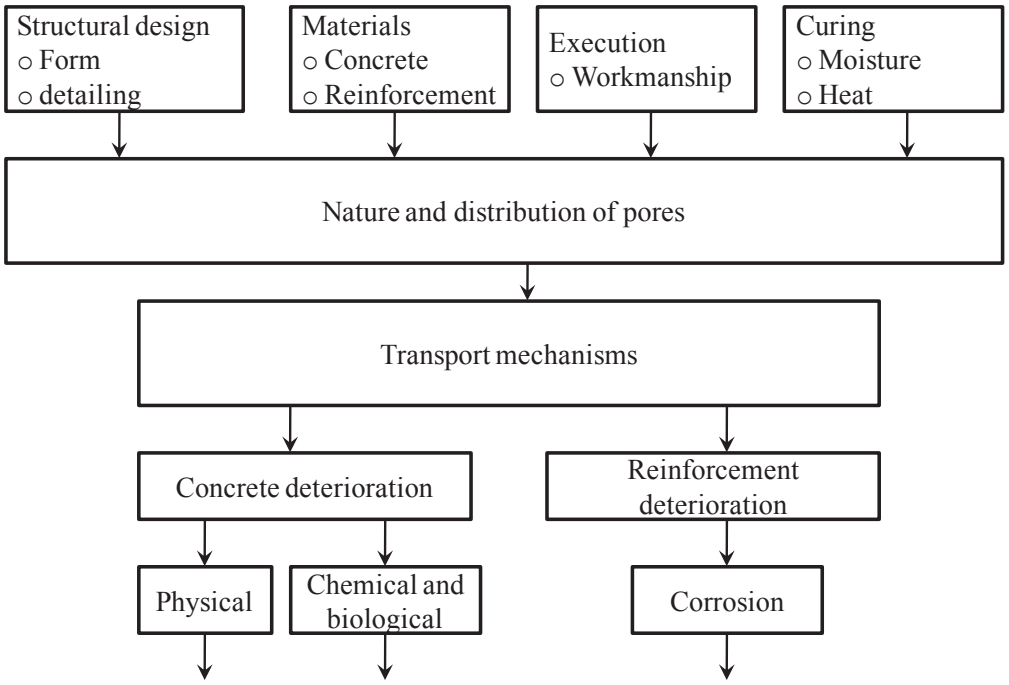

Figure 2.2: Concepts of concrete durability(CEB, 1992)

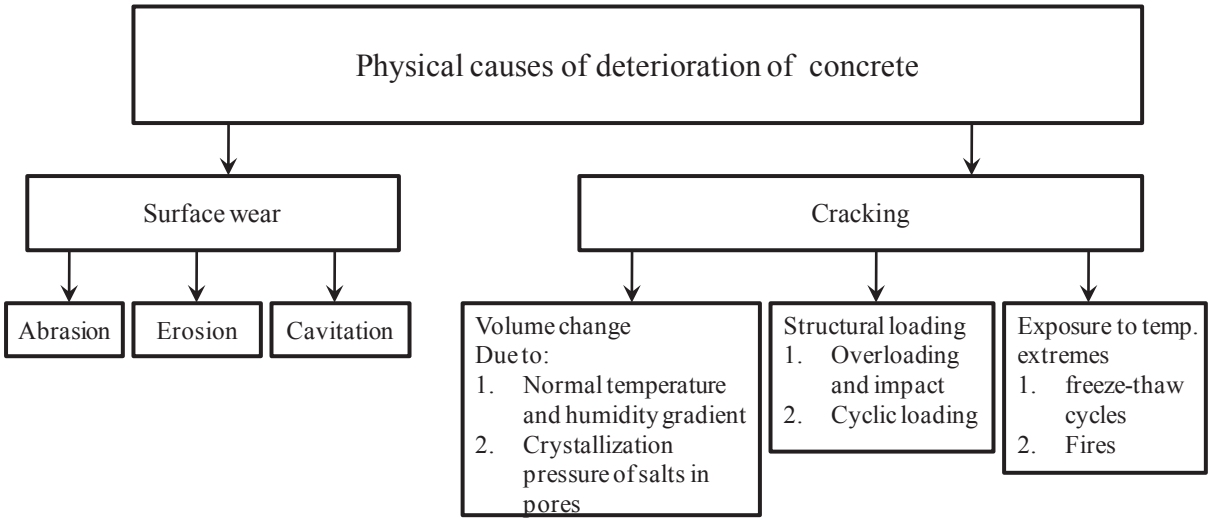

Figure 2.3: Physical causes of concrete deterioration (Mehta and Gerwick, 1982)

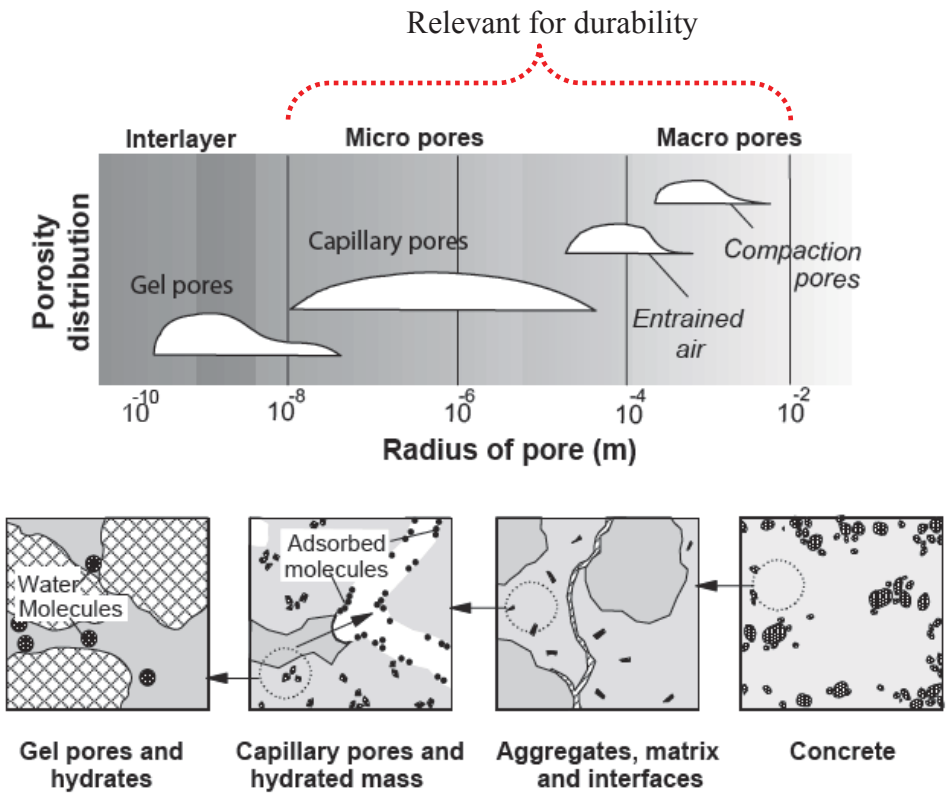

Figure 2.4: Pore size distribution and size range relevant for durability (Maekawa et al., 2009)

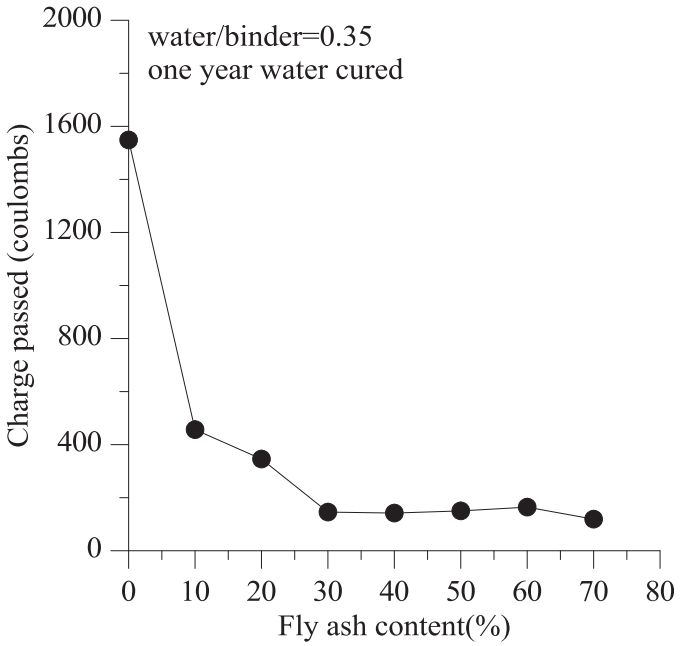

Figure 2.5: Effect of fly ash on the rapid chloride permeability of concrete with a water/cementitious material ratio of 0.35 and one year water curing (Sengul, 2005)

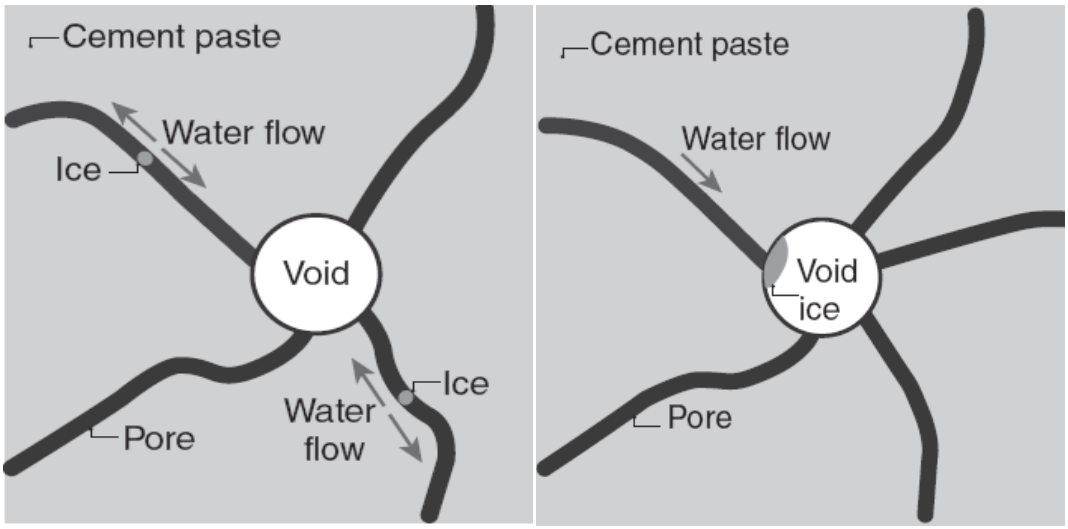

(a) Schematics of ice forming in capillary voids (b) Schematics of ice forming in air voids

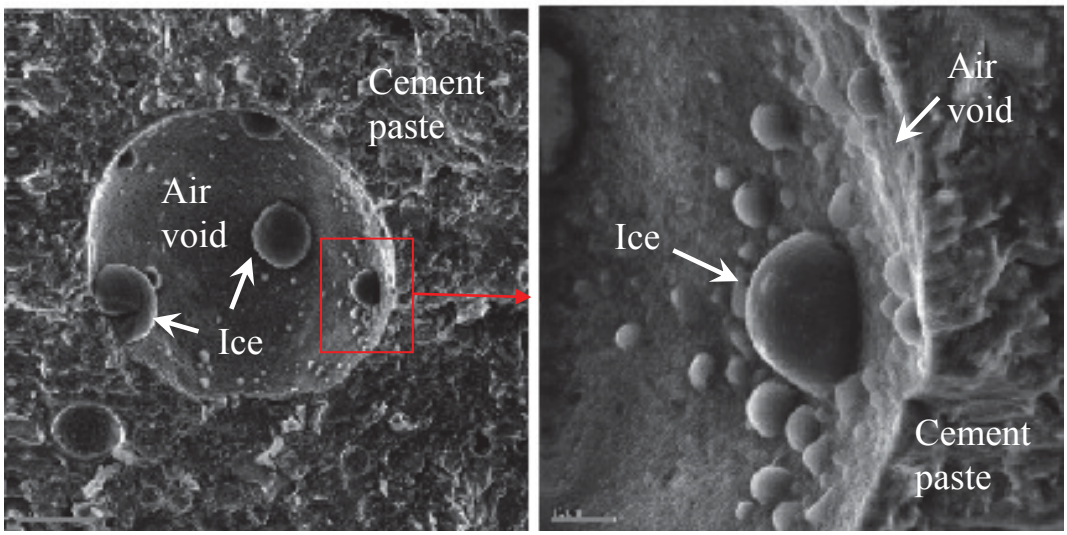

(c) Scanning electron micrograph of ice crystals growing in an air void

Figure 2.6: Ice forming in an air void (Mehta and Monteiro, 2006)

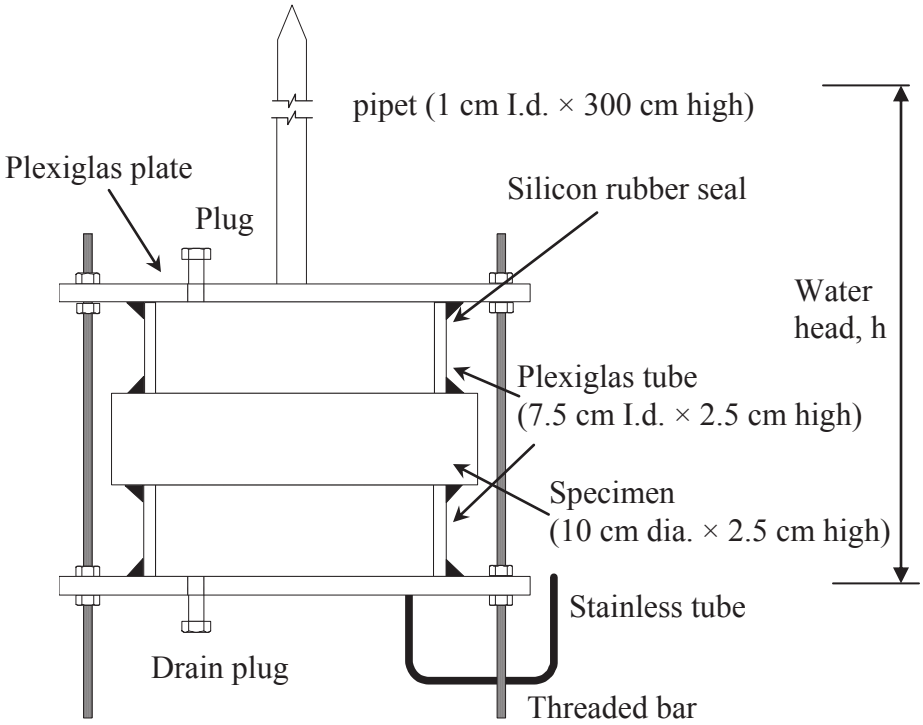

Figure 2.7: Water Permeability Test setup (Wang et al., 1997)

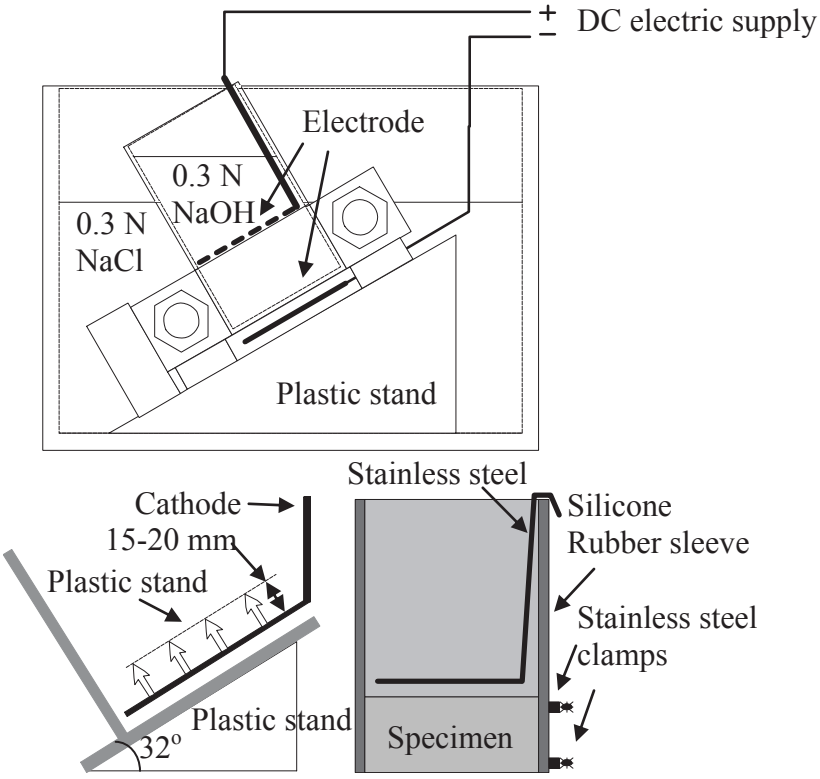

Figure 2.8: Water Permeability Test setup (Kim et al., 2010)

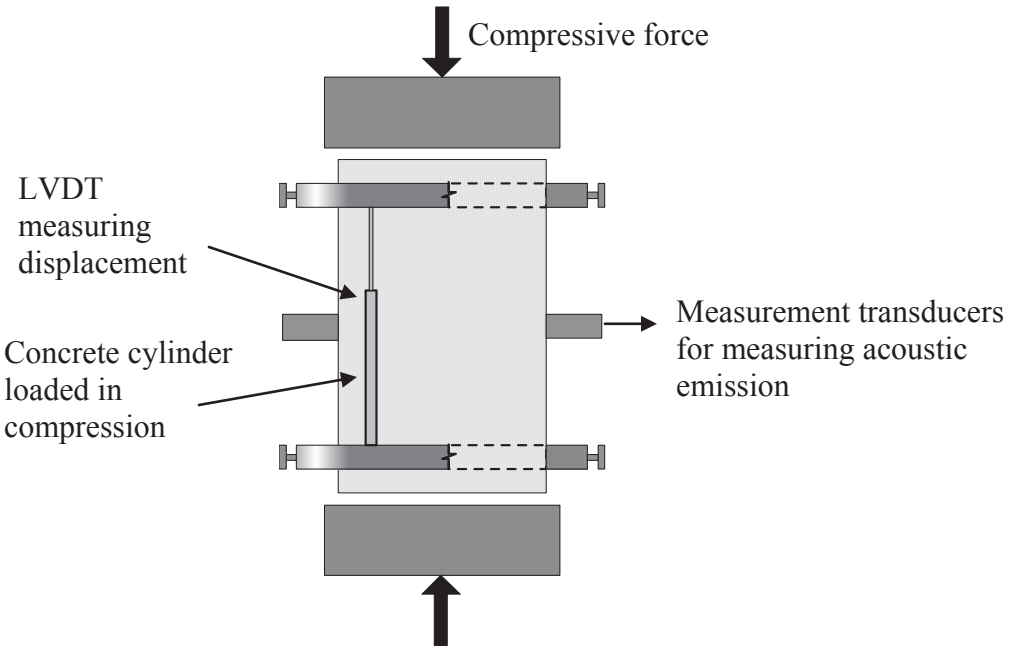

Figure 2.9: Compression Test setup (Hearn, 1999)

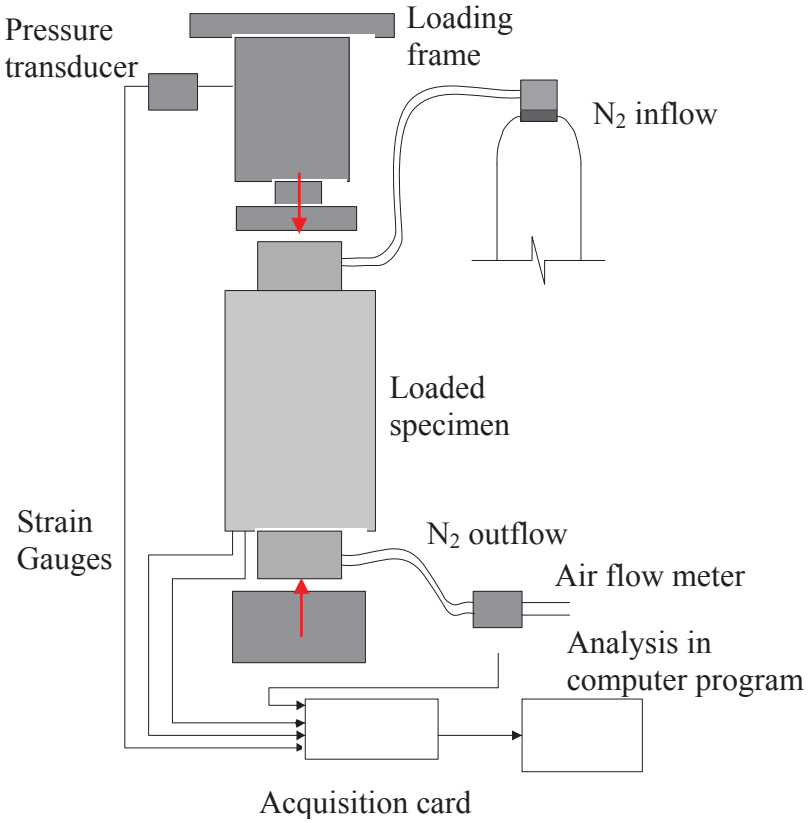

Figure 2.10: Water Permeability Test setup (Hearn, 1999)

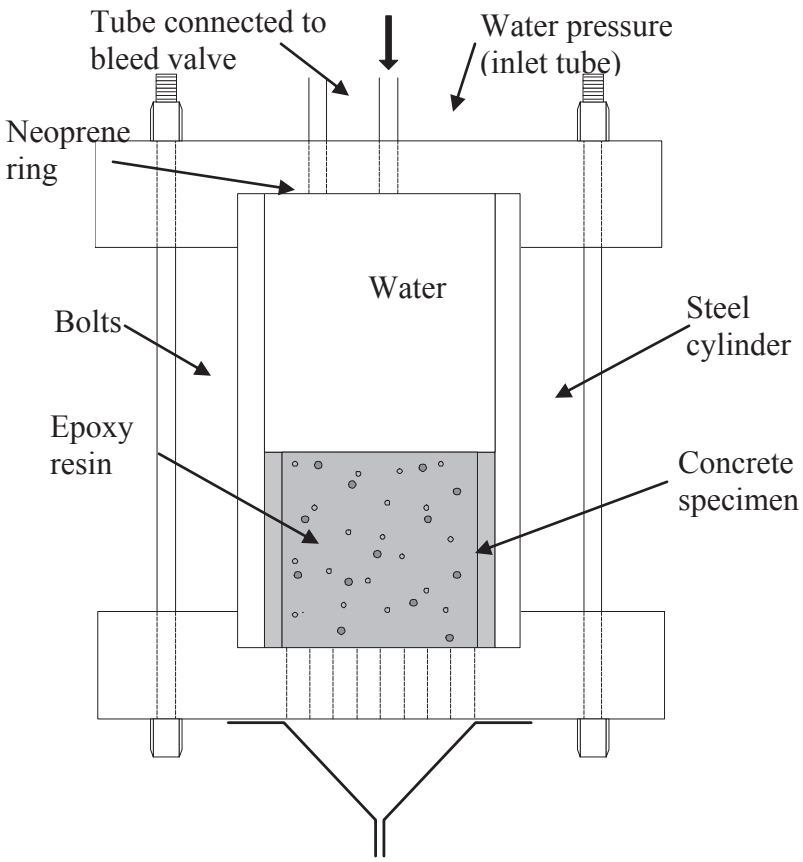

Figure 2.11: Water Permeability Test setup (Kermani, 1991)

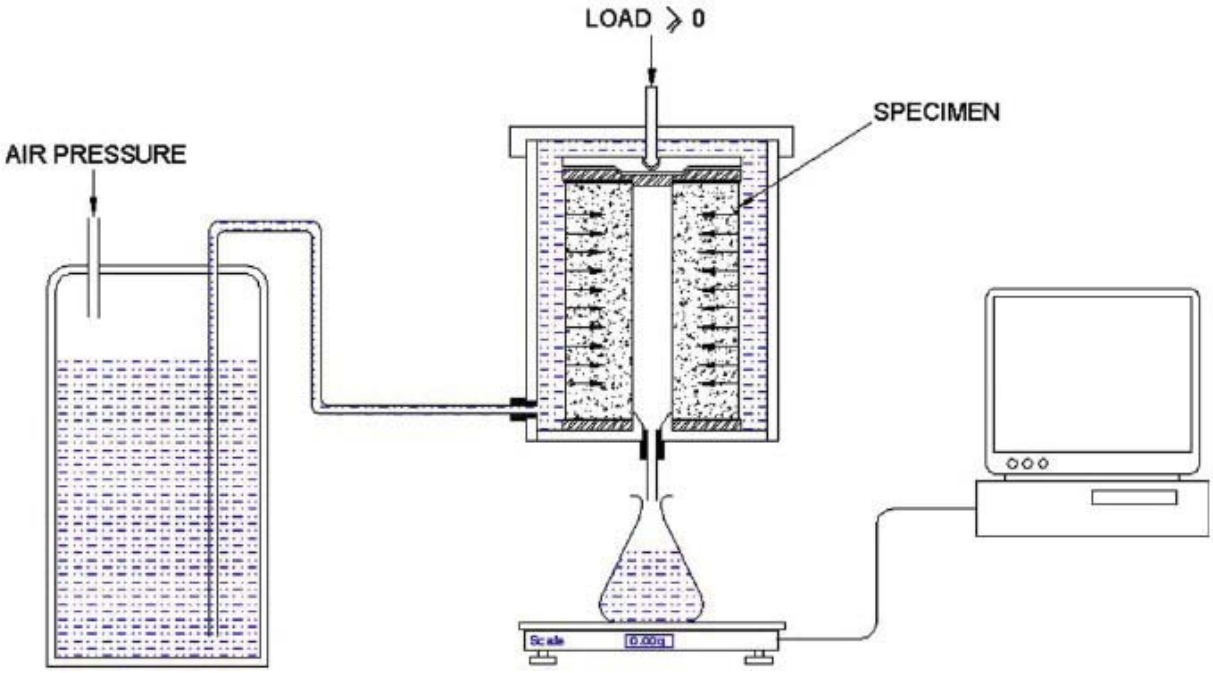

(a) Schematics of test setups

(b) Photos of test setups

Figure 2.12: Water Permeability Test setup (Banthia et al., 2005)

This page has been intentionally left blank.

Chapter 3. Experimental Program

3.1 Introduction

This study focused on evaluating the impact of combined mechanical stresses and freeze-thaw cycles on the durability of air-entrained concrete. Concrete durability is closely related to its water and chloride permeability (CEB, 1992; Mehta and Monteiro, 2006). Therefore the rapid chloride permeability tests were conducted on concrete samples sliced from 100×200 mm (4×8 in.) cylinders. The test procedure is described below.

3.2 Test Procedure

The test procedure is schematically shown in Figure 3.1. 100×200 mm (4×8 in.) concrete cylinders were first subjected to predefined compressive loads after being cured in saturated limewater for 28 days. The cylinders were then exposed to 300 freeze-thaw (F/T) cycles following a procedure similar to that described in ASTM C666. The number of F/T cycles was arbitrarily selected though the total number of F/T cycles a bridge deck may experience throughout its service life may be determined using measured deck temperature data (Wan et al., 2010). Rather than measuring the dynamic moduli and weight losses, rapid chloride ion penetrability (RCIP) tests (ASTM C1202) were conducted to evaluate the chloride permeability of the concrete samples.

3.3 Specimen Design

The experiment matrix is shown in Table 3.1. A total of twenty four cylinders, divided into eight groups of three cylinders, were used in the tests. One group of three cylinders was kept in air as the reference, and the samples sliced from these cylinders were named as RNW specimens hereafter as shown in Table 3.1. Considering that hydration process may continue for the fully saturated cylinders that were subjected to freeze-thaw cycles, another group of three cylinders was kept in water, and the samples from these cylinders were named as RW specimens. The remaining cylinders were subjected to 300 freeze-thaw cycles, among which three cylinders were not subjected to any load, and were named as RD specimens. Other cylinders were subjected to five levels of compressive loads as listed in Table 3.2. For example, specimen D50-2 was the No. 2 sample sliced from a cylinder that was subjected to 50 percent of the ultimate capacity of concrete.

3.3.1 Mixture and Fresh Concrete Properties

Table 3.1 shows the mixture of the air-entrained concrete used in this study which is the standard mixture, Grade A-FA, specified by Wisconsin Department of Transportation (WisDOT) for bridge constructions. The water-cementitious material ratio (w/cm) is 0.4, and the amount of fly ash by weight of total cementitious material is 30 percent. Air 260 from Chryso was used as an air entraining admixture. The fresh concrete properties were measured using ASTM standard tests, including a slump test (ASTM C143), and an air content measurement (ASTM C231). The measured slump was 6 in., and the measured air content of fresh concrete was 7.8 percent, which is within the range of 5 to 8 percent for typical air-entrained concrete (ASTM C260-10a, 2010). Adequate freeze-thaw resistance was thus expected though the spacing factor was not measured.

Timeline of tests is shown in Table 3.2, including the date of mixing, 28 days of lime water curing, the time of freeze-thaw cycles, and the dates of rapid chloride ions permeability tests. Note that the cylinders in the freeze-thaw chamber were kept saturated, therefore the extended curing for these cylinders were deemed sufficient for the concrete with fly ash to develop its desired properties according to Wesche (1991).

3.3.2 Hardened Concrete Properties

Compressive tests of hardened concrete cylinders were conducted using a 2,000 kN (450-kips) compression testing system following ASTM C39, as shown in Figure 3.2. The cylinder ends were capped using high-alloy steel retaining caps with elastomeric pads (ASTM C1231, 2010) during the compressive tests. The elastomeric bearing pads helped to distribute the load uniformly from the piston of the testing machine to the ends of the concrete. Bonded capping was not used because the capped ends may affect the water ingression during the freeze-thaw cycles. The rate of loading was 2.5 kN/s according to the procedures in ASTM C39. The results of the compressive tests for the cylinders at 28 days and 120 days are listed in Table 3.3. The hardened concrete had a compressive strength of 27.1 MPa (3931 psi) at 28 days, which was slightly lower than the target strength, 27.6 MPa (4000 psi). The compressive strength increased to 38.7 MPa (5600 psi) at 120 days, which reflects the typical behavior of concrete with fly ash (Wesche, 1991).

3.3.3 Preloading Concrete Cylinders in Compression

The compressive load levels for the cylinders were selected based on a review of literature on the observed microcracking development in concrete. Hsu et al. (1963) indicated that microcracks initiate within the interfacial transition zones (ITZ) between cement paste and aggregates when concrete is subjected to a compressive load equal to 30 percent of its ultimate load. In addition, microcracks further develop in cement paste and interconnect with each other at about 70 to 90 percent of the ultimate load. Similar observations were made by Van Mier (1984). Therefore the cylinders in this study were subjected to 40 through 80 percent of the measured ultimate compressive load as shown in Table 3.4. Note that the applied compressive stresses do not necessarily reflect those in a bridge deck subjected to daily truck traffic. However, it was reasoned that overweight vehicles may represent the loads on the deck at the ultimate limit state, the design for which typically assumes that the concrete is loaded beyond the strain corresponding to the peak stress (f_c').

3.4 Freeze-Thaw Cycles

The standard freeze-thaw procedure specified in ASTM C 666 was modified as shown in Figure 3.3 because the concrete cylinders used in the study were larger than the standard freeze-thaw specimens. The freeze-thaw chamber at the UWM Concrete Laboratory, as shown in Figure 3.4, was able to lower the chamber temperature from 4.4 to -17.8 ºC (40 to 0 ºF) in two and half hours. The temperature was held at -17.8 ºC (0 ºF) for an hour before being raised back to 4.4 ºC (40 ºF). Similarly, the temperature was then maintained at 4.4 ºC (40 ºF) for an hour to complete a freeze-thaw cycle. The standard freeze-thaw chamber was upgraded to include a closed-loop temperature control for this purpose as shown by an inserted picture in Figure 3.4.

Pictures of cylinders after the 300 freeze-thaw cycles are presented in Figure 3.5 and 3.6. Scaling and smeared voids on the surfaces for those preloading samples after the freeze-thaw

cycles are evident. In addition, some cylinders showed spalling near their ends. Such local damage near the ends may be caused by stress concentration during the compressive loading.

Weight loss has been viewed as an important aspect of the freeze-thaw damage to concrete (CEB, 1992). The weight losses of each group of cylinders, after being subjected to 300 freeze-thaw cycles, are listed in Table 3.5 and plotted in Figure 3.7 against the compressive stresses applied to the cylinders. Most cylinders lost less than 1 percent of their original weight after experiencing 300 freeze-thaw cycles, indicating that the selected air-entrained concrete performed well according to ASTM C 666 procedure A (2003). This was confirmed by the appearance of the cylinders in Figure 3.5 and 3.6: the surfacees of the loaded cylinders slightly degraded, as revealed by the loss of coarse aggregates. Some cylinders experienced local crushing under the compressive loads near the ends of the cylinders. Freeze-thaw resistance may have been further damaged in the crushed regions as indicated by a cylinder with a 2 percent weight loss in Figure 3.7. Such local damage may have been responsible for the variations in the measured weight losses of loaded cylinders.

The weight losses in general increased when the cylinders were loaded at 40 percent of their ultimate capacity. The weight loss increased only slightly for the cylinders subjected to higher compressive loads; however, the levels of related internal damage in concrete, represented by microcracks, were found very different. The physical condition of the specimens of each specimen combined with passing current and charge in RCIP test, as illustrated in Figure 3.15 through 3.70, was presented in the following section.

3.5 Rapid Chloride Ion Penetrability (RCIP) Tests

The internal damage caused by freeze-thaw cycles has been reflected by their dynamic moduli of elasticity in standard tests. Yang et al. (2005) showed that specimens with more microcracks had smaller dynamic moduli measured according to ASTM C215 procedures (2002). Dynamic moduli were not measured for the cylinder specimens in this study because the specimens used in the study were different from the standard specimen stipulated in ASTM C 666. Instead the impact of the internal damage was evaluated using chloride permeability of concrete. Because of a shorter test time needed, rapid chloride ion permeability tests, as schematically shown in Figure 3.8 and Figure3.9, were used in this study as compared to the other tests, such as salt ponding tests (ASTM C1543) and chloride diffusion tests (ASTM C1556) as reviewed in Chapter 2.

Two samples with a thickness of 50.8-mm (2-in.) were sliced from the middle part of each cylinder, as shown in Figure 3.8c and Figure 3.10a. The samples, as shown in Figure 3.10b, were then coated with epoxy before conditioning. Note that the surface of samples should be totally cleaned and polished after saw-cutting and coating by removing any dust and paint, as typical examples illustrated in Figure 3.11 and Figure 3.12. After total 22 hours, A PROOVE'it System by Germann Instruments was used in RCIP tests (Figures 3.9 and 3.13). The data acquisition system connected to PC screen, as shown in Figure 3.14, was used to automatically measure the total coulombs passed through each specimen during the six–hour period.

3.6 Chloride Permeability of Concrete

Two samples were extracted from the middle of each concrete cylinder. All six samples from each group of cylinders were tested simultaneously to minimize the variations for test

conditions. The recorded electric current and temperature over time for all samples are shown below. Two different vertical axes (left and right sides) were used to display electric current and temperature in the plots. The solid lines show the electric current while the dashed lines represent the temperature variation. With the measured 6-hour electric current history, the total charge passed for a sample was derived from the total area covering in current-time curve, following Eq. (2.4). In addition, the sample temperatures were monitored by a thermal probe.

-Samples from reference cylinders kept in water

Samples RW-1/02: RW specimens, cured in saturated limewater for about 120 days, were used as the reference. Figure 3.15 plots the surface conditions of reference cylinder RW-1. Compared with the sample at 28 days shown in Figure 3.15a, the surface of the sample at 120 days indicated high concrete quality. The surface conditions correlated with the close RCIP test results of Samples RW-1 and RW-2. The current-time curve over 6 hours in Figure 3.16a for Sample RW-1 indicated a constant passing rate at about 32.9 mA. The total charge passed was 698 coulombs for Sample RW-1. The measured temperature was constant around 26 degrees, indicating that the sample has a relatively low permeability and relatively low conductivity. Similar observations can be made for Sample RW-2, as shown in Figure 3.16b.

Samples RW-3/4: Samples RW-3 and RW-4 were extracted from the second cylinder in the reference group. Figure 3.17 plots the surface conditions of the reference cylinder. Again the cylinder had a smooth surface, which corresponds to the similar passing current and total charge passed. Figure 3.18a and 3.18b present the recorded electric current/temperature over time for Sample RW-3 and RW-4, respectively. The electric current over 6 hours for both samples was about constant behavior and the temperature was between 23 to 29 degrees over time.

Samples RW-5/6: Samples RW-5 and RW-6 were extracted from the third cylinder in the reference group. Figure 3.19 plots the surface conditions of the reference cylinder. Figure 3.20a and 3.20b present the recorded electric current and temperature over time for Sample RW-5 and RW-6, respectively. The electric currents over time for both samples kept constant and the temperature stayed between 22 and 26 degrees.

Figure 3.21 plots the total charge passed through samples from the reference cylinders. The average charge passed (710 coulombs with a standard deviation of 5 percent) indicated that all six samples from the reference cylinders had very low permeability. This group of cylinders was assumed to reflect the properties durable concrete with fly ash, which can be observed in laboratories.

-Samples from reference cylinders kept in the air

Figure 3.22 plots the conditions of the first reference cylinder cured in the air. The sample did not experience further hydration after the initial 28 days of curing in limewater. Enlarged photo shows a rough surface with voids and a layer of white powdery buildup on the surface. The powdery buildup was the calcium hydroxide deposits (a main component of limewater for curing purposes). Figure 3.23a and 3.23b show the electric current/temperature over time for Samples RNW-1 and RNW-2, respectively. The electric current had a slow increase over time from 70 mA to 81 mA after initial decreasing and the average of current is approximately 70.7 mA. The total charge passed was 1528 coulombs, which is approximately twice the amount of charge passed in the RW samples (cured in water). In addition, temperature increased from 23 to 32 degrees over time.

Figure 3.24 plots the surface condition of the second reference cylinder cured in air. Again, the surface was rough with white powdery buildup. The measured electric current had a slow increase over time shown in Figures 3.25a and 3.25b. The average electric current for sample RNW-3 was 67.8 mA (75.2 mA for RNW-4). The sample temperature again increased from 23 to 32 degrees over the six hours.

Figure 3.26 shows the conditions of the third reference cylinder cured in air. Having been dried in air, the cylinder had a rough surface, and white powdery buildup of calcium hydroxide. The condition of the samples seemed similar to other samples in this group; however these two samples allowed an electric current higher than 90.0 mA, over time as shown in Figures 3.27a and 3.27b. Therefore the total charge passed for Sample RNW-5 is 2021 coulombs and 1844 coulombs for RNW-6. In addition, the sample temperature (up to 34 degrees) was higher than other RNW samples.

Figure 3.28 compared the total charge passed through all six samples. The passing charges in this group (cured in air) were higher than those through the cylinders cured in water, indicating higher permeability of concrete. While this observation restated the importance of curing process on concrete durability, the 15 percent standard deviation observed in this group of tests indicates that the specimens kept in air may have experienced various levels of dry shrinkage.

-Samples from non-loaded cylinders after 300 F/T cycles

Figure 3.29 plots the surface conditions of the first cylinder in this group, which were subjected to 300 F/T cycles. Freeze-thaw cycles caused surface scaling as expected. In addition, voids were observed on the surfaces, indicating the loss of sand particles as part of the frost damage. Figure 3.30a and 3.30b shows the recorded electric current and temperature changes over time for Samples RD-1 and RD-2, respectively. The electric current increased slowly from 104 mA to 110 mA over time, and the amount of total charge passed was 2183 coulombs. The reason for the drop during the first hour shown in Figure 3.30a was not clear. In addition, the temperature of solution increased from 23 to 35 degrees. A similar response is observed in sample RD-2. The amount of total charge passed through Sample RD-2 was 2085 coulombs and its temperature rose to 37 degrees, as shown in Figure 3.30b.

Figure 3.31 plots the surface condition of the second cylinder in this group. Similarly, surface scaling and voids were observed due to 300 freeze-thaw cycles as shown in Figure 3.31. The variation in the electric current and temperature over time for Sample RD-3/4 is presented in Figure 3.32a and 3.32b. Again the electric current increased from about 95 mA to 110 mA, and the temperature increased from 23 to 36 degrees. As a result, the amount of total charge passed through Sample RD-3 was 2100 coulombs and 2193 coulombs for RD-4.

The surface scaling and voids of the third cylinder were similar to others in this group as shown in Figure 3.33. Only one sample was obtained from this cylinder and the other sample was damaged during the slicing process. The electric current for Sample RD-5 was only about 75 mA over time as shown in Figure 3.34, and the total charge passed was 30 percent lower than that observed in other samples. This large variability may have been caused by the heterogeneous nature of concrete materials and uncertainties in the test procedure.

Figure 3.35 compares the total charge passed through all the samples from the unloaded cylinders. All samples except Sample RD-5 had a total charge passed around 2100 coulombs. This is over 60 percent increase compared to reference samples without freeze-thaw action.

-Samples from cylinders loaded at 0.4f_c' after 300 F/T cycles

Samples D40-1 through 6 were sliced from cylinders subjected to 40 percent of measured concrete compressive strength. The surface conditions of these three cylinders are shown in Figures 3.36, 3.38, and 3.40. The F/T cycles caused more severe damage to the cylinder surfaces compared with the reference cylinders shown above. The surface damage was reflected by their weight losses, as shown in Table 3.5 and Figure 3.7. Significant variations were observed in the measured electric current vs. time curves is shown in Figures 3.37, 3.39, and 3.41 and the total charge passed through these samples is shown in Figure 3.42. In general, the electric current, had a 10 percent increase compared with RD samples. Specifically, Samples D40-5 and D40-6 had electric current over 140 mA. The large deviation in the measured passing charges and the observed temperature changes during the tests may have been due to different levels of internal damage in the cylinders caused by compressive loading. Such variations were further explored using image analyses in Chapter 4.

-Samples from cylinders loaded at 0.5f_c' after 300 F/T cycles

Samples D50-1 through 6 were sliced from cylinders subjected to 50 percent of measured concrete compressive strength. The surface conditions of these three cylinders are shown in Figures 3.43, 3.45, and 3.47. In addition to surface scaling, two cylinders in this group developed surface cracks is shown in Figures 3.43 and 3.45. These surface cracks may be indicators of deeper through-sample cracks as shown in Figure 3.45 for Sample D50-4. The measured electric current vs. time curves is shown in Figures 3.44, 3.46, and 3.48 and the total charge passed through these samples is shown in Figure 3.49. This group of samples allowed another 10 % increase in passing charges compared with D40 samples. Sample D50-4 allowed near 4500 coulombs of total passing charges. This was related to the through-sample cracks shown by the sectional image of Sample D50-4 in Figure 4.45. Such through-sample cracks were observed in the microcrack analyses in Chapter 4. Correspondingly, the solution temperature reached at 49 ºC due to the effects of Joule heating, which in turn may accelerate the charge passed, leading to overestimation of the final total charge passed through the sample. The correction of such Joule heating effects is discussion in Section 3.5.3.

-Samples from cylinders loaded at 0.6f_c' after 300 F/T cycles

Samples D60-1 through 6 were sliced from cylinders subjected to 60 percent of measured concrete compressive strength. The surface conditions of these three cylinders are shown in Figures 3.50, 3.52, and 3.54. Again surface scaling and surface cracks developed in the cylinders in this group. Sample D60-6 developed a through-sample crack as shown in Figure 3.54 for Sample D60-6 (the crack went through a coarse aggregate at lower right corner). The measured electric current vs. time curves is shown in Figures 3.51, 3.53, and 3.55 and the total charge passed through these samples is shown in Figure 3.56. The increase in average passing charges in this group of samples over those through D50 samples was not significant. The result of Sample D50-4 was responsible for the situation. The increase in the passing charge became large once the Joule heating effects were considered.

-Samples from cylinders loaded at 0.7f_c' after 300 F/T cycles

Samples D70-1 through 6 were sliced from cylinders subjected to 70 percent of measured concrete compressive strength. The surface conditions of these three cylinders are shown in Figures 3.57, 3.59, and 3.61. The observed damage in the three cylinders of this group varied significantly. Specifically the cylinder No. 2 developed more severe damage, including surface scaling and cracks as shown in Figure 3.59. Through-sample cracks were also observed in the two samples sliced form this cylinder (D70-3 and D70-4). Correspondingly, these two samples allowed much more passing charges as shown in Figure 3.60. D70-3 allowed more than 4500 coulombs of total charge passed. The measured electric current vs. time curves for other samples in this group is shown in Figures 3.58 and 3.62 and the total charge passed through all samples are as summarized in Figure 3.63. The increase in average passing charges in this group of samples over those through D60 samples was more than 10 percent.

-Samples from cylinders loaded at 0.8f_c' after 300 F/T cycles

Samples D80-1 through 6 were sliced from cylinders subjected to 80 percent of measured concrete compressive strength. The high-level loads and the F/T cycles caused major damage to these cylinders as revealed by their surface conditions as shown in Figures 3.64, 3.66, and 3.68. Through-sample cracks are clearly shown in Fig. 3.64 for the first cylinder. The measured electric current vs. time curves is shown in Figures 3.65, 3.67, and 3.69 and the total charge passed through these samples is compared in Figure 3.70. The average passing charges in this group of samples seems lower than that through D70 samples. Again this was attributed to Sample D70-3, which allowed more than 4500 coulombs of total charges. The average passing charges increase about 10 percent over D70 samples once the Joule heating effects were considered.

-Summary of all loaded cylinders

The effects of mechanical loading on permeability of test samples can be evaluated by comparing the measured passing charges to the reference samples while the coupled effects of mechanical loading and freeze-thaw action on permeability properties of concrete may be evaluated by comparing the results of the loaded samples with the reference samples RW as shown in Figure 3.71. In general, the electric current and total charge passed through samples increase with the increase of compressive load level placed on the samples. With the increasing charge passed, the conductivity of concrete is increasing and thus the accompanied temperature of solution also steadily increases, in accordance with Eq. (2.6). The correction of the effect of the Joule heating on the charges passed through test samples, as shown in Figure 3.72 and Figure 3.73.

Samples from RW cylinders allowed very small amount of charge passing through because the cylinders were cured in water for additional 88 days, during which other loaded cylinders were subjected to 300 freeze-thaw cycles. According to the high performance concrete (HPC) Lead State Team established by Federal Highway Administration (FHWA) in 1996 (Shi, 2003), a total passing charge of 715 coulombs indicates that the concrete may be classified as high performance concrete. The RNW cylinders cured in air did not develop such low permeability as shown in Table 3.5. The samples from RNW cylinders allowed more than twice the charge passed though the concrete may still be categorized as high performance concrete according to the test results. Note that the reference values for the rest samples may be between

the results from RW and RNW specimens because the cylinders in the freeze-thaw chamber may have had partially continued hydration process.

The RCIP test results of RD samples indicated that the freeze-thaw cycles caused internal damage in the air-entrained concrete though the measured weight loss was negligible as shown above. The values of total charge passed almost tripled compared with that of RW samples as shown in Table 3.5, indicating that the concrete deteriorated to have moderate chloride permeability (ASTM C1202, 2010) after 300 freeze-thaw cycles. The permeability of concrete samples further increased with an increase in the applied compressive loads as shown in Figure 3.71. The highest observed increase in total charge passed was 55 percent compared with the RD samples from unloaded cylinders. The maximum increase in the total charge passed became 93 percent when the results are compared with RNW samples.

The effect of temperature elevation during the RCIP tests on measured charge passed was evaluated based on Eq. (2.6), and the corrected results are shown in Figure 3.72. A linear correlation between measured charge passed and corrected charge passed is maintained up to the charge passed value of 3000 coulombs within 5 percent difference. Such linear correlation indicates that the effects of temperature are relatively low on the permeability properties of test samples. The larger deviation between charge passed values obtained in standard 6-hour measurement and corrected charge passed values increase with the increase of permeability of sample. The Joule heating appears evident in the higher permeable samples, such as over 4000 coulombs in this study.

According to Eq. (2.3), the charge passed over the first 30 minutes for each specimen was firstly determined by summing up the area of current over the first 30 minutes in accordance with the measured data. With the obtained charge passed over 30 minutes, the corrected charge passed over 6 hours was calculated based on Eq. (2.7) and plotted in Figure 3.73. The temperature modifications did not significantly change the observations shown above though the test results in terms of passing charges looked more reasonable. Specifically, the permeability of concrete samples further increased with an increase in the applied compressive loads. The highest observed increase in total charge passed becomes 33 percent as compared to the RD samples while 82 percent as compared to RNW samples. This may have been due to the fact that higher compressive loads caused more extensive microcracks in concrete. In addition, the initially damaged concrete further degrades under freeze-thaw cycles, which may have further opened and interconnected the microcracks. Therefore the freeze-thaw damage to concrete in the field may be affected by both the air void structures and stress-induced microcracks. The coupled compressive loading, such as that caused by the trucks on a bridge deck, and freeze-thaw cycles may deteriorate laboratory-proven durable concrete.

Table 3.1: Mixture of WisDOT Type A-FA Concrete

Materials	Mixture Designation (kg/cu m)*
Cement	234(395)
Coarse Aggregate	1188(2002)
Fine Aggregate (35%)	638(1075)
Design Water	134(27 gals)
Maximum Water	158(32 gals)
Silica Fume	0
Fly Ash	101(170)
Measured Air Content	7.8%
w/cm	0.4

Note: Water / (cement + fly ash) = 0.4.

*: unit lb/cu yd in round bracket

Table 3.2: Timeline of Tests

Days	Date		Activities
	start	end	
	3/24/2011		Specimen casting
28	3/24/2011	4/21/2011	Specimen curing in saturated limewater
1	4/21/2011	4/22/2011	28-day compressive tests and preloading
88	4/21/2011	7/18/2011	300 Freeze-thaw cycles
6	7/12/2011	7/18/2011	Air dry after saw-cutting
1	7/16/2011		120-day compressive tests
1	7/18/2011	7/19 /2011	D80 RCIP Testing and D70 conditioning
1	7/19/2011	7/20/2011	D70 RCIP Testing and D60/D50 conditioning
1	7/20/2011	7/21/2011	D60/D50 RCIP Testing and D40/RD conditioning
1	7/21/2011	7/22/2011	D40/RD RCIP Testing and RNW conditioning
1	7/22/2011	7/23/2011	RNW RCIP Testing and RW conditioning
1	7/23/2011	7/24/2011	RW RCIP Testing

* 120 days is used for compression tests

Table 3.3: Compressive Tests of Cylinders at 28 and 120 Days Ages

Age (days)	No.	Weight (kg)	Ultimate load (kN)	Compressive strength fc' (MPa)	Average fc' (MPa)	Coefficient of variation	ASTM requirement*	
28	1	3833	207.0	26.35	27.1	2.90%	<	10.90%
	2	3809	208.5	26.55		2.12%	<	
	3	3851	223.4	28.44		-4.66%	<	
120	1	3902	330.0	42.02	38.7	-7.90%	<	10.90%
	2	3799	277.0	35.28		9.69%	<	
	3	3832	304.5	38.80		-.26%	<	

*: Accepted requirement of coefficient of variation for each specimen in ASTM C 39

Table 3.4: Preloading of Test samples

No.		Expected preloading (kN)	Actual load (kN)	Actual stress (MPa)	Coefficient of variation	ASTM requirement*	
D40	D40-1	85.19	85.50	10.88	0.37%	<	10.90%
	D40-2	85.19	85.60	10.90	0.48%	<	
	D40-3	85.19	84.90	10.81	-.34%	<	
D50	D50-1	106.48	107.60	13.70	1.04%	<	10.90%
	D50-2	106.48	107.40	13.67	0.85%	<	
	D50-3	106.48	107.00	13.62	0.48%	<	
D60	D60-1	127.78	127.30	16.20	-.38%	<	10.90%
	D60-2	127.78	128.60	16.37	0.64%	<	
	D60-3	127.78	128.00	16.29	0.17%	<	
D70	D70-1	149.08	148.70	18.93	-.25%	<	10.90%
	D70-2	149.08	149.20	18.99	0.08%	<	
	D70-3	149.08	149.50	19.03	0.28%	<	
D80	D80-1	170.37	170.10	21.65	-.16%	<	10.90%
	D80-2	170.37	171.90	21.88	0.89%	<	
	D80-3	170.37	171.40	21.82	0.60%	<	

*: Accepted requirement of coefficient of variation for each specimen in ASTM C 39

Table 3.5: Summary of Tests

Test No.	Preloading[+] (MPa)	F/T		Water absorption	Charge passed in RCPT (coulombs)	
		F/T (cycles)	Weight loss (%)	Volume ratio (%)	Charge passed	Average charge passed[++]
RW-1	0	0	-	1.4	698	714.83 (5%)
RW-2				1.6	772	
RW-3				1.6	710	
RW-4				1.4	664	
RW-5				1.6	746	
RW-6				2.0	699	
RNW-1	0	0	-	4.5	1528	1629.17 (15%)
RNW-2				4.2	1293	
RNW-3				2.2	1464	
RNW-4				4.1	1625	
RNW-5				4.1	2021	
RNW-6				5.0	1844	
RD-1	0	300	0.25	3.0	2183	2030.80 (11%)
RD-2				2.7	2085	
RD-3			0.18	2.8	2100	
RD-4				3.5	2193	
RD-5			0.25	2.6	1593	
RD-6				-	-	
D40-1	10.9	300	0.08	2.5	1652	2232.33 (21%)
D40-2				2.2	1718	
D40-3	10.9		0.23	2.7	2309	
D40-4				2.6	2077	
D40-5	10.8		0.13	3.2	2856	
D40-6				3.4	2782	
D50-1	13.7	300	0.72	3.5	2804	2757.67 (25%)
D50-2				3.2	2401	
D50-3	13.7		1.01	4.8	2531	
D50-4				4.9	4197	
D50-5	13.6		0.42	3.2	2585	
D50-6				2.8	2028	
D60-1	16.2	300	1.23	3.1	2526	2842.33 (18%)
D60-2				3.7	3086	
D60-3	16.4		0.63	3.2	2391	
D60-4				3.1	2377	

D60-5	16.3		0.35	4.0	2848	
D60-6				3.6	3826	
D70-1	18.9	300	0.30	3.4	2581	3138.17 (25%)
D70-2				3.7	2970	
D70-3	19.0		0.33	5.2	4532	
D70-4				3.9	3612	
D70-5	19.0		1.89	3.3	2051	
D70-6				3.3	3083	
D80-1	21.7	300	0.56	4.3	3872	3044.33 (13%)
D80-2				3.8	3076	
D80-3	21.9		1.25	3.7	2743	
D80-4				3.7	2830	
D80-5	21.8		0.52	3.2	2631	
D80-6				3.6	3114	

F/T: freeze-thaw cycle; RCPT: Rapid chloride ion penetration; RW: references curing in water; RNW: references with air-drying; RD: references in freeze-thaw cycles;
$^{+}$: Ultimate strength=27.1 MPa; $^{++}$: relative standard deviation in round bracket

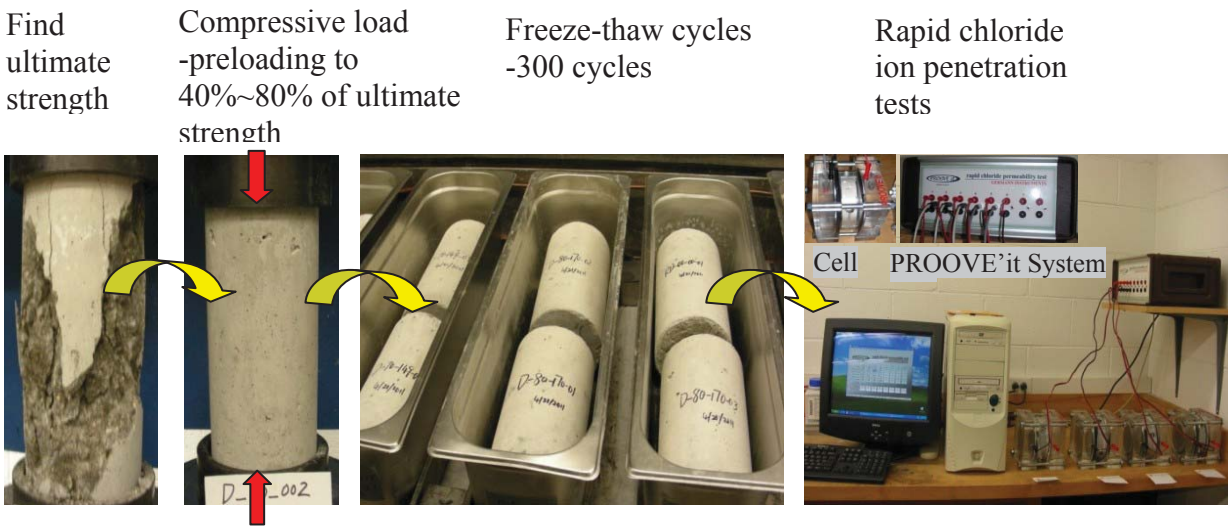

Figure 3.1: Concept of the experimental protocol

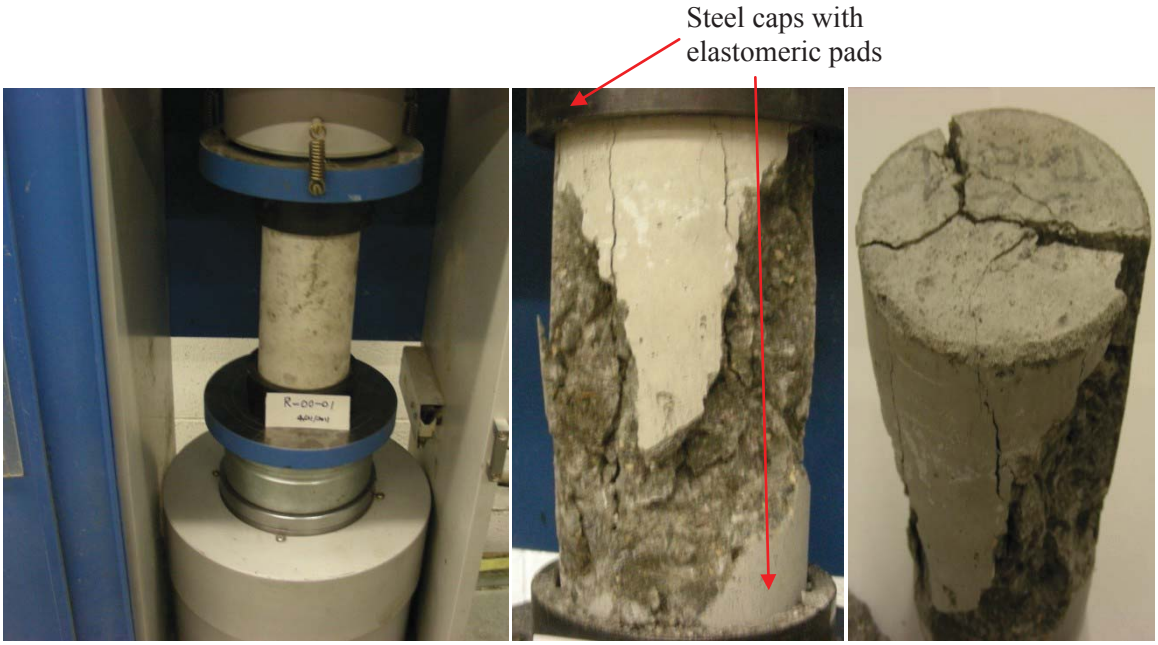

(a) Test setup (b) Typical failure mode

Figure 3.2: Compressive tests of a concrete cylinder

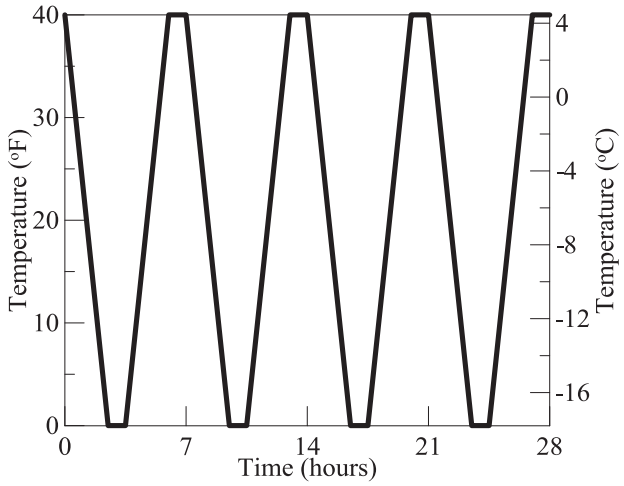

Figure 3.3: Modified freeze-thaw cycles based on ASTM C 666

Figure 3.4: Modified HM-12 Freeze-thaw Test Chamber

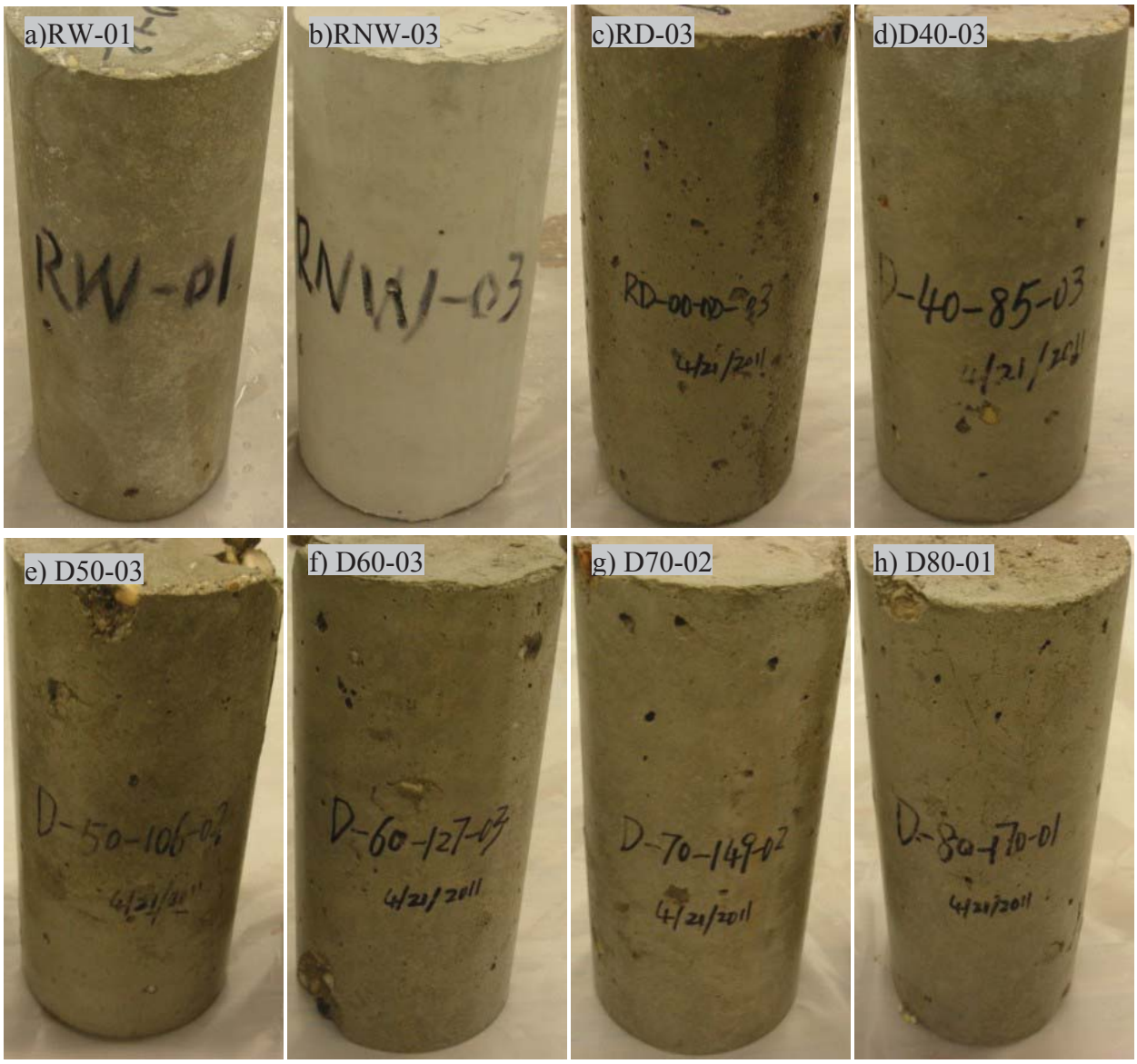

Figure 3.5: Various samples with and without F/T cycles

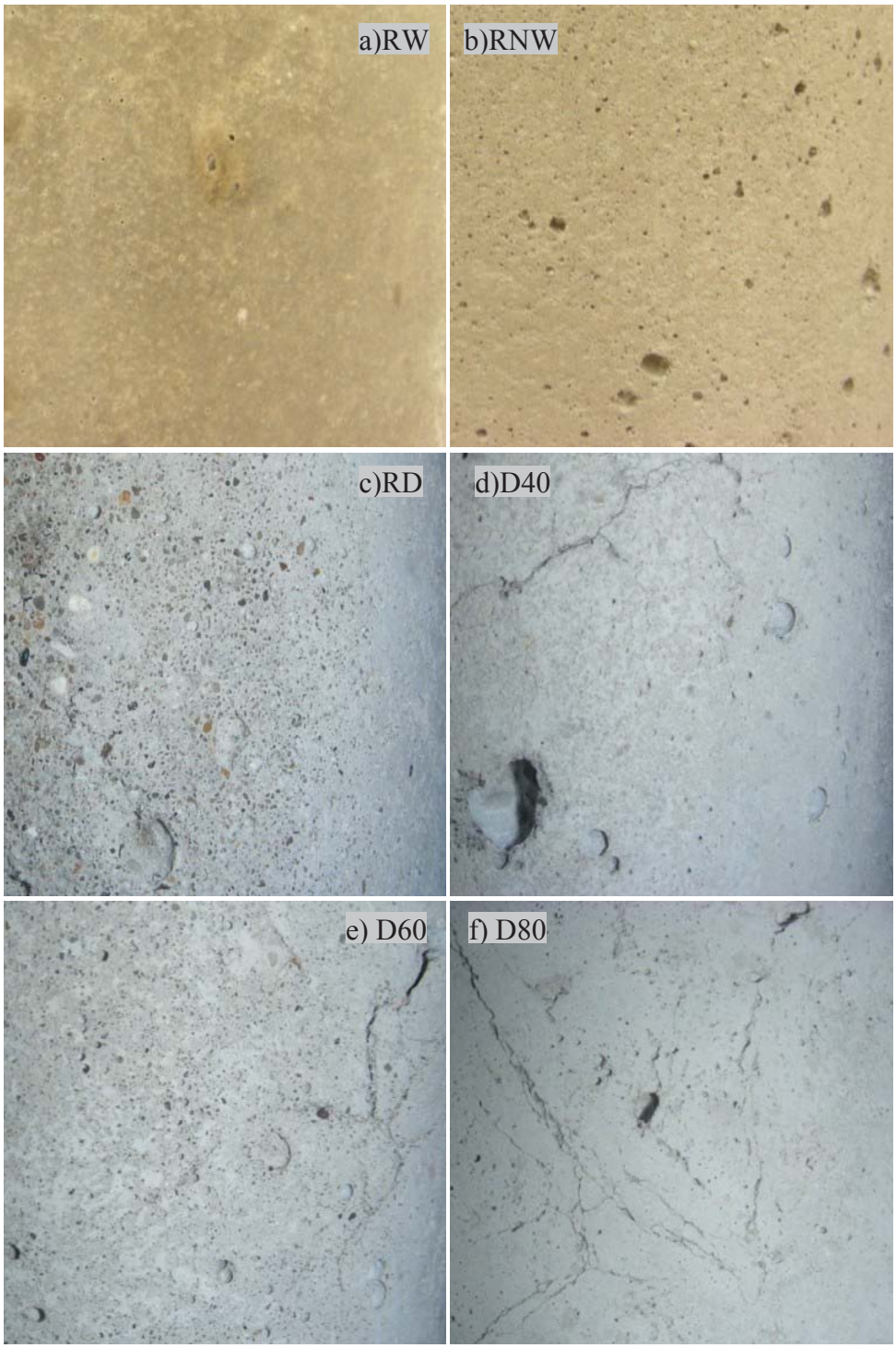

Figure 3.6: Typical surface conditions after F/T cycles

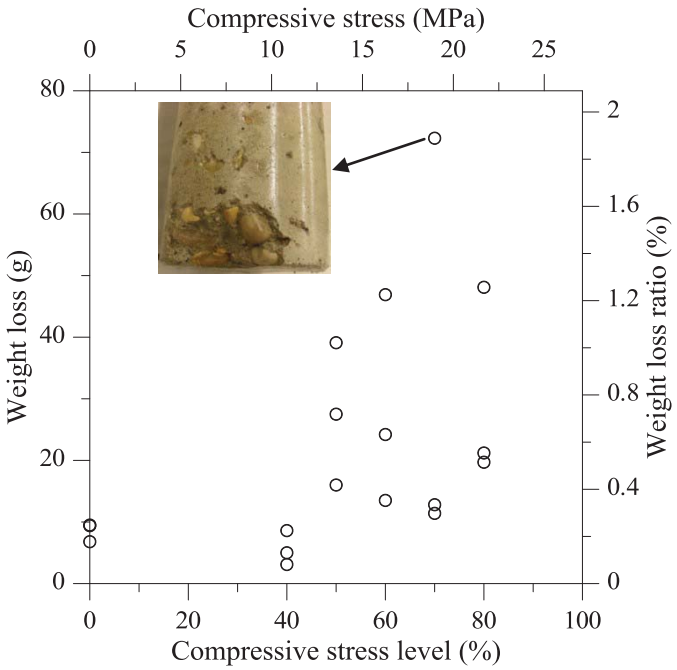

Figure 3.7: Measured weight loss of cylinders after 300 F/T cycles

(a)before F/T cycles (b)after F/T cycles (c) cut 2-inch slice from a specimen

(d) coated specimens (e) specimens under conditioning

Figure 3.8: Preparations for RCIP test

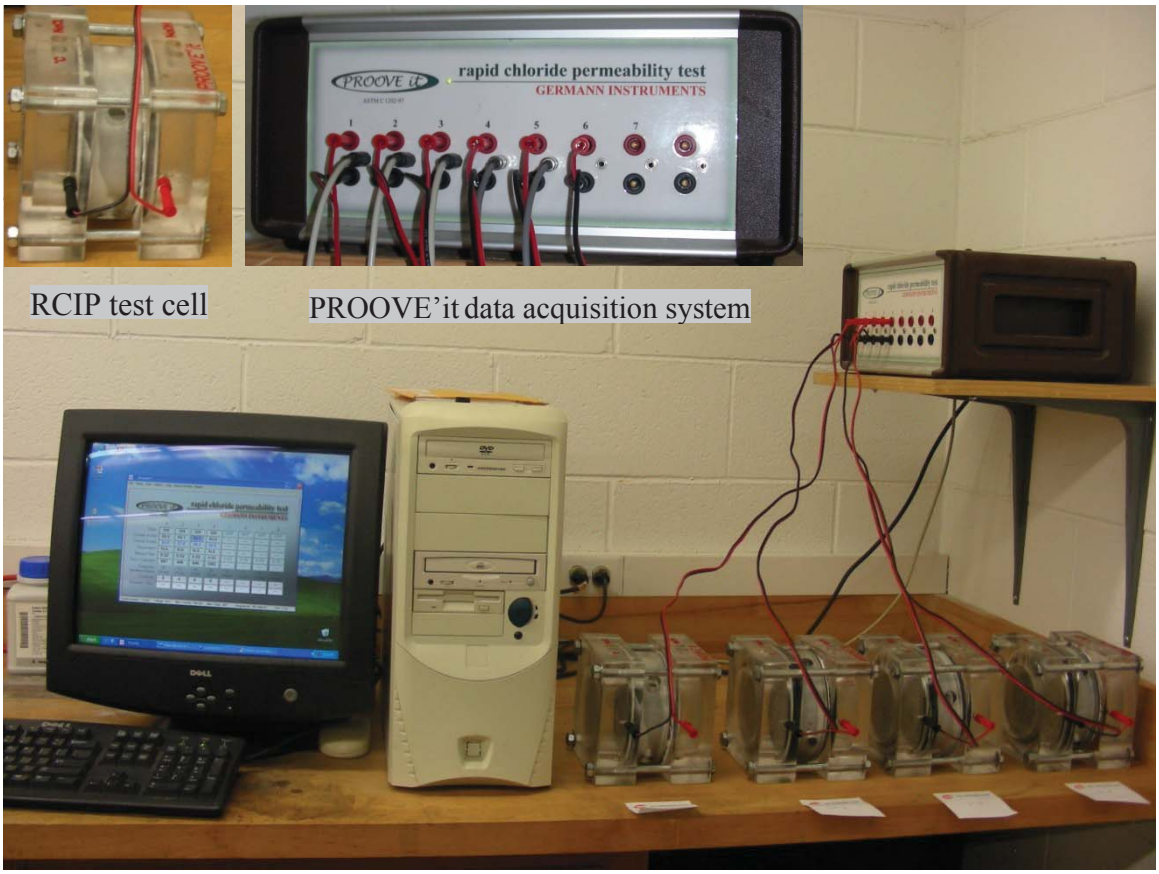

Figure 3.9: RCIP test setup

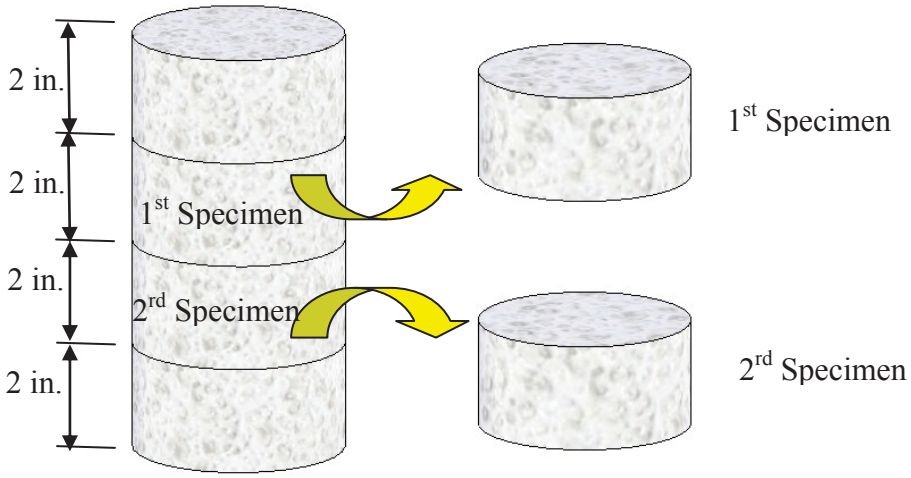

(a) Schematics of sliced two samples for RCIP test

(b) Coating specimens

Figure 3.10: Specimens preparations

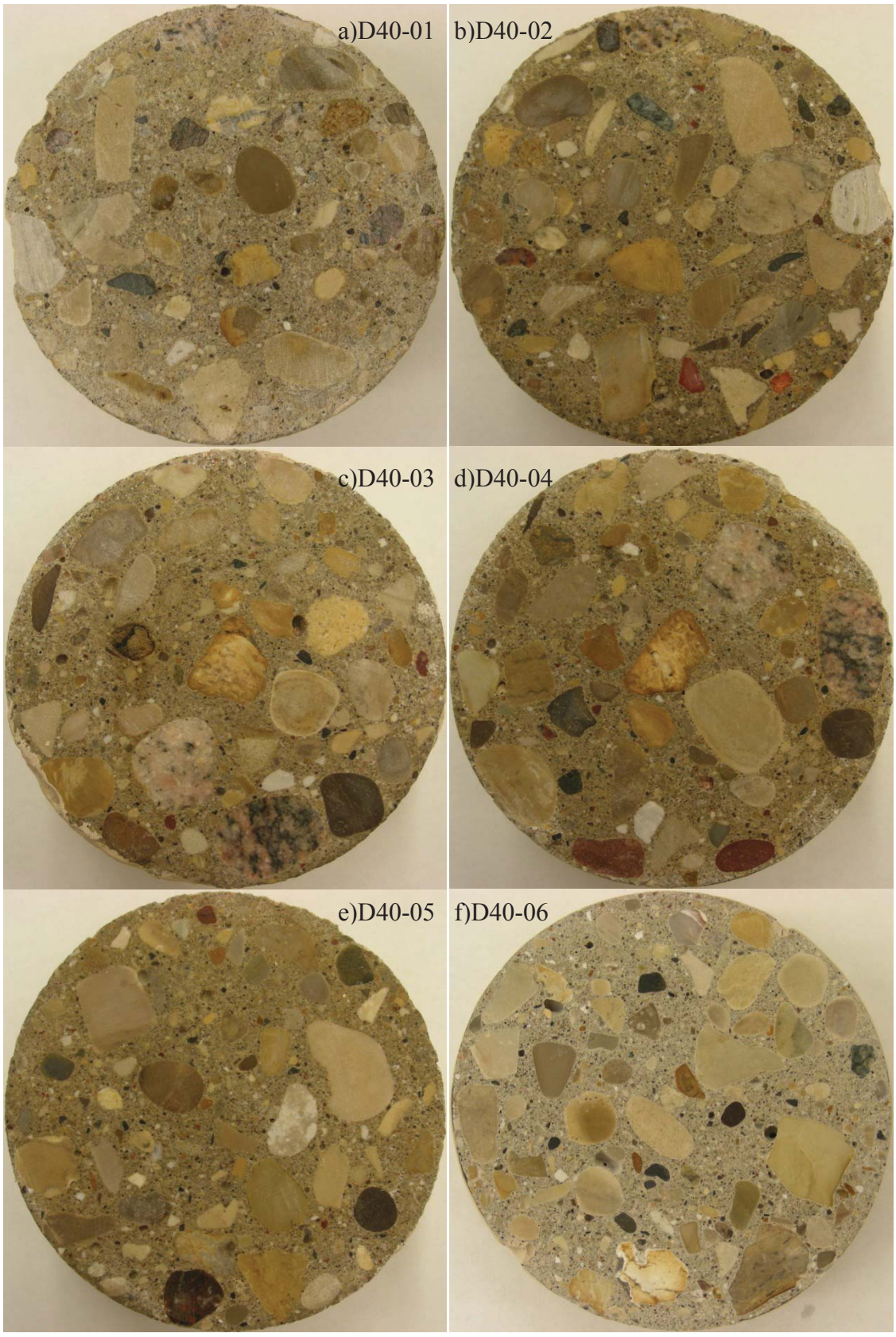

Figure 3.11: Polished samples of samples D40

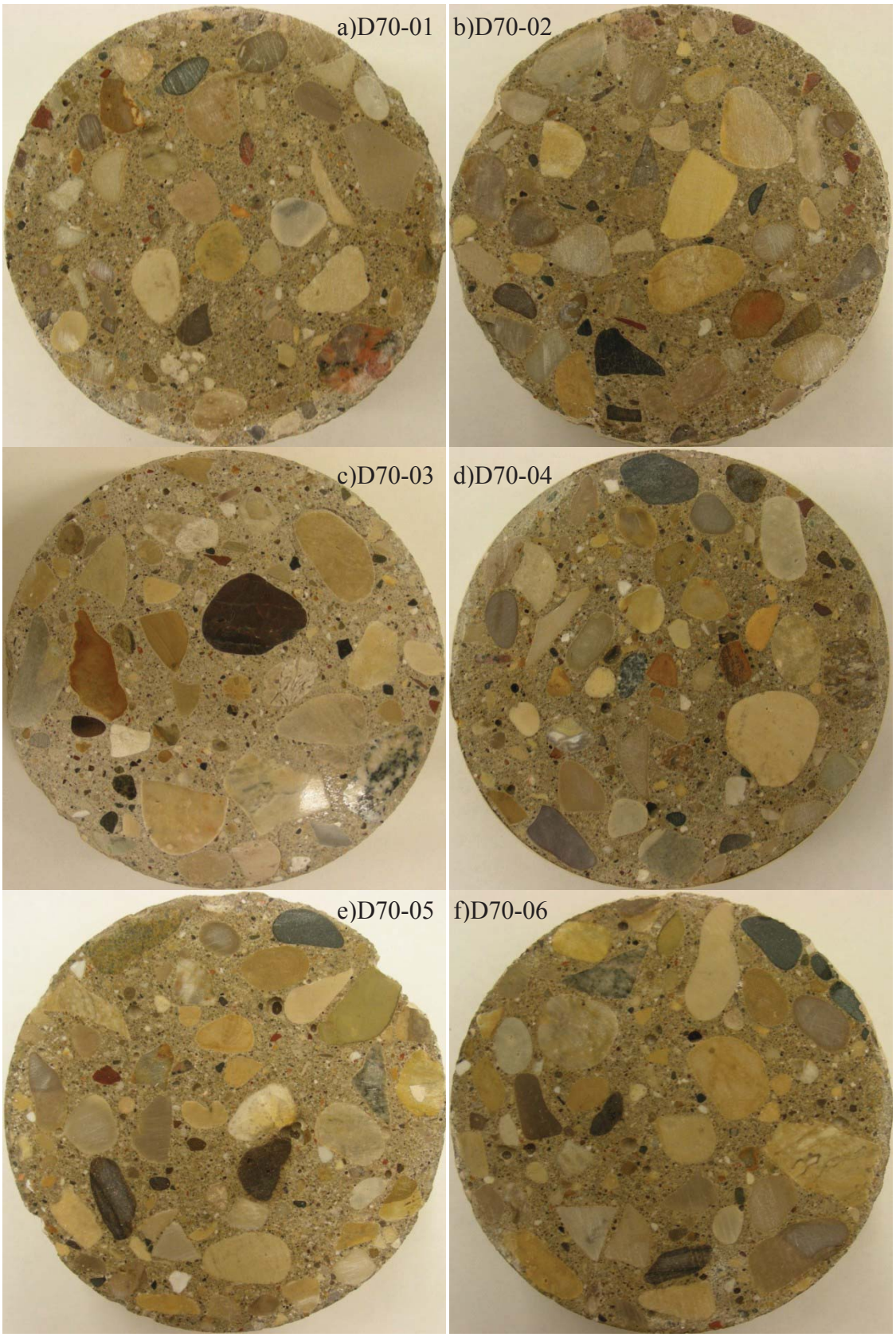

Figure 3.12: Polished samples of samples D70

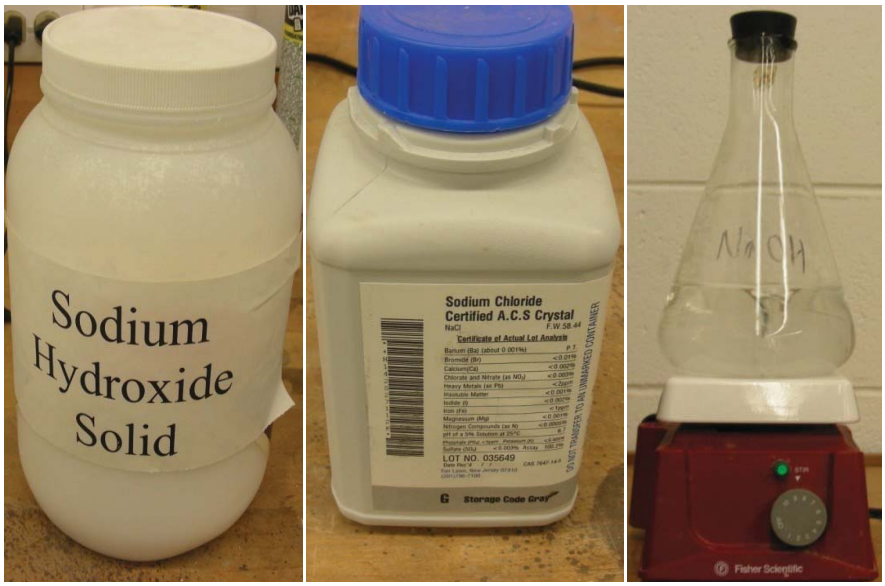

(a) Preparation for solutions (NaCl, NaOH and a magnetic stirrer)

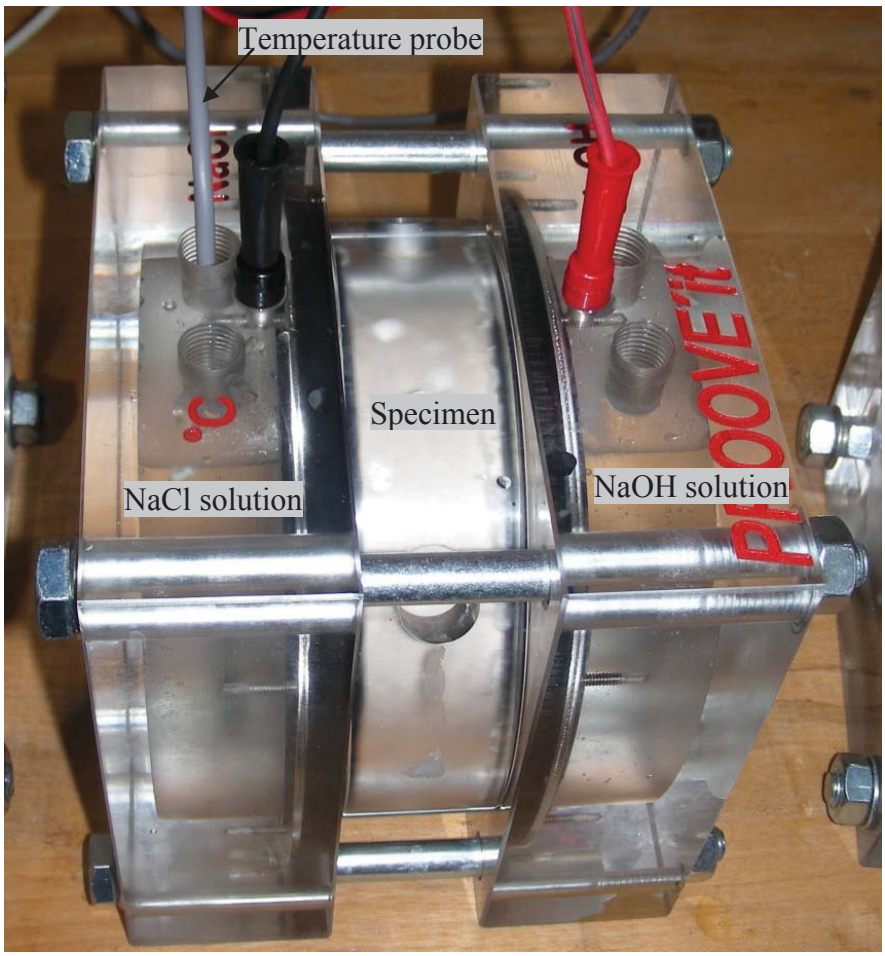

(b) Test cell

Figure 3.13: RCIP test preparation

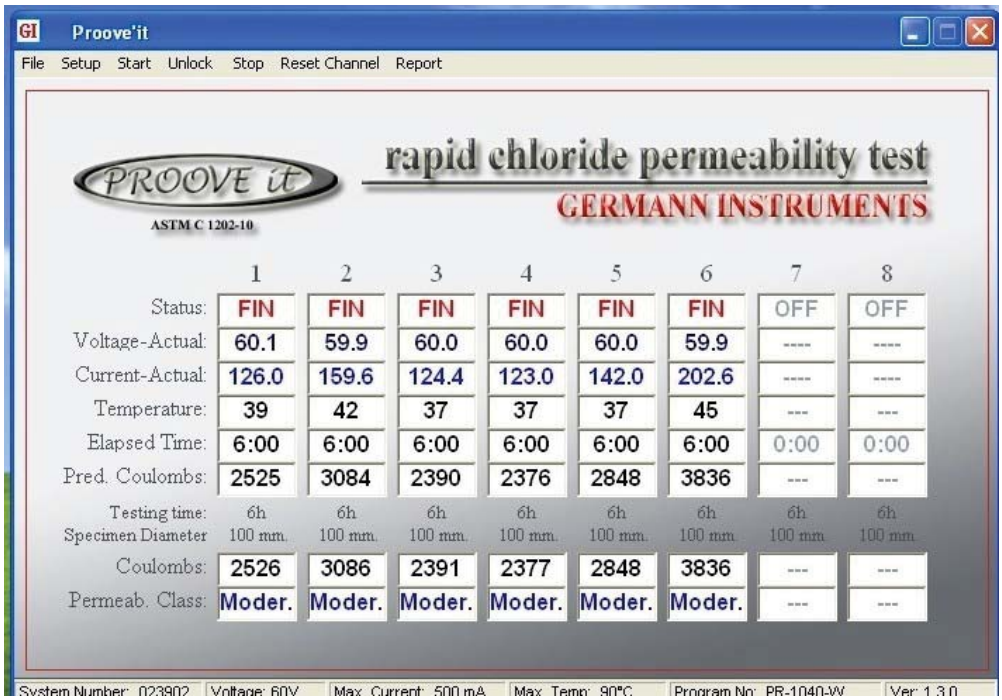

Figure 3.14: PROOVE'it© software in PC screen to run the test and acquire the data

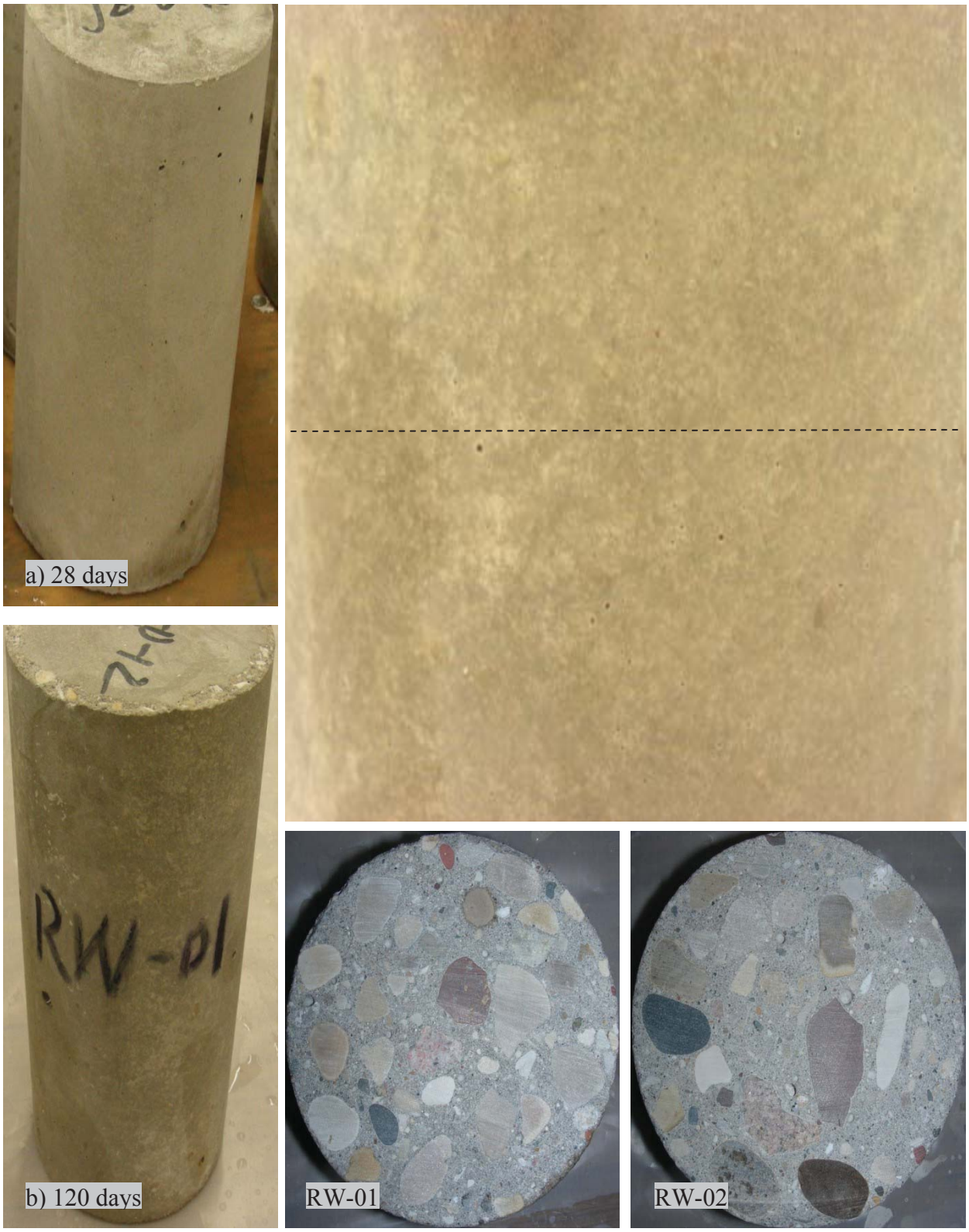

Figure 3.15: Surface conditions of reference samples RW-01/02

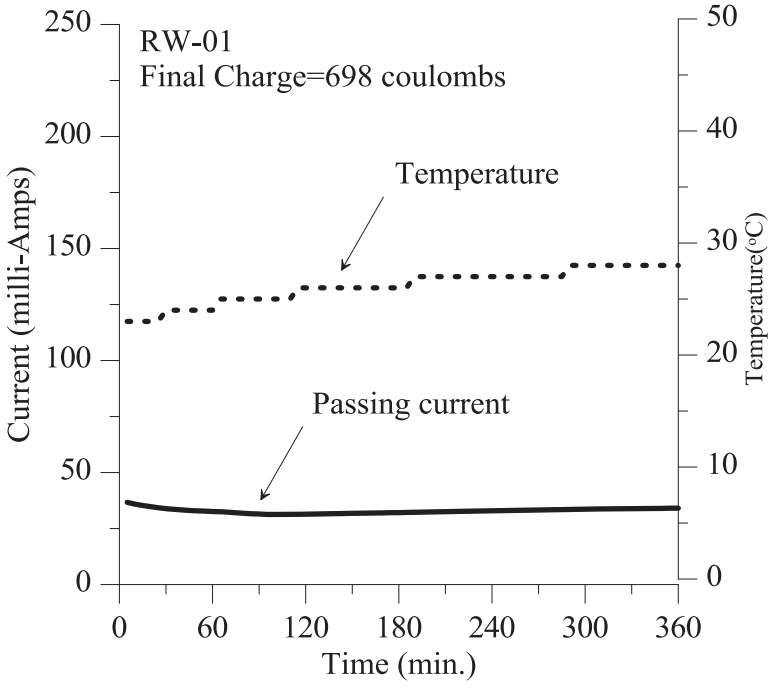

(a)RW-01

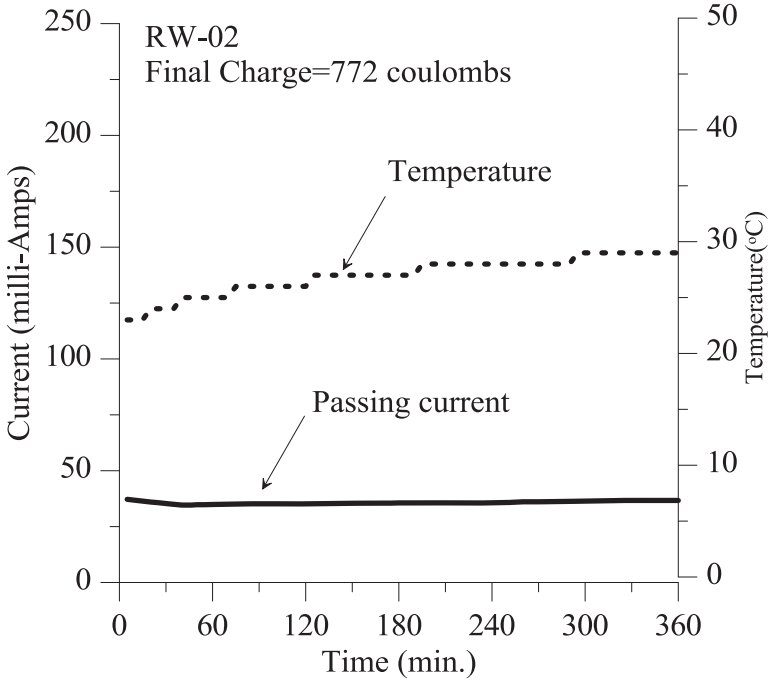

(b)RW-02

Figure 3.16: Passing current/temperature vs. time for samples RW-01/02

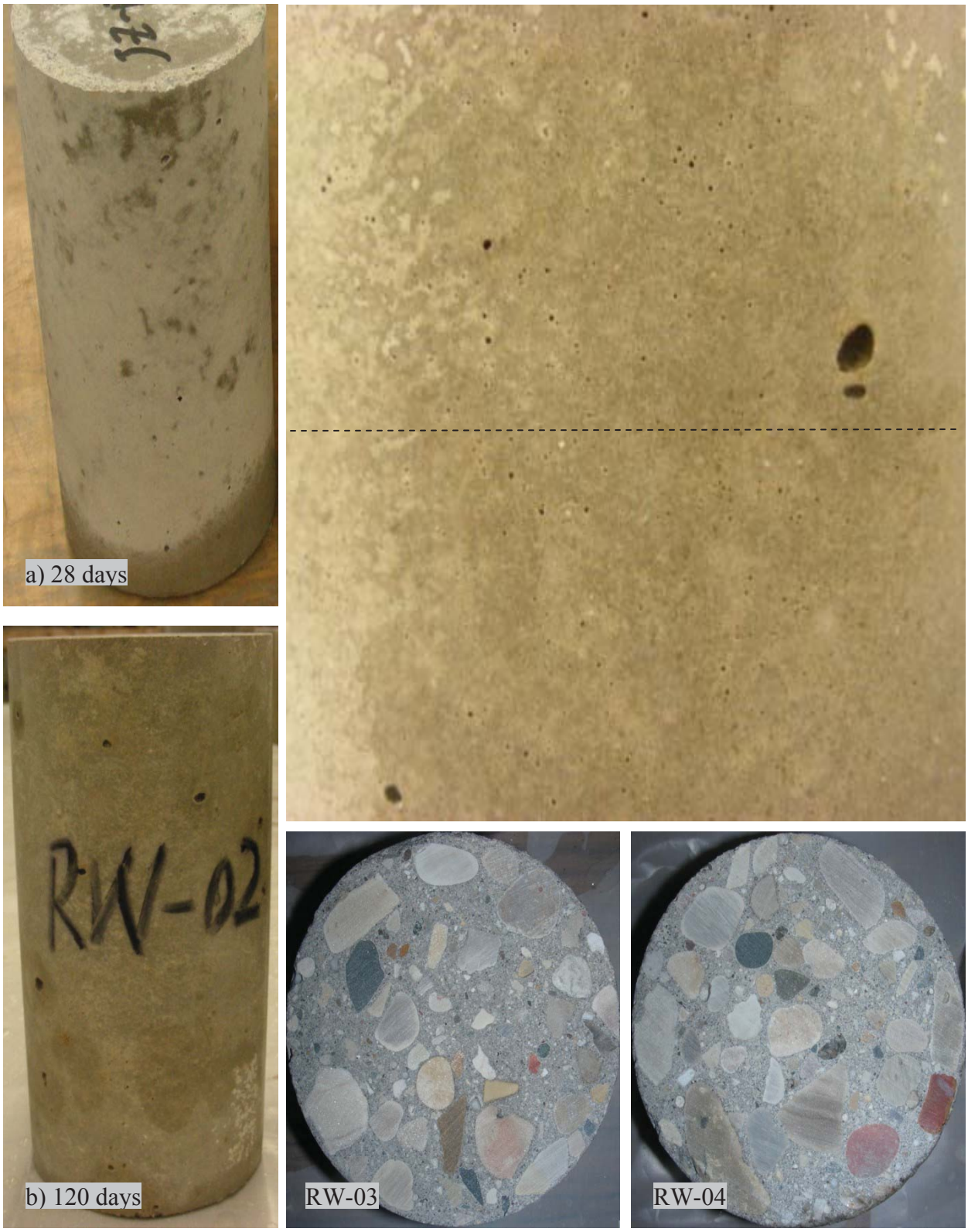

Figure 3.17: Surface conditions of reference samples RW-03/04

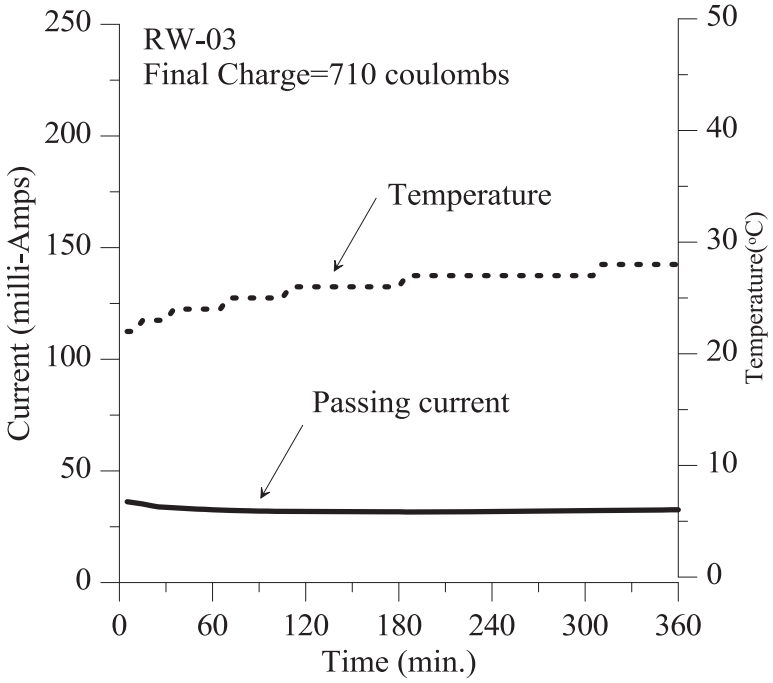

(a)RW-03

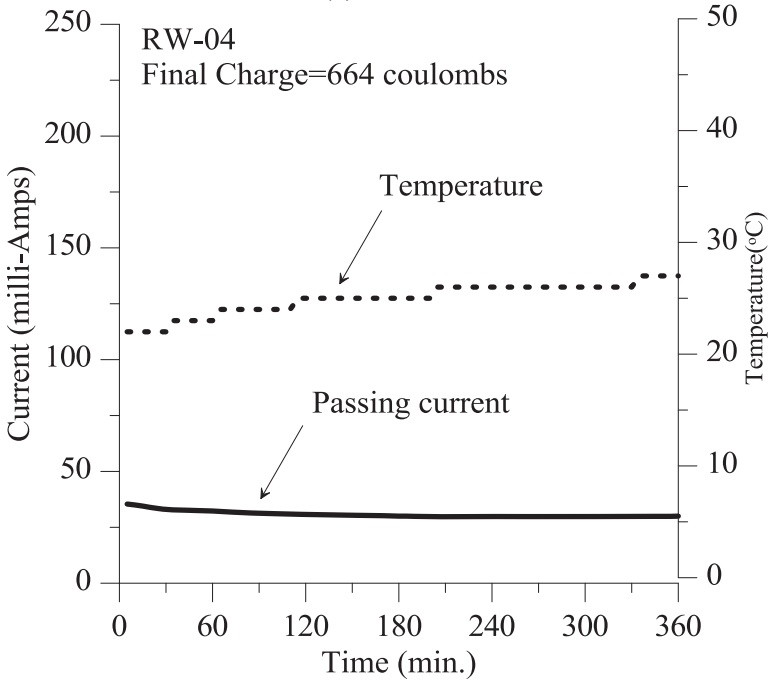

(b)RW-04

Figure 3.18: Passing current/temperature vs. time for samples RW-03/04

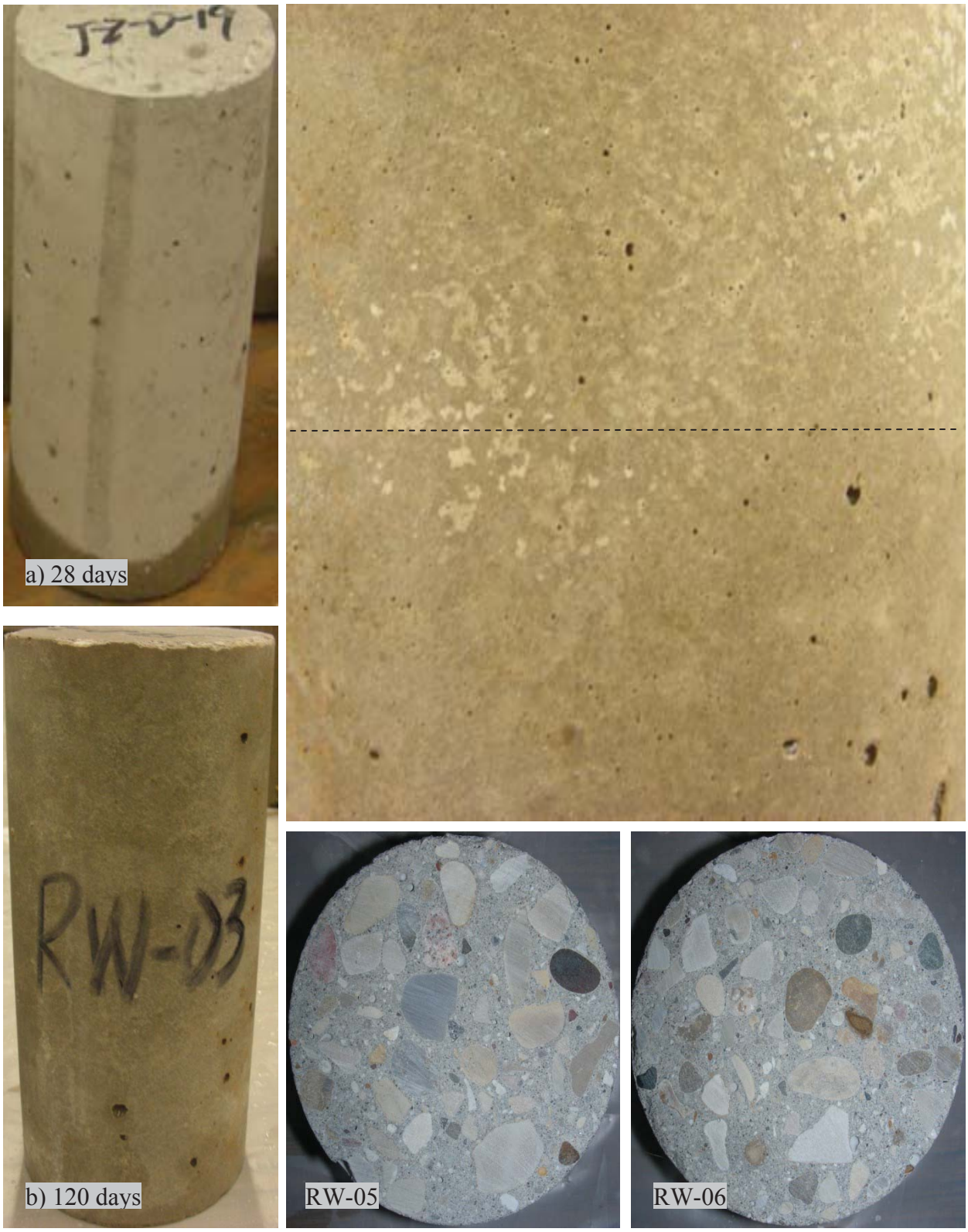

Figure 3.19: Surface conditions of reference samples RW-05/06

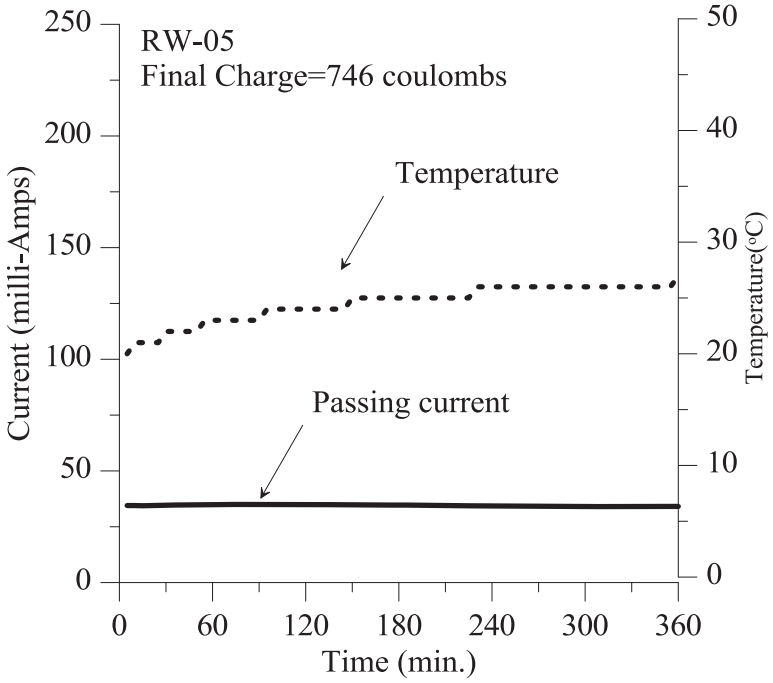

(a)RW-05

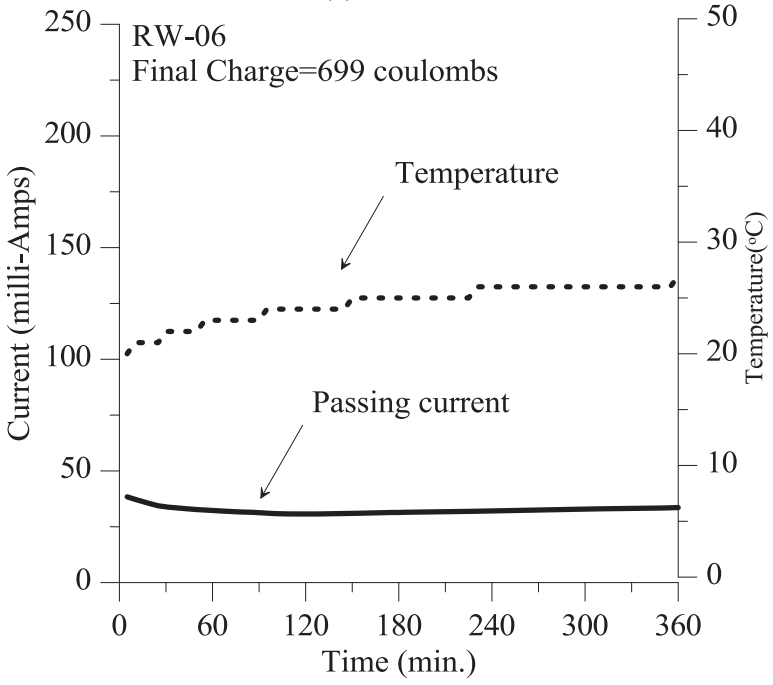

(b)RW-06

Figure 3.20: Passing current/temperature vs. time for samples RW-05/06

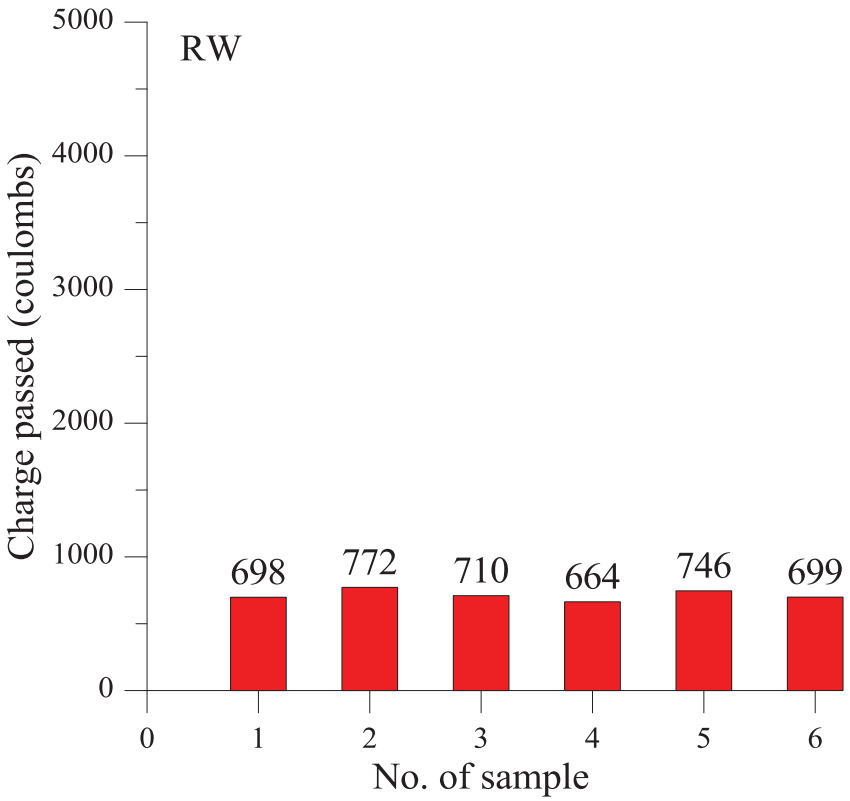

Figure 3.21: Charge passed through samples RW

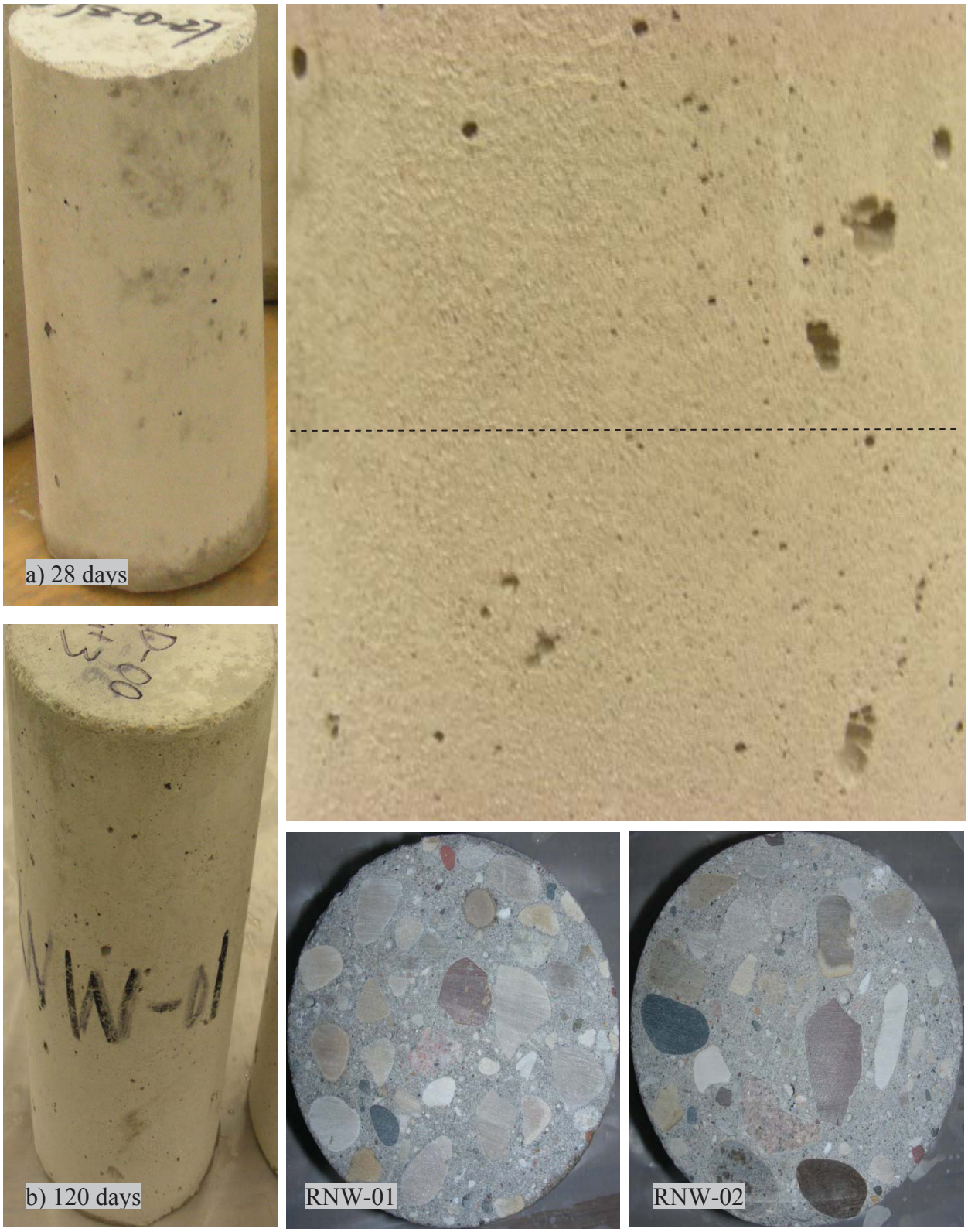

Figure 3.22: Surface conditions of reference samples RNW-01/02

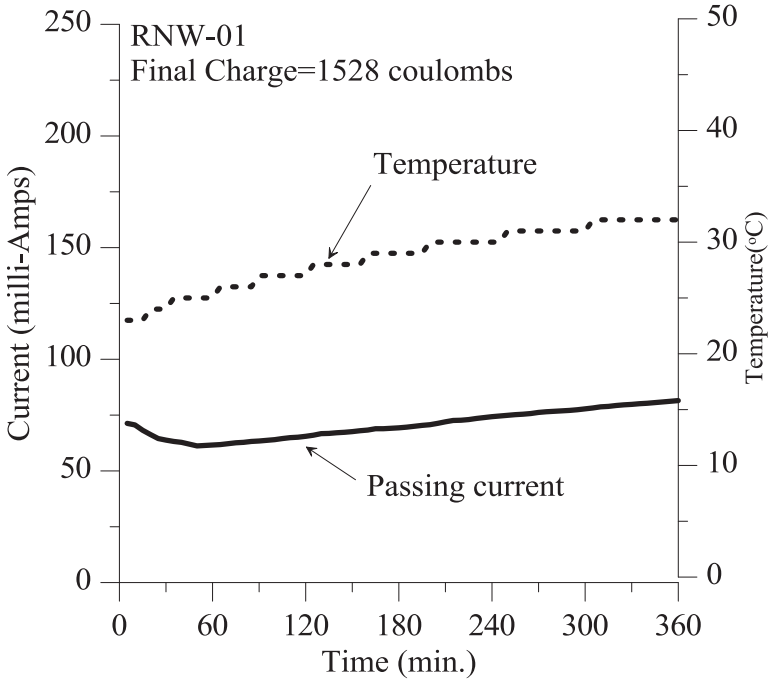

(a)RNW-01

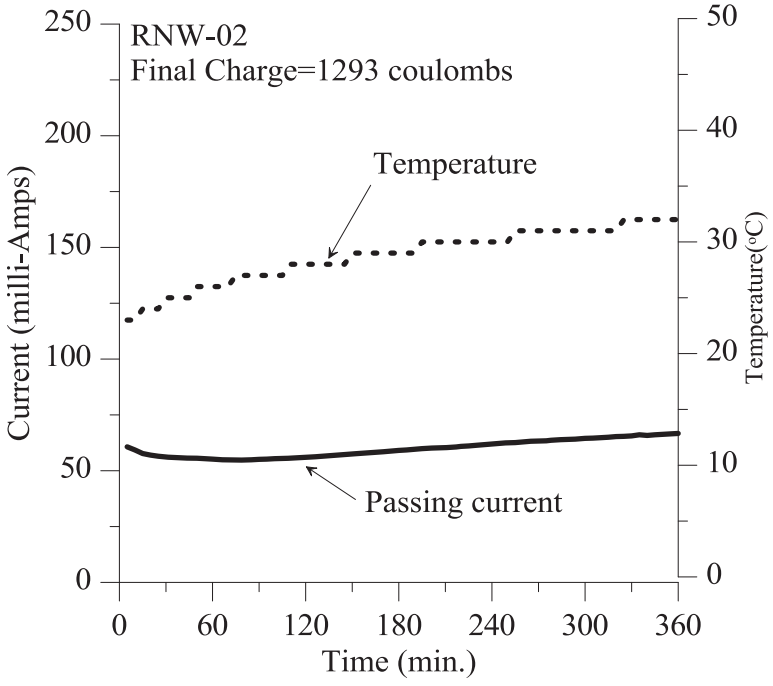

(b)RNW-02

Figure 3.23: Passing current/temperature vs. time for samples RNW-01/02

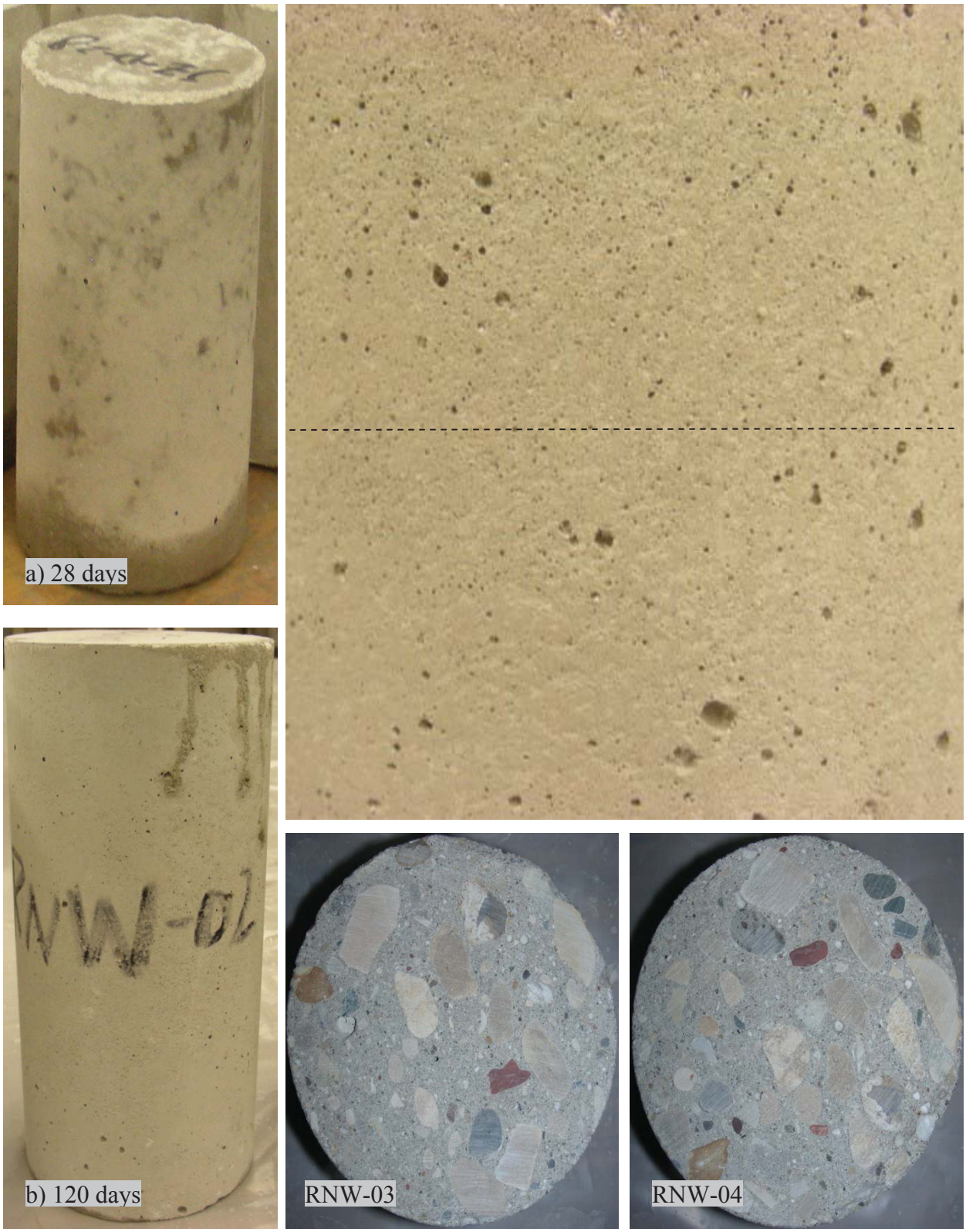

Figure 3.24: Surface conditions of reference samples RNW-03/04

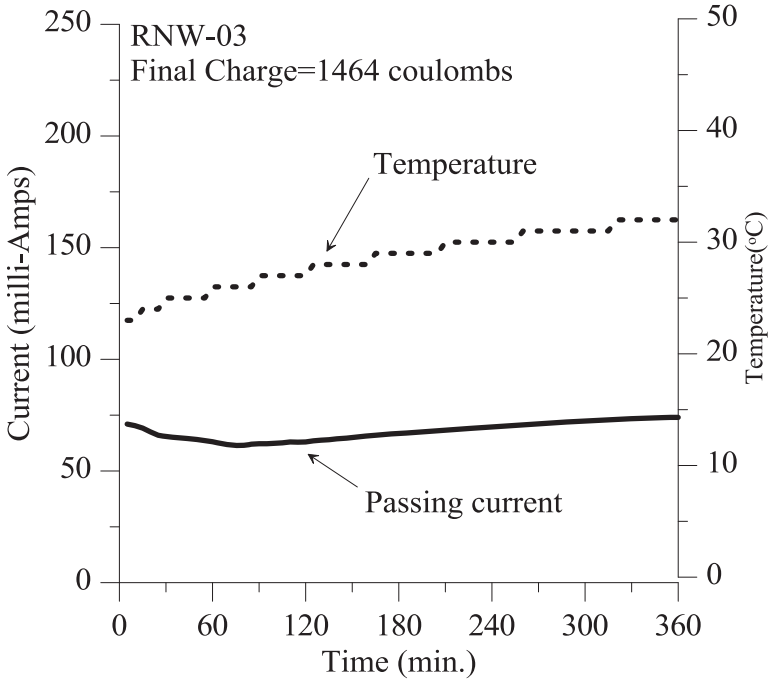

(a)RNW-03

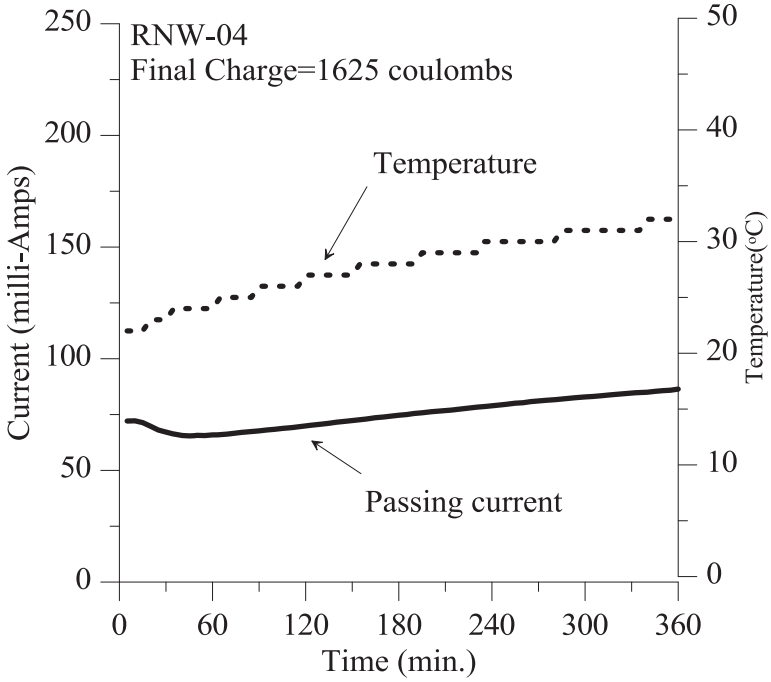

(b)RNW-04

Figure 3.25: Passing current/temperature vs. time for samples RNW-03/04

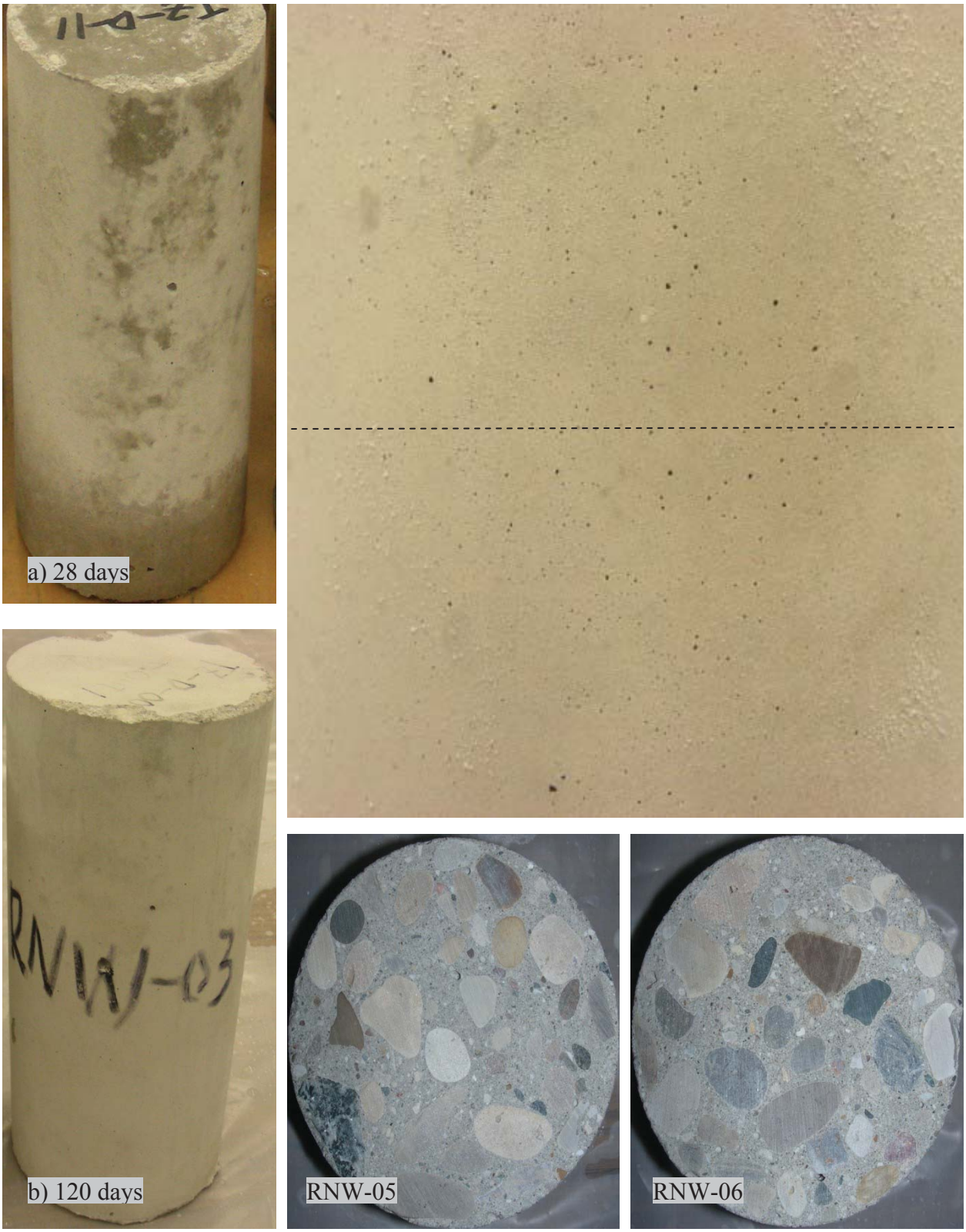

Figure 3.26: Surface conditions of reference samples RNW-05/06

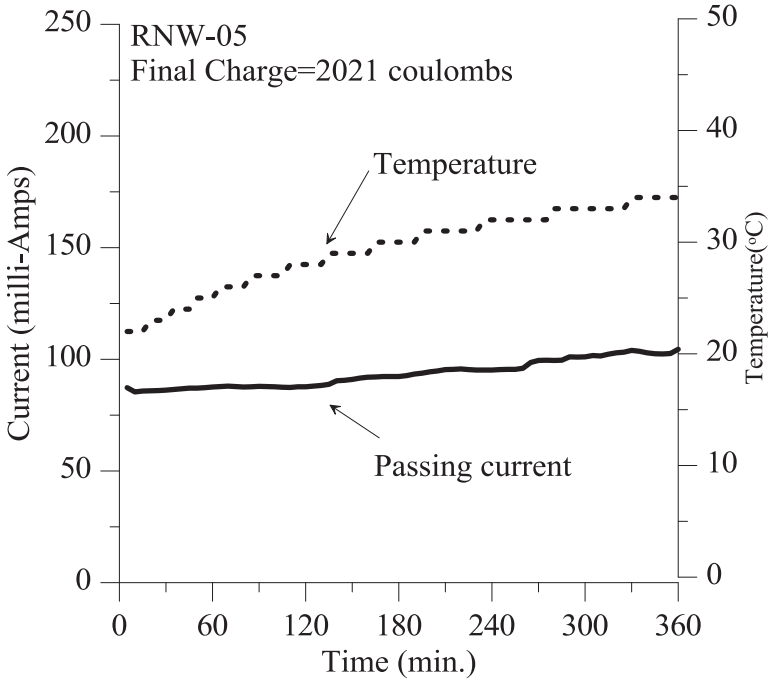

(a)RNW-03

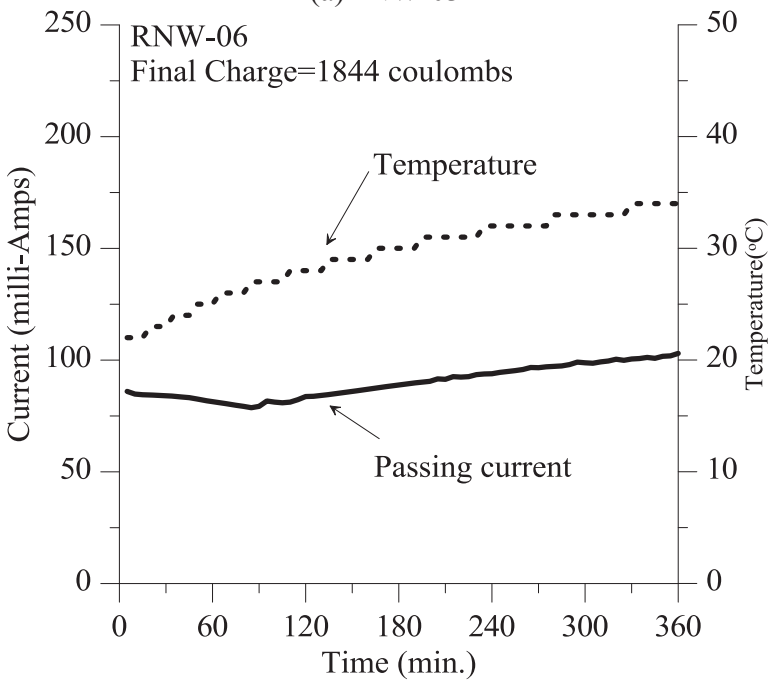

(b)RNW-04

Figure 3.27: Passing current/temperature vs. time for samples RNW-05/06

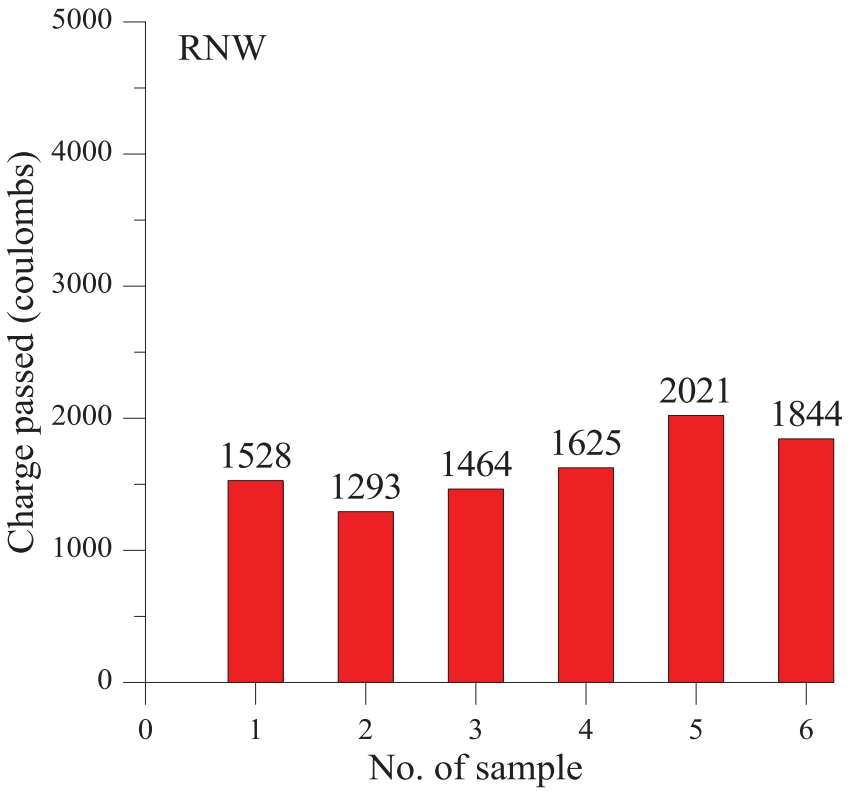

Figure 3.28: Charge passed through samples RNW

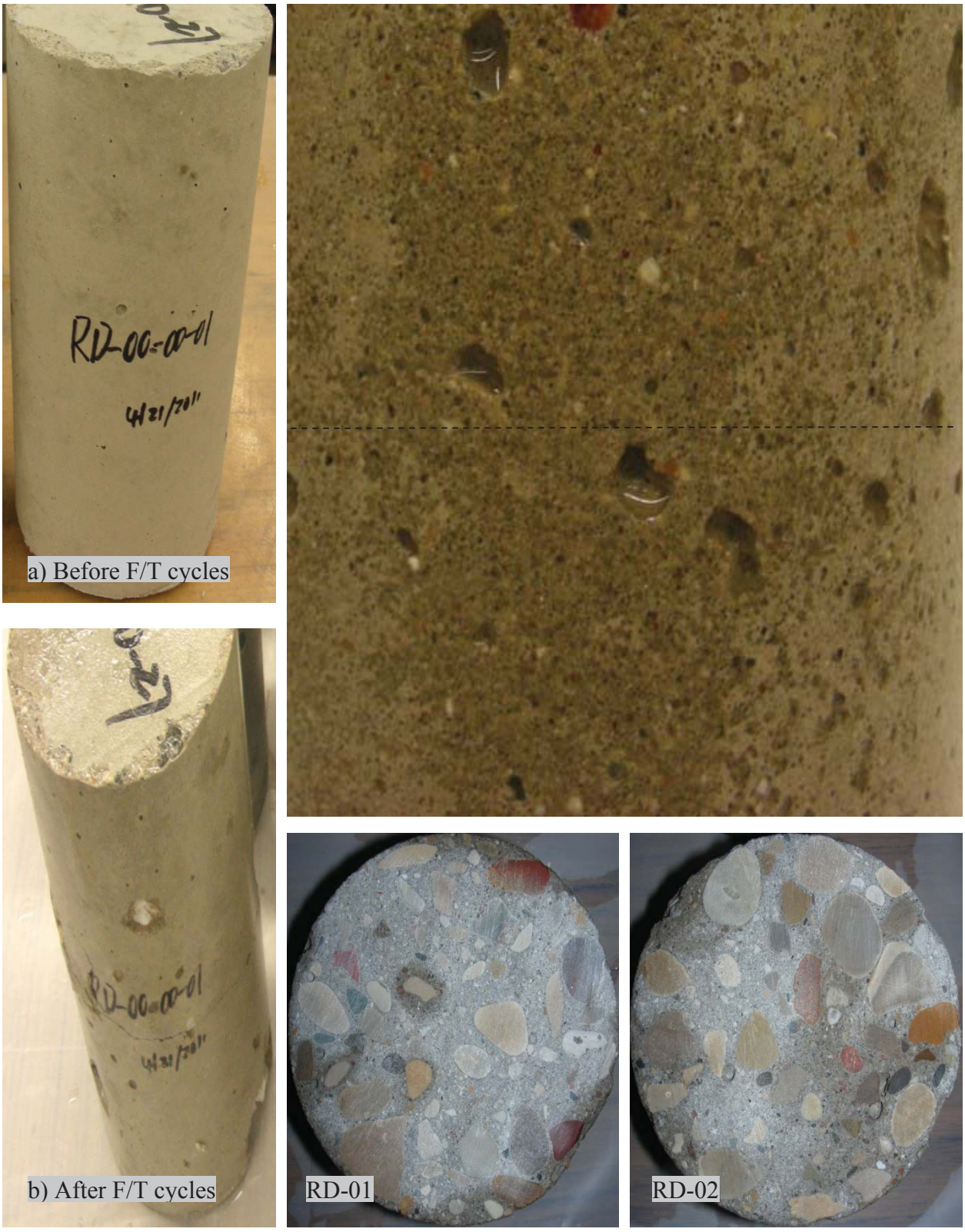

Figure 3.29: Surface conditions of reference samples RD-01/02

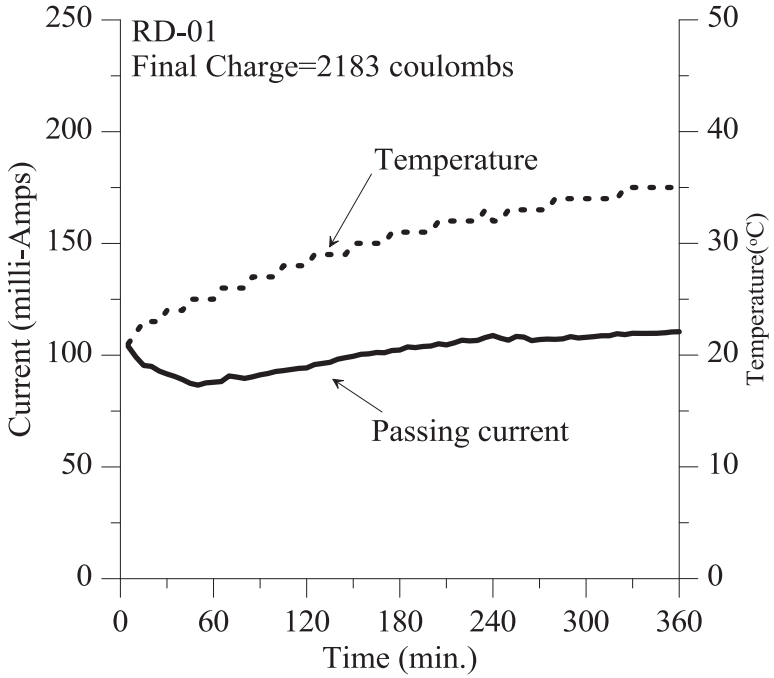

(a)RD-01

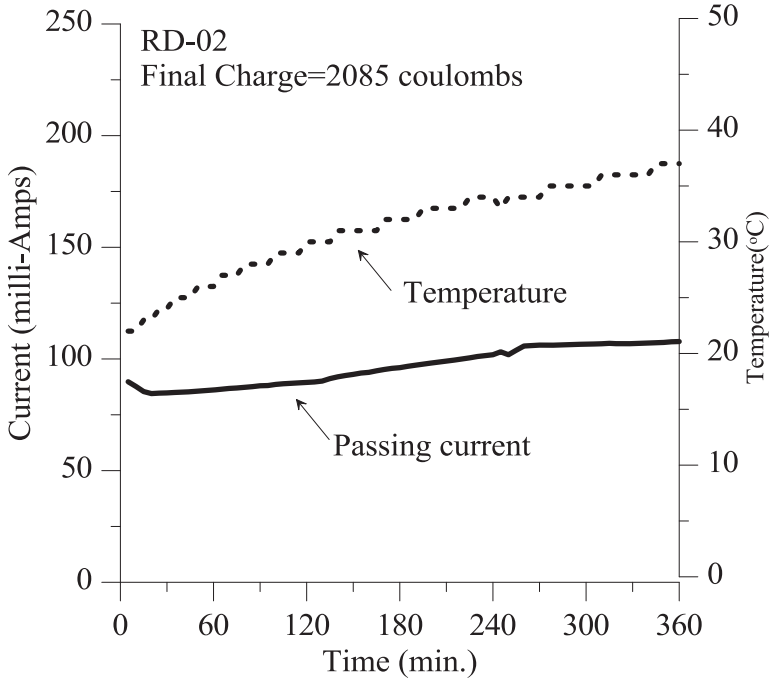

(b)RD-02

Figure 3.30: Passing current/temperature vs. time for samples RD-01/02

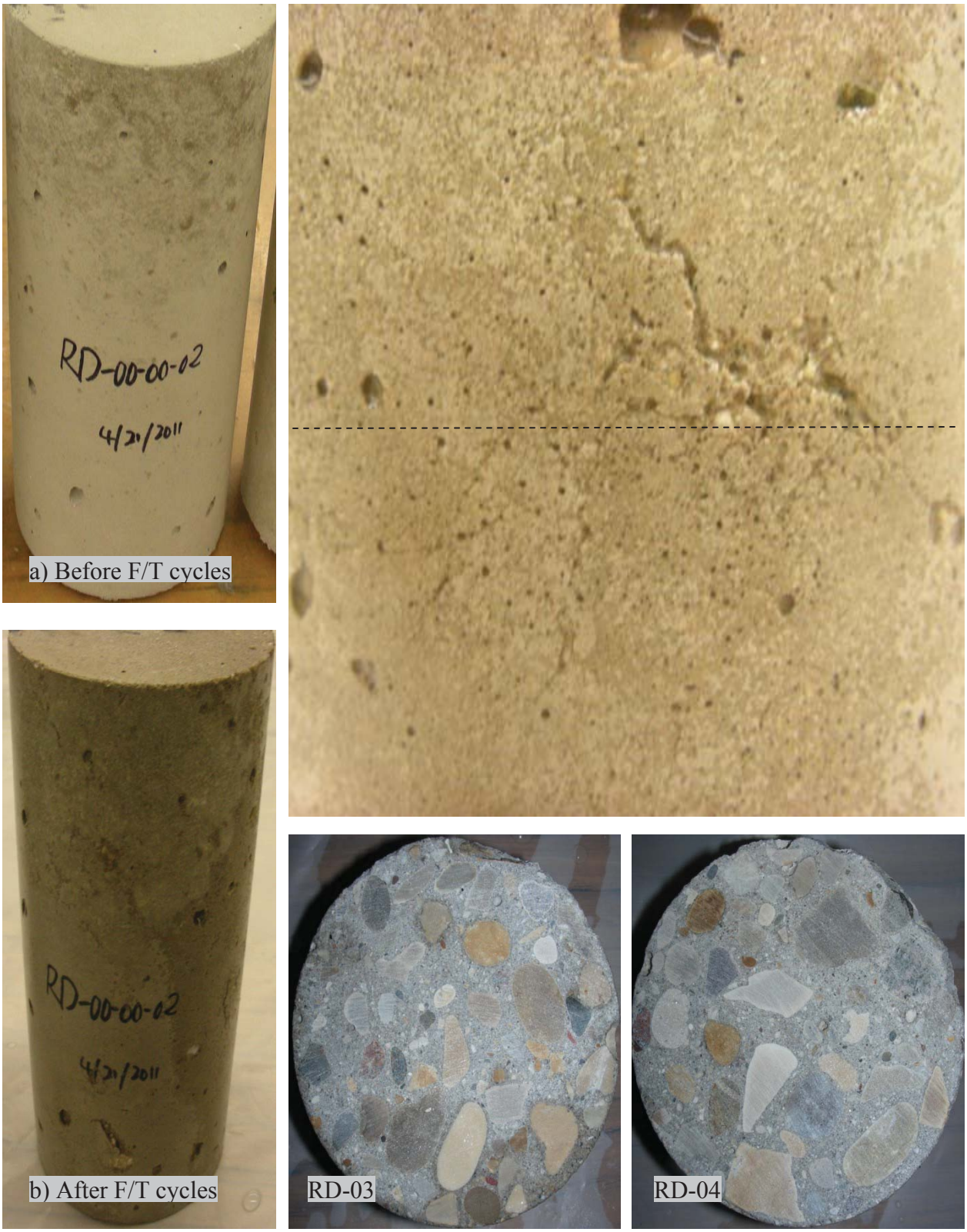

Figure 3.31: Surface conditions of reference samples RD-03/04

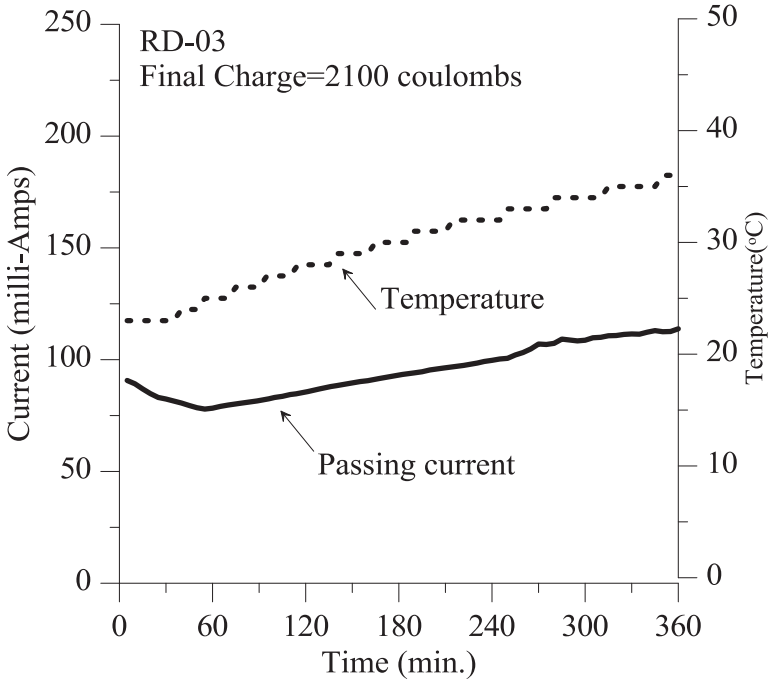

(a)RD-03

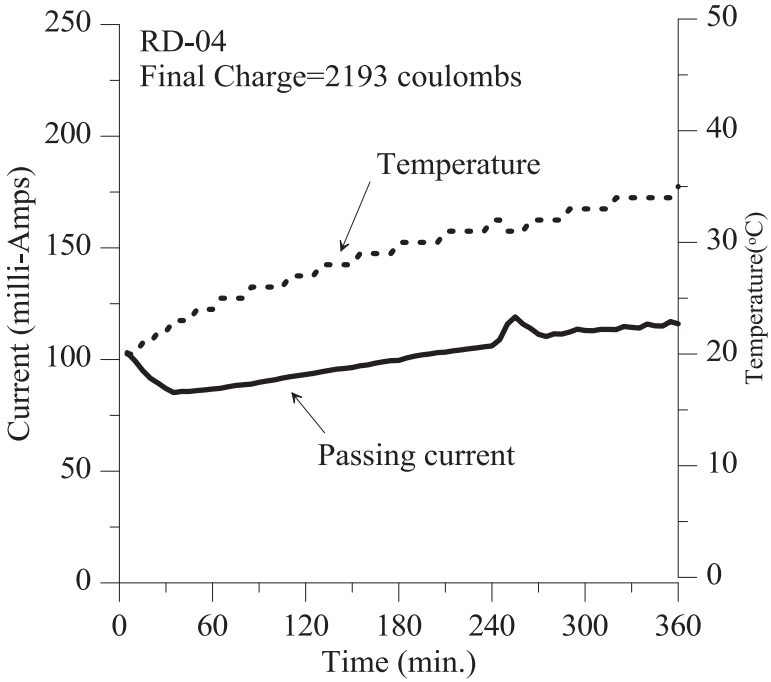

(b)RD-04

Figure 3.32: Passing current/temperature vs. time for samples RD-03/04

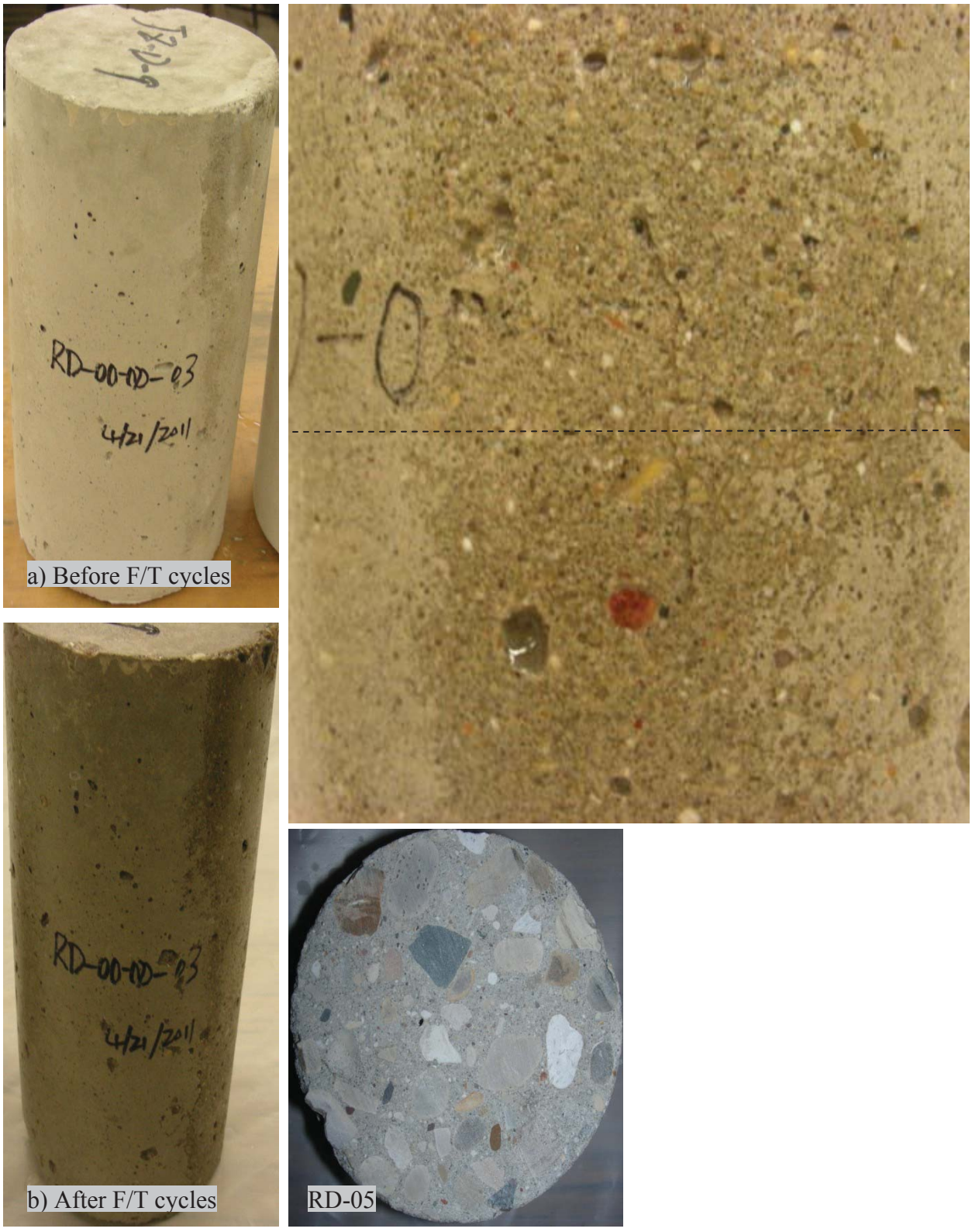

Figure 3.33: Surface conditions of reference samples RD-05

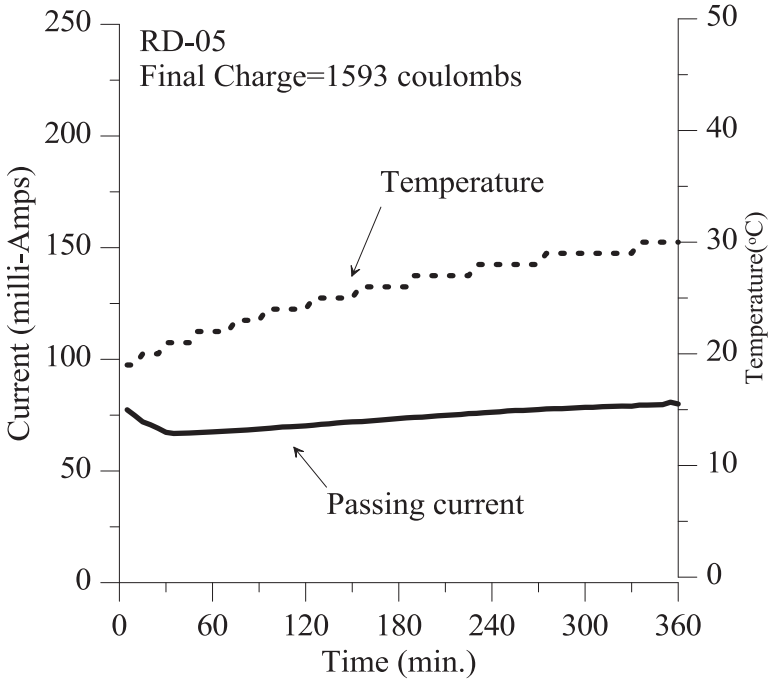

Figure 3.34: Passing current/temperature vs. time for samples RD-05

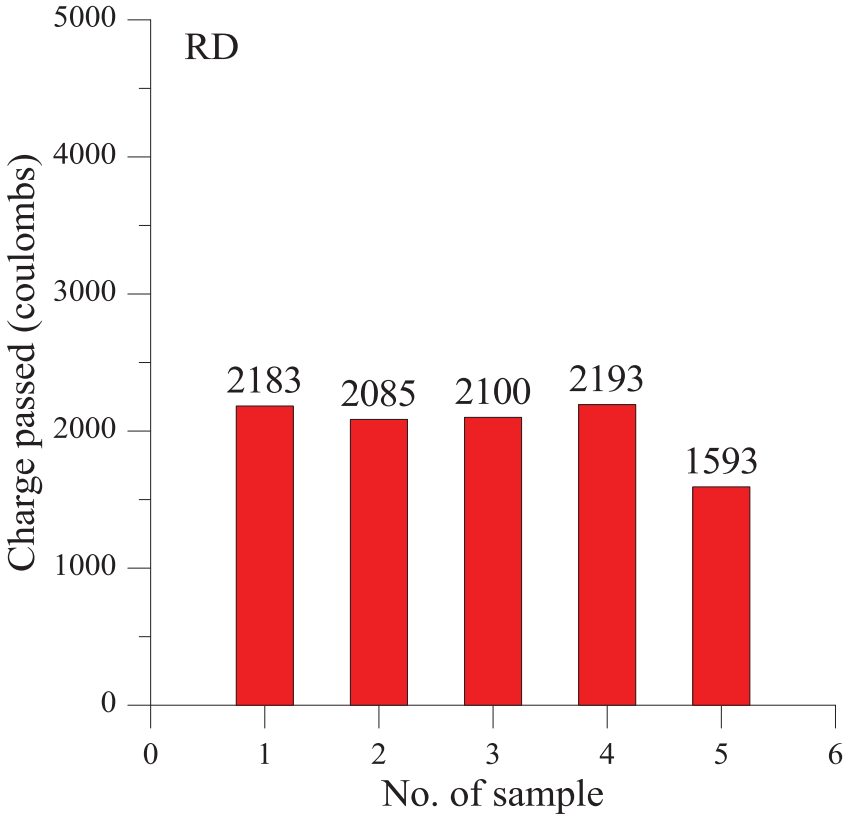

Figure 3.35: Charge passed through samples RD

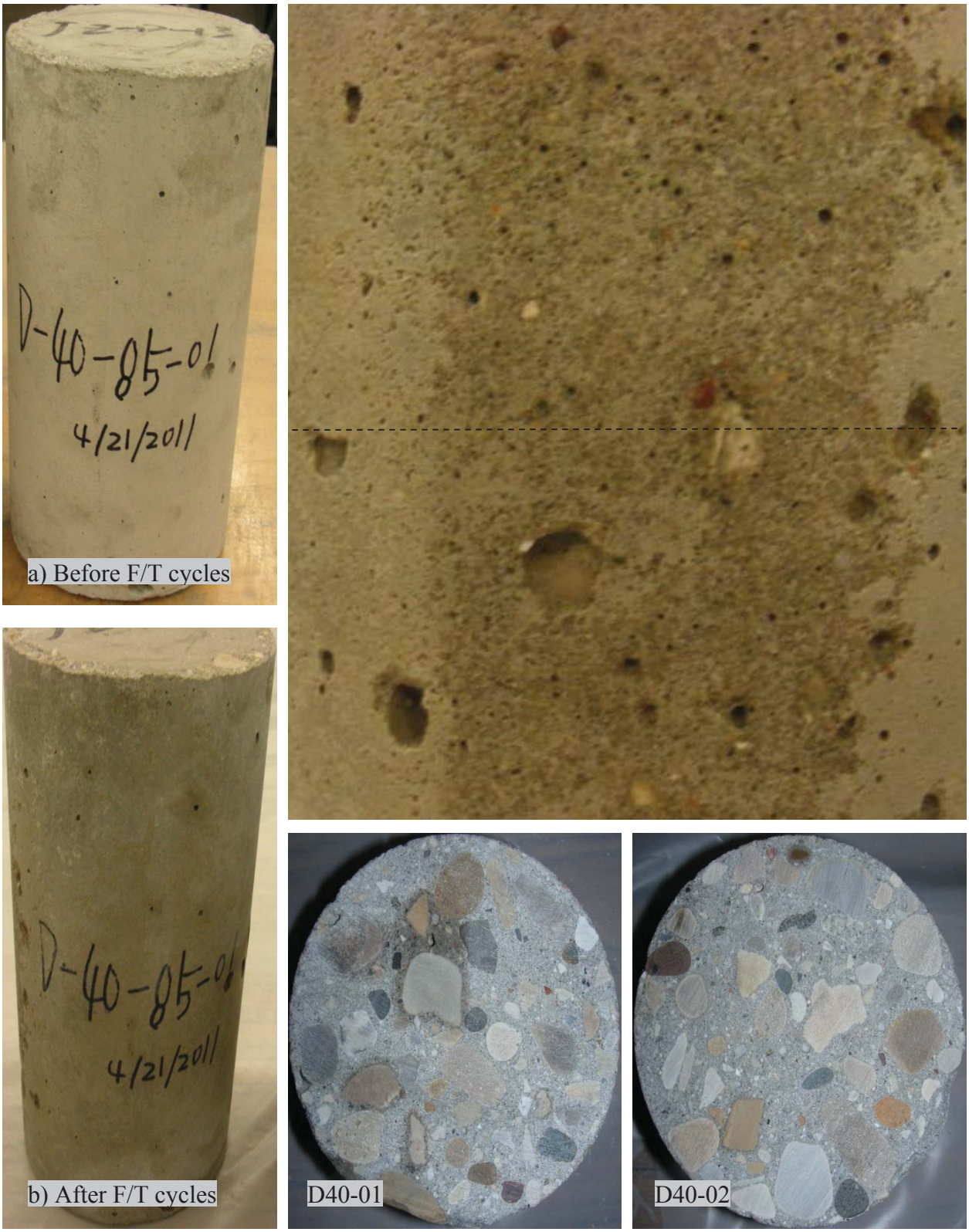

Figure 3.36: Surface conditions of samples D40-01/02

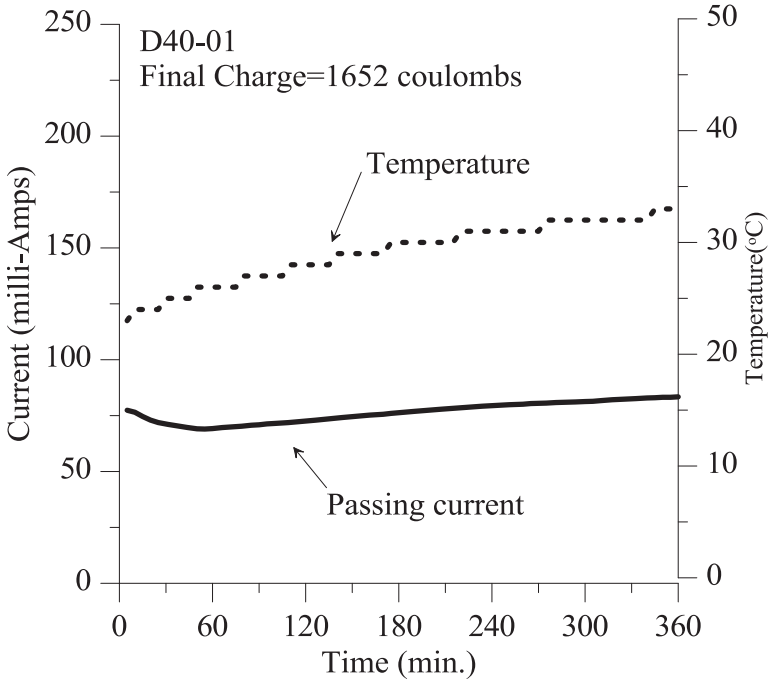

(a)D40-01

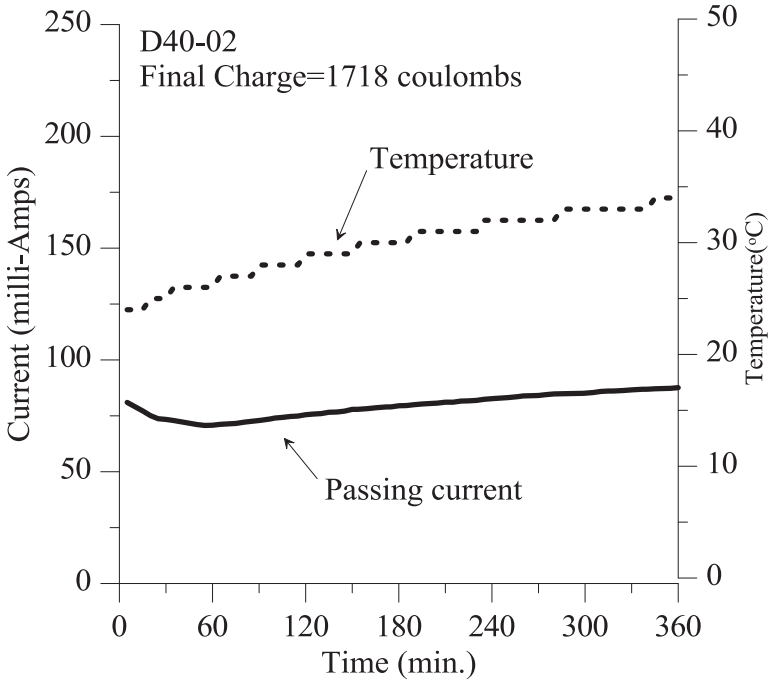

(b) D40-02

Figure 3.37: Passing current/temperature vs. time for samples D40-01/02

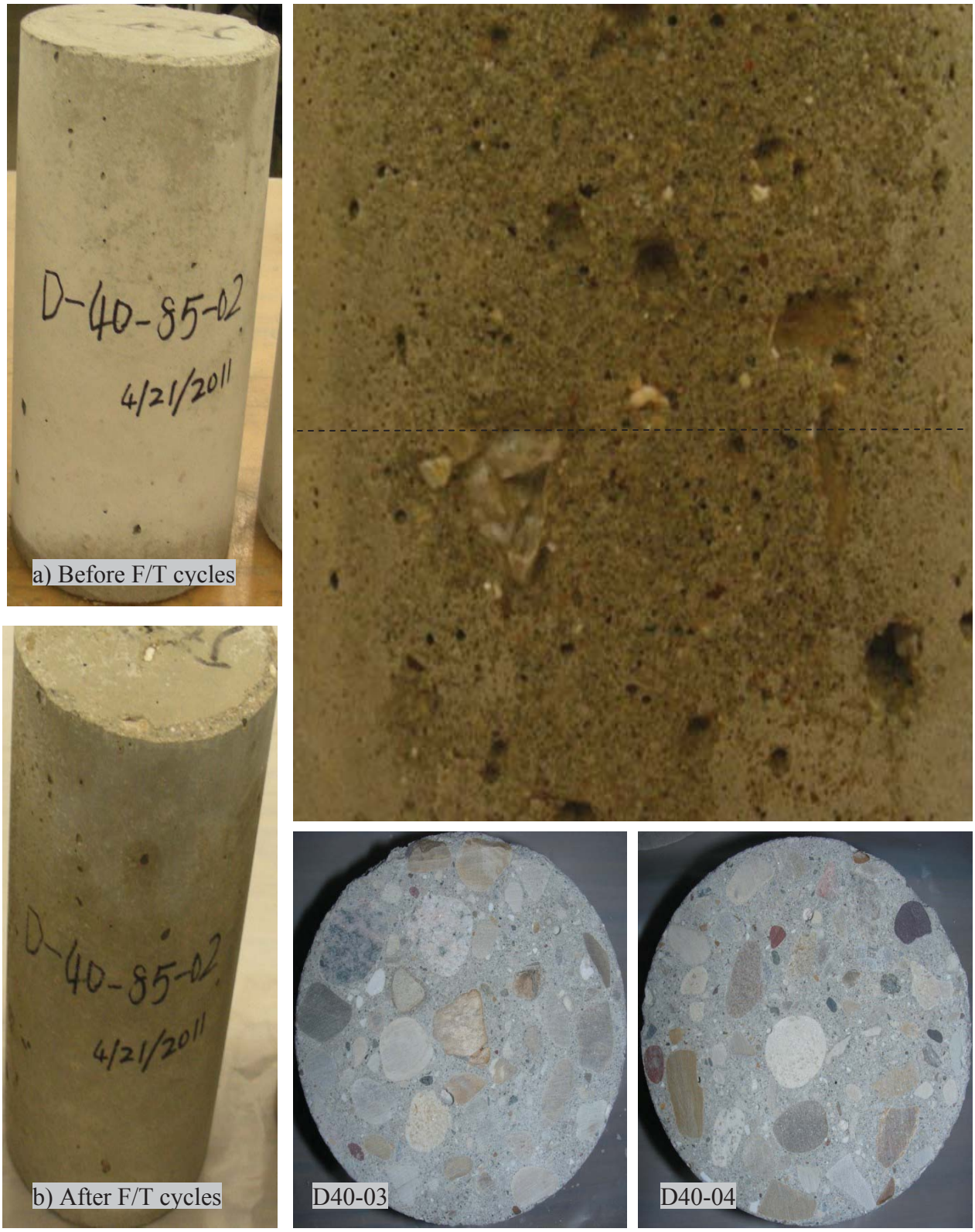

Figure 3.38: Surface conditions of samples D40-03/04

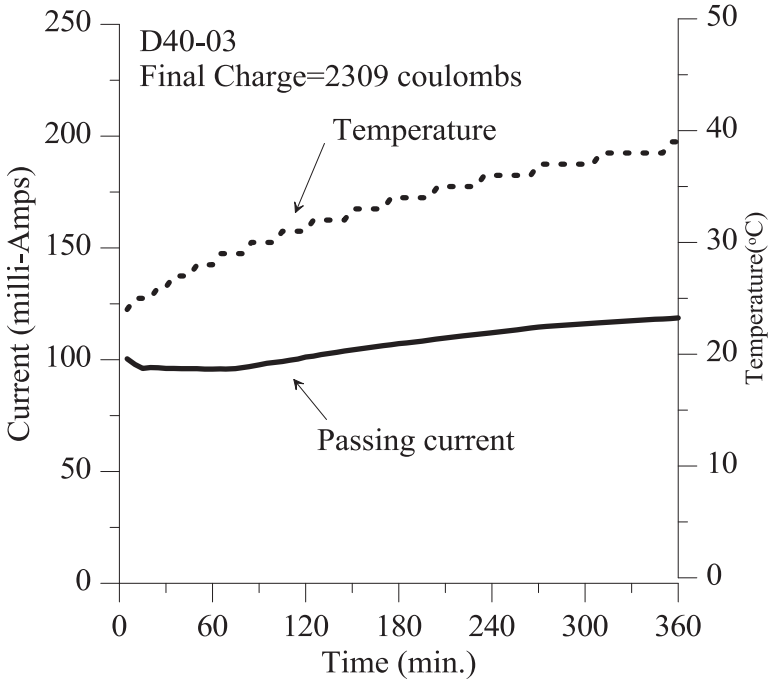

(a)D40-03

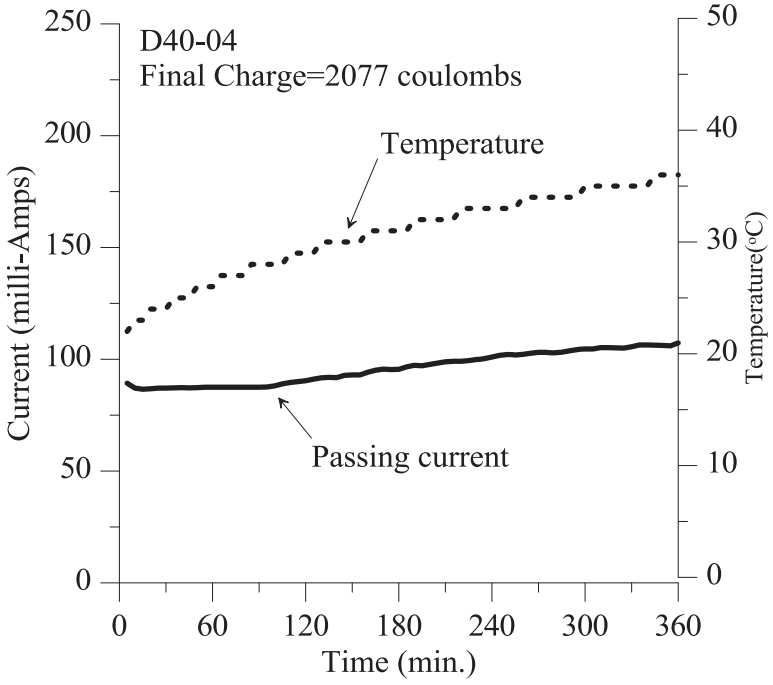

(b) D40-04

Figure 3.39: Passing current/temperature vs. time for samples D40-03/04

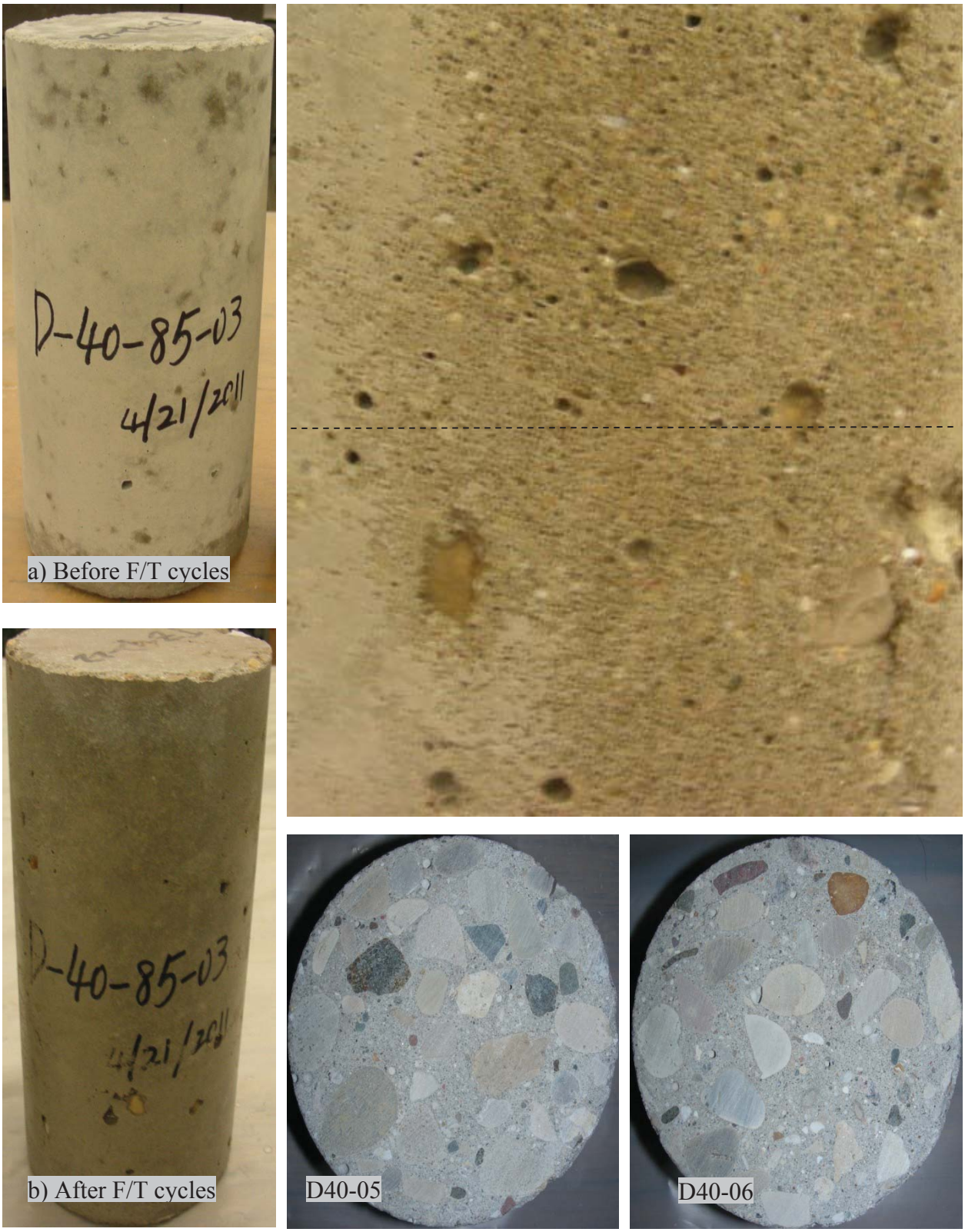

Figure 3.40: Surface conditions of samples D40-05/06

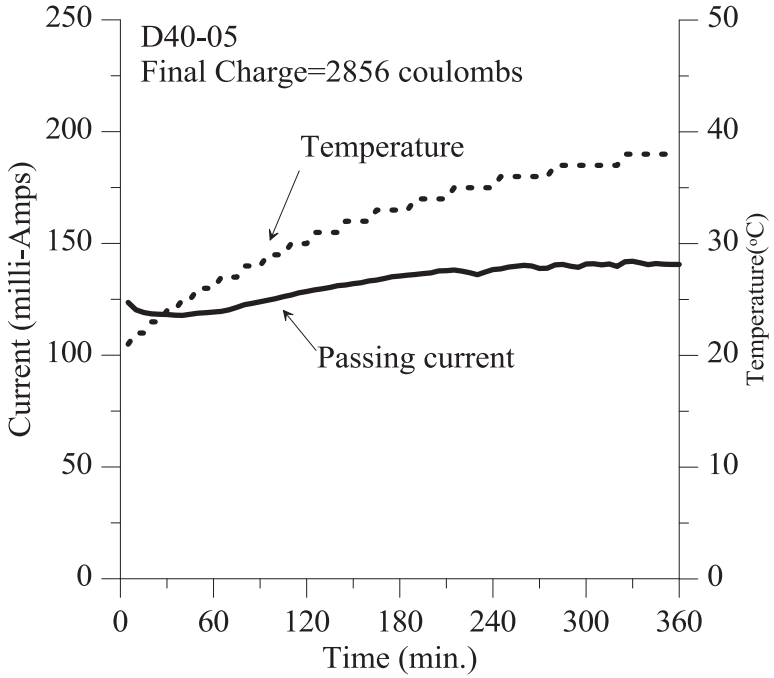

(a)D40-05

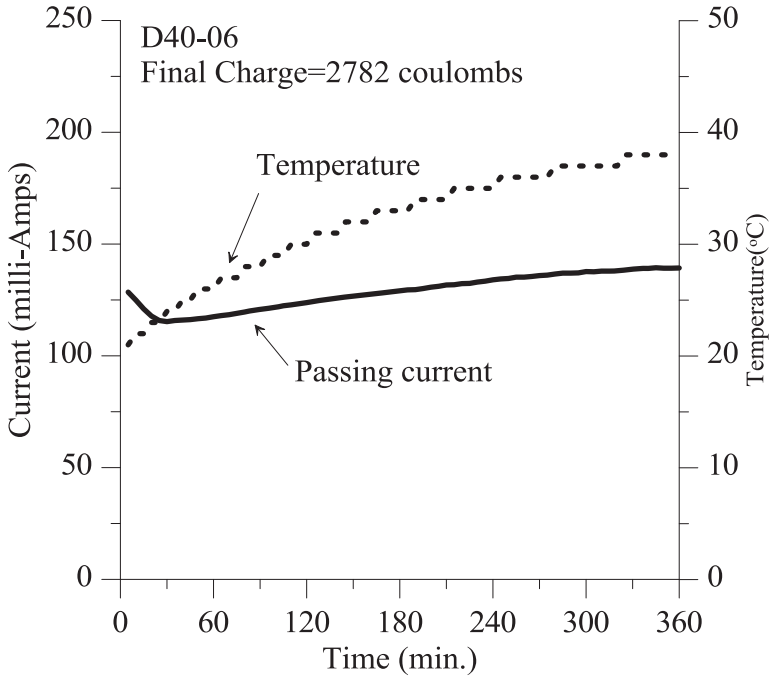

(b) D40-06

Figure 3.41: Passing current/temperature vs. time for samples D40-05/06

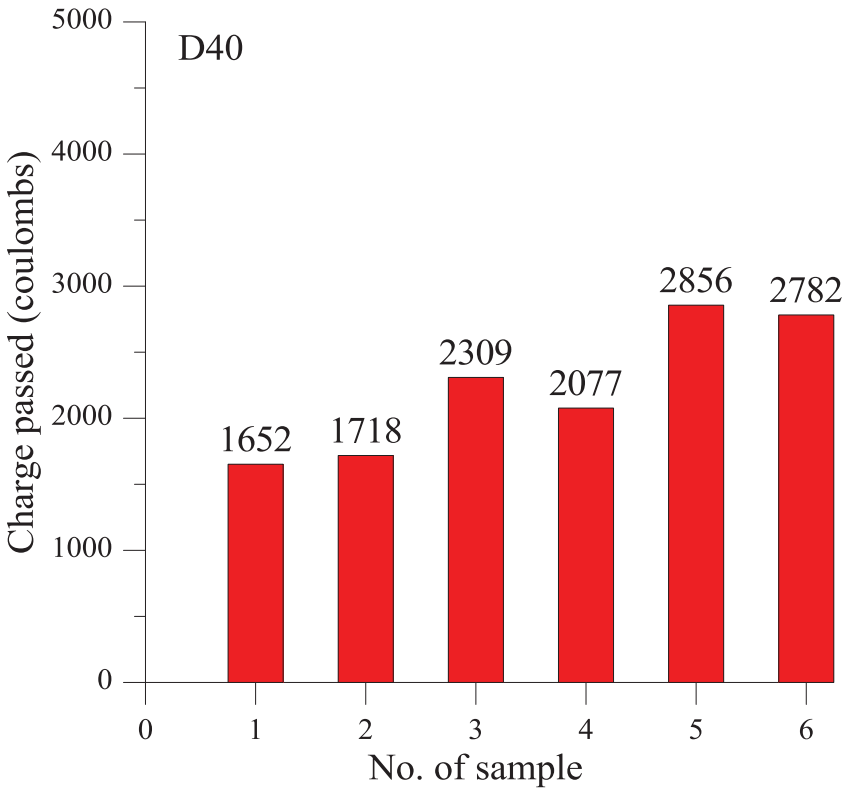

Figure 3.42: Charge passed through samples D40

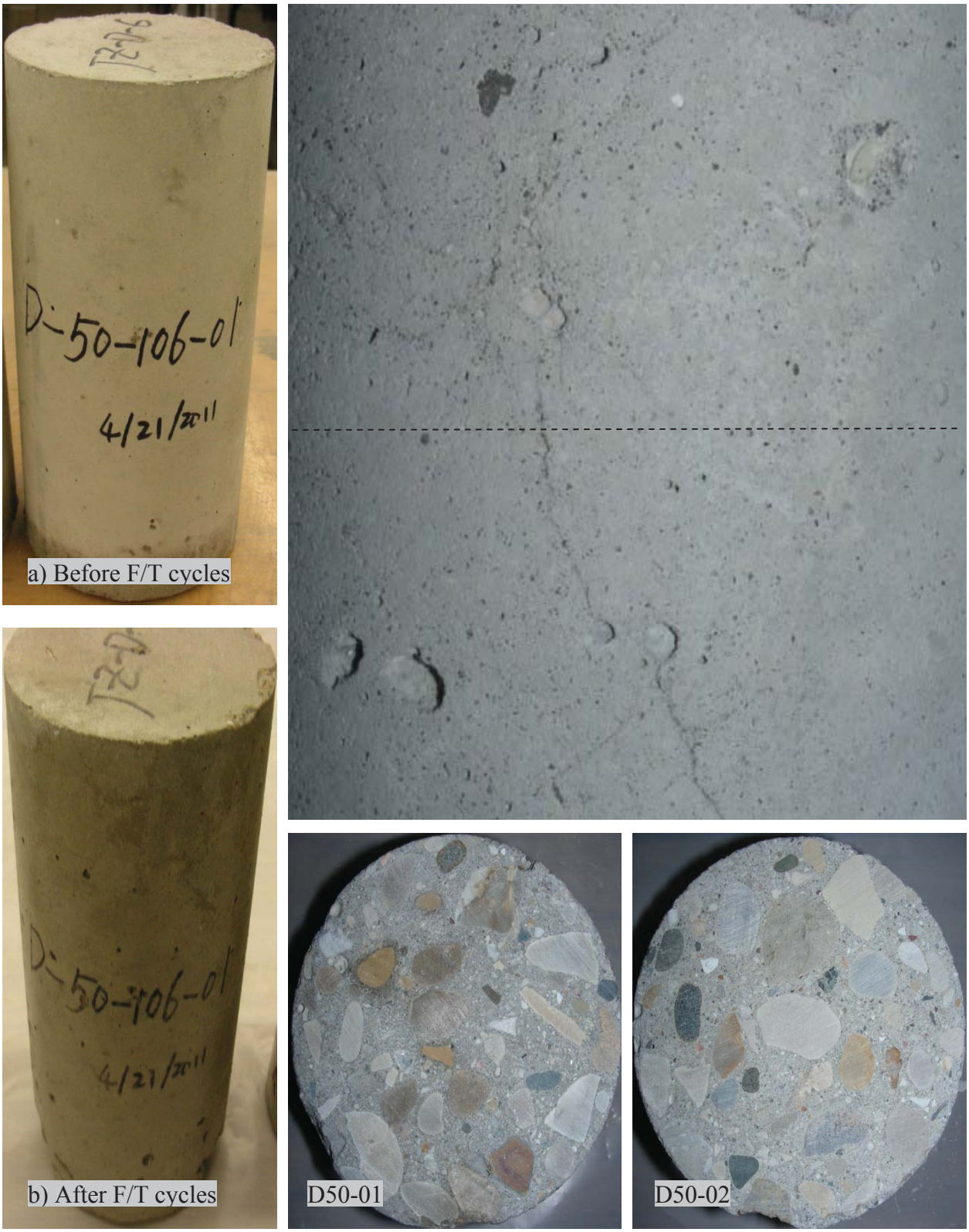

Figure 3.43: Surface conditions of samples D50-01/02

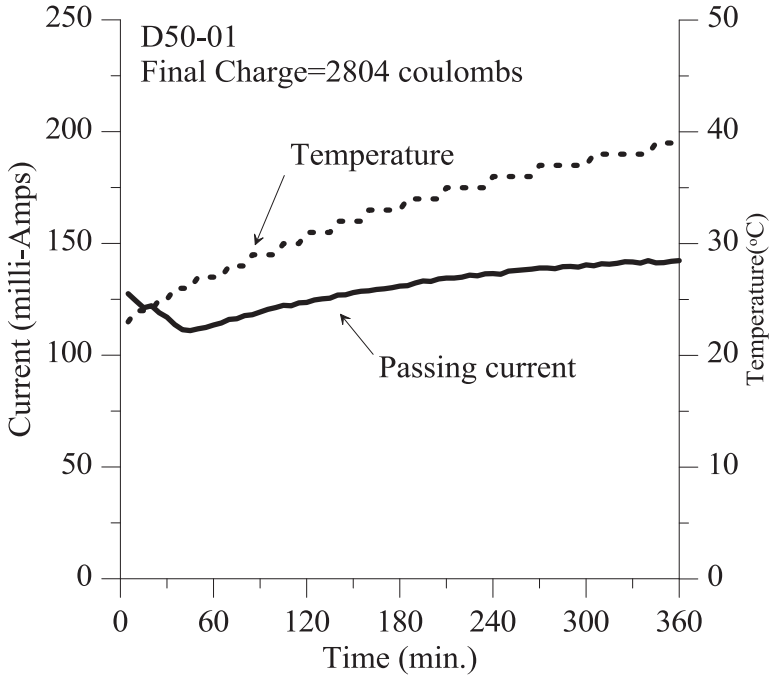

(a)D50-01

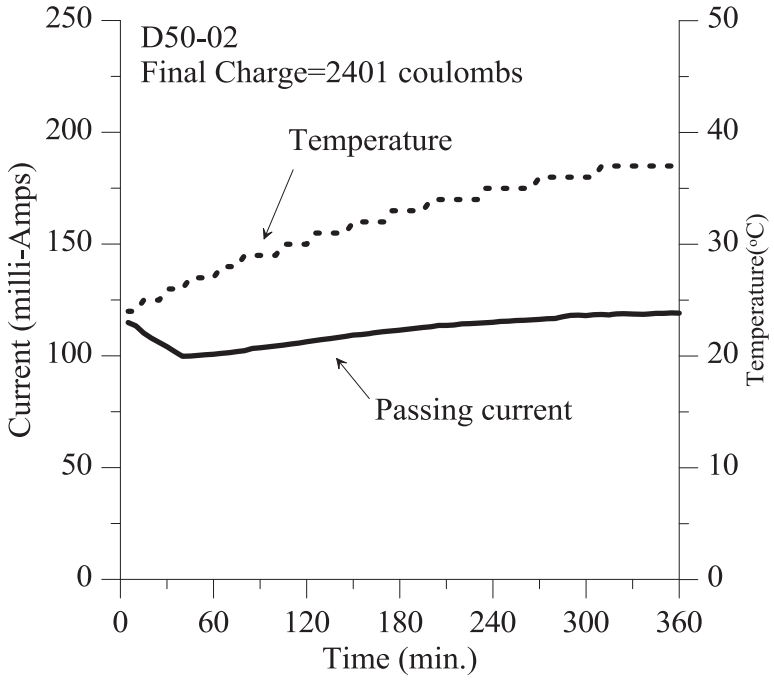

(b) D50-02

Figure 3.44: Passing current/temperature vs. time for samples D50-01/02

Figure 3.45: Surface conditions of samples D50-03/04

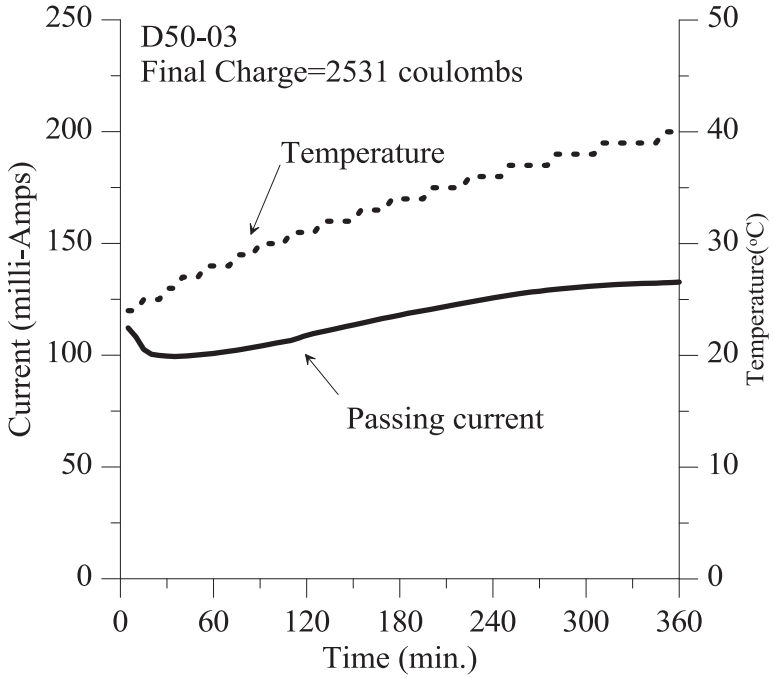

(a)D50-03

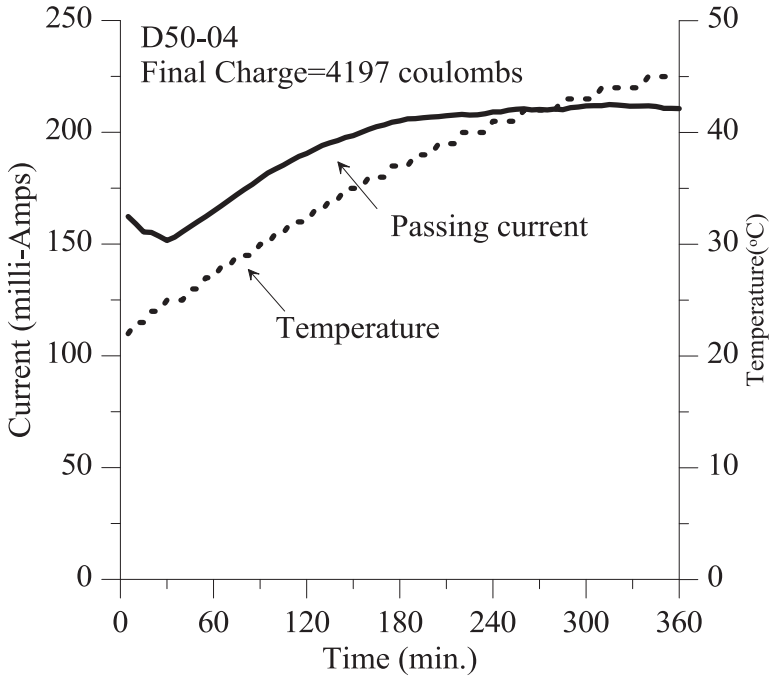

(b) D50-04

Figure 3.46: Passing current/temperature vs. time for samples D50-03/04

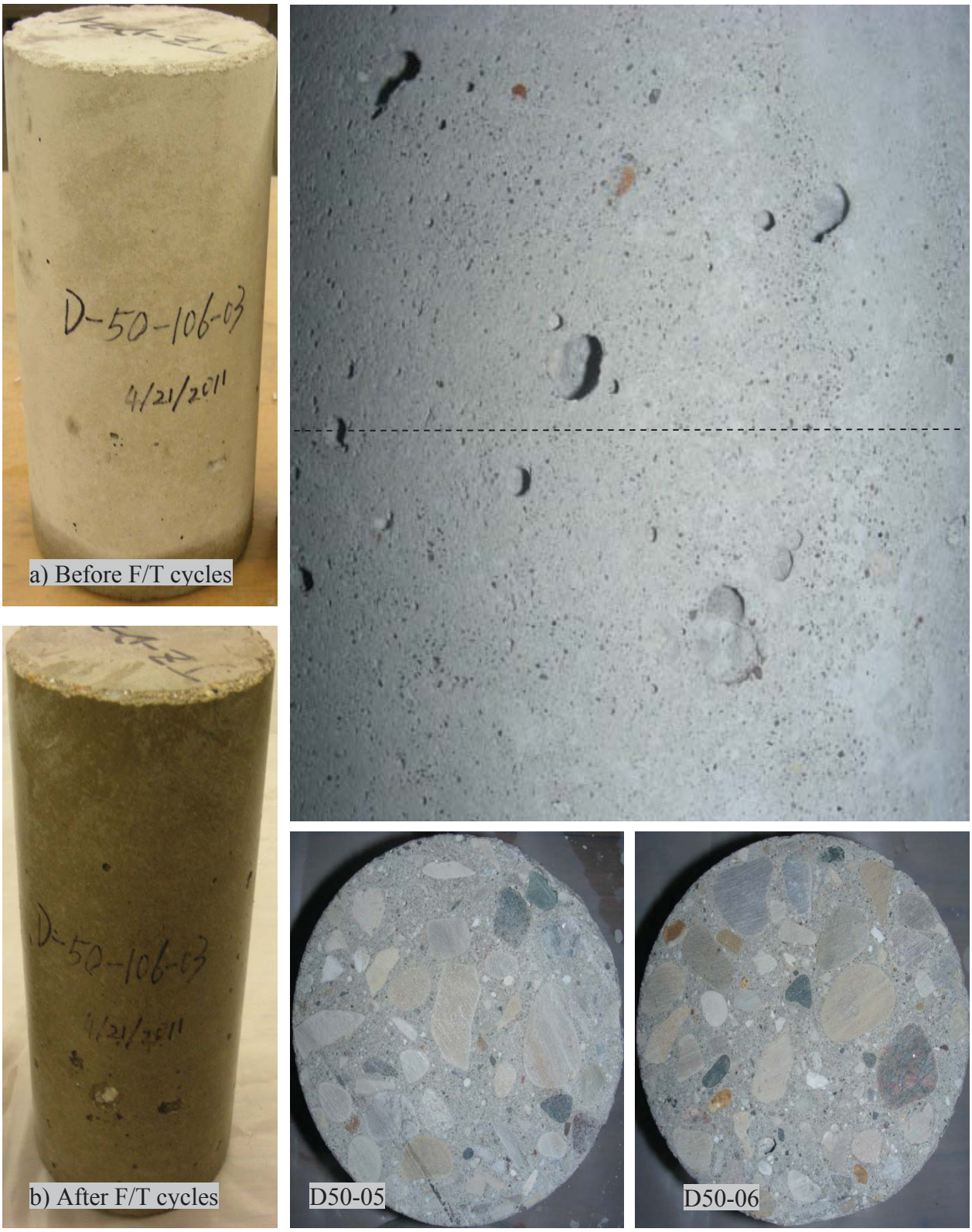

Figure 3.47: Surface conditions of samples D50-05/06

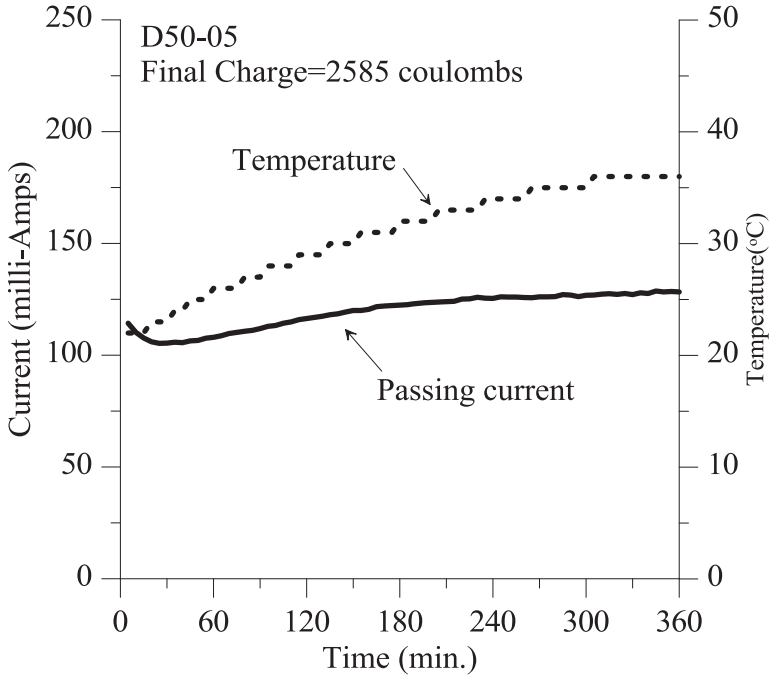

(a)D50-05

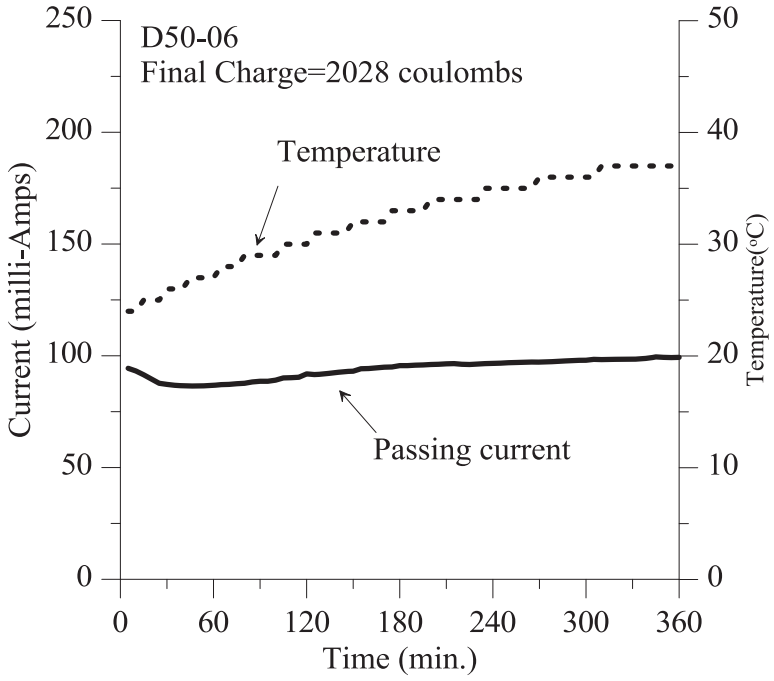

(b) D50-06

Figure 3.48: Passing current/temperature vs. time for samples D50-05/06

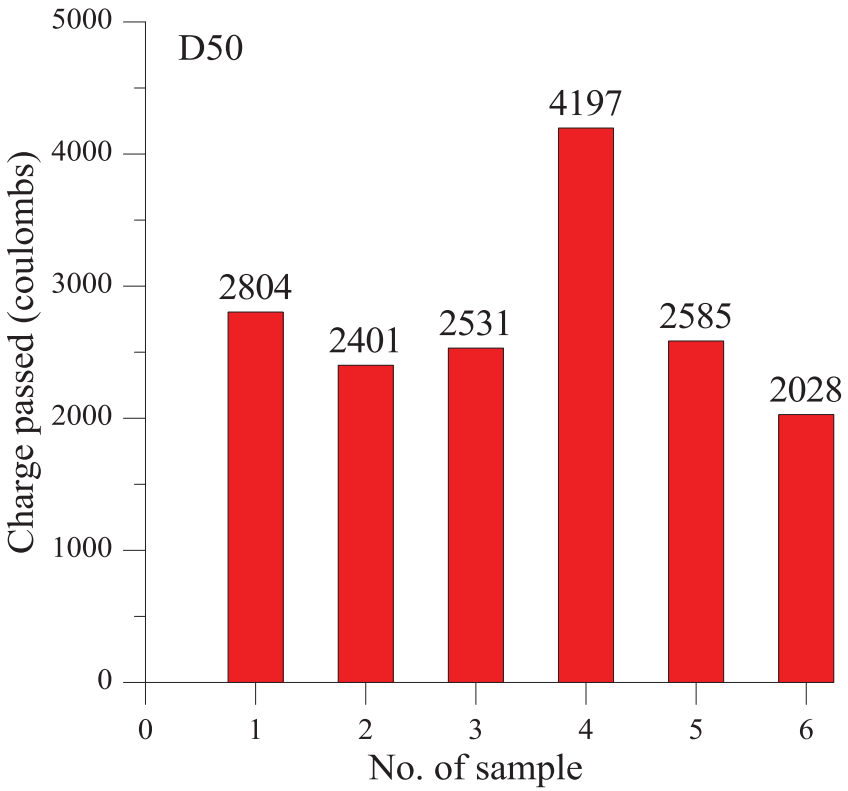

Figure 3.49: Charge passed through samples D50

Figure 3.50: Surface conditions of samples D60-01/02

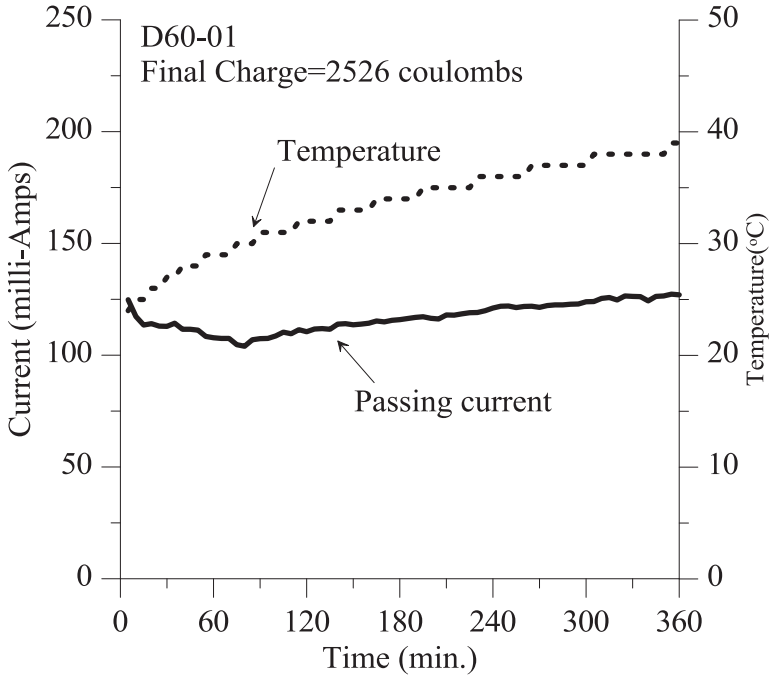

(a)D60-01

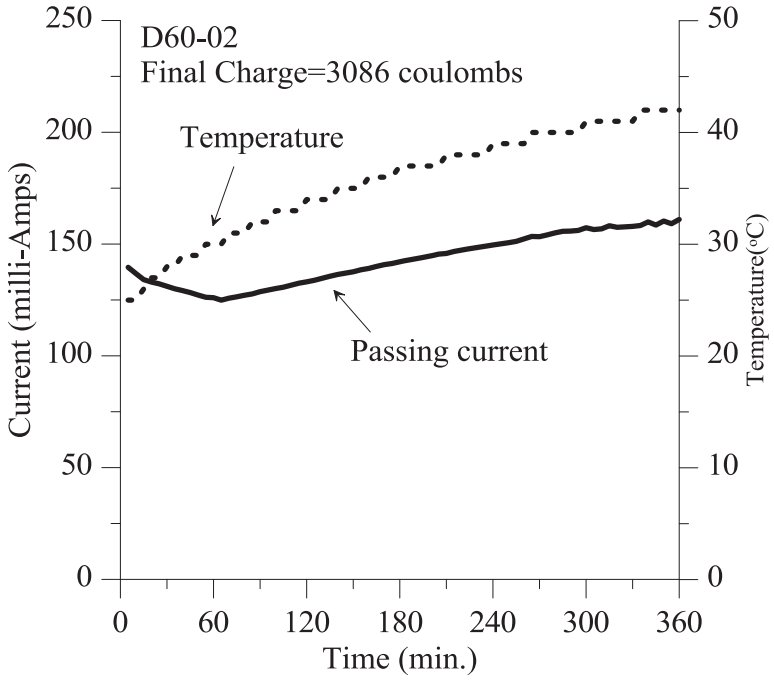

(b) D60-02

Figure 3.51: Passing current/temperature vs. time for samples D60-01/02

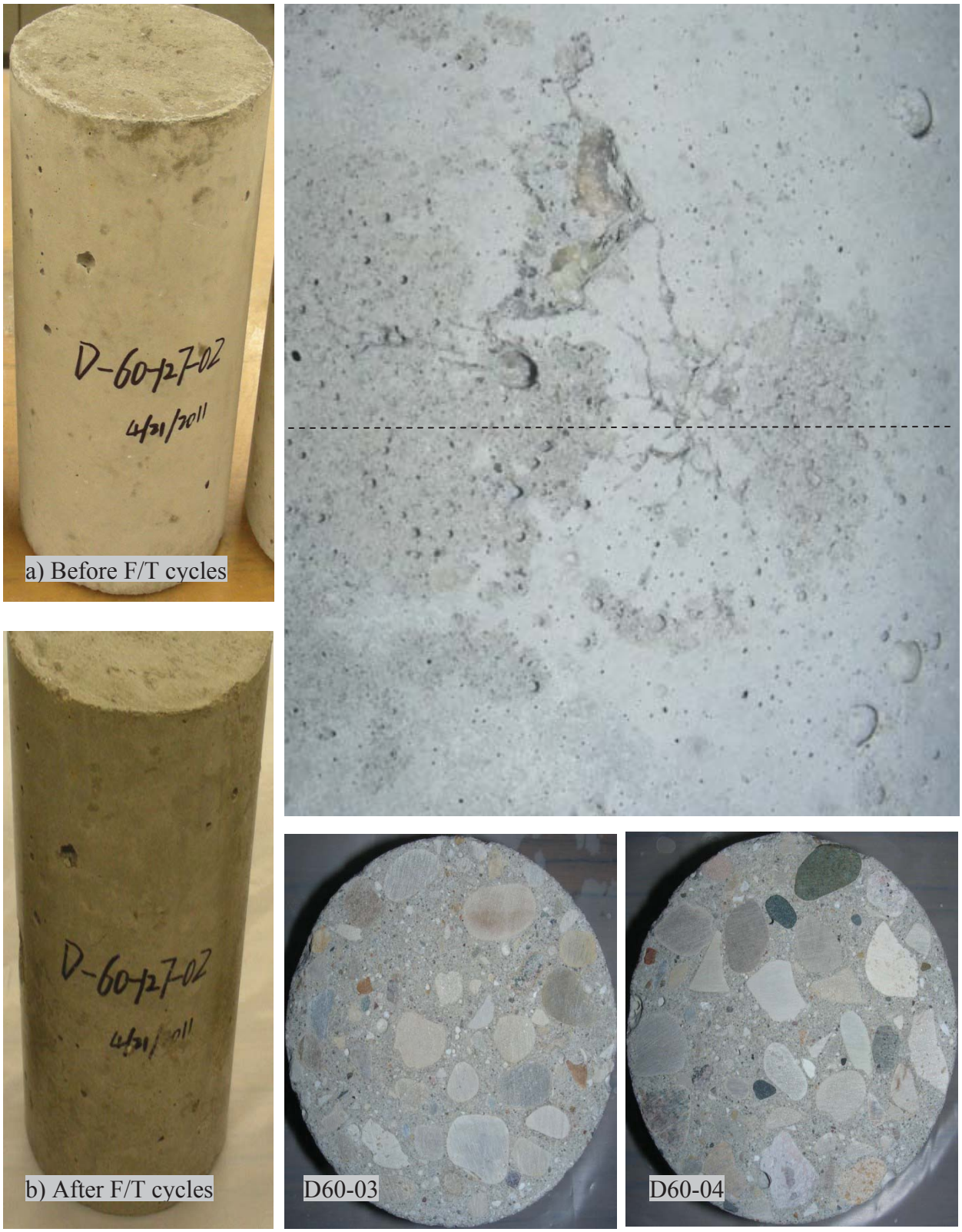

Figure 3.52: Surface conditions of samples D60-03/04

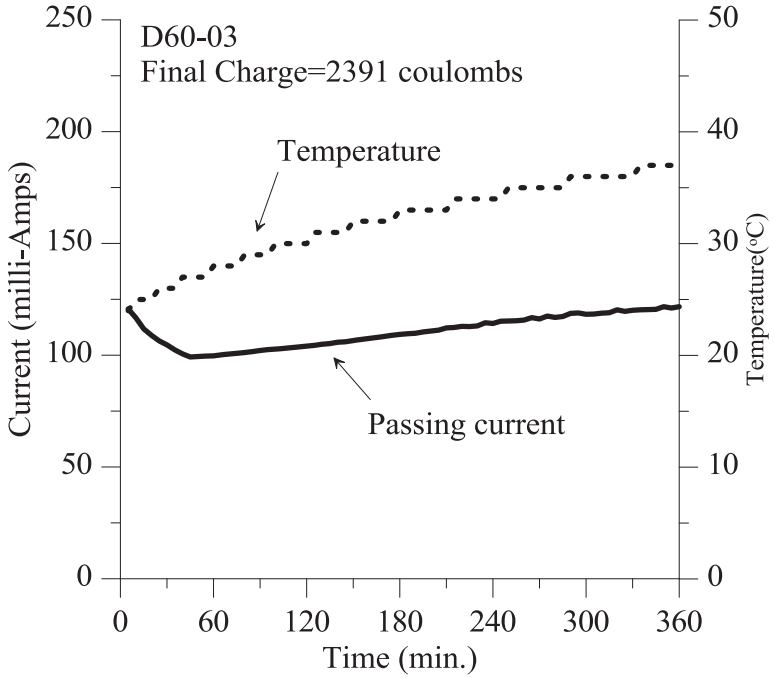

(a)D60-03

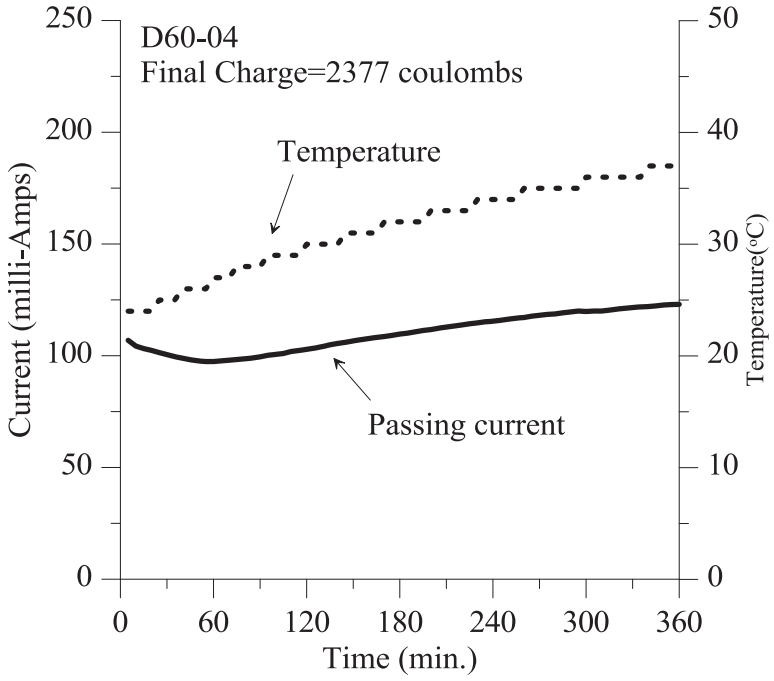

(b) D60-04

Figure 3.53: Passing current/temperature vs. time for samples D60-03/04

Figure 3.54: Surface conditions of samples D60-05/06

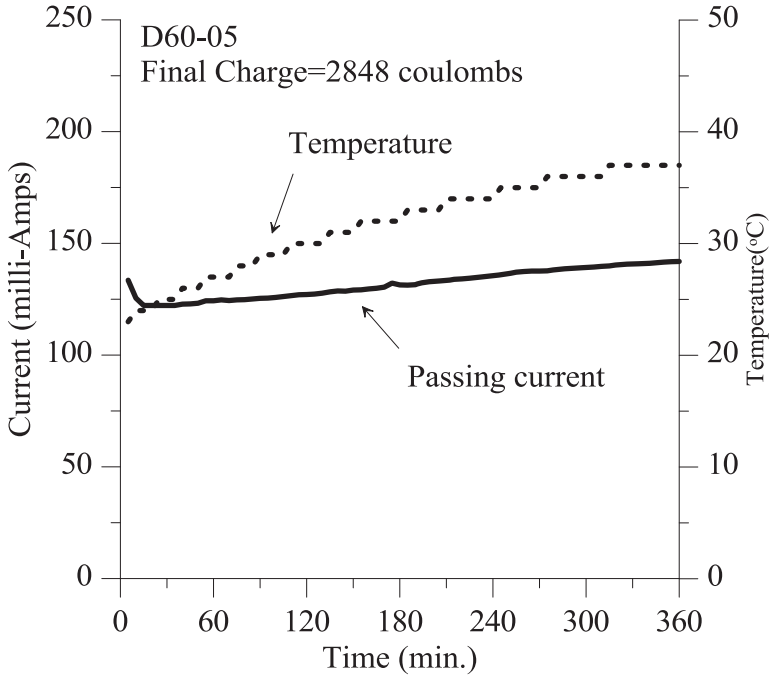

(a)D60-05

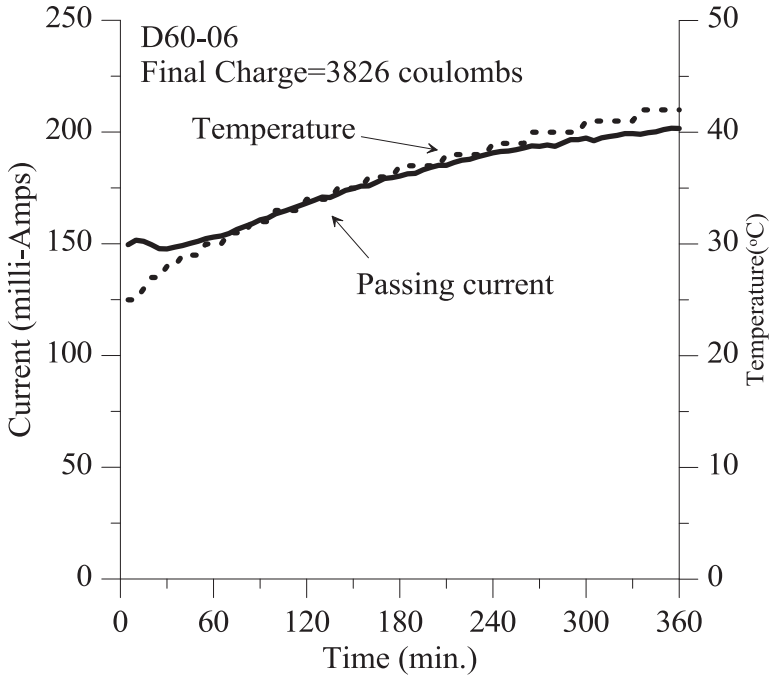

(b) D60-06

Figure 3.55: Passing current/temperature vs. time for samples D60-05/06

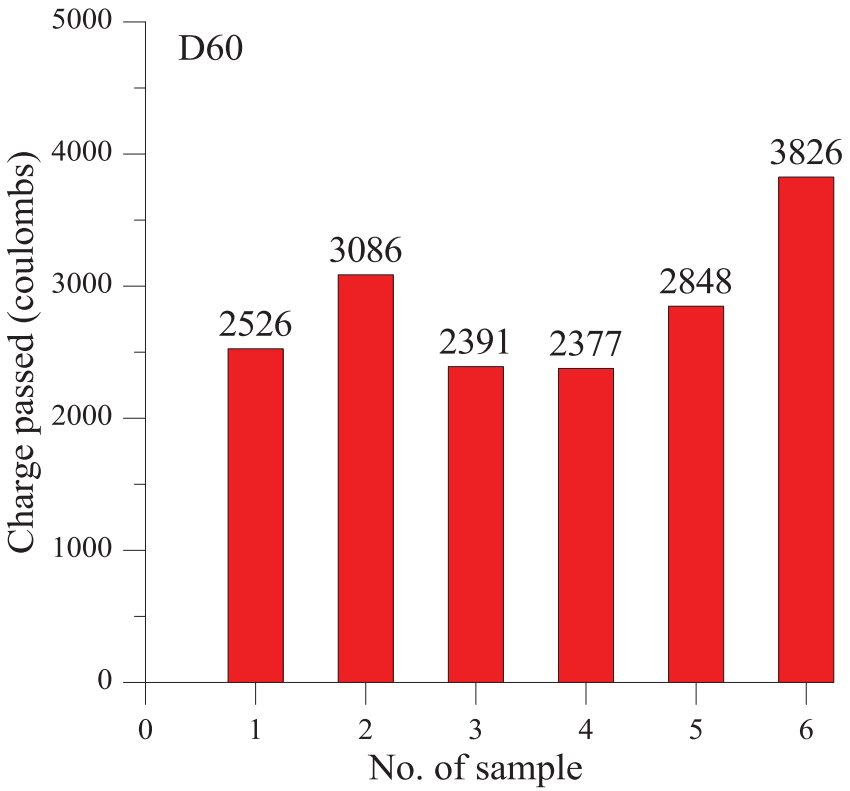

Figure 3.56: Charge passed through samples D60

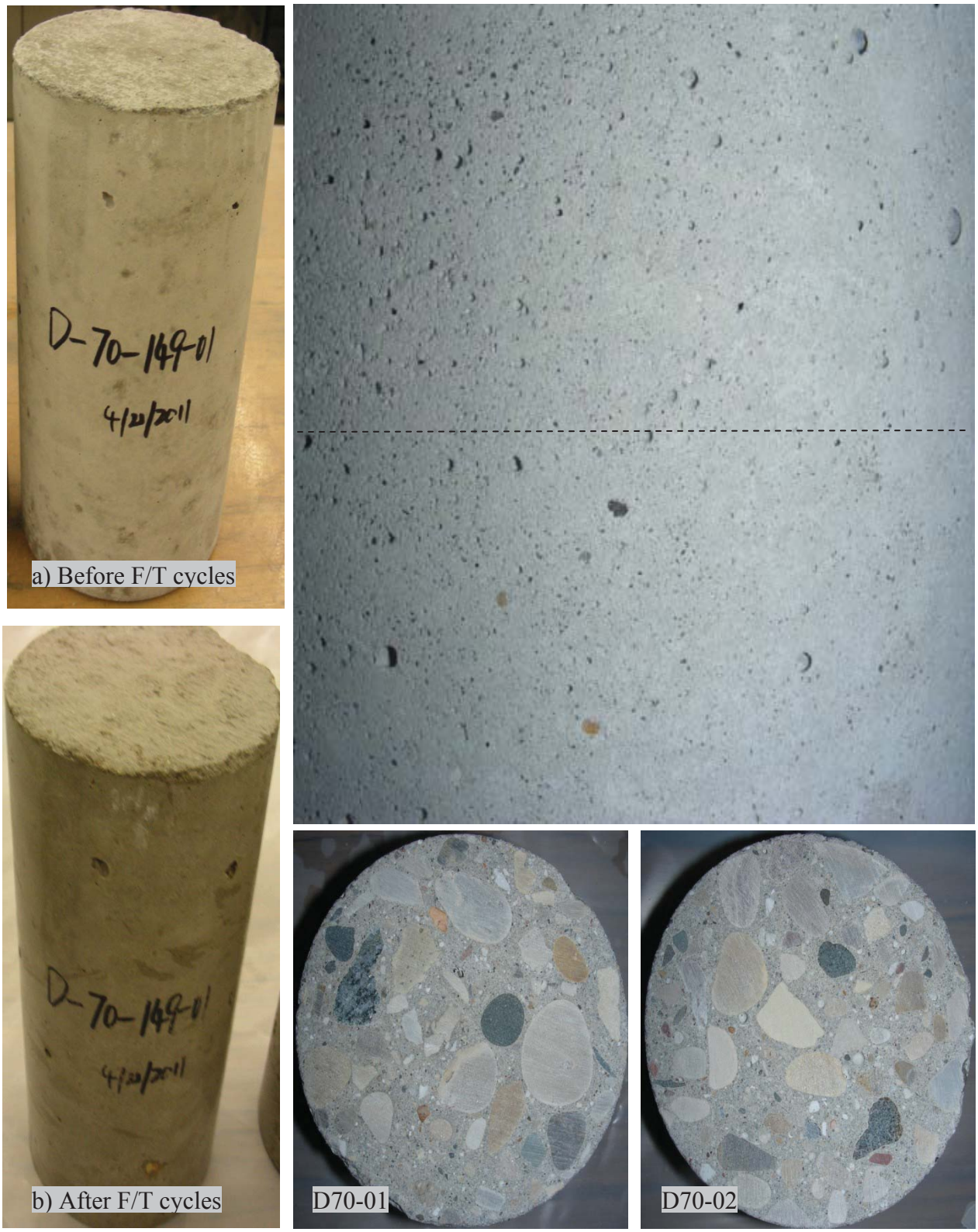

Figure 3.57: Surface conditions of samples D70-01/02

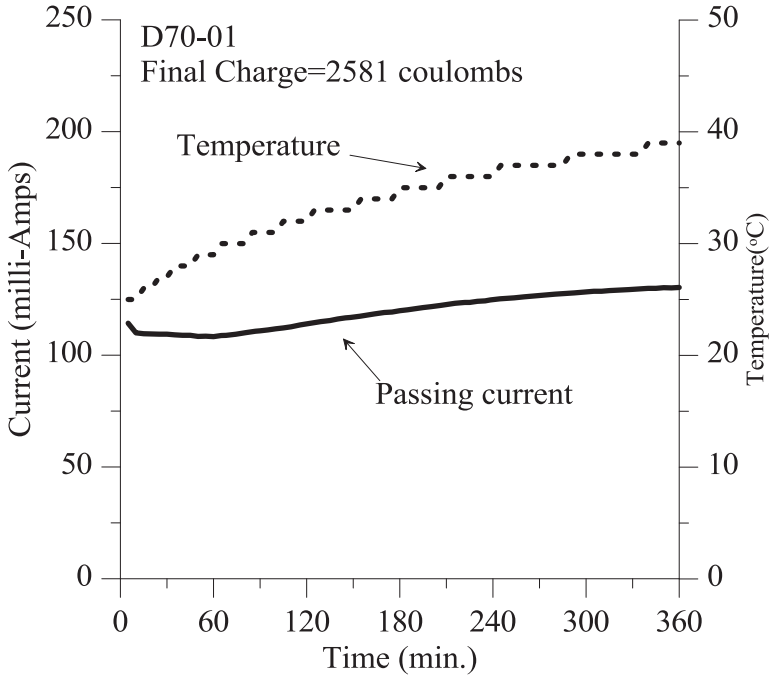

(a)D70-01

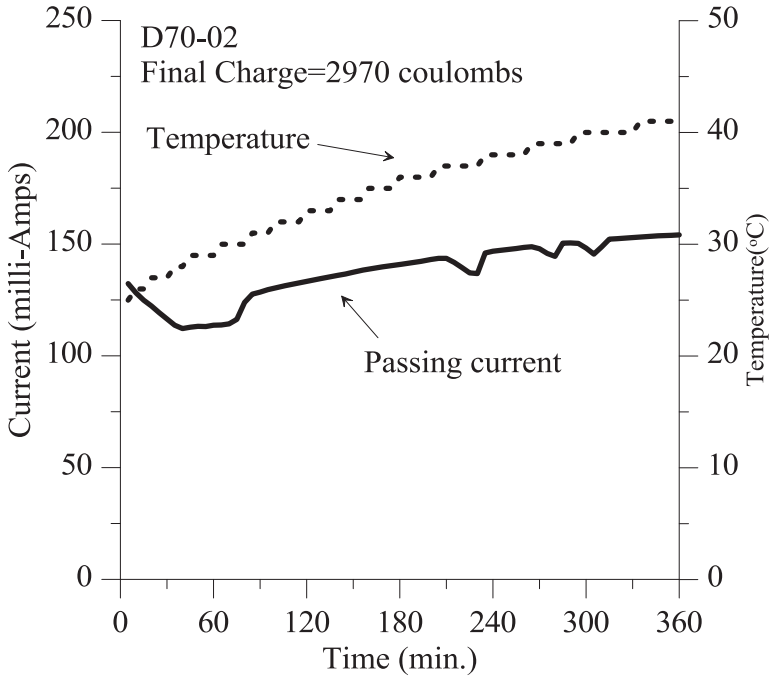

(b) D70-02

Figure 3.58: Passing current/temperature vs. time for samples D70-01/02

Figure 3.59: Surface conditions of samples D70-03/04

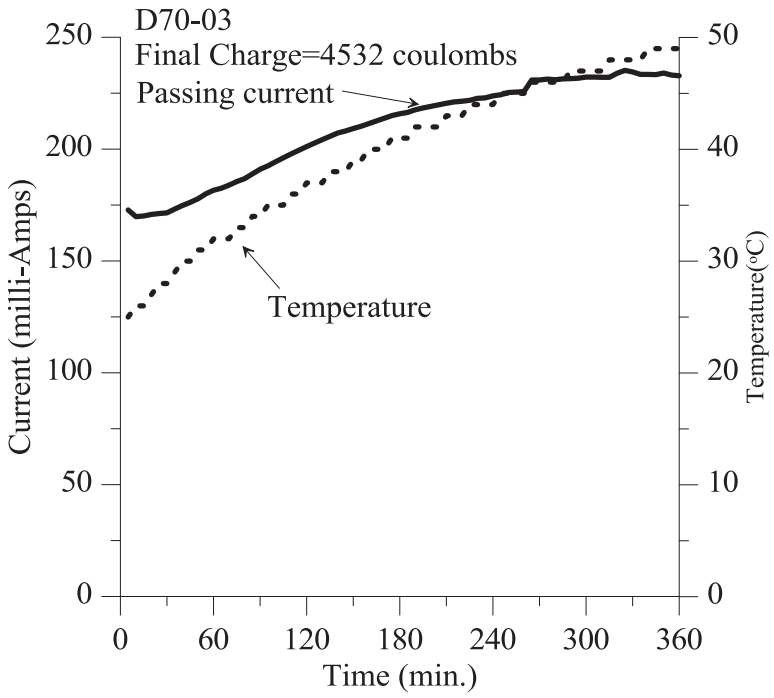

(a)D70-03

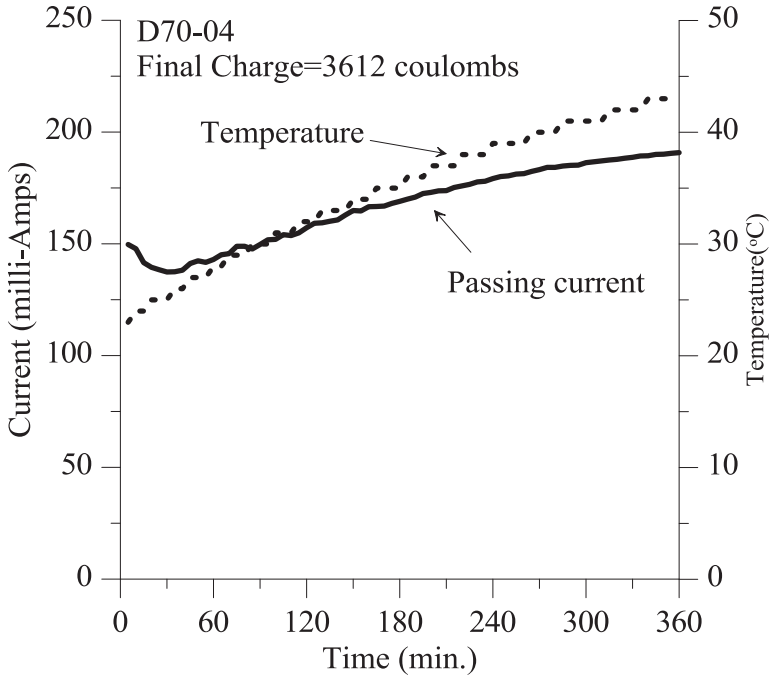

(b) D70-04

Figure 3.60: Passing current/temperature vs. time for samples D70-03/04

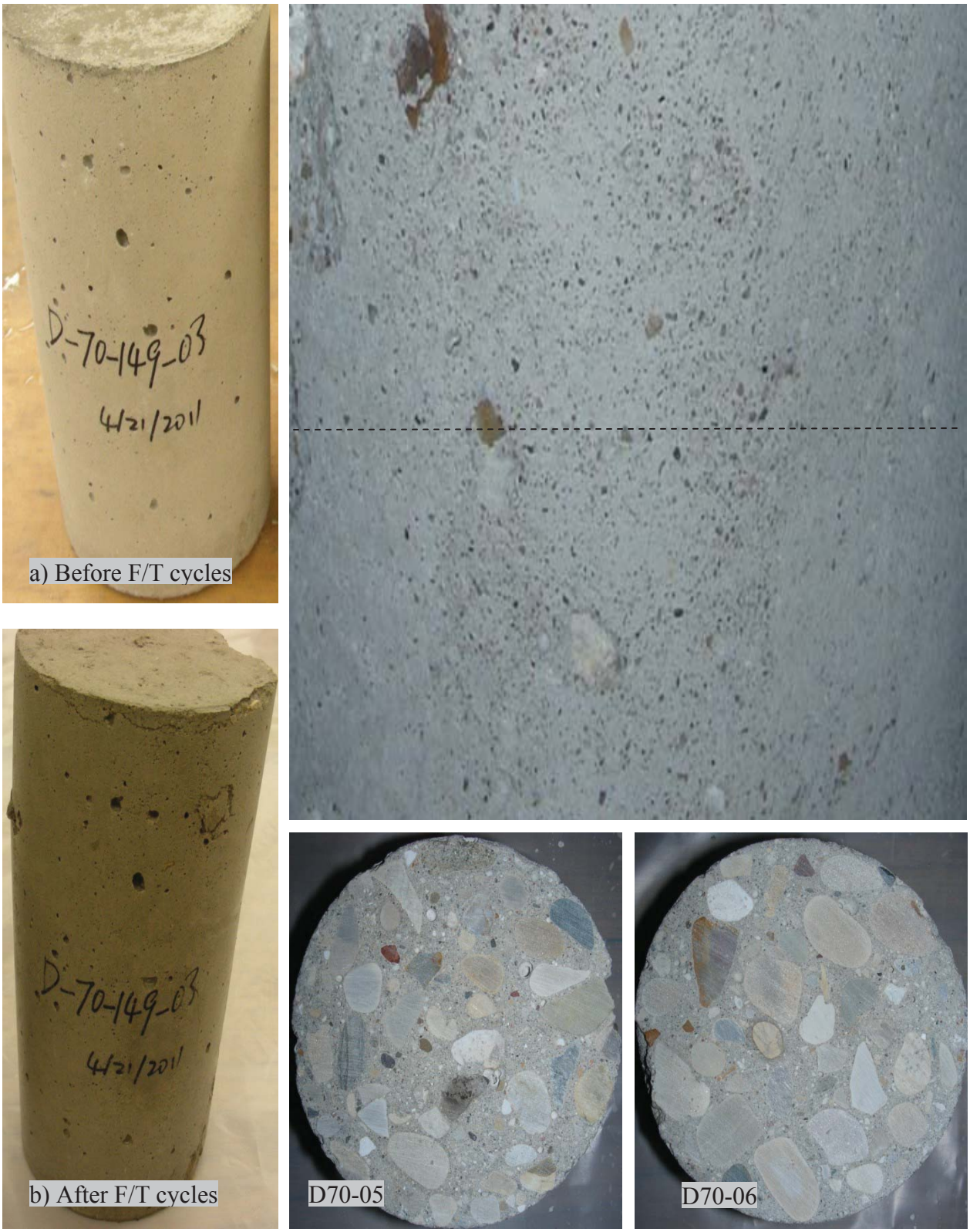

Figure 3.61: Surface conditions of samples D70-05/06

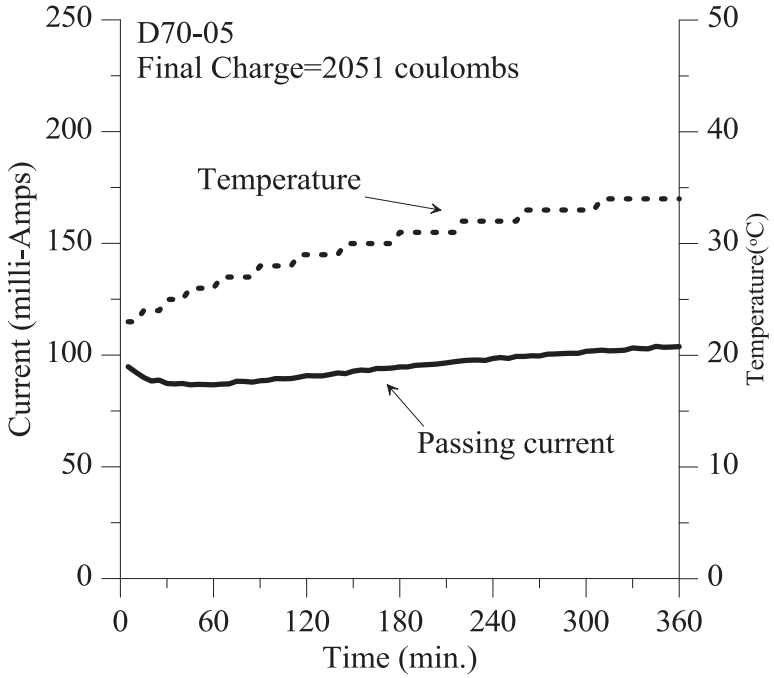

(a)D70-05

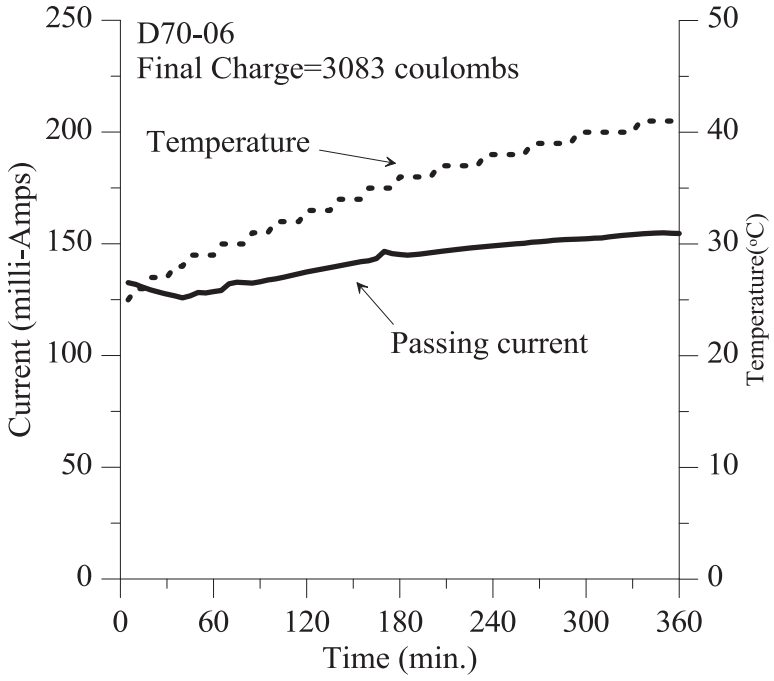

(b) D70-06

Figure 3.62: Passing current/temperature vs. time for samples D70-05/06

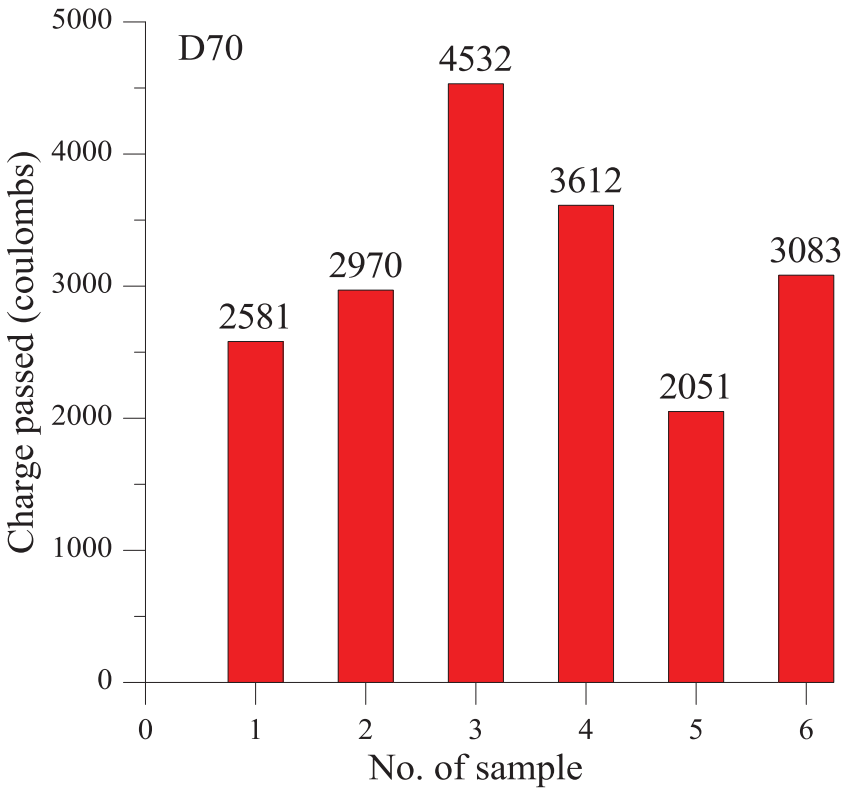

Figure 3.63: Charge passed through samples D70

Figure 3.64: Surface conditions of samples D80-01/02

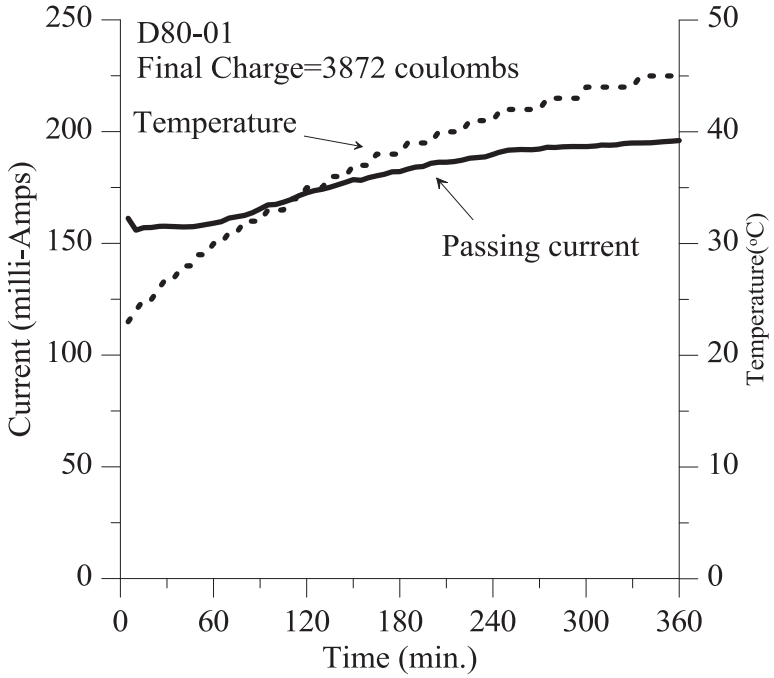

(a)D80-01

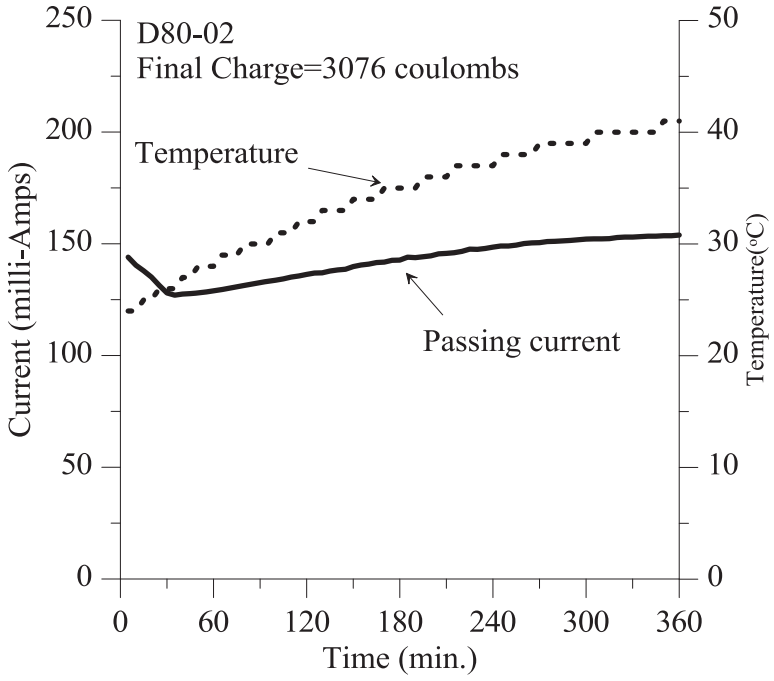

(b) D80-02

Figure 3.65: Passing current/temperature vs. time for samples D80-01/02

Figure 3.66: Surface conditions of samples D80-03/04

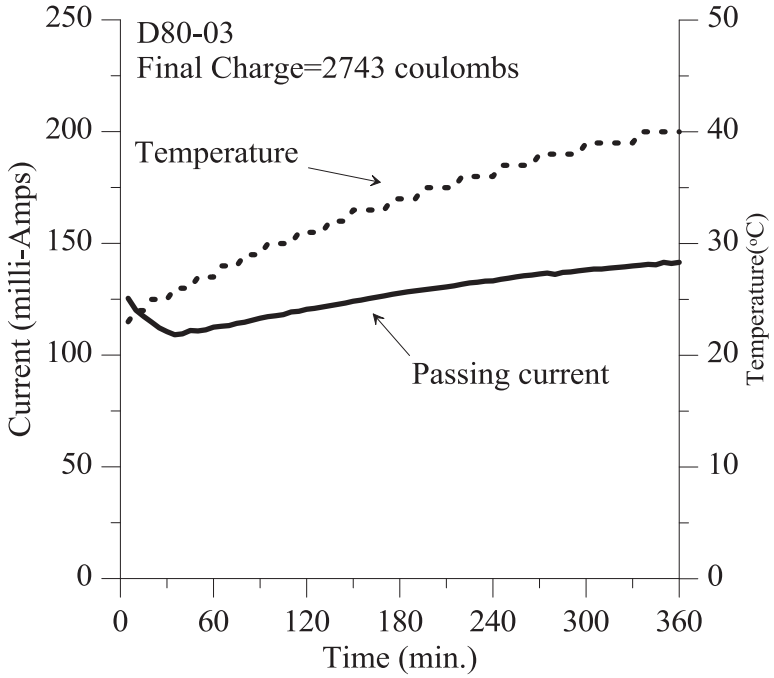

(a)D80-03

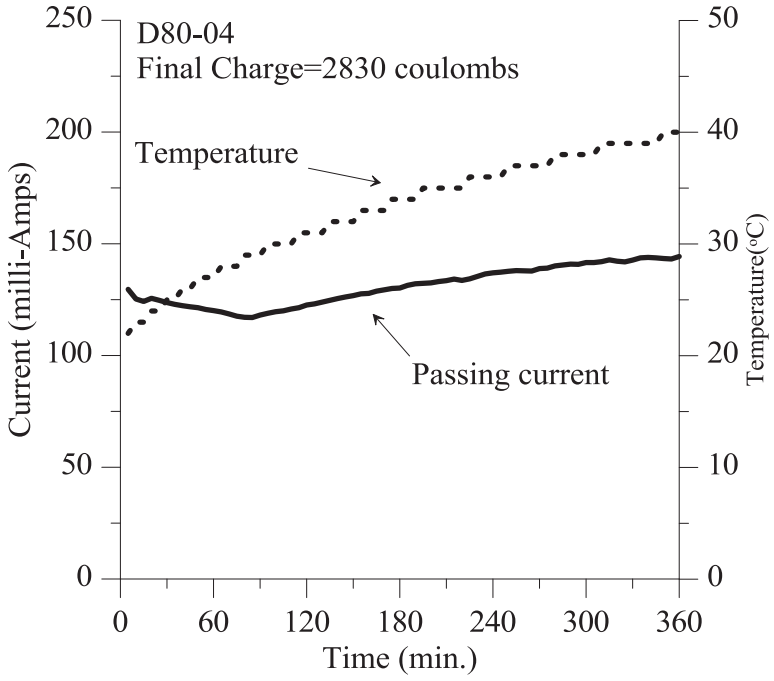

(b) D80-04

Figure 3.67: Passing current/temperature vs. time for samples D80-03/04

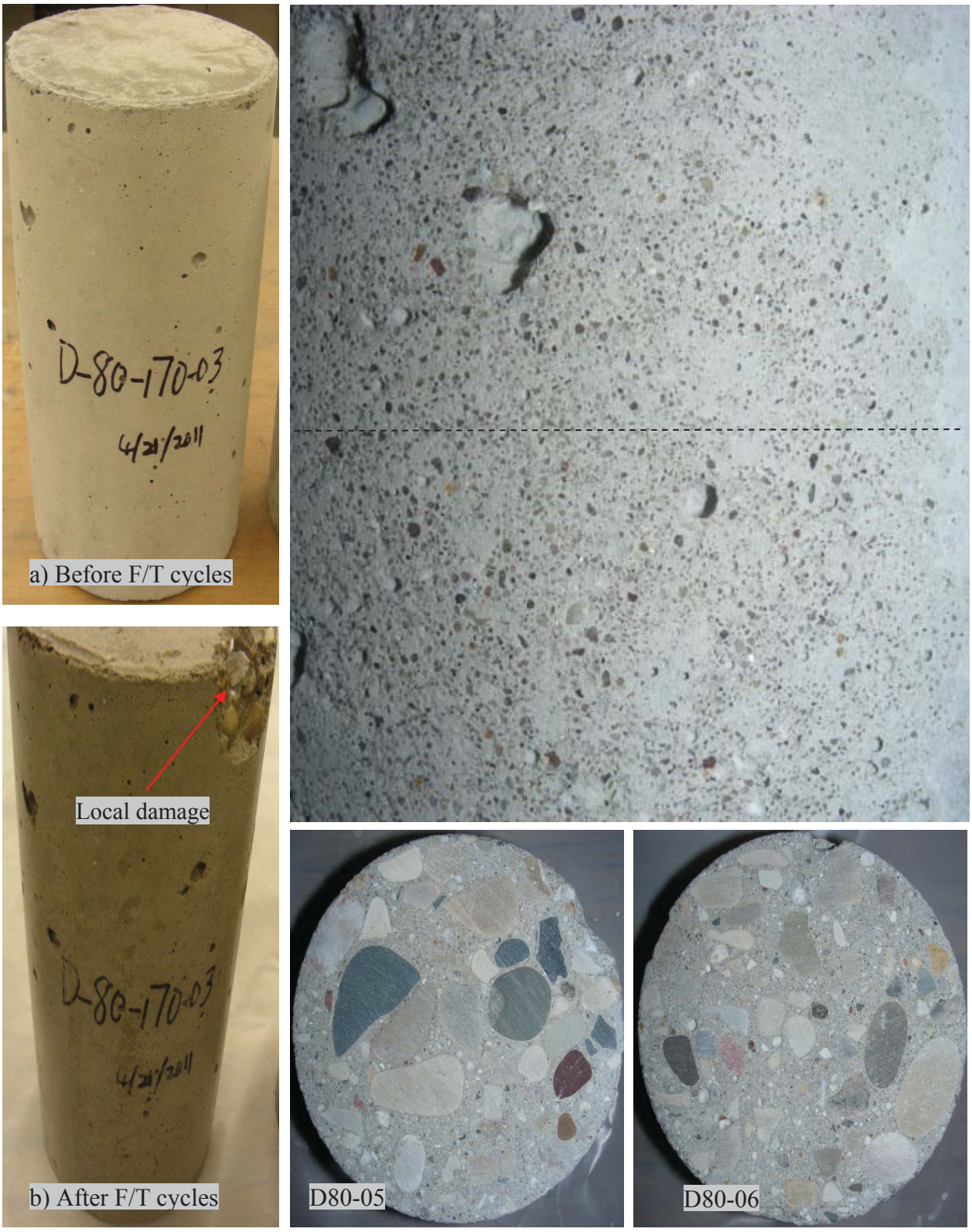

Figure 3.68: Surface conditions of samples D80-05/06

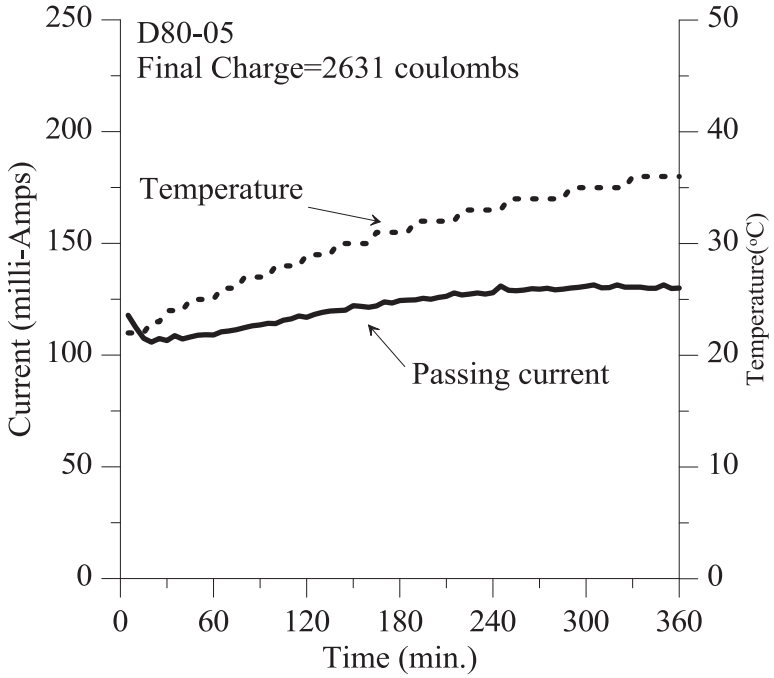

(a)D80-05

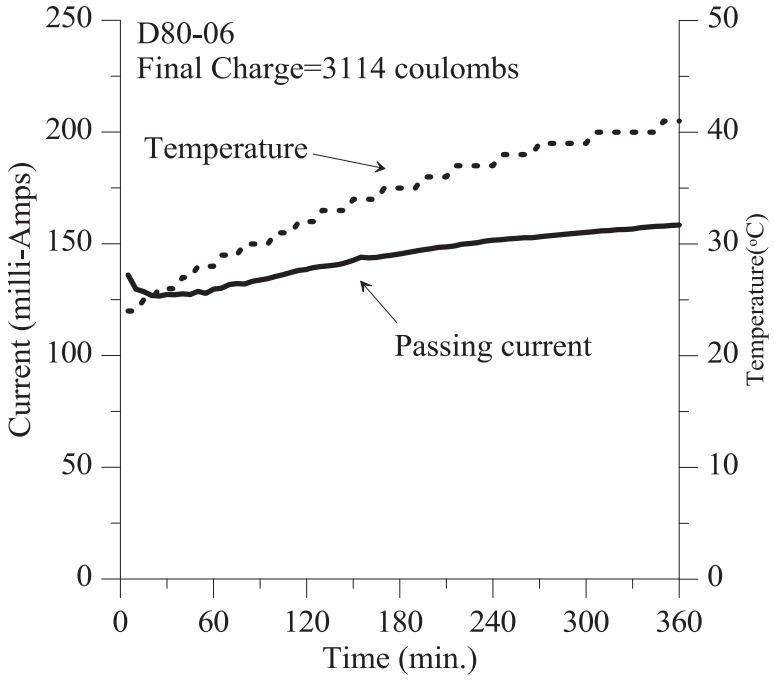

(b) D80-06

Figure 3.69: Passing current/temperature vs. time for samples D80-05/06

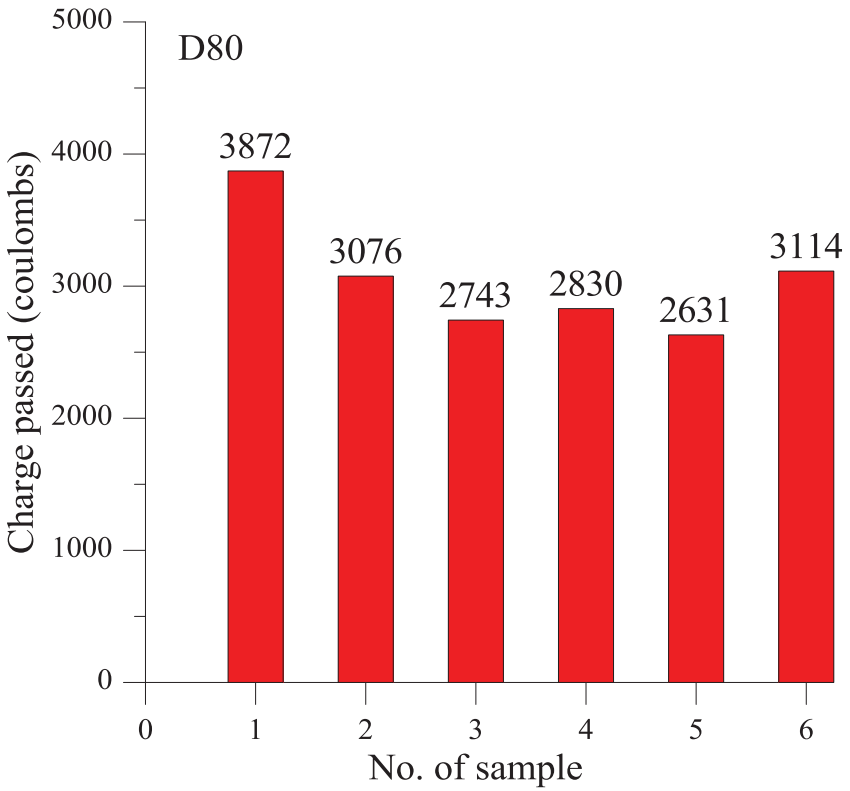

Figure 3.70: Charge passed through samples D80

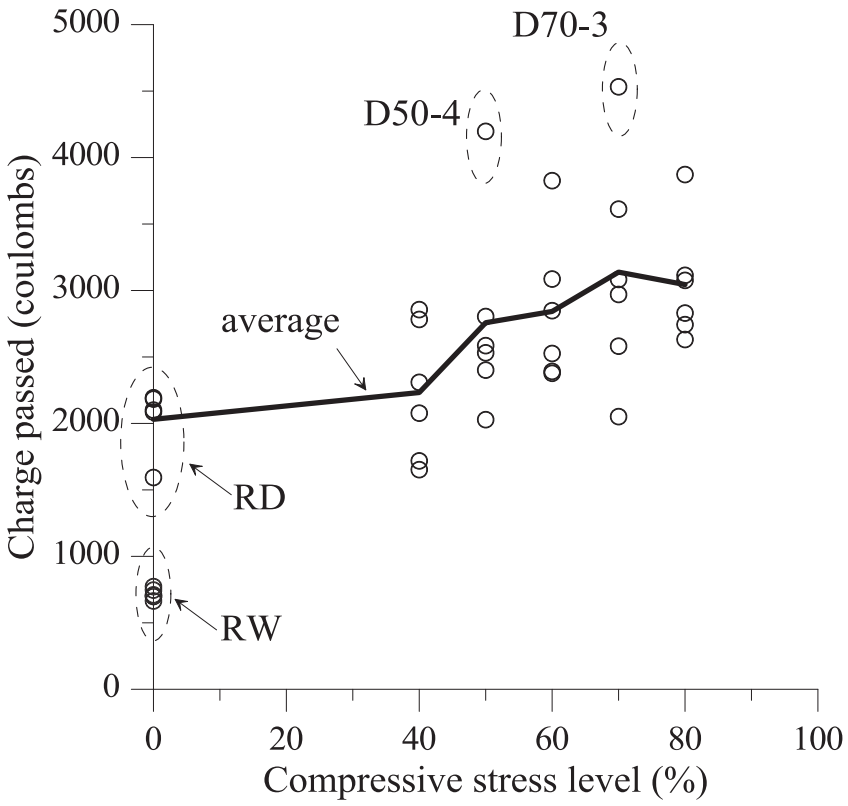

Figure 3.71:

Figure 3.72: Charge passed through samples subjected to various levels of loads

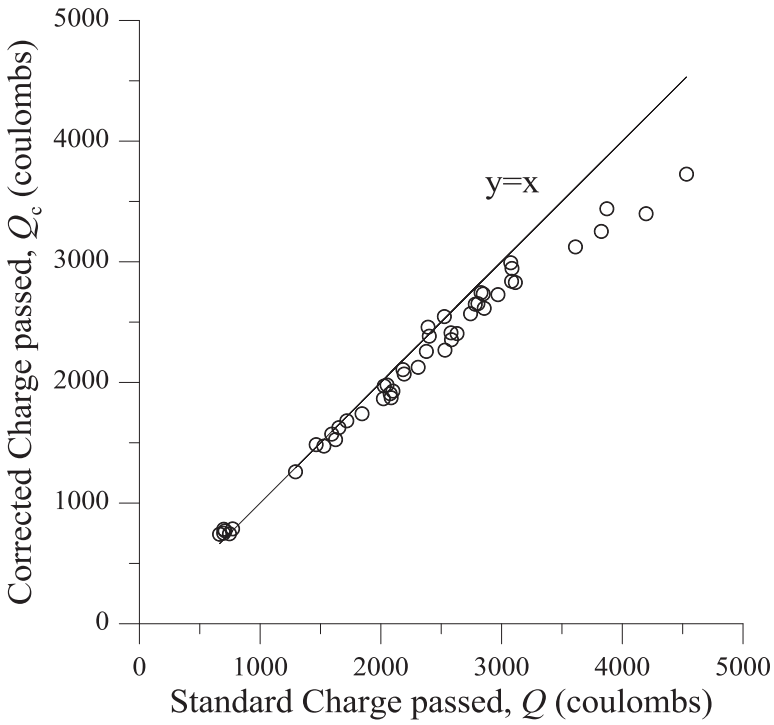

Figure 3.73: Charge passed over 6 hours vs. corrected charge pass

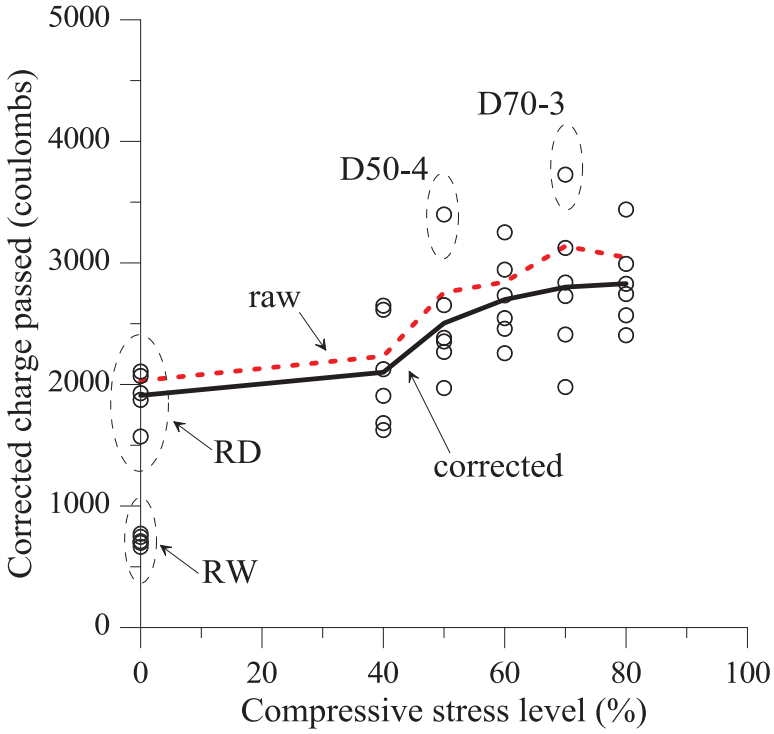

Figure 3.74: Corrected charge passed through samples

This page has been intentionally left blank.

Chapter 4. Microstructures and Microcrack Analysis

4.1 Introduction

Microcracks caused by compressive loading and freeze-thaw cycles are the key to understanding the permeability of concrete shown in Chapter 3. Modern complex digital imaging techniques, such as optical microscope and scanning electron microscope, allow the examination of microcracks. The observed images under meso- or micro-scopic scale help explain the permeability test results. In addition, a short-term sorptivity test was used to quantify the microcracks in each sample.

The features of the concrete under meso- or micro-scopic scale were observed using a Zeiss Stemi 2000-C optical microscope with a digital camera (Figure 4.1) and a Topcon SM300 SEM in conjunction with an image analyzer (Figure 4.6). Samples for the optical microscope were 10-mm (0.39-in.) thick samples sliced from the cylinders along the transverse direction, perpendicular to the compressive direction while the samples for SEM were 20x20x10 mm (0.79x0.79x0.39 in.) blocks cut from the center of the cylinders along longitudinal direction, parallel to the compressive direction.

4.2 Optical Microscopic Imaging

The specimens extracted from the concrete cylinders were 101.6 mm (4 in.) diameter Sample with an approximate thickness of 10 mm (0.39 in.). One face of each sample was ground and polished with 120, 220, and 600 grit fixed-SiC sandpapers by applying hand pressure on a rotating grinder (Figure 4.2), respectively.

Figure 4.3 showed typical photographs of samples RW and RNW using the optical microscope. Micrographs of smooth interfacial transition zones were illustrated in samples RW and RNW at the 6.25x resolution. No major cracks were found in these samples. Images of samples RD and D40 are shown in Figure 4.4. Specifically, similar observation in samples D40 in Figure 4.4b indicates that no major cracks exist in the samples, even though the average value of charge passed through D40 samples had an increase of 50 percent compared with RW samples.

The microscopic images did not reveal observable cracks in most specimens except that several samples from the cylinders that showed exceptionally high passing charges in Figure 3.71. Specifically, Specimens D50-4 and D70-3 allowed about 4500 coulombs of total charge passed. The spikes caused two peaks in the average curve in Figure 3.71. The microscopic image of Sample D50-4, shown in Figure 4.5a, indicates that the compressive load caused localized damage to a relatively weak coarse aggregate. Similarly, Sample D70-3 also had a major localized crack as shown in Figure 4.5b. Such localized large cracks may have been resulted from uncertainties in the concrete material and in the process of load application. These cracks, different from the more uniformly distributed microcracks, were responsible for the large total charge passed shown in Figure 3.71.

These results indicated that smaller-size cracks (i.e., microcracks) may be responsible for the increased total charges passed shown in Table 3.5 for samples subjected to higher loads. Note that such macrocracks have been the subject of previous study (Wang et al., 1997), Microcracks

caused by combine mechanical compressive stresses and F/T cycles were examined using a scanning electron microscope (SEM) in this study.

4.3 Scanning Electron Microscopic Imaging

The scanning electron microscope (SEM) is an effective instrument for the image analysis of the microstructure of concretes (Diamond and Mindess, 1980; Nemati, 1997; Ramachandran and Beaudoin, 2001). Diamond and Mindess (1980) originally implemented the SEM technology to capture images from surface cracks of the concrete specimens subjected to loading. The microcracks of samples were observed in this study using a Topcon SM300 SEM, as shown in Figure 4.6 through Figure 4.8.

The procedure for imaging analyses using SEM is schematically shown in Figure 4.9. Blocks (20 x 20 x 10 mm) were cut from the middle of selected samples and the observed surfaces were parallel to the applied compressive loads to reveal the through-sample microcracks in the samples. Unlike previous studies (Nemati, 1997; Ramachandran and Beaudoin, 2001), no additional surface polish was applied in order to preserve the air void structures and the distribution of microcracks. The blocks were subjected to a heat treatment under 40 ºC for 24 hours before being coated in Denton Desk II Sputter Coater (Figure 4.8). The coated blocks were observed using a scanning electron microscope (Figure 4.6 and Figure 4.7).

The backscattered electron image of a sample cut from a RW cylinder is shown in Figure 4.10a and 4.10b. Air voids that were measured with diameters of about 30 μm-340 μm within the typical entrained air bubbles were consistently distributed in the cement matrix and the matrix seemed free of microcracks, which correlated with the observed small charges passed in the RCIP test in Table 3.5.

Corresponding to higher charges passed in the RCIP test of RD samples, the SEM image of RD samples shown in Figure 4.11a indicated that microcracks formed around a relatively large void (with a diameter of about 495 μm) and in the interfacial transition zones. This correlates with the observed F/T damages in the literature. For example, similar cracking images have been obtained by Yang et al. (2005) in a study of the internal damage caused by freeze-thaw cycles. The microcracks, as that shown in Figure 4.11a, were deemed to be responsible for the observed increase in chloride permeability by a 25 percent increase compared to RNW samples and a 184 percent increase compared to RW samples.

The effect of dry shrinkage on microcrack development was deemed negligible because the concrete samples were not restrained from deformation. Therefore, microcracks were also caused by mechanical loading as shown by Figure 4.11b. In addition to the microcracks near a large void (with a diameter of about 552 μm), concrete in a D40 sample also developed cracks near smaller voids and in the cement matrix. A closer look at the D40 sample shown in Figure 4.12 indicates that some cracks had connected into a passageway for chloride ions. As a result, the average value of charge passed allowed by D40 samples had an increase of 10 percent compared with RD samples. This observed increase in the chloride permeability of concrete subjected to a relatively low compressive stress level is different from other observations in the literature that the chloride permeability of concrete using the same standardized RCIP test is not affected by compressive stresses below 70 percent of the ultimate strength (Samaha and Hover, 1992; Saito and Ishimori, 1995).

It was expected that concrete develops more interconnected microcracks when subjected to higher compressive loading, as pointed out by Hsu et al. (1963) and Nemati et al. (1998). This trend was observed as shown in Figure 4.13, For example, at a stress level of 0.7fc', wider microcracks (about 4 μm) at an interfacial transition zone connected with a microcrack in the cement matrix, forming a more direct passageway for chloride ions. Similar interconnected microcracks were observed in specimens subjected to 0.8fc' as shown in Figure 4.14 for sample D80-1. It is envisioned that the density of such microcracks caused by both mechanical loading and F/T cycles can be critical for the permeability of concrete. However, quantifying the number and the dimensions of such microcracks was difficult with a scanning electronic microscope because the images do not provide a 3D configuration of the microcracks. Instead the water absorption capacities were measured for the samples before the rapid chloride permeability tests to reflect the amount of microcracks in concrete.

4.4 Short-Term Sorptivity Tests

As mentioned earlier in section 2.2.4 for water absorption in Chapter 2, in a standard water absorption test, a specimen is placed into a triaxial cell and vacuum saturated (CRD-C 163-92, 1992). A pressure gradient is developed and recorded through two ends of the specimen using a high hydraulic pressure when a radial pressure remains around it. The water volume flow rate is measured to obtain permeability of the specimen using Darcy's law (Cemica, 1995).

In addition to the standard water absorption test, various methods have been proposed, as summarized by Hoseini et al. (2009), such as low-pressure permeability tests (Yang et al., 2005; Wang et al., 1997; Hearn, 1999) and high-pressure test (Kermani, 1991). Water absorption at the first several hours, defined as the short-term sorptivity, reflects a measure of water filling up those relatively large pores and cracks (Yang et al., 2005; Marchand et al., 1997; Martys and Ferraris, 1997). During this short-term period, the presence of more microcracks/cracks in concretes may have higher short-term sorptivity values. Rather than low-pressure water permeability test, a relatively high-pressure test may reduce test time while short-term water absorption allows the determination of the effects of microcracks on permeability of concrete. Standard RCIP Test preconditioning procedures (ASTM C1202-10, 2010) meet these requirements and were then implemented to determine water absorption of concrete in this study.

The water absorption test in this study was different from the standard test. The samples sliced from the cylinders were washed and dried in laboratory room condition for one week. Although such dried samples still contain moistures, it was believed that the drying process removed the moisture from the accessible microcracks and voids, which are critical to the chloride permeability. Standard RCIP Test preconditioning procedures were followed to saturate the samples: The dried specimens were placed in a vacuum desiccator, and vacuum was applied for three hours maintaining an inside pressure of 6.7 KPa (1.0 psi). The vacuumed specimens built a negative pressure inside the accessible microcracks and air voids when the de-aerated water was added to the vacuum desiccators. The specimens were kept in the vacuum desiccators for 18 hours such that most accessible microcracks and air voids were filled with water. The specimens were then dried to a saturated surface-dry condition. The weight difference of the samples at the room dried condition and the saturated surface-dry condition provided the amount of water ingress into concrete and reflected the volume of accessible microcracks and air voids.

The measured water absorption of the samples is plotted in Figure 4.15 against the applied compressive loads. In general the water absorption, which indicates the amount of accessible microcracks and air voids, increased with an increase in the applied load. The RW specimens, cured in water, had the least water absorption, which corresponds to their low charge passed in RCPT observed in Figure 3.71. The RNW specimens were cured in air such that a dense microstructure similar to that of RW specimens as shown in Figure 4.10 was not developed. The water absorption of RNW specimens was high, corresponding to increased charge passed as shown in Table 3.5 compared with RW specimens**.**

The measured water absorption had variations similar to that of measured passing charges shown in Figure 4.15. Therefore, the water absorption of a concrete sample was plotted against the passing charges as shown in Figure 4.16. The measured passing charges strongly correlated with the measured water absorption as shown by a linear trend line in Figure 4.16. Although drying the concrete samples in the laboratory room condition for one week was somewhat arbitrary, the measured water absorption reflected the accessible microcracks and air voids, which contributes to the chloride permeability. On the other hand, the RNW specimens (dried in air at 120 days) were able to absorb relatively more water while they did not allow corresponding amount of charge passing the specimens. This may have been due to the fact that the microcracks in RNW specimens did not form passageways for water and chloride ions in these specimens.

The strong correlation between the measured water absorption and the chloride permeability in Figure 4.16 indicated that the microcracks and air voids in concrete that can be accessed by outside water and aggressive chemical are critical for the concrete durability. Such microcracks may originate from environmental attacks represented by freeze-thaw cycles and mechanical loading such as the truck loads on bridge decks. It is envisioned that other damage to concrete protective layers such as salt scaling and abrasion would increase the accessibility to the microcracks and air voids, thus increase the permeability of concrete. It can be suggested that new test methods are needed to evaluate the durability of concrete in the field.

4.5 Summary

This study presented a laboratory investigation of the permeability of air-entrained concrete after being subjected to mechanical compressive stresses and freeze-thaw cycles. Air-entrained concrete has shown great freeze-thaw resistance in laboratory tests per ASTM C 666. The impact of combined loading and freeze-thaw actions were evaluated using rapid chloride permeability tests.

The freeze-thaw resistance of air-entrained concrete was evaluated under an idealized-simulated field condition. Concrete in the field is subjected to mechanical loading as well as various environmental attacks; therefore concrete cylinders in the described laboratory tests were subjected to several levels of compressive loads, which caused microcracks inside concrete. The microcracks further developed and interconnected into passageways for water and chloride ions after the preloaded cylinders were subjected to 300 freeze-thaw cycles. The impact of combined actions was found negligible when the weight loss and surface spalling were evaluated according to the existing standards such as ASTM C666. However, the impact of combined actions on concrete permeability was significant as it was represented by the results of rapid chloride permeability tests.

The concrete samples were examined using an optical microscope and a scanning electronic microscope (SEM). The SEM images of concrete samples in the direction parallel to the applied compressive load revealed the through-thickness microcracks that were responsible for the observed increase in chloride permeability in loaded specimens. The amount of microcracks as well as air voids was indirectly measured using water absorption values. A strong relationship was identified between the chloride permeability and the water absorption, which outlined a new test method, which can be used to evaluate the durability of concrete in the field.

Figure 4.1: Optical microscope used to observe microcracks in samples

Figure 4.2: A semi-auto Grinder-Polisher used to polish samples

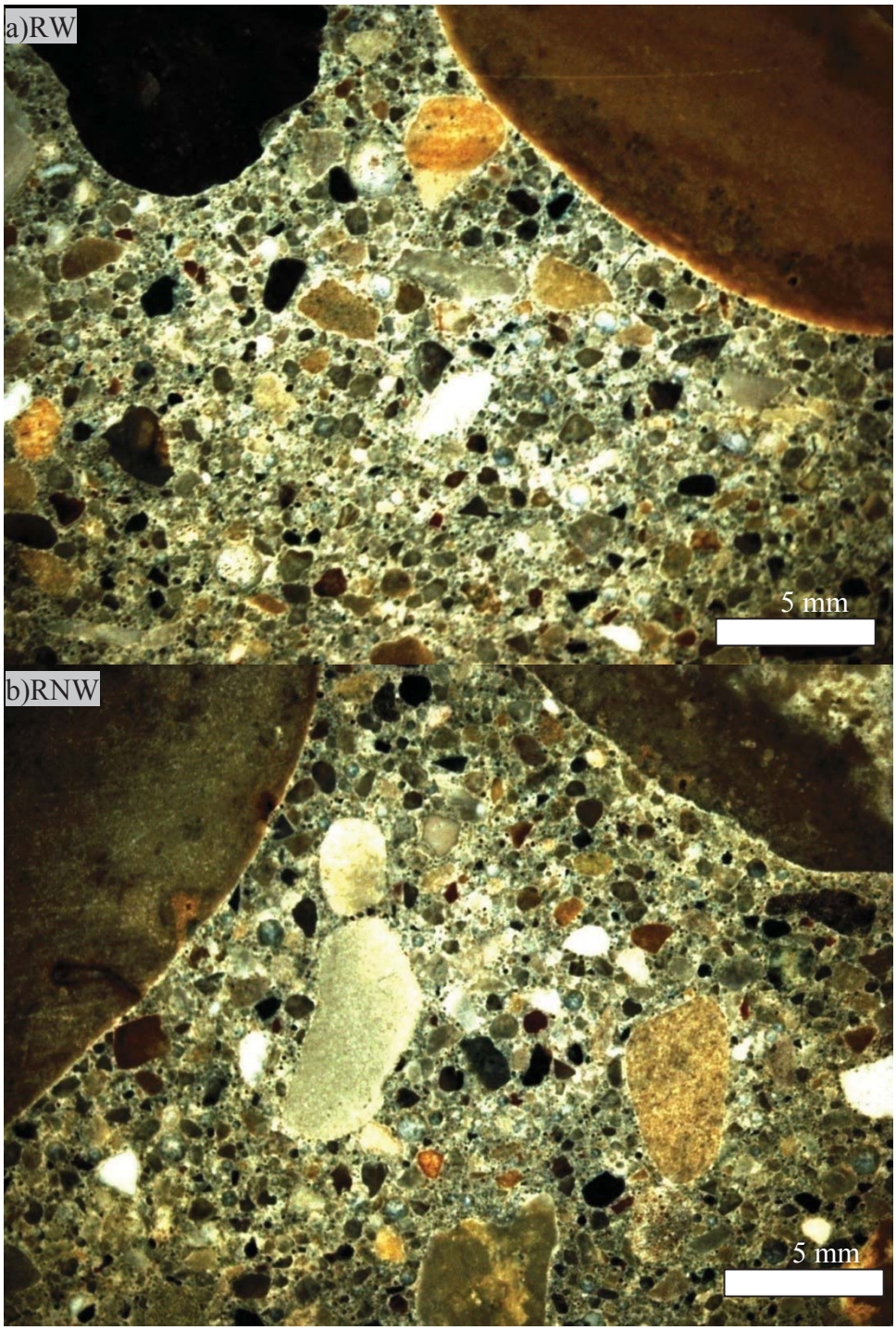

Figure 4.3: Sample RW and RNW using optical microscope (6.25X)

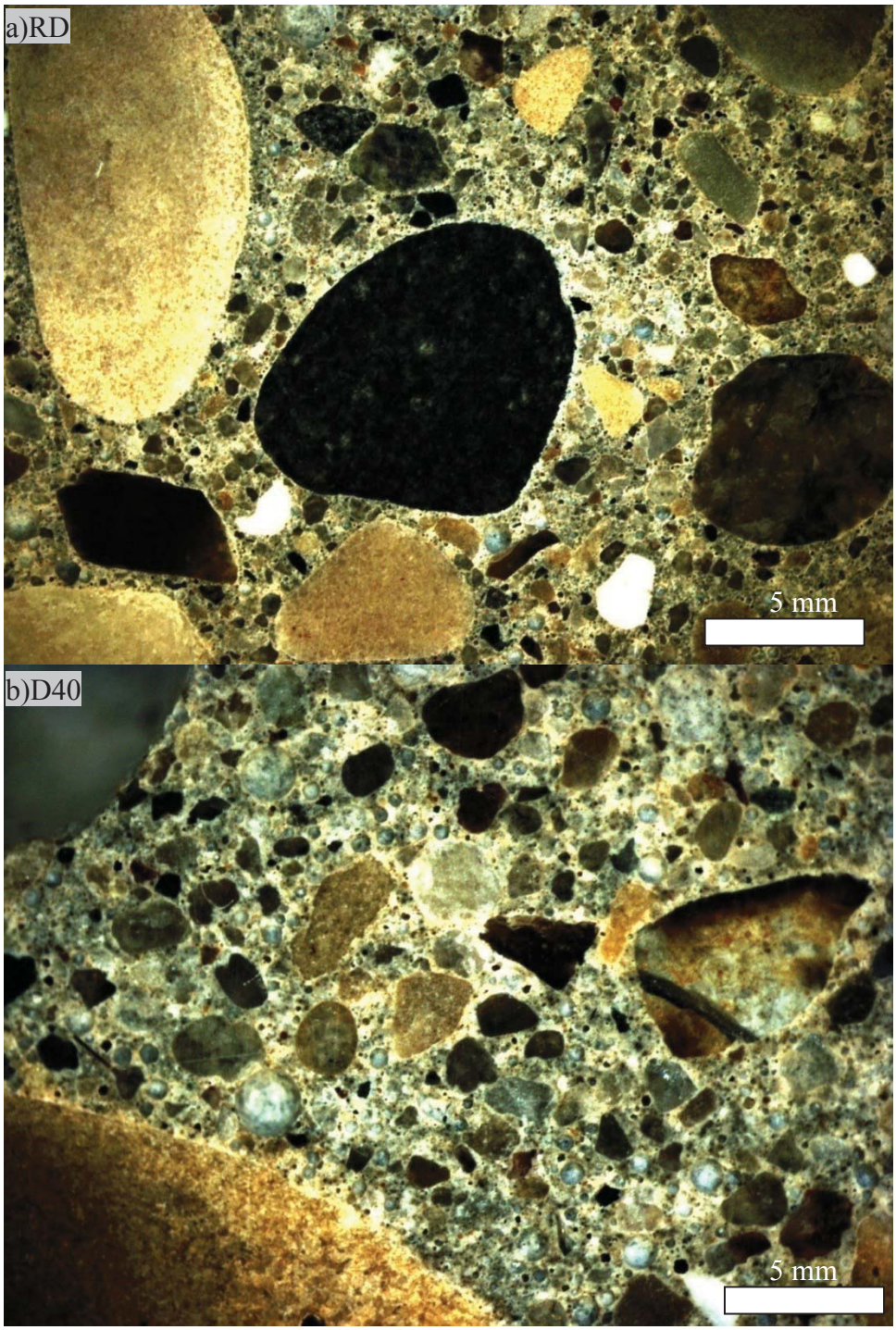

Figure 4.4: Sample RD and D40 using optical microscope (6.25X)

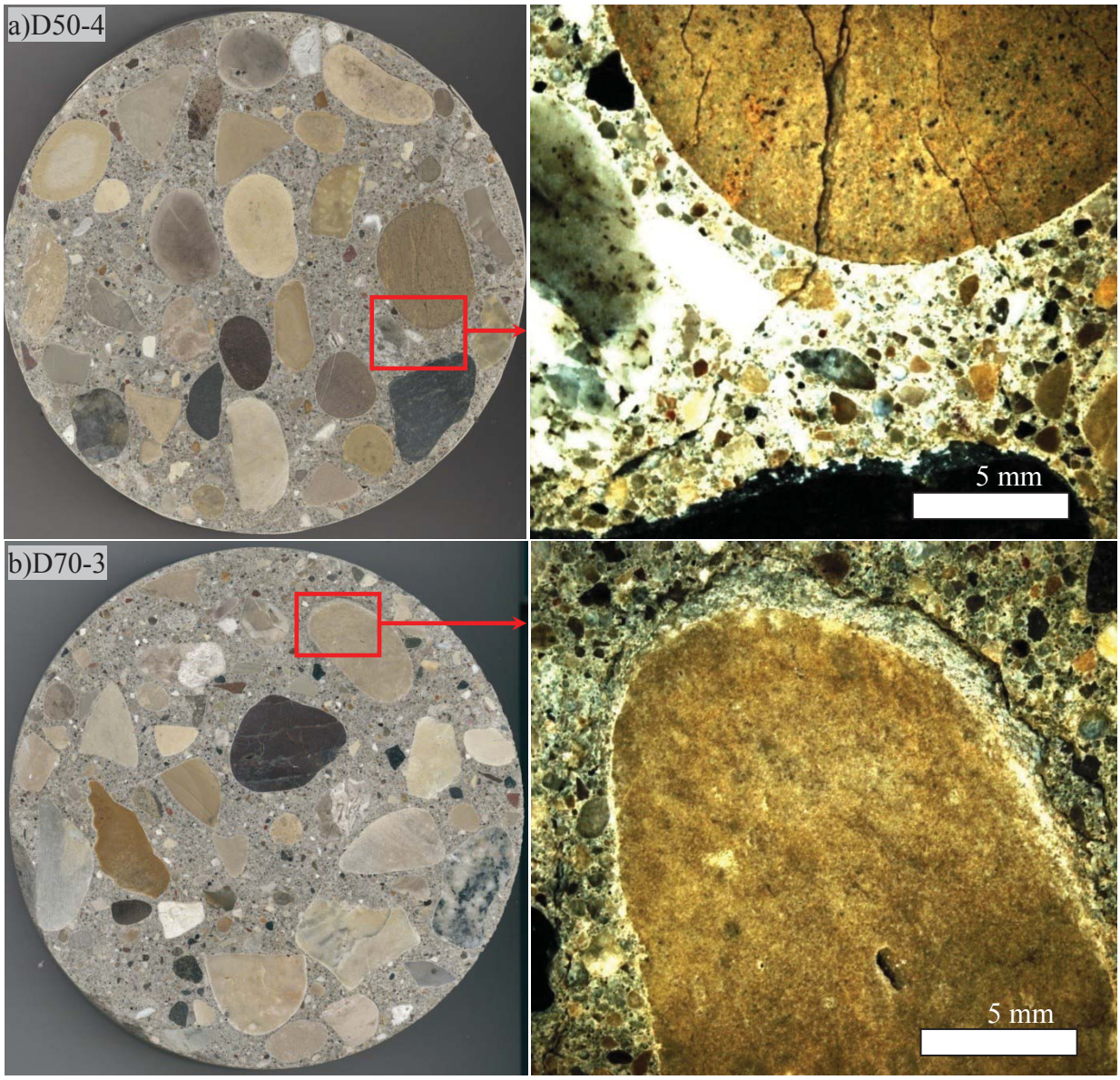

Figure 4.5: Cracks in concrete after F/T cycles using optical microscope (6.25X)

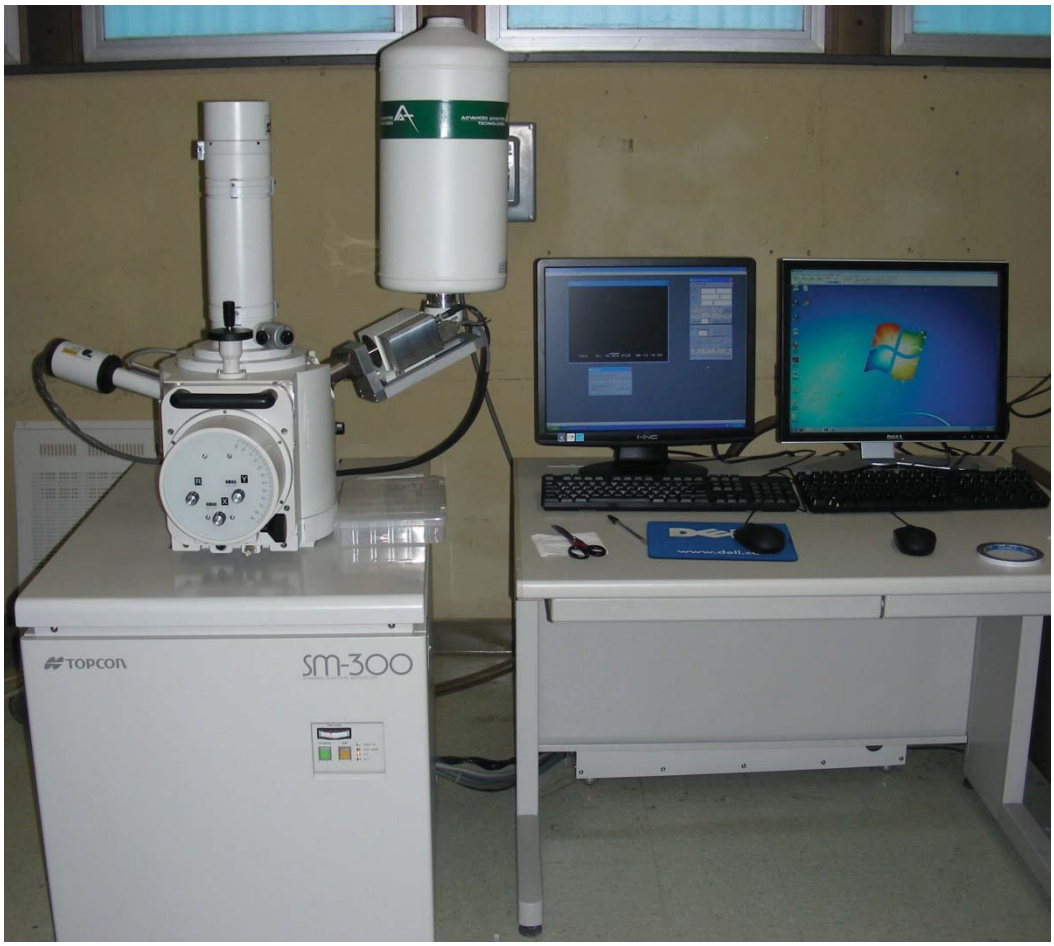

Figure 4.6: Using (Topcon SM300) SEM techniques to capture the microstructures of concrete

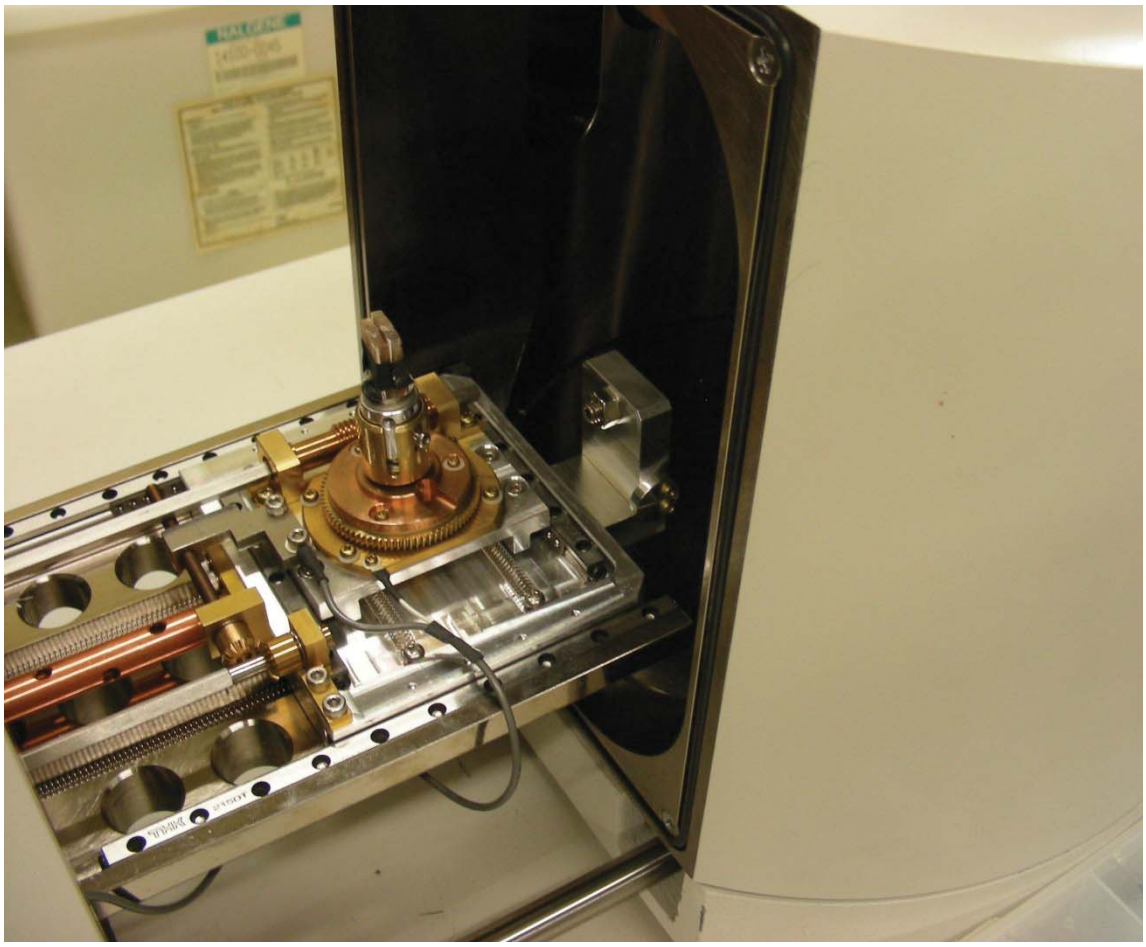

Figure 4.7: Loading a sample into the Topcon SM300 SEM core.

Figure 4.8: Denton Desk II Sputter Coater and coated samples

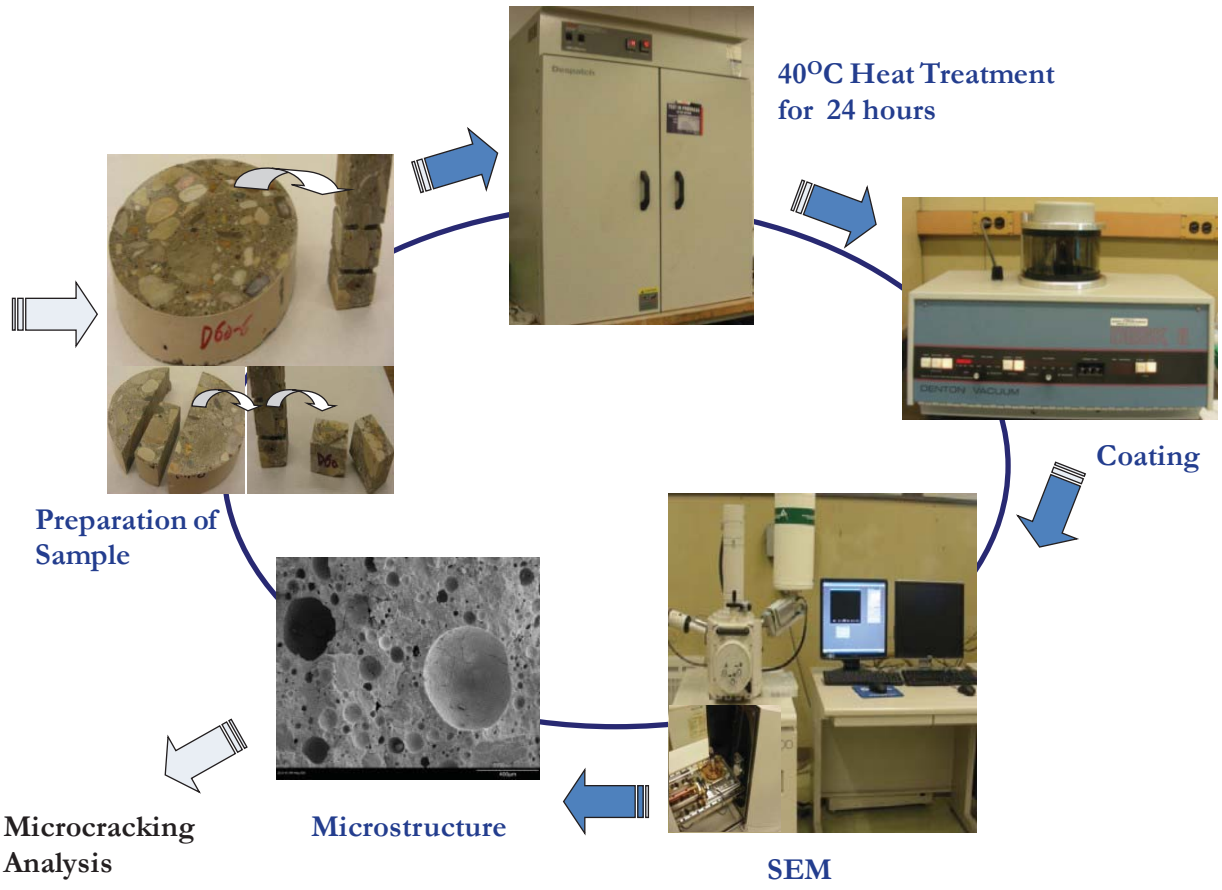

Figure 4.9: Experimental protocol of microcrack analysis

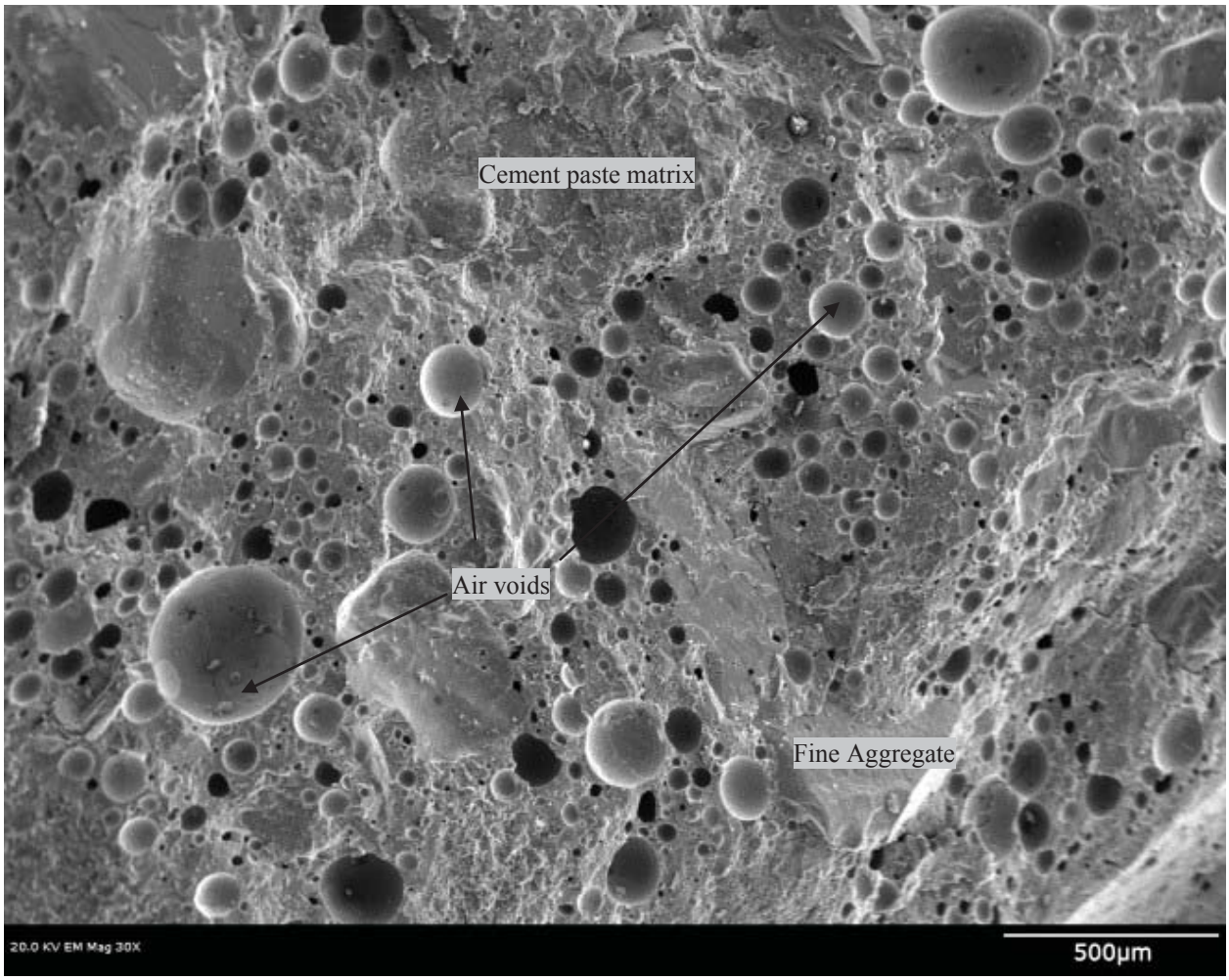
Cement paste matrix
Air voids
Fine Aggregate
20.0 KV EM Mag 30X
500µm

(a)

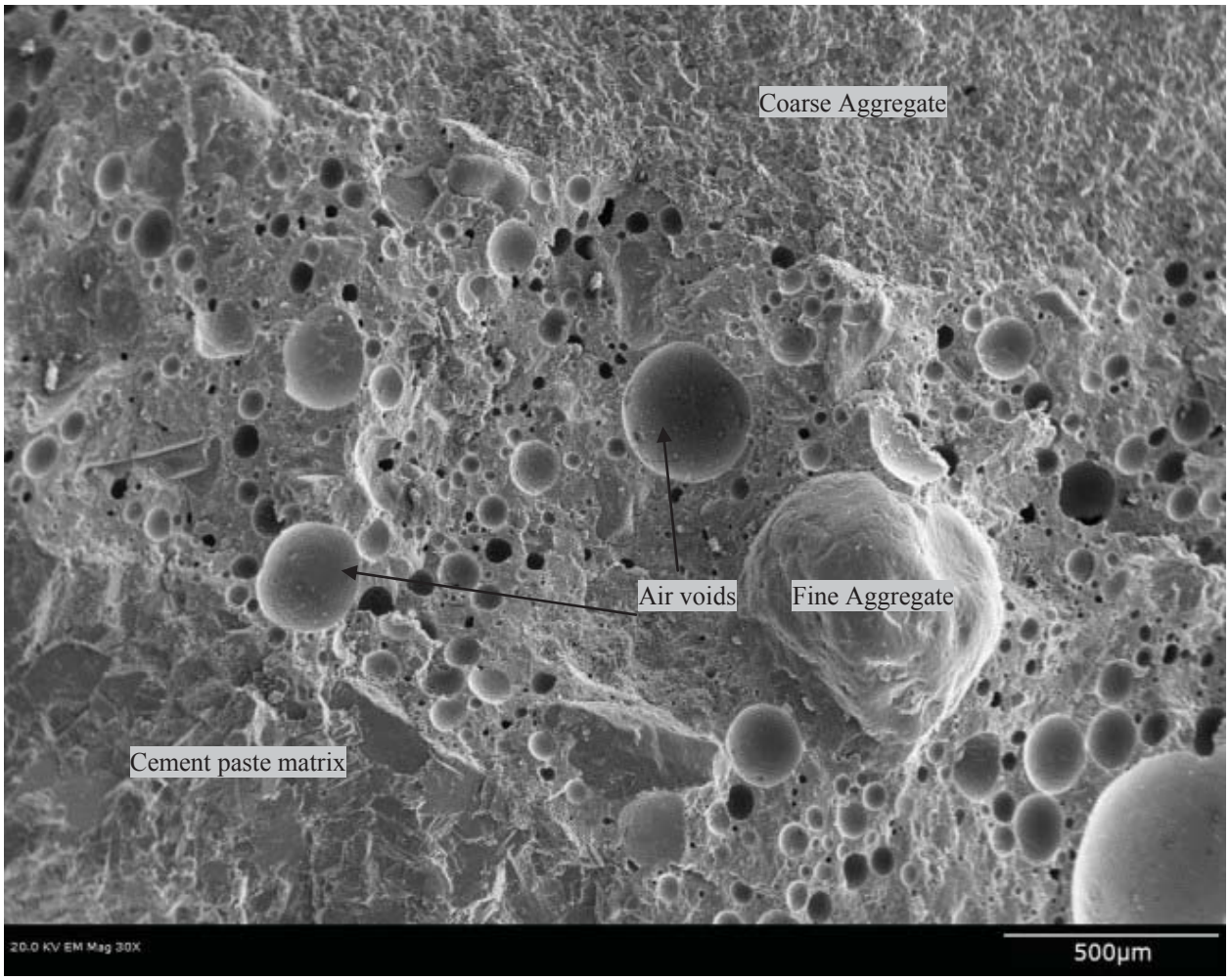

(b)

Figure 4.10: Typical gray level backscattered electron image for RW sample (air voids with diamters of about 30 µm-340 µm)

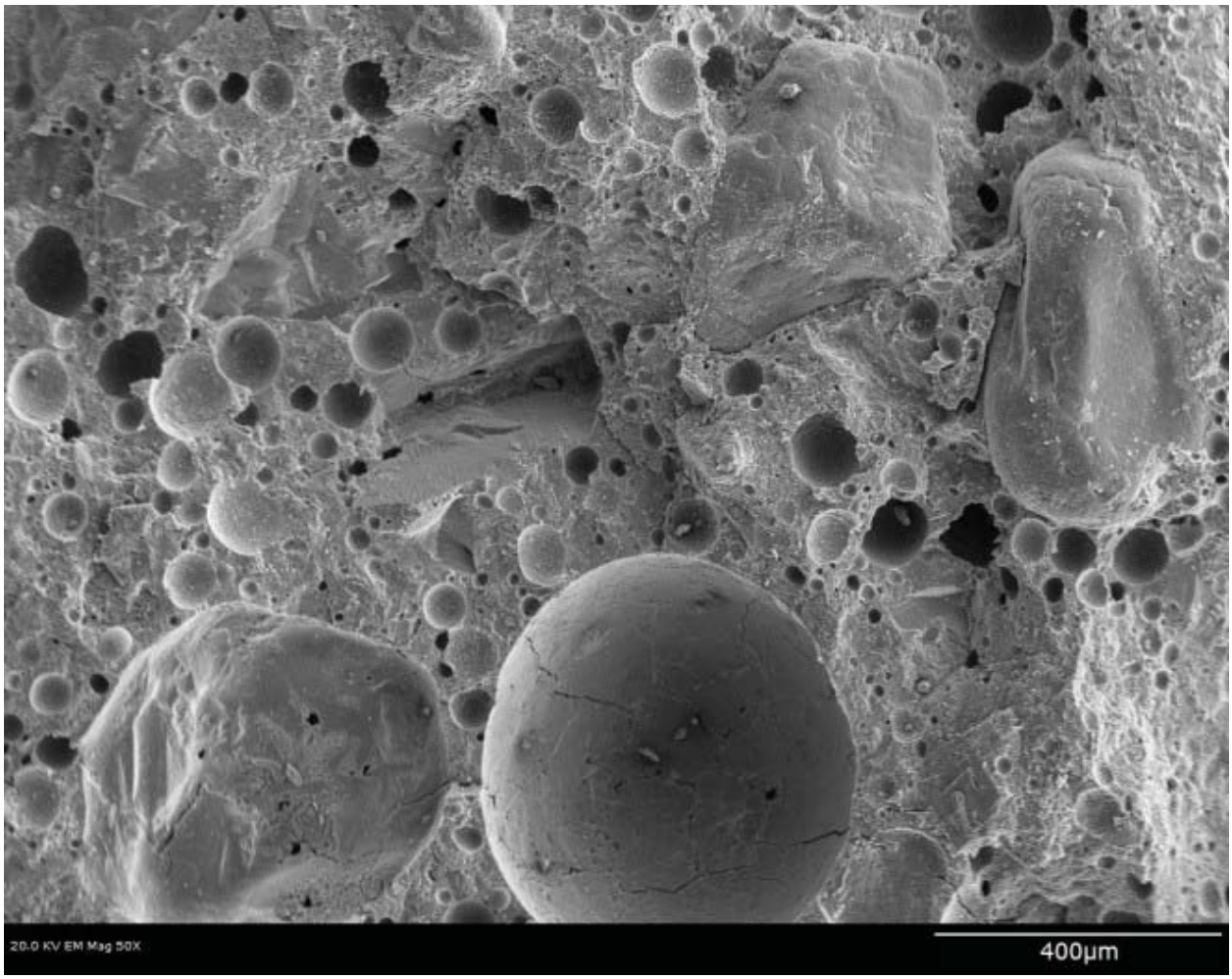

(a) RD-1

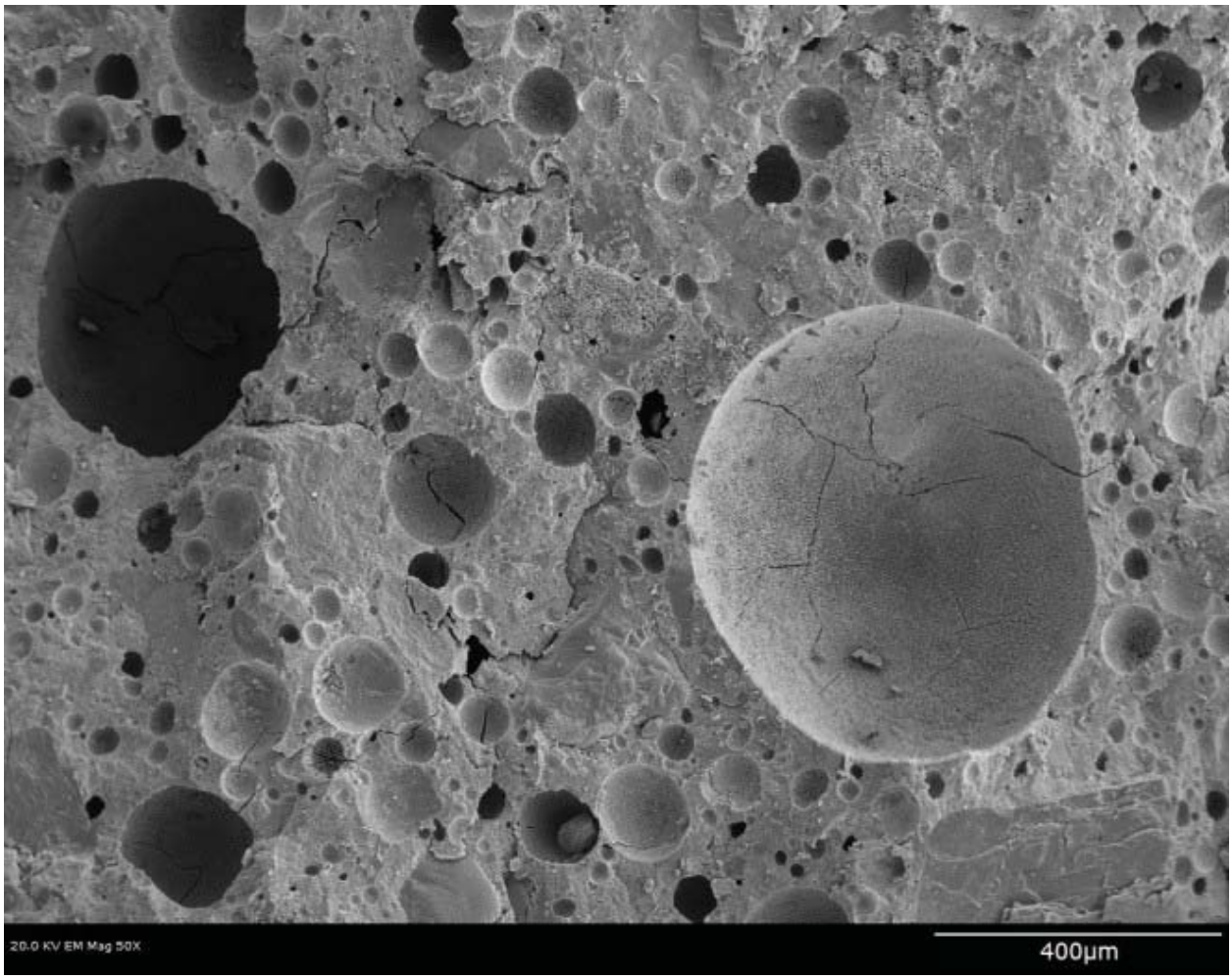

(b) D40-6

Figure 4.11: Comparison of micrographs for samples RD-1 and D40-6

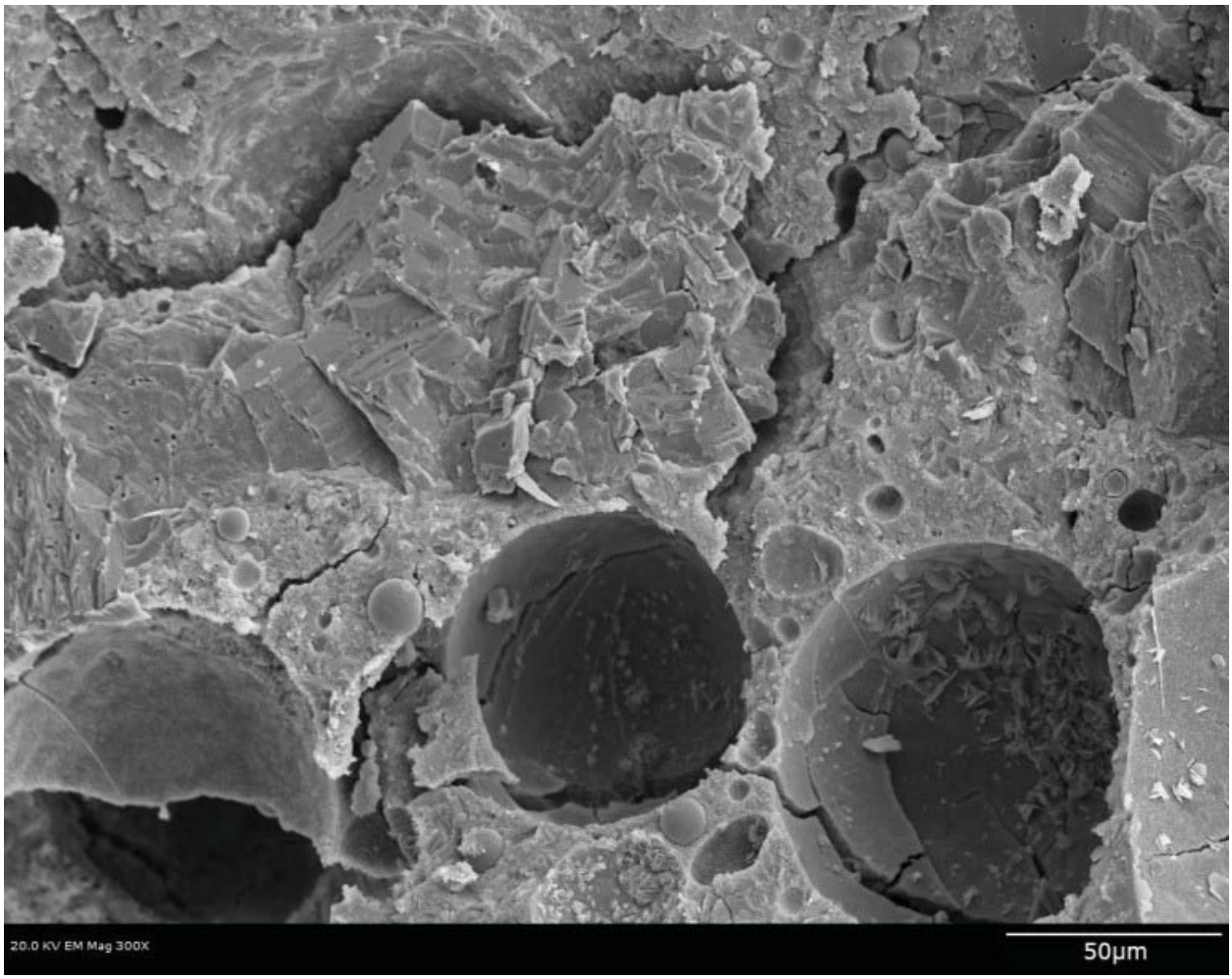

Figure 4.12: SEM micrograph of microcracks bridging pores in sample D40-6

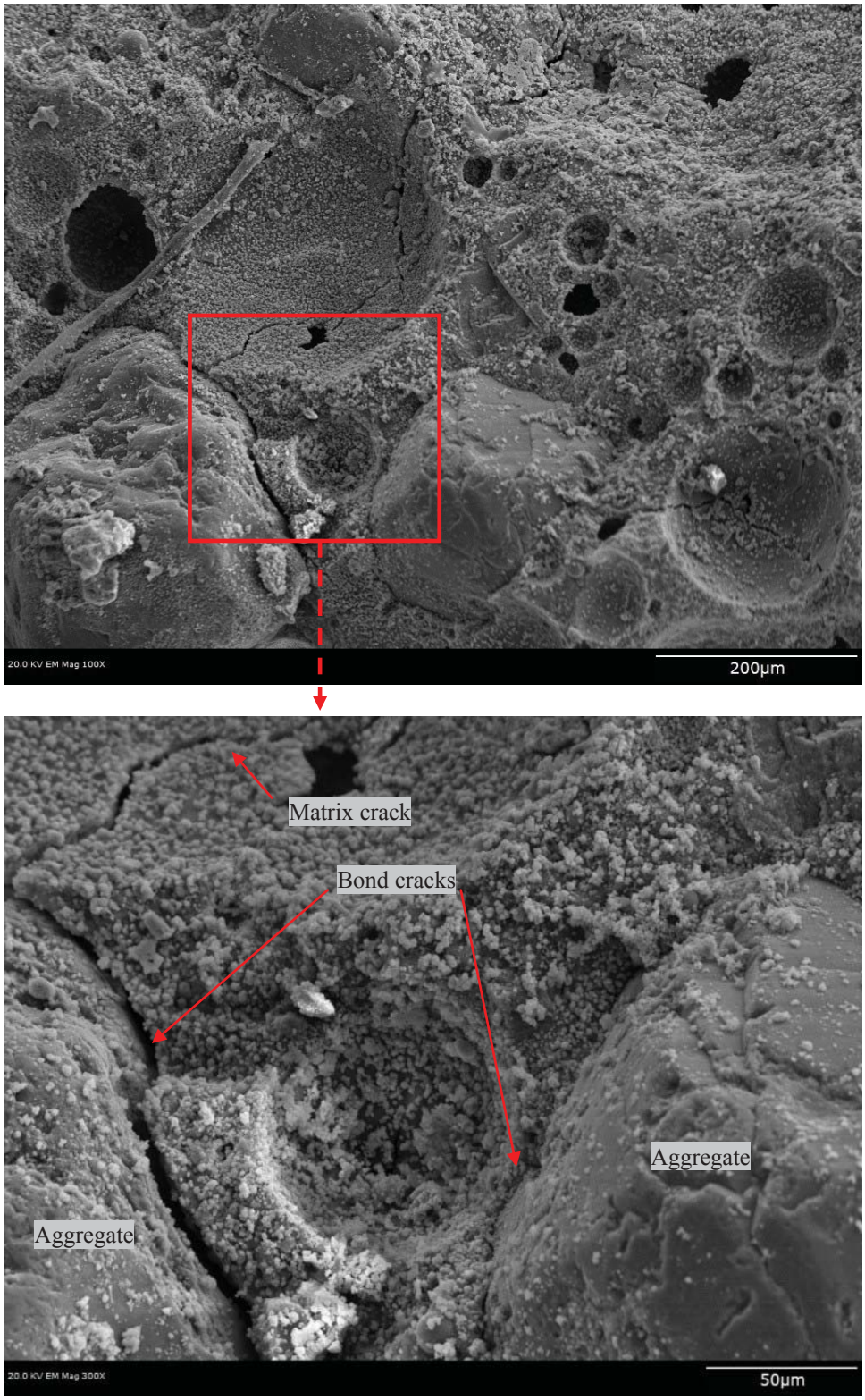

Figure 4.13: Microcracks at ITZ and matrix in D70-2 sample

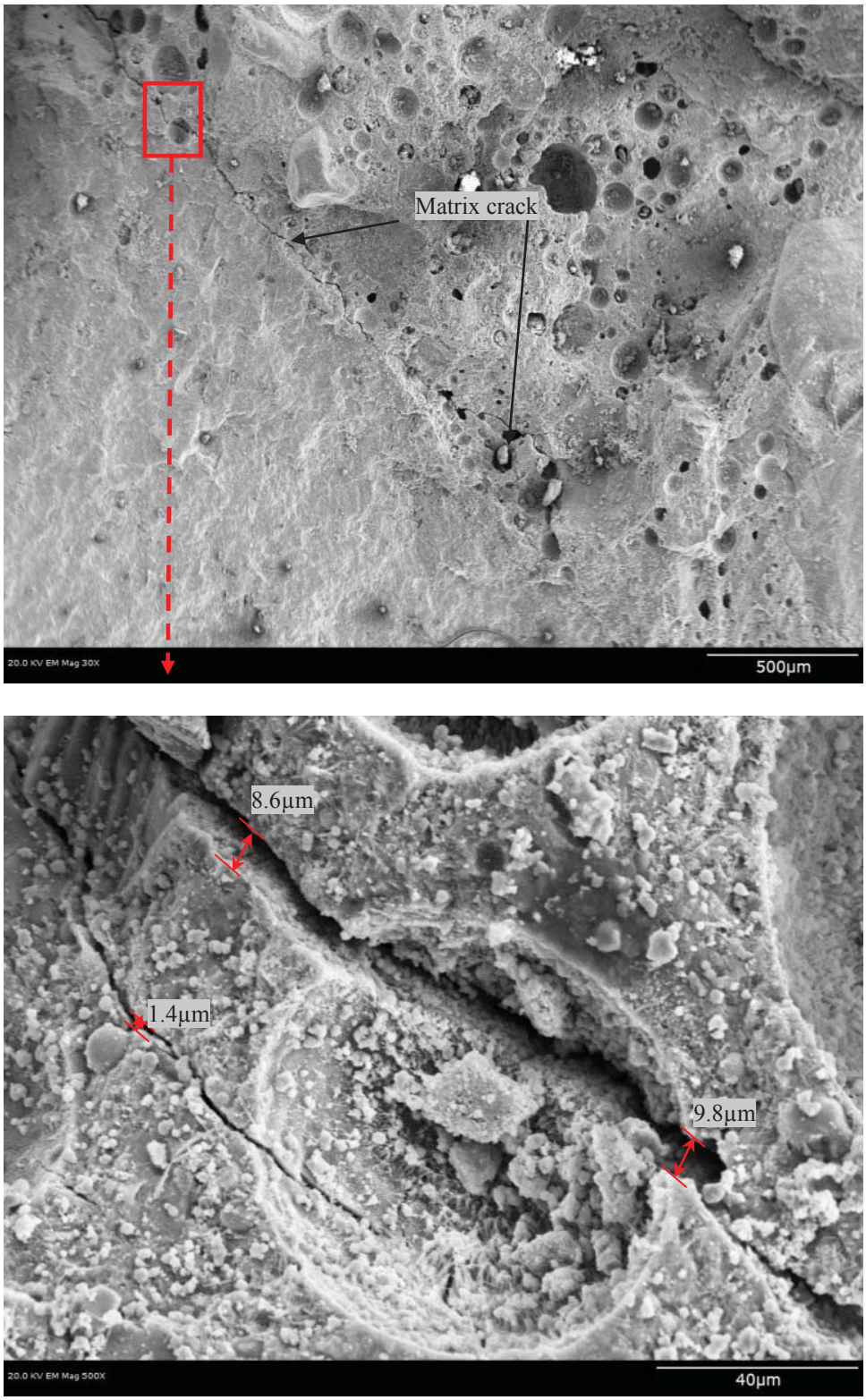

Figure 4.14: Micrograph of continuous crack-bridging in D80-1 sample

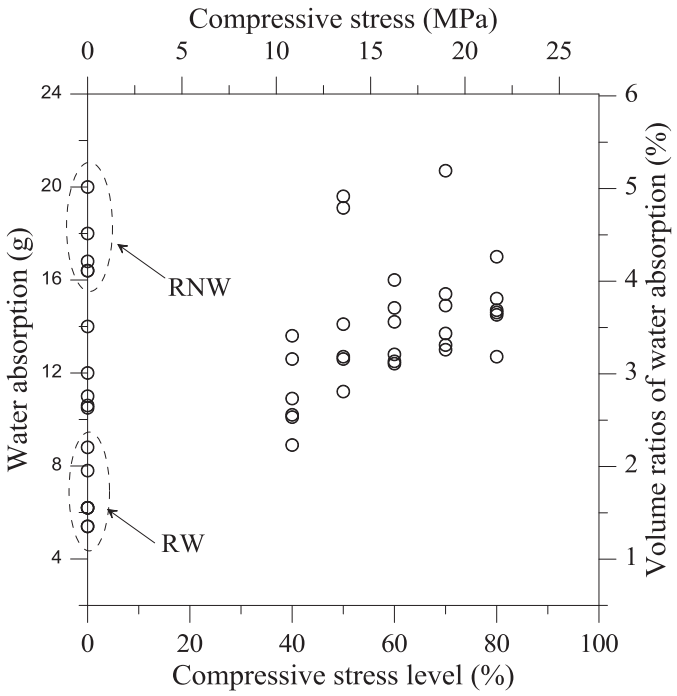

Figure 4.15: Measured water absorption of concrete samples

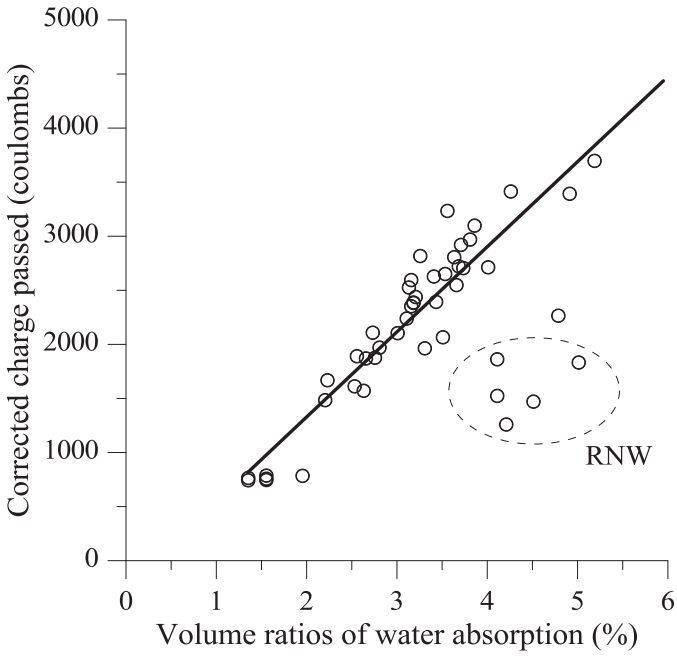

Figure 4.16: Corrected charge passed through samples with various levels of microcracks

Chapter 5. Bridge Deck Analyses

5.1 Introduction

Concrete in bridge decks under a vehicular load is subjected to complex stresses. The actual complex stress states were not simulated in the laboratory tests on concrete permeability in this study. While further research is needed, the bridge deck analyses were conducted to investigate stress distributions and stress levels in typical concrete bridge decks subjected to high axle loads. The ultimate goal of such analyses is to evaluate the potential internal damage caused by overweight vehicles and to link the potential damage levels to those simulated in the laboratory tests described in Chapters two through four.

5.2 General Bridge Selection

The majority of the bridges in Wisconsin are slab bridges and multi-girder bridges as shown in Figure 5.1. The bridge deck analyses thus should focus on these two types of bridges. Meanwhile, the stresses in a bridge deck under an overweight truck are affected by its span length, deck thickness, and girder spacing (Bae and Oliva, 2009; Wan et al., 2010).

The selection of the span length of slab bridges and girder bridges in design is usually guided by the WisDOT Bridge Manual (2008) as shown in Table 5.1. The distribution of the span lengths in Wisconsin was studied using NBI database (2010), as shown in Figures 5.2 and 5.3. The slab bridge analyses thus should consider these common span lengths: 20 to 50 ft. In addition, the analyses of multi-girder bridges should consider this range of spans: 50 to 130 ft.

The minimum of design depth for bridge decks specified in AASHTO LRFD (2010) is shown in Table 5.2. In addition, WisDOT Bridge Manual (2009) stipulates that the minimum of design depth of bridge deck is 7.0 in. (8.0 in. for new bridges) while the deck depth of above12 in. should be specified by owners. These regulations indicated that the bridge deck analyses should consider the deck thickness ranging from 8.0 to 10.0 in. The typical girder spacing for bridges is 8 to 10 ft according to WisDOT Bridge Manual. Specifically, the typical spacing for prestressed concrete girder bridges is from 6 to 12 feet as shown in Table 5.4. In addition, WisDOT Bridge Manual (2009) specifies that the girder spacing shall not exceed 7, 8, and 9 ft, when deck depth is 8, 8.5, and 9.0 in., respectively.

The consideration of all these typical design parameters resulted in an impractically large number of bridges to be analyzed as summarized in Table 5.5. Note that the focus of this study was on the impact of overweight vehicles with high axle loads. Therefore the deck analysis was conducted on idealized bridge models using finite element methods as shown below following a model verification analysis as described below.

5.3 Finite Element Techniques and Verification in Bridge Analysis

The bridge analyses were conducted using a commercial finite element (FE) software ABAQUS® (Simulia 6.10). To verify the FE modeling techniques for bridge deck analyses, a design example in WisDOT Bridge Manual (2009) was first simulated and the obtained stresses in the deck compared with the calculated values provided in the manual. Figure 5.4a shows the

continuous multi-girder bridge with a total length of 240 ft, and Figure 5.4b shows the dimensions of superstructure cross section. Steel plate girders are used in this example bridge and its cross section through the whole spans is plotted in Figure 5.4c. The girders have a spacing of 117 in., and the concrete deck has a 9 in. thickness. The haunch is 3 in. measured from the top of girder top flange to the bottom of the deck slab. The material properties for the concrete deck slab are assumed in the analysis as: the Young's modulus is 3604 ksi for the concrete with a compressive strength of 4000 psi (assumed in the design example) and the Poisson's ratio is 0.15 while steel girder has a Young's modulus of 29000 ksi and yield strength of 60 ksi.

This example bridge is designed in accordance with the design criteria from the WisDOT bridge manual (2009) conforming to the AASHTO LRFD bridge design specifications (2007). The superstructure configuration is illustrated in Figure 5.4b. In the sample design document, the dead load consists of concrete parapets, future wearing suface and other miscellaneous loads, such as cross frames and stiffeners. The parapets were treated as a line load uniformly for all of the girders in girder design while uniformly distributed surface load for deck slab. The future wearing surface was assumed as a dead load and treated as the same as the parapets: line load for girder design and surface load for deck slab. The live load considered was the HL-93 loading with a dynamic load allowance of 1.33.

The finite element model is shown in Figure 5.5a. where the parapets is not included for simpificity and its weight was converted as a uniformly distributed loading on the top of concrete slab, as specified in the design manual. Full two-span multi-gider superstructure was modeled as shown in Figure 5.5a. The concrete bridge deck was modeled using solid brick elements while the steel girders using thin-walled shell elements. Perfect bond and full composite action between the girders and the bridge deck were assumed by using tie restraint function in ABAQUS such that the matching joints between them may deform consistently without slipping. The meshing scheme is shown in Figuare 5.4e, in which total 214,896 solid elements were used for bridge deck and 10,800 shell elements for steel girders. A total of six element layers were meshed through the deck depth to capture the longitudinal normal stress on the top of slab.

The boundary conditions were set similar to the assumptions adopted in the design example as shown in Figure 5.4a. The two-span continuous bridge has two roller supports at the ends, simulating the bearings that allow temperature related horizontal movement parallel to the bridge. The horizontal displacement was restrained at the nodes of intersection of web and bottom flange at the middle support to ensure the stability of the model during the analysis. The vertical displacements were restrained at all three supports at the bottom of the girders by restraining the nodes of intersection between the web and bottom flange.

The design example includes the stresses calculated for the deck for the Service II limit states, which includes the stress calculated from the moments due to a) the weight of the parapet and the future wearing surface and b) the AASHTO design truck (including the dynamic allowance factor of 1.33) with design lane load. The same loads were used in the analysis. The weight of the parapet and the future wearing surface was added to the bridge model as a surface load of 0.000255 kips/in.^{2}, and the surface load was applied to the entire bridge deck. The self-weight of the concrete deck was not included similar to the design calculation because the resulted deformation has been accommodated by the wet concrete, which does not cause any stresses in the bridge deck. The loads from the design truck were modeled as the compression between six blocks and the concrete deck. In order to obtain the maximum flexural stress, the

design truck loads were positioned in the longitudinal direction such that the 40%-span (0.4L) line from the end support was placed between the two rear axles as shown in inserted plot in Figure 5.5a. Two lateral locations were simulated for the truck loads: 1) the truck was placed on the top of an interior girder and 2) the truck on the top of an exterior girder. In addition, the girders were located in between the wheel lines with a spacing of 6 ft. The design lane load was represented by a surface load of 0.000518 kips/in.^{2} over the two lanes through the span, on which the design truck was placed.

The normal stress contour in the longitudinal direction under the surface load simplified from the weight of the parapet and future wearing surface is shown in Figure 5.6a and 5.6b. The longitudinal normal stress on the top of the slab was about -0.10 to -0.11 ksi at 0.4*L*, which is very close to the stress level obtained in the design example (-0.09 ksi) as documented in the WisDOT Bridge Manual (2009). When the bridge was subjected to the design live loads, the longitudinal normal stress on the top of the slab at the 0.4*L* varied from -0.58 to -0.61 ksi as shown in Figure 5.7a and 5.7b. This is also comparable to the stress of -0.62 ksi predicted by the design procedures in the WisDOT Bridge Manual (2009).

A close look at the normal stress contour in Figure 5.7a indicated that the maximum normal stress in the longitudinal direction was not located at 0.4*L* as predicted in the design procedures but near the wheels, as shown in Figure 5.7a. The absolute maximum normal stress is -0.75 ksi near the wheels, which is 20 percent higher as compared to the calculated stress (-0.62 ksi). This stress increase may have been due to stress concentration near the wheels.

The results of the FE analyses matched well with those calculated in the WisDOT Bridge Manual. This indicates that the adopted analysis technique was appropriate. More importantly, the stress contours shown in Figures 5.6 and 5.7 show that the stress elevation occurs locally at the wheels. Therefore rather than FE analyses with arbitrary bridges with numerous bridge configurations, including the span length, girder spacing, and deck depth, and so on, the stresses in bridge decks may be captured using idealized bridge models that contains a segment of bridges near the truck loads.

5.4 Idealized Bridge Models

For multi-girder bridges, point loads from the wheels of an overweight truck are mainly transferred to the girders in the transverse direction, which carry the loads to their supports. In the meantime, the longitudinal load transfer causes various levels of bending moments and stresses in bridge deck through composite action along the span. Therefore, three-dimensional bridge deck stresses under a point load may be evaluated as a combination of the longitudinal flexural stresses and the transverse stresses including local stress concentration as illustrated in Figure 5.8. The flexural stress in the longitudinal direction, as demonstrated in the design example in section 5.3, accounts for the global bridge behavior including the self weight and vehicle loading, which is calculated in a design/rating process as specified in WisDOT Bridge Manual. The longitudinal stresses in a bridge deck are related to the bending moment developed in the bridge superstructure, which varies along with the location through the span. Therefore, the longitudinal stresses in a bridge deck was simplified as an initial tress applied to the finite element model, and the initial stress varies from $0.1f'_c$ (tension) through $-0.4f'_c$ (compression) to represent the different locations in a bridge through the span, where f'_c is the concrete compressive strength. Note that the stresses up to $0.4f'_c$ in compression were selected based on

common design assumptions for bridges under service loads though the stresses seem high compared with those observed in the above full-deck analysis. The stresses in transverse direction and accompanying stress increase in longitudinal direction in the deck slab of a multi-girder bridge were determined using finite element models of a segment of the bridge superstructure. Details on the finite element modeling are presented in Section 5.5.

Truck tires have complex structure as illustrated in Fig. 5.9a. The contact area of a truck tire is close to a rectangle as shown in Figure 5.9b (Majumdar et al., 2007). Therefore the vehicle wheel loads were applied to the bridge deck using 12-inch square blocks with elastic material properties. Instead of the use of a variety of overweight truck, the AASHTO design truck, as shown in Figure 5.10a, was used in majority of the FE analyses, in which the bridge configurations were the main variable. The idealized axle loads used in this study were 32 kips placed on the top of the bridge deck, as shown in Figure 5.10b. Additional group of analyses were conducted to investigate the impact of high axle loads.

5.5 Finite Element Models of Bridge Decks

With the above idealized bridge model and idealized loads, bridge deck models, as shown in Figure 5.11a, were analyzed using ABAQUS V 6.10.2 (Simulia, 2010). The matrix of the deck analyses is shown in Table 5.6. A total of thirty analyses are presented below for bridge deck models subjected to two idealized vehicle locations. In the proposed analyses, the girder spacing and deck depth are the key parameters. In addition, the length of modeled deck segment was varied to study the sensitivity of that model dimension. The concrete deck was modeled using 3D brick elements with a linear concrete material model (further studies are needed to consider nonlinear concrete materials). The compressive strength of concrete was assumed as 4000 psi, thus the Young's modulus of concrete was 3604 ksi following the ACI 318 recommendations and the Poisson's ratio was assumed as 0.15. Five steel plate girders with these assumed dimensions were placed underneath the bridge deck: 12 by 1.5 in. for both the top and the bottom flanges and 54 by 0.5 in. for the web plate chosen from the recommended dimension in bridge manual (AISI, 1995). The steel plate girders were modeled using 3-D shell elements. The Young's modulus, E_g, and the Poisson's ratio of material properties are 29000 ksi and 0.3 for girders. Perfect bond and full composite action between the girders and the bridge deck was assumed in the analysis.

A specimen with a deck depth of 9 in. and a girder spacing of 9 ft. was used as the reference as shown by the highlighted rows in Table 5.6. In addition, the deck thickness varied from 7 to 12 in. while the girder spacing from 7 to 12 ft. The girder stiffness also varied to represent different types of bridge superstructures by changing the Young's modulus E. Most analyses were conducted with the design truck, which has two rear axle loads of 32 kips while the axle load varied in one group of analyses form 32 to 72 kips, which is the highest axle load recorded by Weigh-in-Motion system in Wisconsin in 2007 (Zhao and Tabatabai, 2009).

5.5.1 Meshing, Initial Stress and Boundary Conditions

A typical finite element model and its meshing scheme are illustrated in Figure 5.11b for the reference bridge model. A total of 127,872 solid elements were used for the bridge deck while the steel girders had 10,800 shell elements. Local refined meshing was used for the lanes loaded with the truck loads, as shown in Figure 5.12. The reduced integration scheme in

ABAQUS was used for the 8-node brick elements to minimize shear locking effects. Note that such effects may also be alleviated by using a denser mesh, but with an increase in computation time. Seven layers of elements were used through the deck depth to accurately capture the bending stresses.

The normal stresses in the longitudinal direction due to the global bending moment as illustrated in the bridge analysis in Section 5.3 were considered using an initial normal stress to the considered segments. Such initial stress in the longitudinal direction was applied to the model ranging from $0.1f'_c$ to $-0.4f'_c$ to represent the bending stresses in the longitudinal direction in a variety of bridges under various loading. The details on the predefined stresses in ABAQUS are shown in Appendix A. Again, the longitudinal displacements at the ends of the deck segments were restrained while all other degrees of freedom were released. On the top end of girders, horizontal and vertical displacements were restrained to keep the FE model form rigid-body motions and to avoid singularities in the stiffness matrix.

5.5.2 Load Patterns and Stress of Interest

To locate the maximum responses in the transverse direction due to an applied load, the bridge model can be treated as a four-span continuous beam (Figure 5.13a). The influence lines of bending moment at mid-support and the middle of the first and the second span were shown in Figures 5.13b through 5.13d. This influence lines indicated the positions of the wheel loads, which were defined as the load pattern 1 through load pattern 3. Specifically, Load pattern 1 was used to locate the maximum negative bending moment at mid-support while load pattern 3 provided the maximum positive bending moment at middle of the first span. Load patterns 1 and 3 were used in all analyses. Note that the dynamic allowance factor included in the bridge analyses in Section 5.3 was not included in this group of analysis.

A finer mesh was used in the idealized FE models compared with those of bridge analysis described in Section 5.3 in order to accurately capture the locally elevated stress near the wheels. Figure 5.14 plotted the third principal stress contour near the wheel load, where the blue color represents the higher stress value while the red color shows the lower stress values. The principal stresses elevated as expected near the loading. Therefore the stresses at four locations were evaluated, referred to as A1 through A4 hereafter, in which A1 is from the element below the loading patch while the rest of locations are from the elements just outside the loading patchs. It should be noted that the concrete at the location A1 is likely subjected to triaxial compression, the impact which on concrete deterioration has not been evaluated through laboratory tests.

A Cartesian coordinate system was used to describe the stress components in the finite element analysis. The x-axis represents the transverse direction; the y-axis represents the direction of the deck depth; and the z-axis represents the longitudinal direction. For example, σ_z represents the longitudinal normal stress while τ_{xz} shows the shear stress on the planes parallel to the deck surface.

5.5.3 Segment Length and Longitudinal Stress

The idealized bridge segment model must have a short length in order to accommodate fine meshes. In addition the finite segment length may also impact the transverse response of the model bridge deck. To determine the segment length used in the bridge analysis, a series of four analyses with a segment length varying from 9 to 54 ft were conducted using the reference bridge section subjected to an initial longitudinal normal stress of $-0.1f_c'$. Figure 5.15a and 5.15b

plotted the stresses in longitudinal and transverse directions. The maximum stresses in both longitudinal and transverse directions remains within 7 percent for all cases with different segment lengths, indicating that the local stress elevation can be treated as a local effect. Thus, a segment length of 36 ft was used in the rest of the analyses.

5.6 Stress Levels in Bridge Decks Analysis

Bridge analyses results are listed in Tables 5.8 through 5.12 while stress contours and the effects of each factor on stress level are plotted in Figure 5.16 through 5.27. Detailed discussion of these results is provided in the following sections.

5.6.1 Stress Contour and Distribution

The compressive stresses on the top surface of the modeled bridge decks under consideration were presented in Figure 5.16 through Figure 5.27. The contour of the minimum principal stresses between two girders was presented followed by four a locally enlarged areas including half of loading patch. It should be mentioned that the stress distribution of stresses components in all cases were similar to the presented typical cases. The stress contours are for both Load patterns 1 and 3 as discussed below. Cases BD_9_9_5 through BD_9_9_10 show the predicted results under Load pattern 1 and Cases BD_9_9_11 through BD_9_9_15 for Load pattern 3. The bridge model with a 9-in. deck and 9-ft girder spacings subjected to the rear axle of the AASHTO design truck with a load of 16 kips at each wheel were used for all of the twelve cases while the input initial longitudinal stress σ_{z0} varied from $0.1f'_c$ to $-0.4f'_c$. The stresses at the top surface of the deck slab between the girders are presented, including the 2nd and 3rd principal stress (minimum principal stress), the transverse stress (σ_x), and the longitudinal stress (σ_z).

Figures 5.16a through 5.16e plotted the stress contours at the top surface of a deck slab with an initial longitudinal stress σ_{z0} of $-0.1f'_c$. Again, this applied longitudinal stress represents that observed at a certain location along the span of a bridge. In general, the local effects near the wheel loads were demonstrated in Figure 5.16a by stress contour showing higher stresses in blue color adjacent to the wheel loading. The maximum transverse stress at the top surface of the slab between the girders was -0.2 ksi ($0.05f'_c$). A closer look at the stress contour showed that the maximum transverse stresses occur in an element adjacent to the wheel loading. The maximum stress in the longitudinal direction reached -0.58 ksi near the location of loading. The stress contour along the longitudinal direction rapidly decreased from -0.58 ksi at the location of loading to -0.4 ksi (the applied initial longitudinal stress) at locations away from the loading (beyond half of girder spacing). This is consistent with the previous observation in section 5.5.2 that the elevated longitudinal deformation and the transverse deformation decrease rapidly.

Figures 5.16b through 5.16c plotted the 2nd and 3rd principal stresses on the top of deck slab. The stress contours indicate that the z-direction stresses should be the 1st principal stress (the maximum stress). It is known that the shear stress along x-z plane near the loading in the deck slab approaches zero when it is subjected to a point load at the middle of the girder spacing. The other two shear stresses along x-y and y-z planes near the middle of the girder spacing can be approximately derived from the applied loading against the rectangular area through the depth ($\frac{16\text{ kips}}{4\times12\times9\text{ in.}} = 0.04\text{ ksi}$). Note that the shear stresses of 0.04 ksi at x-y and y-z planes were

relatively small as compared to the transverse and longitudinal stress. As a result, the transverse stress σ_x and the longitudinal stress σ_z were approximately the 2nd and 3rd principal stress. Similar observations were made in the case BD_9_9_3 for Load pattern 3, in which the transverse stress increased to -0.25 ksi ($0.06f'_c$) and the principal stress had a slight increase as compared to that observed in Load pattern 1.

Figures 5.17 through 5.19 plot the stress contour in the model BD_9_9_8 to BD_9_9_10 for Load pattern 1, and Figures 5.22 through 5.25 for Load pattern 3 under initial longitudinal stress σ_{z0} varying from $-0.2f'_c$ to $-0.4f'_c$, respectively. Figure 5.20 and Figure 5.26 plotted the stress components, including the 2nd and 3rd principal stress, the transverse stress σ_x, and the longitudinal stress σ_z on the top surface of the deck slab. These cases with zero initial longitudinal stress represent the inflection point or the simple supports in a bridge. Again, the transverse stress and longitudinal stress correspond to the 2nd and 3rd principal stresses, respectively. The transverse stress increase remains constant at all of these cases because the deck thickness and the girder spacing were kept same in this group of analyses. Unlike other cases where the longitudinal stress controls the 3rd principal stress, the 3rd principal stresses in these cases were governed by the transverse stresses.

In general, the location at A3 experiences higher transverse stress compared to the location at A2 and A4 for both Load pattern 1 and Load pattern 3 as shown in Tables 5.7 and 5.13. The location at A1 is directly underneath the wheel such that the concrete may experience tri-axial compression, and the stresses at A1 thus should have a small impact on concrete internal damage. The location at A4 may observe high values of longitudinal stresses compared to those at A2 and A3. Thus, the locations at A3 and A4 were used to present the stress levels in the following sections.

5.6.2 Effects of Initial Stress on Stress Levels

The transverse stress, longitudinal stress and the 3rd principal stress at locations A3 and A4 were plotted in Figure 5.28 and Figure 5.29. The transverse stress remained largely constant (-0.2 ksi for Load pattern 1 and -0.25 ksi for Load pattern 3) for the bridge model subjected to various levels of initial longitudinal stresses. Again this indicates that the transverse stresses caused by a 32-kip axle load (two 16-kip wheels with a spacing of 6 ft.) are constant when the load moves from one end of a bridge to the other end. This is consistent to the fact that the deck in multi-girder bridges carry loads mainly through one-way action and the influential factors are the deck thickness and the girder spacing.

Meanwhile, the 3rd principal stresses were very close to the longitudinal stress at all case as shown in Figures 5.29a and 5.29b. In addition, the 3rd principal stress at both A3 and A4 increased with an increase in the initial longitudinal stress. This indicates that the longitudinal normal stress, if includes the local effects near the wheel, can be used to estimate the 3rd principal stress. The local effects are mainly related to the level of wheel load.

5.6.3 Effects of Deck Depth on Stress Levels

A group of FE analyses were conducted to study the impact of deck depths. In this group of analyses, the girder spacing was 9 ft, the initial longitudinal stress was $0.1f'_c$, and the wheel loads were 16 kips. The results were summarized in Table 5.10 and plotted in Figures 5.30a and 5.30b. The deck depth has significant impact on the transverse stress levels in the bridge deck. The transverse stress had a 153 percent increase from -0.13 ksi to -0.33 ksi at the location A4 as

the thickness of deck slab decreased from 12 to 7 in. More considerable increase was observed at the location A3: from -0.14 to -0.4 ksi. The 3rd principal stress also increased from -0.52 to -0.71 ksi at the location A4. Such stress increases were not proportional to the deck thickness because the deck thickness affects the section modulus of the member, which in turn affects the stress values. The 3rd principal stresses were very close to the longitudinal stress including the local effects.

5.6.4 Effects of Girder Spacing on Stress Levels

The impact of varying girder spacing on the stress levels were investigated using another group of FE analyses as shown in Table 5.6. In this group of analyses, the bridge models had a girder spacing ranging from 7 to 12 ft. while all other parameters were the same as the reference model. The initial longitudinal stress was $-0.1f'_c$. The calculated stresses are shown in Table 5.11 and plotted in Figures 5.31a and 5.31b. A smaller impact was observed compared that of deck thickness in Section 5.6.3. The transverse stress increased from -0.19 to -0.25 ksi at the location A4 as the girder spacing increased from 7 to 12 ft. The stress at the location A3 had an increase from -0.21 to -0.29 ksi. Meanwhile, the 3rd principal stress increased from -0.57 to -0.64 ksi at the location A4 and the increase was from -0.54 to -0.60 ksi at the location A3 when the girder spacing increased from 7 to 12 ft. The stress increases were largely proportion to the variation in the girder spacing likely because the deck moment in the transverse direction is related to the span of the continuous beam (represented by the girder spacing).

5.6.5 Effects of Girder Stiffness on Stress Levels

The effects girder types on the deck stresses were represented by the bridge models with a variety of girder stiffness. The results of this group of analyses are shown in Table 5.12. It seems that the stiffness of girder had negligible effects on the stress levels. It is likely because the stress components are a local effect in transverse direction while the girder stiffness may affect the longitudinal stresses. The entire bridges must be modeled to capture such impact.

5.6.6 Effects of axle loading on Stress Levels

The local stress elevations are mainly related to the level of wheel loads as shown in Section 5.3. Heavy trucks are usually allowed to operate on highways with a permit. Some overweight trucks can have high axle loads. The impact of overweight loading on the stress level was investigated in the last group of analyses as shown in Table 5.6. In the group of analyses, the axle load varied from 32 kips to 72 kips. The predicted stresses are listed in Table 5.13, and plotted in Figure 5.32. When the bridge is subjected to the AASHTO design truck (32-kip axles), the transverse stress on the top surface of the deck slab was -0.25 ksi at the location A3 ($0.06f'_c$), and the 3rd principal stress (or longitudinal stress) was -0.6 ksi, which had a 50 percent increase when compared to the applied initial longitudinal stress ($-0.1f'_c$). When the bridge was subjected to the overweight truck with an axle load of 72 kips, the transverse stress increased up to -0.56 ksi at the location A3 ($0.14f'_c$) and the 3rd principal stress (or longitudinal stress) was -0.84 ksi ($0.21f'_c$), a 110 percent increase as compared to initial longitudinal stress ($0.1f'_c$).

5.7 Summary

The bridge analyses were conducted to investigate stresses in bridge decks using the idealized bridge models. Following the validation of the proposed technique by comparing the analysis of a bridge model with the documented design calculations, a parametric study was carried out in order to identify the most relevant factors. The following observations were made:

- Deck stresses in both longitudinal and transverse directions can be significantly affected by the axle loads, especially at the locations near the wheels.
- Under the same overweight truck, the transverse and longitudinal stresses can be affected by the thickness of bridge deck and the girder spacing.
- The design truck has a small impact on the stress levels, represented by the minimum principal stress. Hence, the design truck may not cause significant damage to concrete, which may accelerate the deterioration of the bridge deck.
- Overweight trucks, especially those with high axle loads, however, may cause bridge deck to develop higher stresses such as $0.4f'_c$. Such stresses are high enough to cause internal micro-cracks in concrete, which increases the permeability of concrete, and accelerate the deck deterioration.

The material nonlinearity of concrete was not investigated in this study. Bridge deck may develop cracks with the actual concrete material included in the analyses. The moment of inertia of the deck slab reduces significantly when flexural cracks form in concrete, leading to higher stresses in bridge deck. Further studies that include material nonlinearity of concrete are required. Nevertheless, the linear analyses shown in this chapter provided important information on the stress levels in a bridge deck. Empirical equations were proposed based on the analyses in the next chapter.

Table 5.1: Typical Span lengths (WisDOT Bridge Manual, 2009)

Bridge Type	Span length range (ft)
Slabs (reinforced, cast-in-place concrete slabs)	
Flat slab	20 to 60
Multi-girders:	
Prestressed Concrete Girders	
36" girder	40 to 75
36W" girder	60 to 100
45 W" girder	90 to 120
54 W" girder	110 to 135
72 W" girder	120 to 160
Steel rolled beams	50 to 90
Steel welded plate girders	120 to 300

Table 5.2: Design depth of slab system (AASTHO LRFD, 2007)

Bridge Type	Minimum overall depth (ft)	
	Simple span	Continuous spans
Slabs (reinforced, cast-in-place concrete slabs)		
Flat slab throughout	$\frac{1.2(L+10)}{30}$	$\frac{(L+10)}{30}$>0.54 ft
Multi-girders:		
Prestressed Concrete Girders	0.045 L	0.04 L
Steel rolled beams	0.04 L	0.032 L
Steel welded plate girders		

Table 5.3: Girder spacing of prestressed girder system (WisDOT bridge manual, 2009)

Girder spacing	28W" girder		36W" girder		45W" girder		54W" girder		72W" girder	
	Single span	2 equal spans	Single span	2 equal spans	Single span	2 equal spans	Single span	2 equal spans	Single span	2 equal spans
6'-0	57'	61'	73'	78'	102'	108'	134'	138'	161'	165'
6'-6	55'	59'	70'	75'	97'	105'	130'	136'	157'	164'
7'-0	53'	57'	68'	73'	94'	102'	126'	133'	153'	161'
7'-6	52'	55'	66'	70'	91'	97'	123'	130'	149'	157'
8'-0	50'	54'	64'	68'	89'	95'	120'	127'	146'	154'
8'-6	48'	52'	62'	66'	85'	92'	117'	124'	143'	150'
9'-0	47'	50'	55'	64'	82'	90'	114'	121'	139'	147'
9'-6	44'	49'	54'	62'	80'	85'	111'	118'	136'	144'
10'-0	42'	47'	52'	56'	78'	83'	106'	114'	132'	139'
10'-6	41'	44'	51'	54'	74'	80'	104'	112'	129'	136'
11'-0	39'	43'	49'	53'	68'	78'	101'	107'	125'	132'
11'-6	38'	42'	48'	51'	67'	75'	99'	105'	123'	130'
12'-0	37'	40'	47'	50'	65'	71'	95'	103'	120'	127'

Table 5.4: Summary of prototype bridges

Bridge Type	Span length (ft)	Deck depth (in.)	Girder spacing (ft)
Slabs (reinforced, CIP concrete slabs)			
Flat slab throughout	20 to 50	12 to 24	-
Multi-girders:			
Prestressed Concrete Girders			
36" girder	40 to 75	8 to 10	See table 5.4
36W" girder	60 to 100		
45 W" girder	90 to 120		
54 W" girder	110 to 135		
72 W" girder	120 to 160		
Steel rolled beams	50 to 130*	8 to 10	8 to 12
Steel welded plate girders	120 to 130	8 to 10	8 to 12

*: may be limited by the standard size.
**: selected in accordance with the corresponding deck depth as well.
***: selected in accordance with existing prestressed girder types.

Table 5.5: Comparison of normal stress results on top of deck

Load combination	Longitudinal stress (ksi)		
	Design manual	**FEA (location of 48ft)**	**FEA (adjacent to loading patch)**
Parapet + future wearing (0.000255 ksi)	0.09	0.10~0.11	0.10
Live Load – HL-93*	0.62	0.58~0.61	0.75

Note that: dynamic allowance factor 1.33 is included in design live loads.

Table 5.6: Normal stress results under different loads

Load combination	Longitudinal stress (ksi)		
	Design manual	**FEA (location of 48ft)**	**FEA (adjacent to loading patch)**
Parapet + future wearing (0.000255 ksi)	-	0.10~0.11	0.10
Live Load – HL-93*	-	0.78~0.90	1.23

Table 5.7: Matrix of bridge deck analysis

No.	Case ID	Load Pattern	Long. stress σ_{z0}	Segment length (ft)	Girder spacing (ft)	Deck depth (in.)	$E_{gc}I_{gc}/E_{gr}I_{gr}$	Wheel loading (kips)
1	BD_9_9-1	3	-0.1f'_c	9	9	9	1	16
2	BD_9_9-2	3	-0.1f'_c	18	9	9	1	16
3	BD_9_9-3	3	-0.1f'_c	36	9	9	1	16
4	BD_9_9-4	3	-0.1f'_c	54	9	9	1	16
5	BD_9_9-5	1	0.1f'_c	36	9	9	1	16
6	BD_9_9-6	1	0	36	9	9	1	16
7	BD_9_9-7	1	-0.1f'_c	36	9	9	1	16
8	BD_9_9-8	1	-0.2f'_c	36	9	9	1	16
9	BD_9_9-9	1	-0.3f'_c	36	9	9	1	16
10	BD_9_9-10	1	-0.4f'_c	36	9	9	1	16
11	BD_9_9-11	3	0.1f'_c	36	9	9	1	16
12	BD_9_9-12	3	0	36	9	9	1	16
3	BD_9_9-3	3	-0.1f'_c	36	9	9	1	16
13	BD_9_9-13	3	-0.2f'_c	36	9	9	1	16
14	BD_9_9-14	3	-0.3f'_c	36	9	9	1	16
15	BD_9_9-15	3	-0.4f'_c	36	9	9	1	16
16	BD_9_7	3	-0.1f'_c	36	9	7	1	16
17	BD_9_8	3	-0.1f'_c	36	9	8	1	16
3	BD_9_9-3	3	-0.1f'_c	36	9	9	1	16
18	BD_9_10	3	-0.1f'_c	36	9	10	1	16
19	BD_9_12	3	-0.1f'_c	36	9	12	1	16
20	BD_7_9	3	-0.1f'_c	36	7	9	1	16
21	BD_8_9	3	-0.1f'_c	36	8	9	1	16
3	BD_9_9-3	3	-0.1f'_c	36	9	9	1	16
22	BD_10_9	3	-0.1f'_c	36	10	9	1	16
23	BD_12_9	3	-0.1f'_c	36	12	9	1	16
24	BD_9_9-16	3	-0.1f'_c	36	9	9	0.5	16
3	BD_9_9-3	3	-0.1f'_c	36	9	9	1	16
25	BD_9_9-17	3	-0.1f'_c	36	9	9	2	16
26	BD_9_9-18	3	-0.1f'_c	36	9	9	5	16
27	BD_9_9-19	3	-0.1f'_c	36	9	9	10	16
3	BD_9_9-3	3	-0.1f'_c	36	9	9	1	16
28	BD_9_9-20	3	-0.1f'_c	36	9	9	1	24
29	BD_9_9-21	3	-0.1f'_c	36	9	9	1	30
30	BD_9_9-22	3	-0.1f'_c	36	9	9	1	36

Note that: BD_9_9 is the case name of bridge deck analysis based on girder spacing and deck depth;
f'_c is concrete compressive strength (4 ksi used in this study)

Table 5.8: Stresses in deck of a bridge with a 9-ft girder spacing and 9-inch slab with varying longitudinal stresses (ksi)-Load pattern 1

Initial Longitudinal stress σ_{z0}	Location	S_1	S_2	S_3	Von Misses σ_s	Transverse (σ_x)	σ_y	Longitudinal (σ_z)
Negative moment zone $0.1f'_c$ (0.4 ksi)	A1	0.24	-0.07	-0.10	0.32	-0.10	-0.06	0.23
	A2	0.25	-0.03	-0.21	0.40	-0.19	-0.05	0.25
	A3	0.24	-0.04	-0.24	0.41	-0.22	-0.05	0.24
	A4	0.22	-0.03	-0.14	0.32	-0.14	-0.03	0.22
Inflection points $0.0f'_c$ (0.0 ksi)	A1	-0.06	-0.12	-0.18	0.10	-0.12	-0.07	-0.17
	A2	-0.03	-0.15	-0.20	0.15	-0.18	-0.04	-0.15
	A3	-0.03	-0.15	-0.23	0.17	-0.21	-0.05	-0.16
	A4	-0.02	-0.15	-0.19	0.15	-0.15	-0.03	-0.18
Positive moment zone $-0.1f'_c$ (-0.4 ksi)	A1	-0.08	-0.14	-0.57	0.46	-0.14	-0.08	-0.57
	A2	-0.03	-0.18	-0.54	0.46	-0.17	-0.04	-0.54
	A3	-0.02	-0.21	-0.54	0.45	-0.20	-0.03	-0.54
	A4	-0.03	-0.16	-0.58	0.50	-0.16	-0.03	-0.58
Positive moment zone $-0.2f'_c$ (-0.8 ksi)	A1	-0.08	-0.16	-0.97	0.85	-0.16	-0.09	-0.97
	A2	-0.02	-0.17	-0.94	0.85	-0.16	-0.03	-0.94
	A3	-0.03	-0.20	-0.95	0.85	-0.19	-0.04	-0.95
	A4	-0.03	-0.17	-0.98	0.89	-0.17	-0.03	-0.98
Positive moment zone $-0.3f'_c$ (-1.2 ksi)	A1	-0.09	-0.19	-1.37	1.23	-0.18	-0.09	-1.37
	A2	-0.02	-0.15	-1.33	1.25	-0.14	-0.03	-1.33
	A3	-0.02	-0.18	-1.34	1.24	-0.18	-0.03	-1.34
	A4	-0.03	-0.18	-1.38	1.28	-0.18	-0.03	-1.38
Positive moment zone $-0.4f'_c$ (-1.6 ksi)	A1	-0.10	-0.21	-1.77	1.62	-0.21	-0.10	-1.77
	A2	-0.02	-0.14	-1.73	1.65	-0.13	-0.02	-1.73
	A3	-0.02	-0.17	-1.73	1.64	-0.17	-0.03	-1.73
	A4	-0.03	-0.19	-1.78	1.67	-0.19	-0.04	-1.78

Note that: f'_c is concrete compressive strength (4 ksi used in this study).

S_1 is the first principal stress

S_2 is the second principal stress

S_3 is the third principal stress

σ_s is the von Misses stress strength

σ_x is the normal stress along x-axis (transversal direction)

σ_y is the normal stress along y-axis (vertical, depth direction)
σ_z is the normal stress along x-axis (longitudinal direction)

A1-A4 represent the location of stress around the loading as shown:

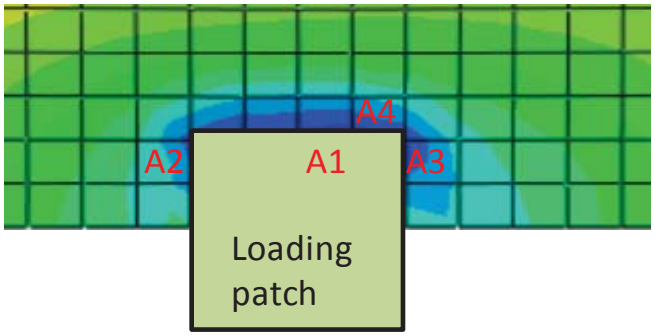

Table 5.9: Stress level of bridge with a 9 ft spacing and 9 inches depth under varying longitudinal stress (ksi)-Load pattern 3

Initial Longitudinal stress σ_{z0}	Location	S_1	S_2	S_3	Von Misses σ_s	σ_x	σ_y	σ_z
Negative moment zone $0.1f'_c$ (0.4 ksi)	A1	0.20	-0.15	-0.29	0.43	-0.25	-0.19	0.19
	A2	0.24	-0.04	-0.28	0.45	-0.27	-0.05	0.24
	A3	0.24	-0.04	-0.28	0.45	-0.27	-0.05	0.24
	A4	0.21	-0.05	-0.21	0.37	-0.21	-0.05	0.20
Inflection points $0.0f'_c$ (0.0 ksi)	A1	-0.14	-0.20	-0.30	0.14	-0.25	-0.18	-0.21
	A2	-0.04	-0.17	-0.27	0.20	-0.25	-0.05	-0.17
	A3	-0.04	-0.17	-0.27	0.20	-0.26	-0.05	-0.17
	A4	-0.03	-0.19	-0.23	0.18	-0.21	-0.05	-0.20
Positive moment zone $-0.1f'_c$ (-0.4 ksi)	A1	-0.16	-0.27	-0.61	0.41	-0.25	-0.18	-0.60
	A2	-0.04	-0.25	-0.57	0.46	-0.24	-0.05	-0.57
	A3	-0.04	-0.25	-0.57	0.46	-0.24	-0.05	-0.57
	A4	-0.03	-0.19	-0.60	0.51	-0.19	-0.03	-0.60
Positive moment zone $-0.2f'_c$ (-0.8 ksi)	A1	-0.16	-0.27	-1.00	0.79	-0.25	-0.18	-1.00
	A2	-0.03	-0.24	-0.96	0.85	-0.23	-0.04	-0.96
	A3	-0.03	-0.24	-0.96	0.84	-0.23	-0.04	-0.96
	A4	-0.03	-0.20	-1.00	0.89	-0.20	-0.03	-0.99
Positive moment zone $-0.3f'_c$ (-1.2 ksi)	A1	-0.16	-0.26	-1.40	1.19	-0.25	-0.18	-1.39
	A2	-0.03	-0.22	-1.36	1.24	-0.22	-0.04	-1.36
	A3	-0.03	-0.23	-1.36	1.24	-0.22	-0.04	-1.36
	A4	-0.03	-0.21	-1.39	1.28	-0.21	-0.03	-1.39
Positive moment zone $-0.4f'_c$ (-1.6 ksi)	A1	-0.17	-0.26	-1.79	1.58	-0.26	-0.17	-1.79
	A2	-0.03	-0.21	-1.75	1.64	-0.20	-0.03	-1.75
	A3	-0.03	-0.22	-1.75	1.64	-0.21	-0.03	-1.75
	A4	-0.04	-0.22	-1.78	1.66	-0.22	-0.04	-1.78

Table 5.10: Stress level of bridge with a 9 ft spacing under varying depths (ksi)-Load pattern 3

Depths (in.)	Location	S_1	S_2	S_3	Von Misses σ_s	σ_x	σ_y	σ_z
7	A1	-0.21	-0.40	-0.72	0.45	-0.38	-0.24	-0.70
	A2	-0.05	-0.39	-0.66	0.52	-0.38	-0.07	-0.65
	A3	-0.06	-0.41	-0.66	0.52	-0.40	-0.07	-0.65
	A4	-0.06	-0.33	-0.71	0.57	-0.33	-0.06	-0.70
8	A1	-0.18	-0.32	-0.65	0.42	-0.30	-0.21	-0.64
	A2	-0.04	-0.31	-0.60	0.49	-0.30	-0.06	-0.60
	A3	-0.04	-0.32	-0.60	0.48	-0.31	-0.06	-0.60
	A4	-0.05	-0.26	-0.64	0.52	-0.26	-0.05	-0.64
9	A1	-0.16	-0.27	-0.61	0.41	-0.25	-0.18	-0.60
	A2	-0.04	-0.25	-0.57	0.46	-0.24	-0.05	-0.57
	A3	-0.04	-0.25	-0.57	0.46	-0.24	-0.05	-0.57
	A4	-0.03	-0.19	-0.60	0.51	-0.19	-0.03	-0.60
10	A1	-0.14	-0.23	-0.58	0.40	-0.21	-0.16	-0.57
	A2	-0.03	-0.21	-0.54	0.45	-0.20	-0.04	-0.54
	A3	-0.03	-0.21	-0.54	0.45	-0.20	-0.04	-0.54
	A4	-0.04	-0.18	-0.57	0.47	-0.18	-0.04	-0.56
12	A1	-0.12	-0.17	-0.53	0.39	-0.16	-0.14	-0.53
	A2	-0.02	-0.15	-0.51	0.43	-0.14	-0.03	-0.51
	A3	-0.02	-0.15	-0.50	0.43	-0.14	-0.03	-0.50
	A4	-0.03	-0.13	-0.52	0.45	-0.13	-0.03	-0.52

Note that: initial longitudinal stress σ_{z0}= -0.1 f'_c remains constant for all these analyses.

Table 5.11: Stress level of bridge with a 9 in. depth under varying spacing (ksi)-Load pattern 3

Spacing (ft)	Location	S_1	S_2	S_3	Von Misses σ_s	σ_x	σ_y	σ_z
7	A1	-0.15	-0.24	-0.59	0.40	-0.22	-0.17	-0.58
	A2	-0.03	-0.21	-0.55	0.45	-0.20	-0.04	-0.54
	A3	-0.03	-0.22	-0.54	0.45	-0.21	-0.04	-0.54
	A4	-0.04	-0.19	-0.57	0.48	-0.19	-0.04	-0.57
8	A1	-0.15	-0.26	-0.26	0.40	-0.24	-0.18	-0.59
	A2	-0.03	-0.23	-0.56	0.46	-0.22	-0.04	-0.56
	A3	-0.03	-0.24	-0.56	0.46	-0.23	-0.05	-0.56
	A4	-0.04	-0.20	-0.58	0.49	-0.20	-0.04	-0.58
9	A1	-0.16	-0.27	-0.61	0.41	-0.25	-0.18	-0.60
	A2	-0.04	-0.25	-0.57	0.46	-0.24	-0.05	-0.57
	A3	-0.04	-0.25	-0.57	0.46	-0.24	-0.05	-0.57
	A4	-0.03	-0.19	-0.60	0.51	-0.19	-0.03	-0.60
10	A1	-0.16	-0.28	-0.62	0.42	-0.26	-0.18	-0.62
	A2	-0.04	-0.27	-0.58	0.47	-0.26	-0.05	-0.58
	A3	-0.04	-0.27	-0.58	0.47	-0.26	-0.05	-0.58
	A4	-0.04	-0.23	-0.61	0.51	-0.23	-0.05	-0.61
12	A1	-0.17	-0.31	-0.65	0.43	-0.29	-0.19	-0.64
	A2	-0.04	-0.30	-0.61	0.49	-0.29	-0.05	-0.60
	A3	-0.04	-0.30	-0.60	0.49	-0.29	-0.05	-0.60
	A4	-0.05	-0.25	-0.64	0.52	-0.25	-0.05	-0.64

Note that: initial longitudinal stress σ_{z0}= -0.1 f'_c remains constant for all these analyses.

Table 5.12: Stress level of bridge with a 9 in. depth and 9 ft girder spacing under varying stiffness ratio to reference girder-Load pattern 3

$E_{gc}I_{gc}/E_{gr}I_{gr}$	Location	S_1	S_2	S_3	Von Misses σ_s	σ_x	σ_y	σ_z
0.5	A1	-0.16	-0.28	-0.62	0.42	-0.26	-0.18	-0.62
	A2	-0.04	-0.26	-0.58	0.47	-0.25	-0.05	-0.58
	A3	-0.04	-0.27	-0.58	0.47	-0.26	-0.05	-0.58
	A4	-0.04	-0.22	-0.61	0.51	-0.22	-0.05	-0.61
1	A1	-0.16	-0.27	-0.61	0.41	-0.25	-0.18	-0.60
	A2	-0.04	-0.25	-0.57	0.46	-0.24	-0.05	-0.57
	A3	-0.04	-0.25	-0.57	0.46	-0.24	-0.05	-0.57
	A4	-0.03	-0.19	-0.60	0.51	-0.19	-0.03	-0.60
2	A1	-0.15	-0.26	-0.60	0.40	-0.24	-0.18	-0.59
	A2	-0.03	-0.24	-0.56	0.46	-0.23	-0.05	-0.56
	A3	-0.04	-0.25	-0.56	0.46	-0.24	-0.05	-0.56
	A4	-0.04	-0.21	-0.59	0.49	-0.21	-0.04	-0.58
5	A1	-0.15	-0.26	-0.59	0.40	-0.24	-0.18	-0.59
	A2	-0.03	-0.23	-0.55	0.45	-0.22	-0.04	-0.55
	A3	-0.03	-0.24	-0.55	0.45	-0.23	-0.05	-0.55
	A4	-0.04	-0.20	-0.58	0.48	-0.20	-0.04	-0.57
10	A1	-0.15	-0.25	-0.59	0.40	-0.23	-0.18	-0.58
	A2	-0.03	-0.22	-0.54	0.45	-0.21	-0.04	-0.54
	A3	-0.03	-0.24	-0.55	0.45	-0.23	-0.04	-0.55
	A4	-0.04	-0.20	-0.57	0.47	-0.20	-0.04	-0.57

Note that: initial longitudinal stress σ_{z0}= -0.1 f'_c remains constant for all these analyses.

Table 5.13: Stress level of bridge with a 9 in. depth and 9 ft girder spacing under varying axle loading-Load pattern 3

Axle loads (kips)	Location	S_1	S_2	S_3	Von Misses σ_s	σ_x	σ_y	σ_z
32	A1	-0.16	-0.27	-0.61	0.41	-0.25	-0.18	-0.60
	A2	-0.04	-0.25	-0.57	0.46	-0.24	-0.05	-0.57
	A3	-0.04	-0.25	-0.57	0.46	-0.24	-0.05	-0.57
	A4	-0.03	-0.19	-0.60	0.51	-0.19	-0.03	-0.60
48	A1	-0.23	-0.40	-0.72	0.43	-0.37	-0.27	-0.71
	A2	-0.06	-0.38	-0.66	0.52	-0.36	-0.07	-0.65
	A3	-0.06	-0.39	-0.65	0.52	-0.37	-0.07	-0.65
	A4	-0.06	-0.32	-0.70	0.56	-0.32	-0.07	-0.69
60	A1	-0.29	-0.50	-0.81	0.45	-0.47	-0.34	-0.78
	A2	-0.07	-0.47	-0.72	0.57	-0.46	-0.09	-0.72
	A3	-0.07	-0.49	-0.72	0.57	-0.47	-0.09	-0.72
	A4	-0.07	-0.40	-0.78	0.61	-0.40	-0.09	-0.77
72	A1	-0.34	-0.59	-0.90	0.48	-0.56	-0.41	-0.86
	A2	-0.08	-0.57	-0.79	0.63	-0.55	-0.11	-0.78
	A3	-0.09	-0.58	-0.79	0.63	-0.56	-0.11	-0.78
	A4	-0.09	-0.47	-0.86	0.67	-0.48	-0.10	-0.84

Note that: initial longitudinal stress σ_{z0}= -0.1 f'_c remains constant for all these analyses.

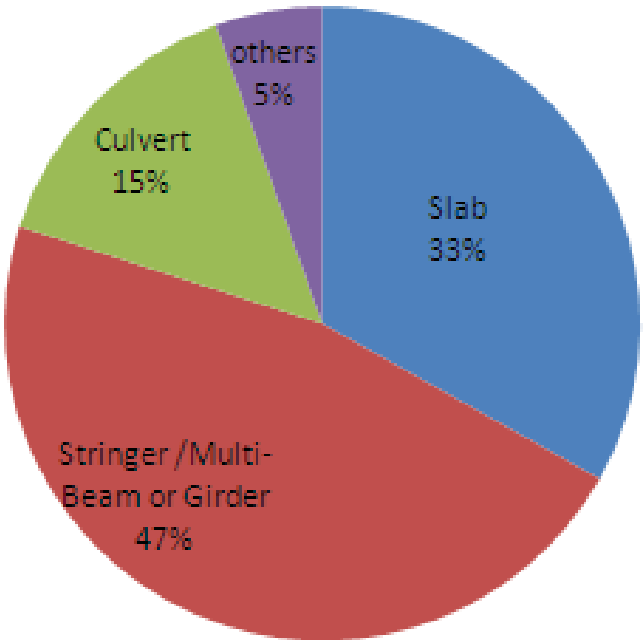

Figure 5.1: Percentile proportion of bridge types in Wisconsin at 2010 (FHWA)

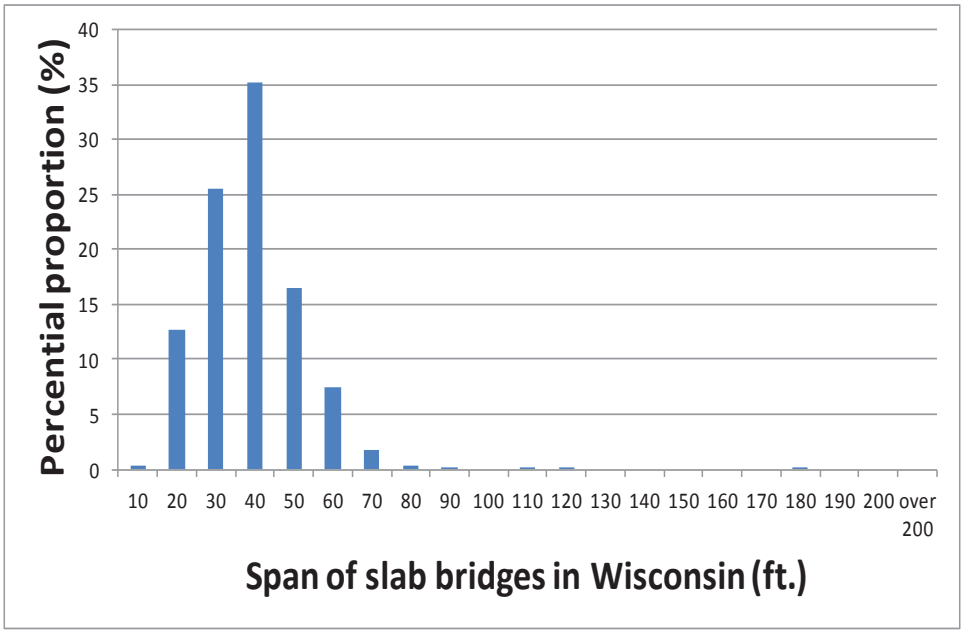

Figure 5.2: Percentile proportions of span of the slab bridges in Wisconsin

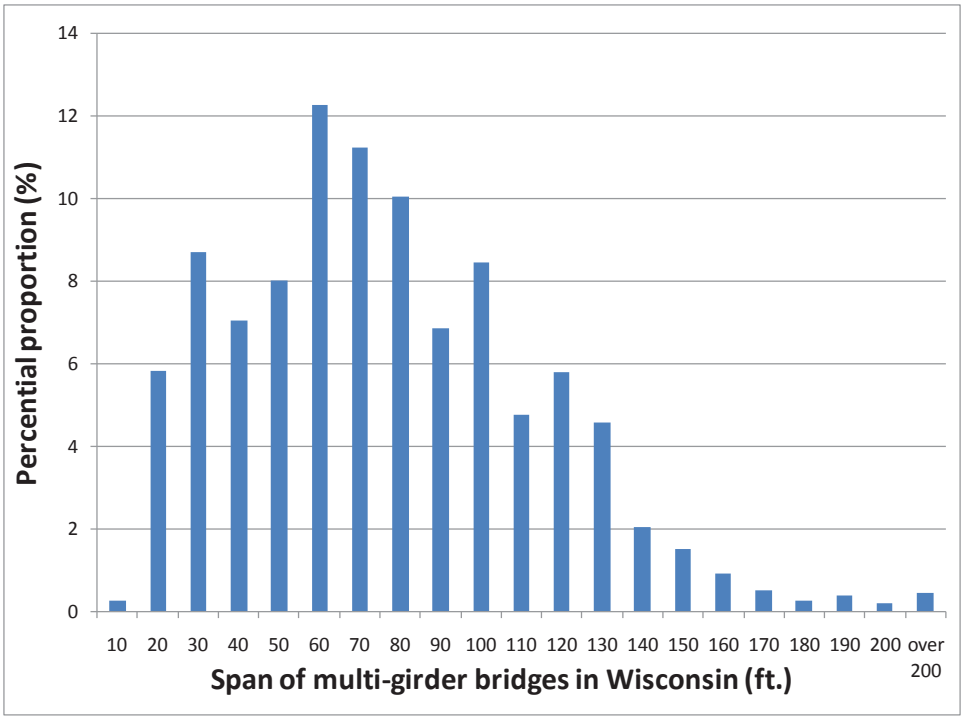

Figure 5.3: Percentile proportions of span of the multi-girder bridges in Wisconsin

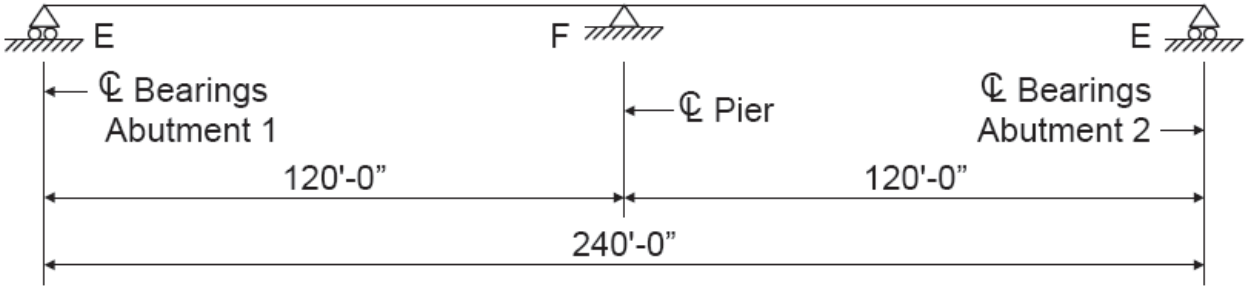

(a) A two-equal-span continuous bridge (WisDOT, 2009)

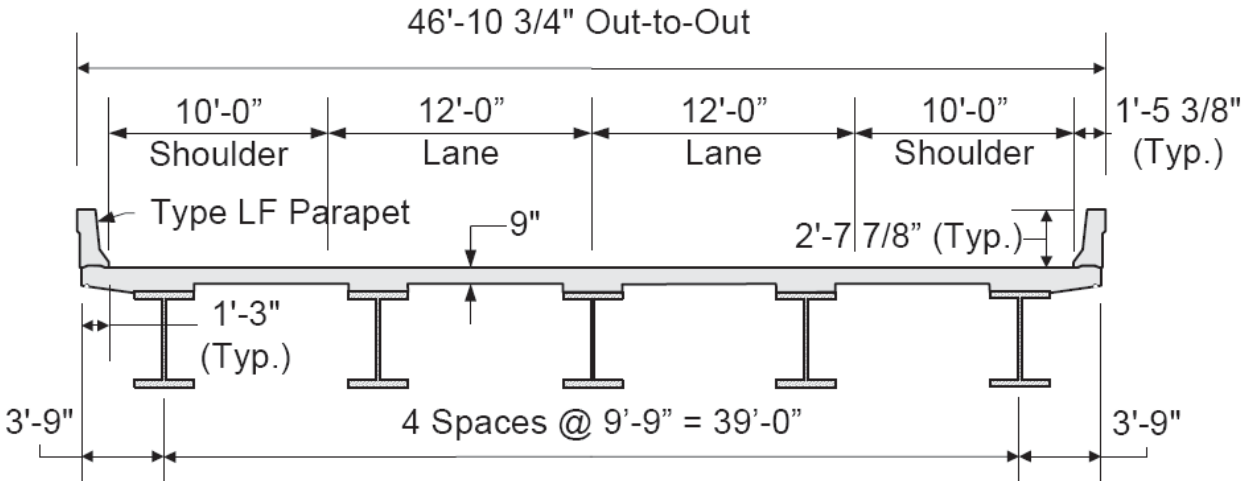

(b) Superstructure cross section (WisDOT, 2009)

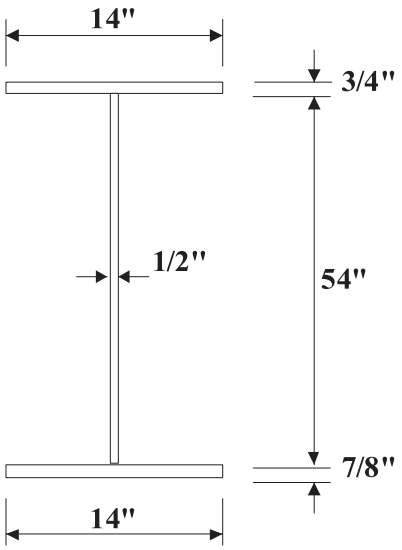

(c) Cross section of steel plate girder through the whole span (not to scale)

Figure 5.4: Design example in WisDOT design manual

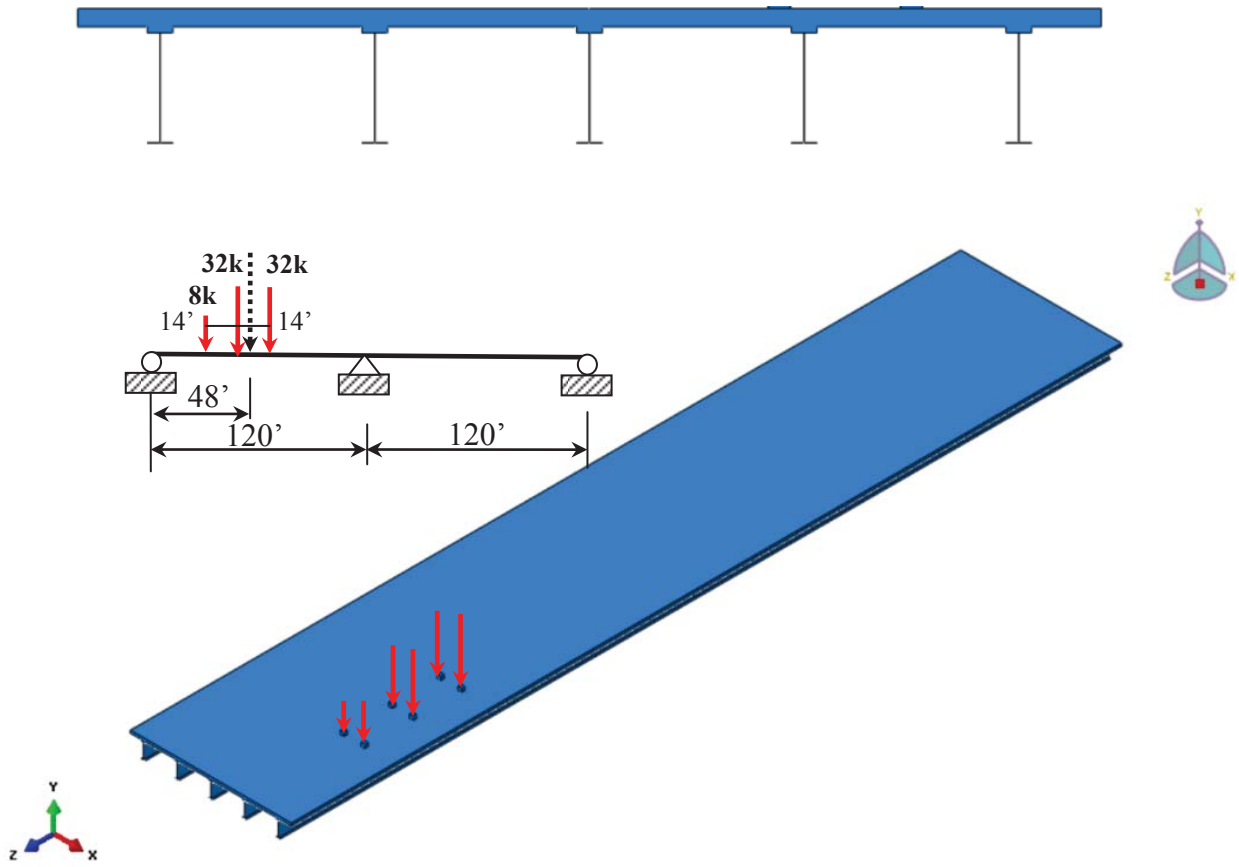

(d) Finite element bridge configuration model

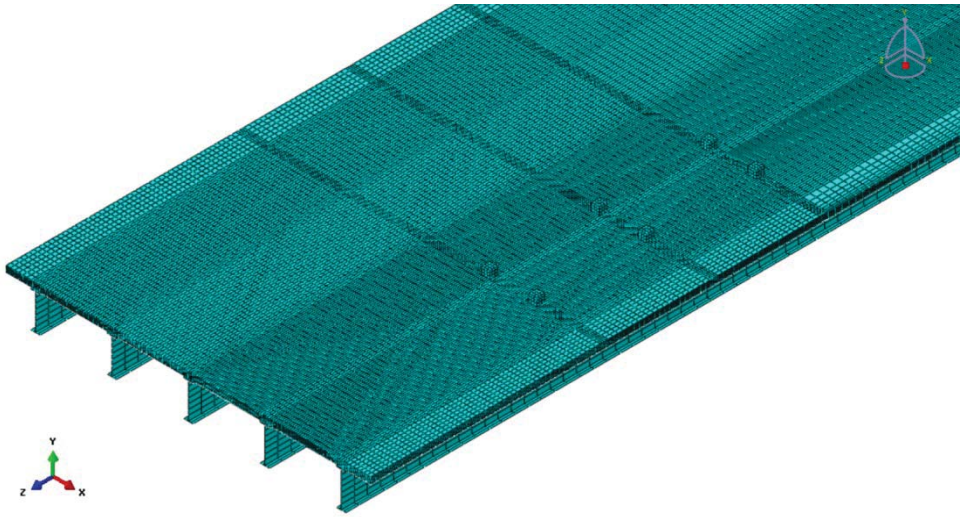

(e) Meshing scheme (214896 solid elements for deck slab and 10800 shell elements for girders)

Figure 5.5: Modeling the example bridge

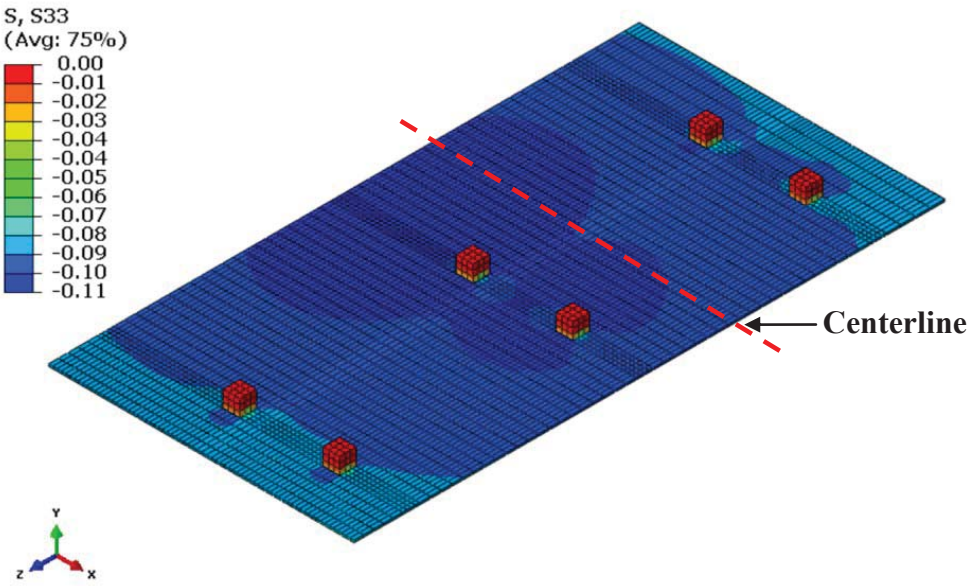

(a) Stress contour map (ksi)

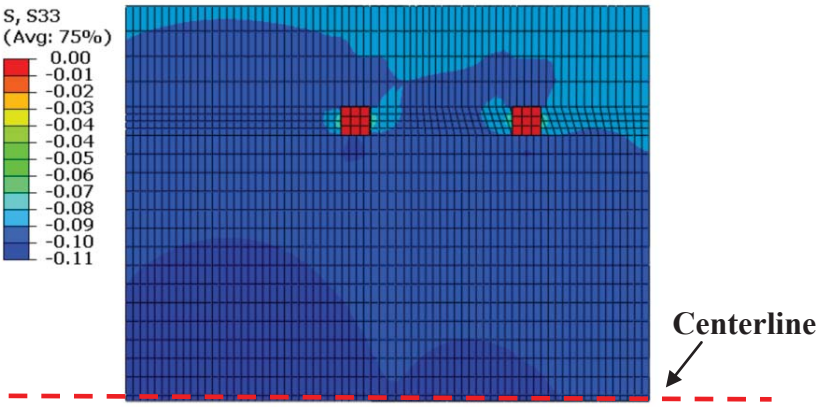

(b) Stress contour map at the centerline of design truck of 48 ft from the left end (ksi)

Figure 5.6: Stress distribution under parapet and future wearing loading

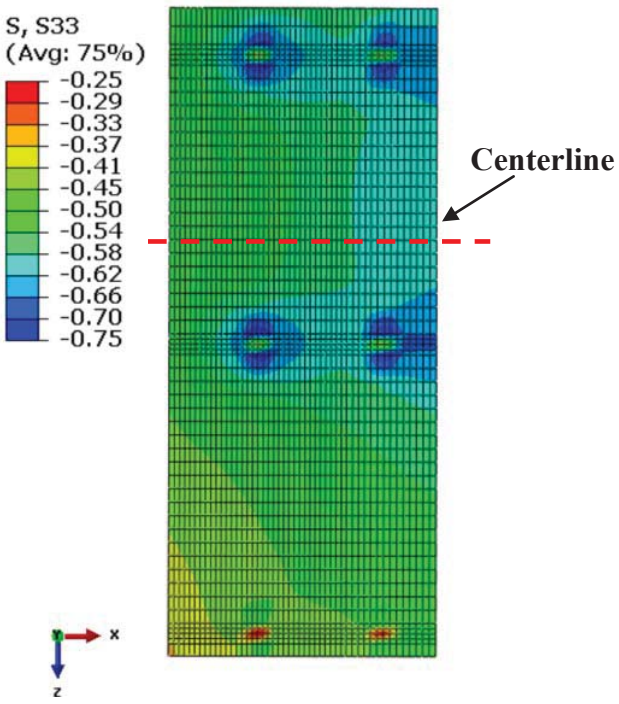

(a) Stress contour map (ksi)

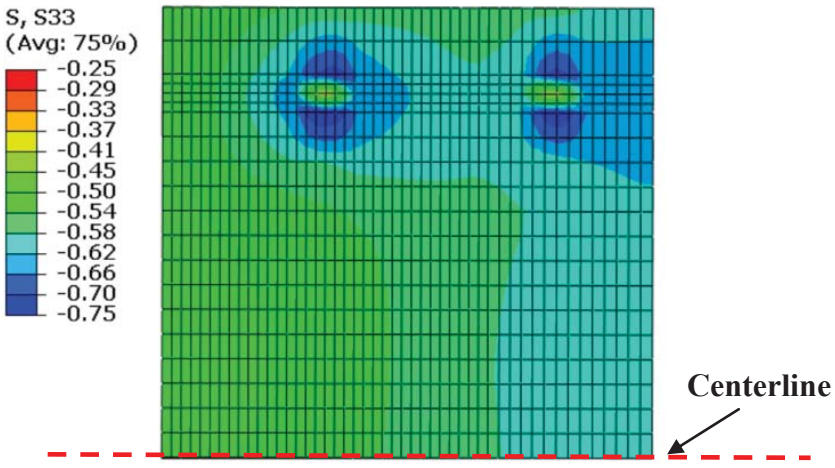

(b) Stress contour map at the centerline of design truck of 48 ft from the left end (ksi)

Figure 5.7: Stress distribution under design truck and design lane loading

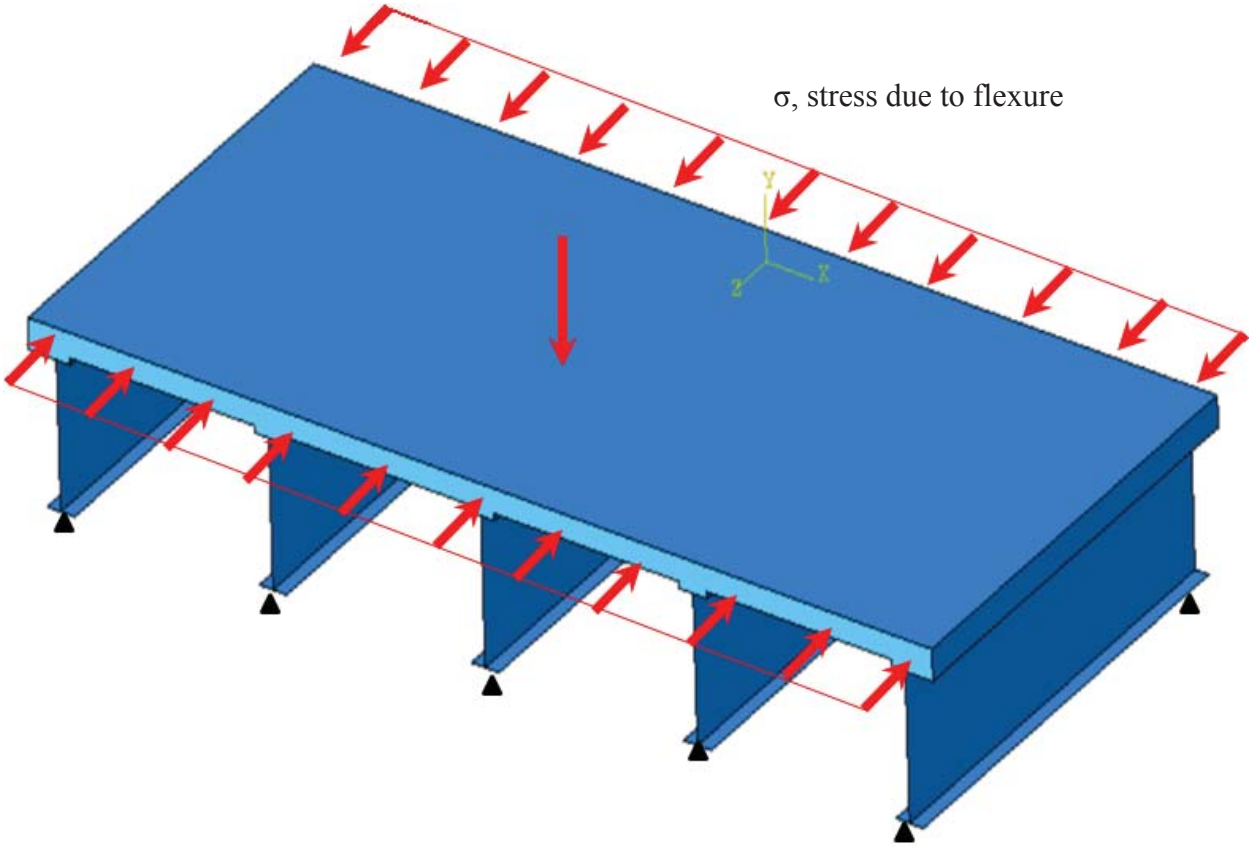

Figure 5.8: Concept of idealized bridge model

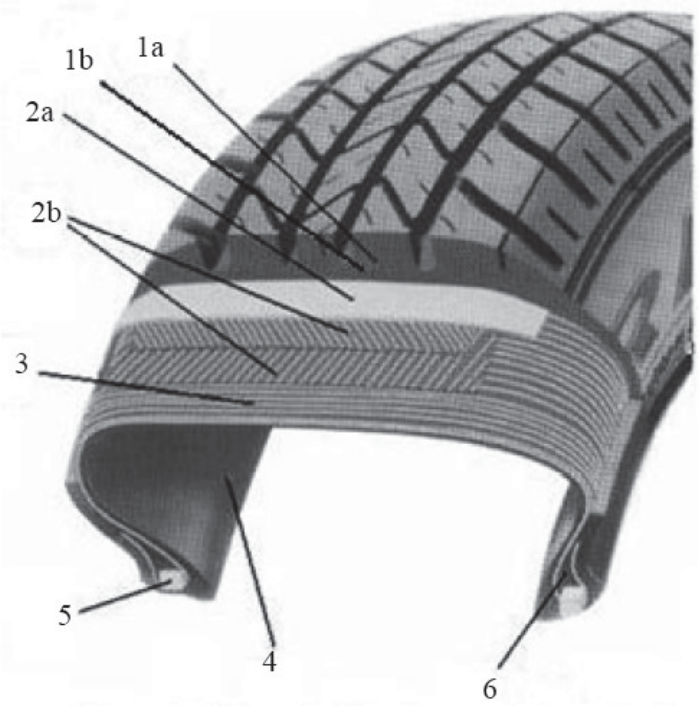

Elements of the radial tire: *1a* – protector part with a pattern, *1b* – continuous protector part, *2b* – breaker, *2b* – breaker, *3* – radial ply, *4* – inner sealing layer, *5* – fixing ring, *6* – sidewall belts

(a)

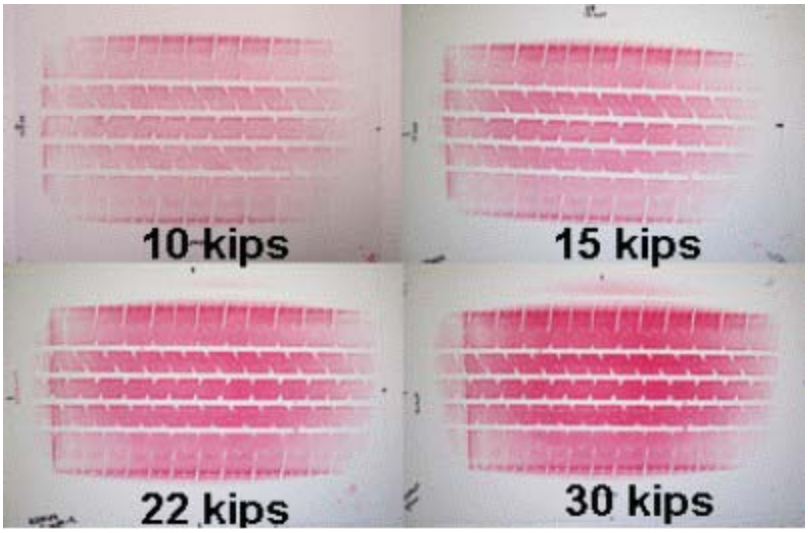

(b)

Figure 5.9: A typical tire structure (a) components (Sapragonas and Dargužis, 2011); (b) footprint of tire under varying loading (Majumdar et al., 2007).

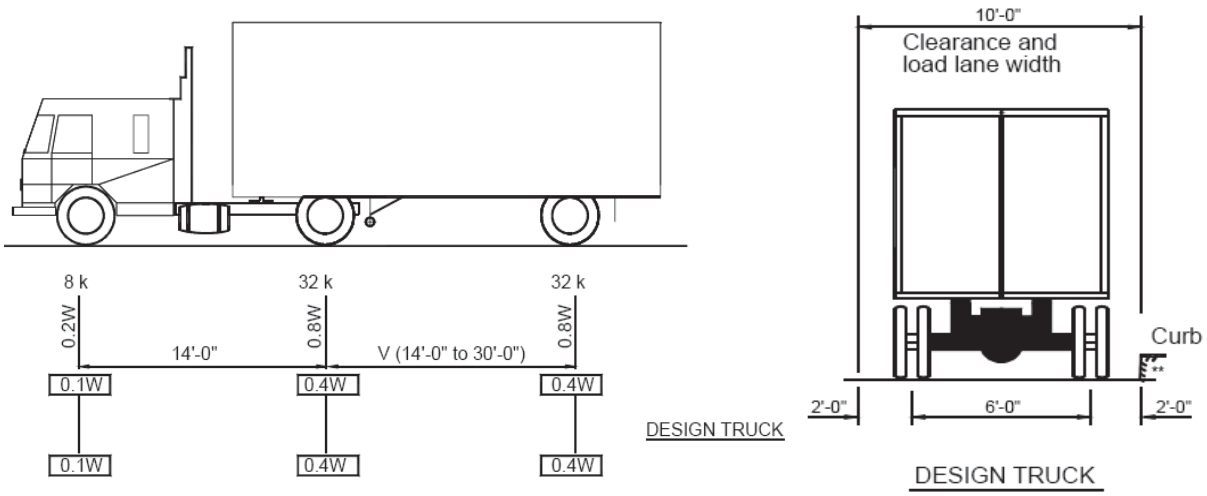

(a) AASHTO Design truck (AASHTO, 2010)

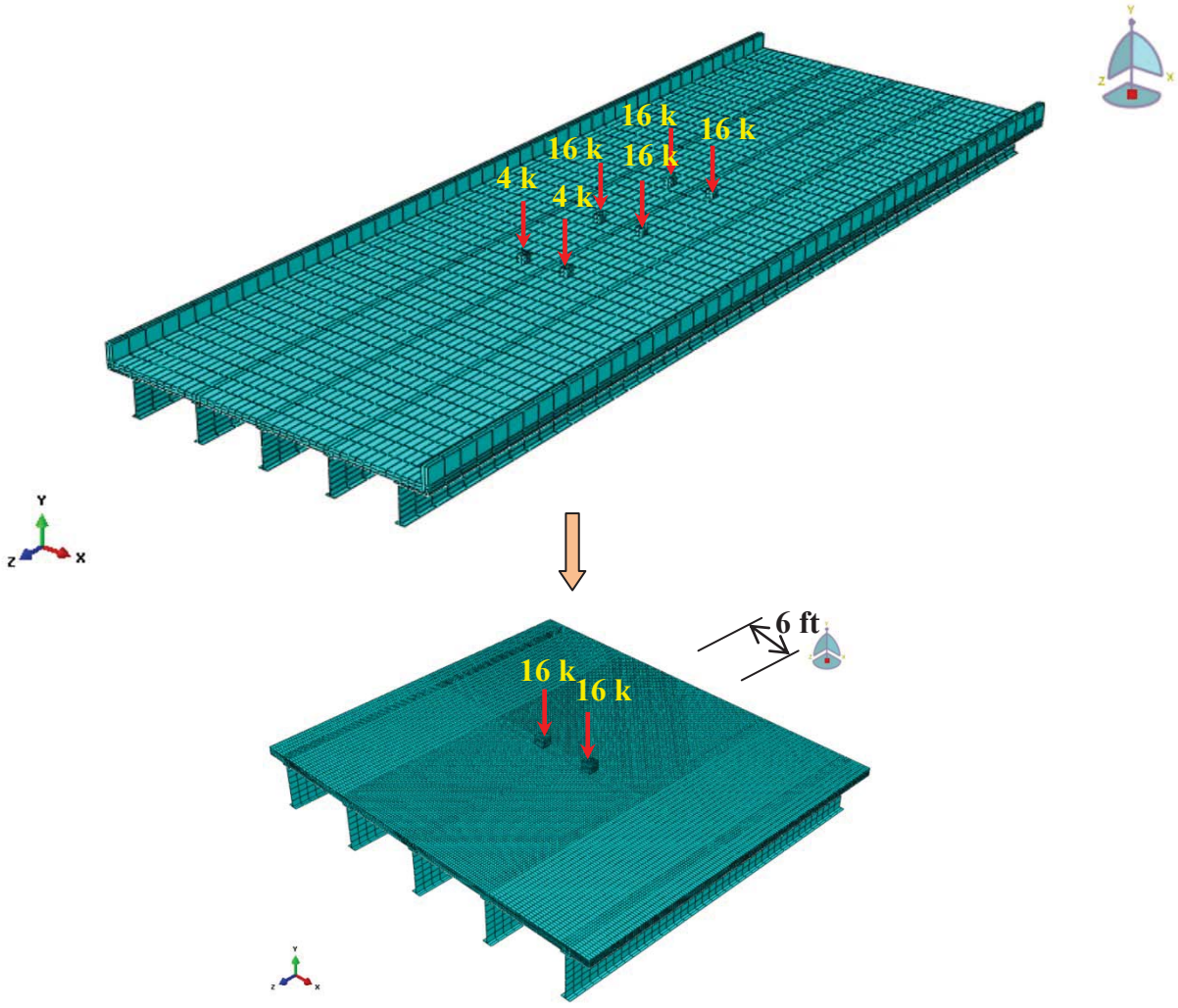

(b) Idealized loading

Figure 5.10: Design truck and simplified axle loading

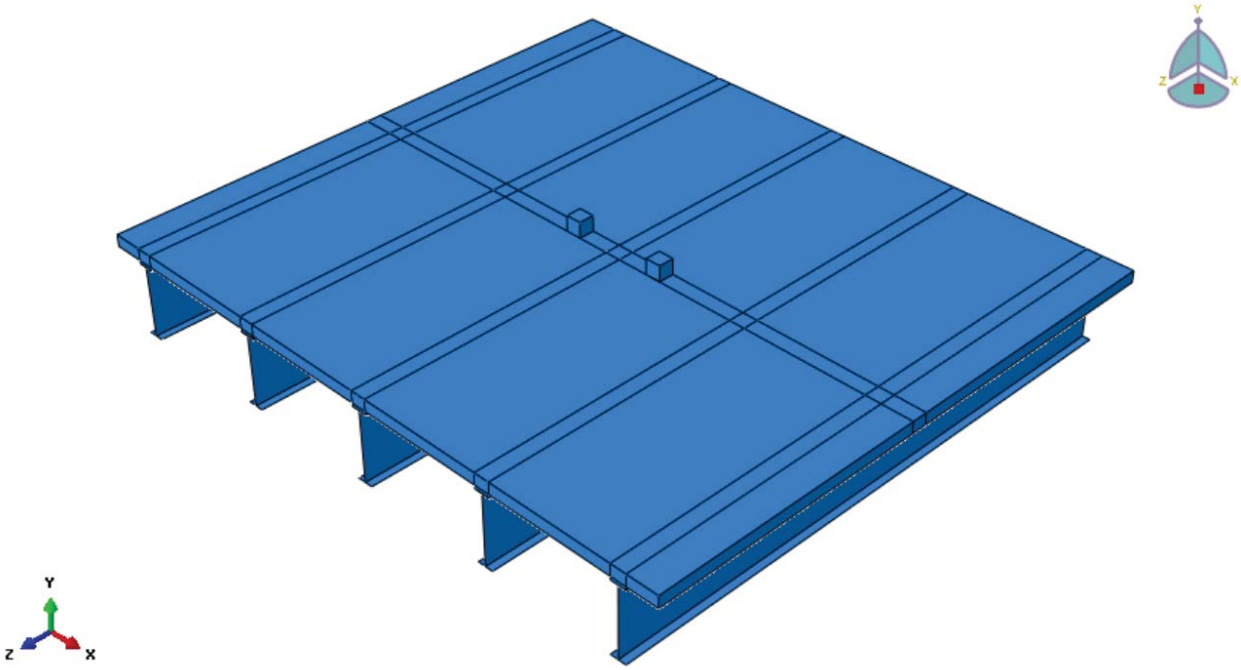

(a) Geometrical model

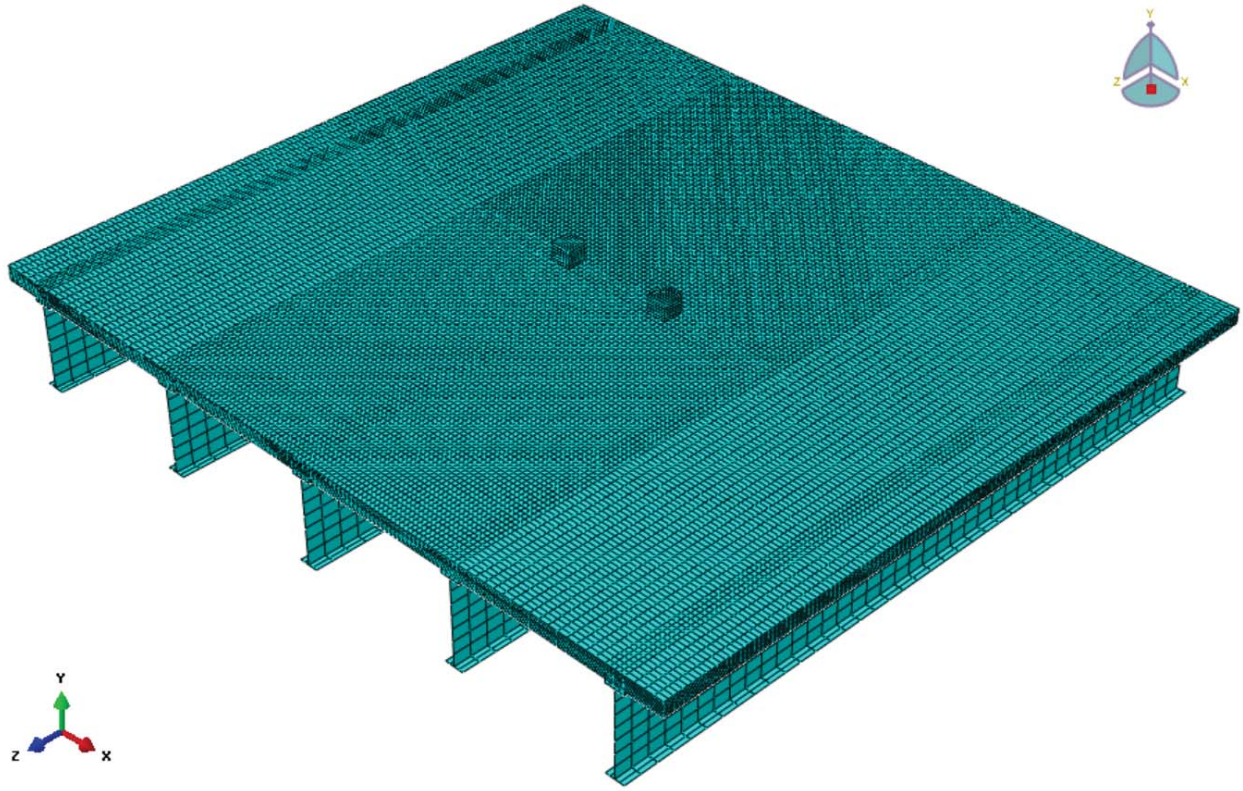

(b) Meshing scheme nearby the loading

Figure 5.11: Multi-girder bridge superstructure model

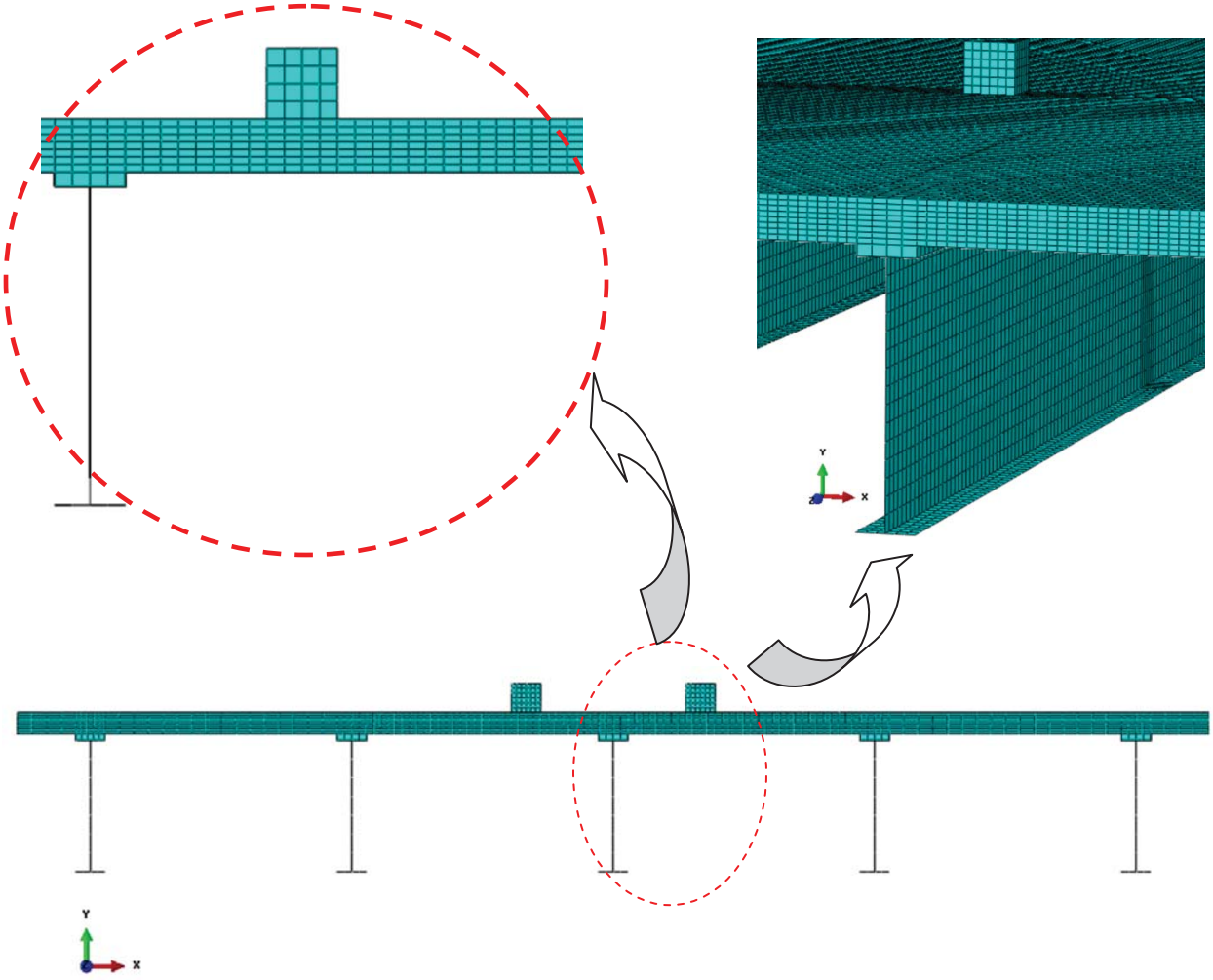

Figure 5.12: Bridge finite element model in details

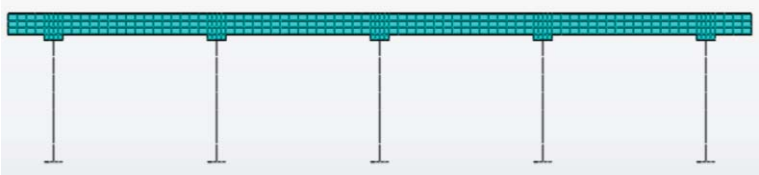

(a) Idealized four-span continuous beam

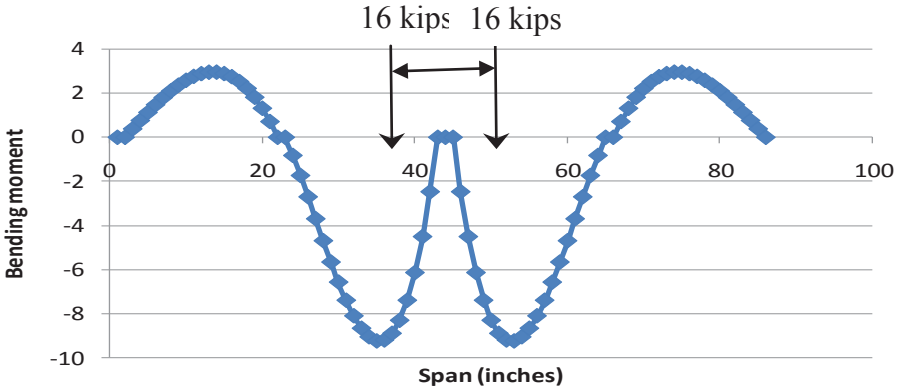

(b) Load pattern 1

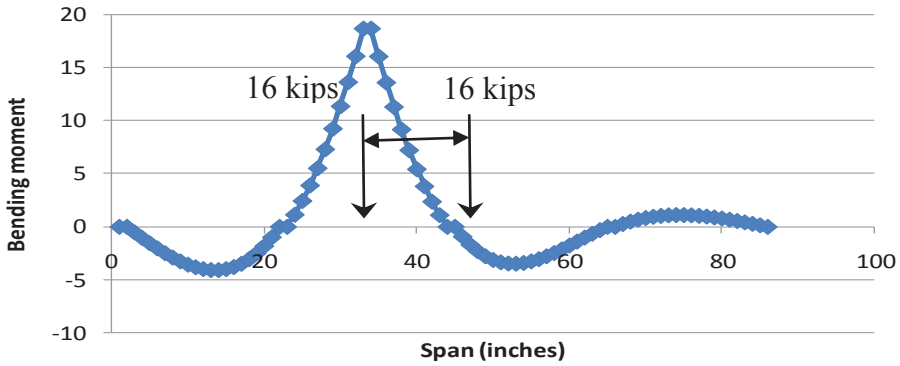

(c) Load pattern 2

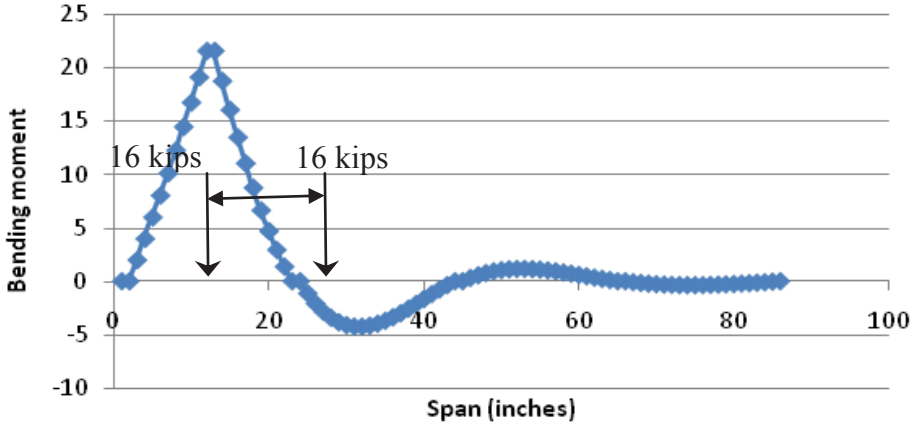

(d) Load pattern 3

Figure 5.13: Load patterns for bridge deck analysis based on influence line

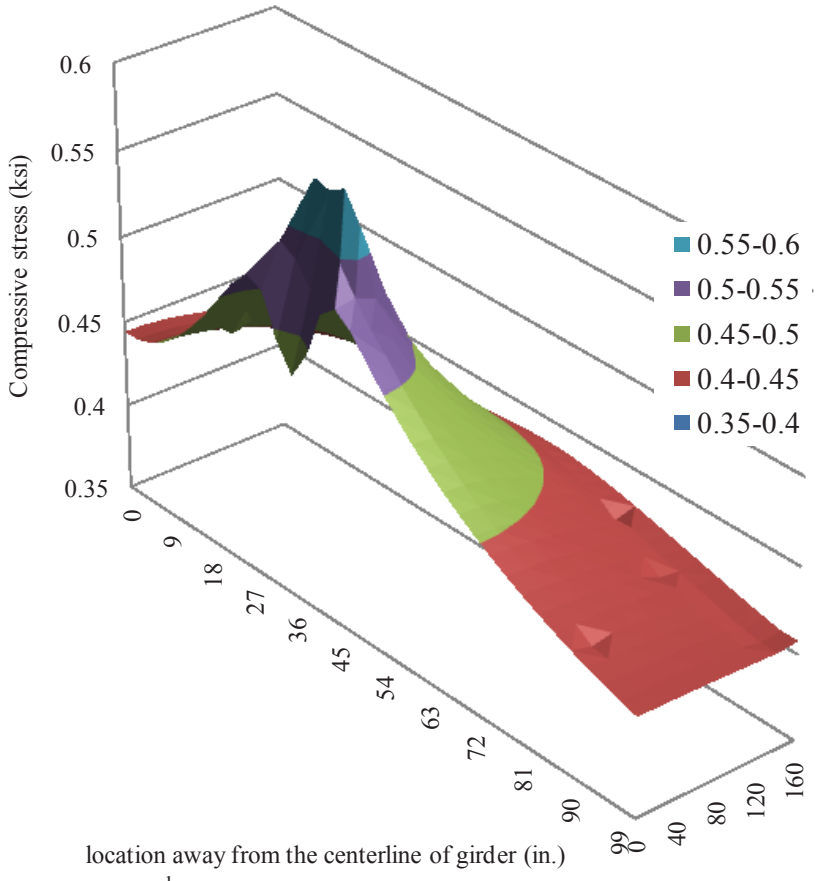

(a) 3rd principal stress contour around the loading

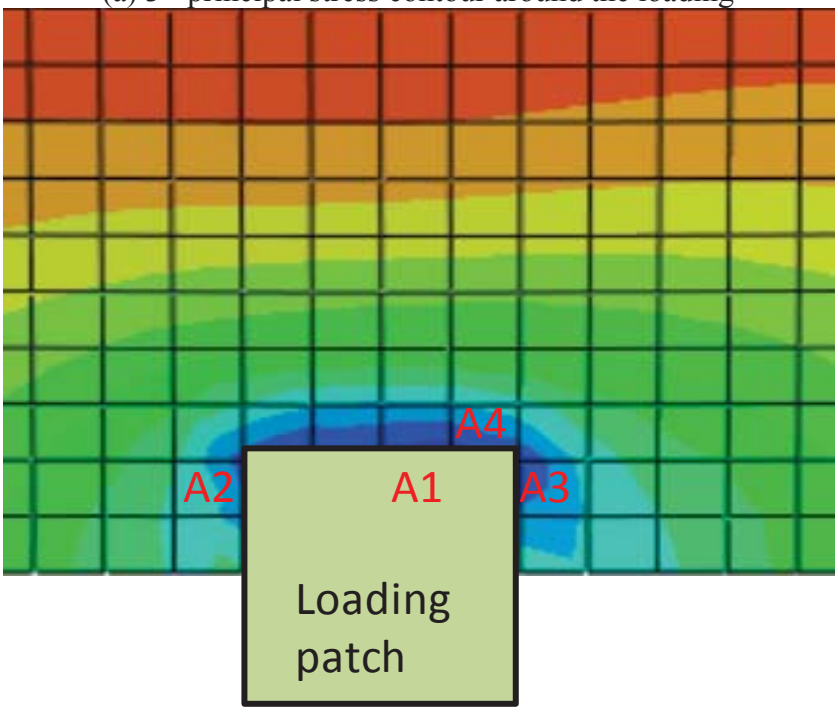

(b) Location picked up for stress analysis

Figure 5.14: Stress concentrated around the loading location(the 3rd principal stress)

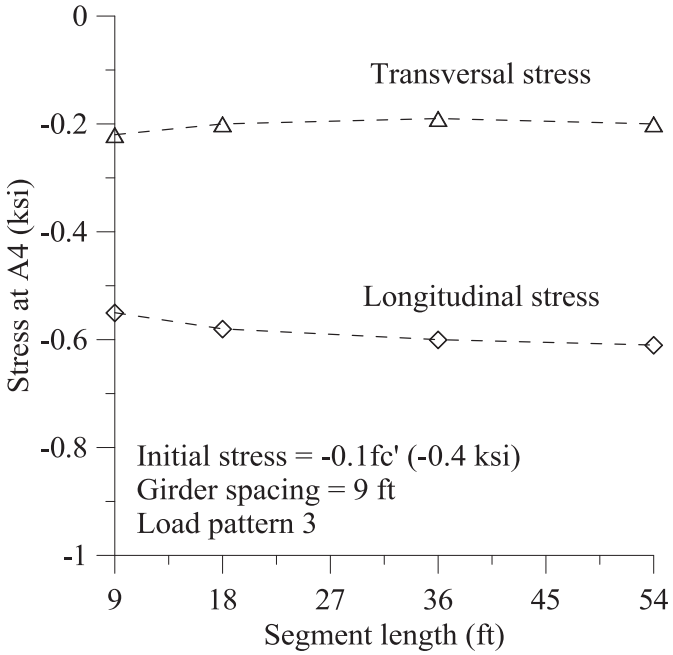

(a) Stress A4

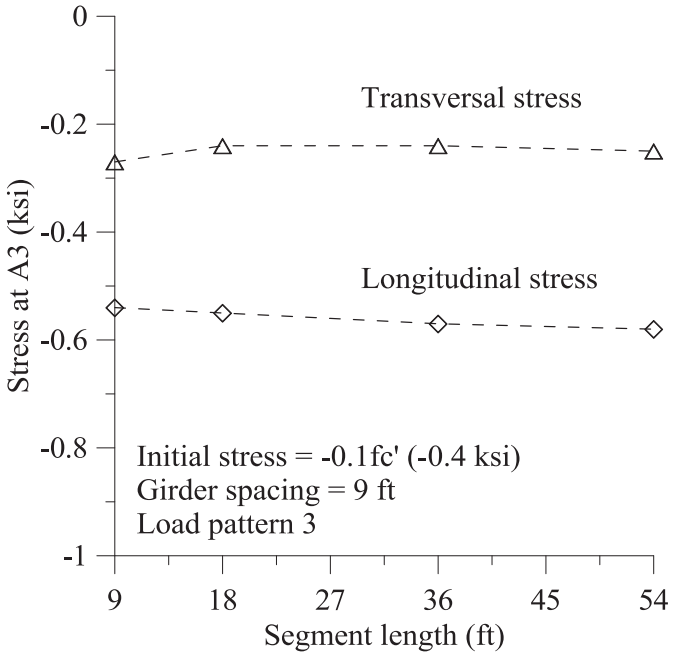

(b) Stress A3

Figure 5.15: Varying segment length on the longitudinal stress

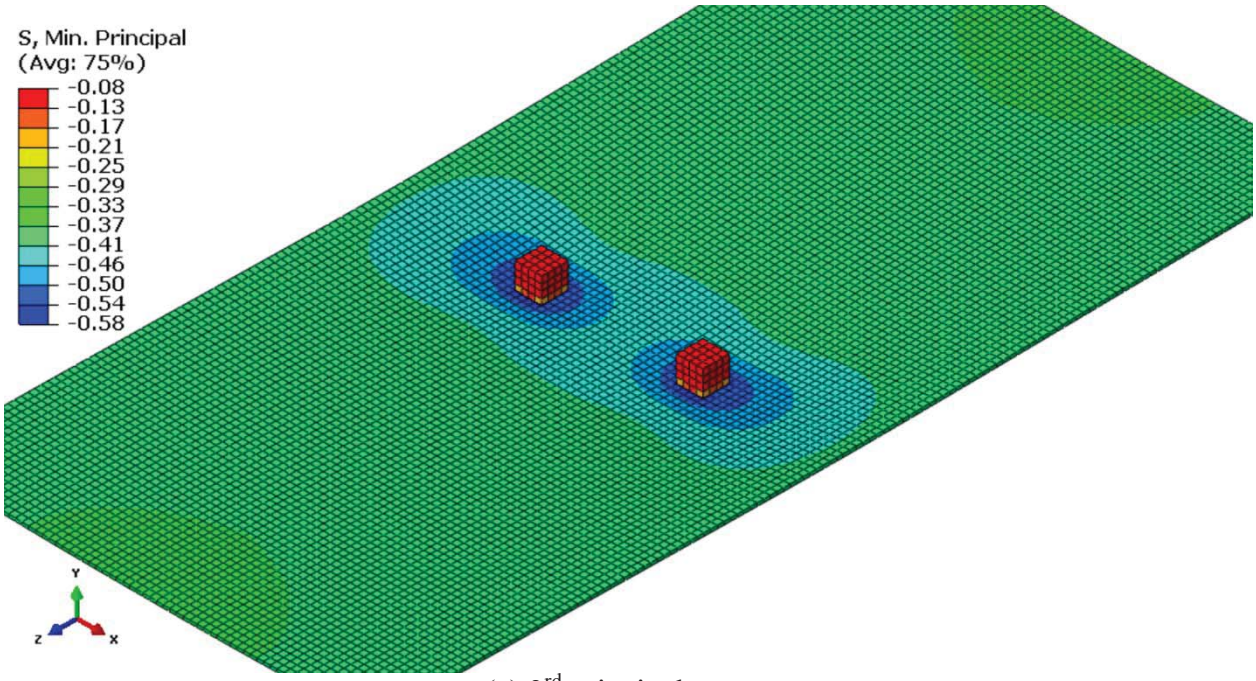

(a) 3rd principal stress

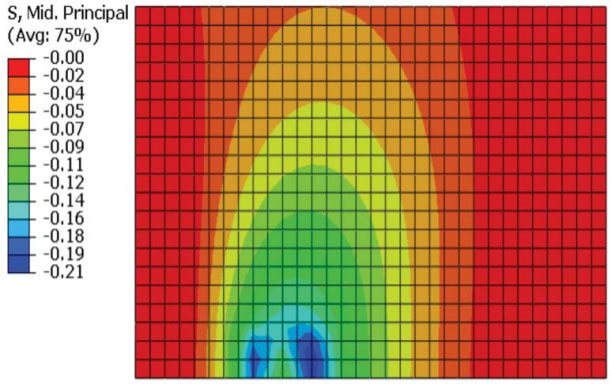

(b) 2nd principal stress

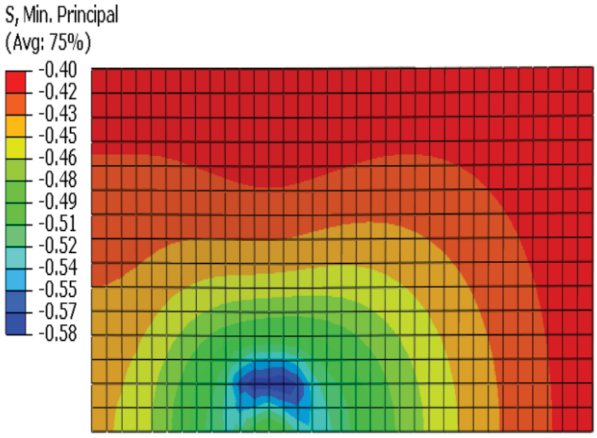

(c) 3rd principal stress

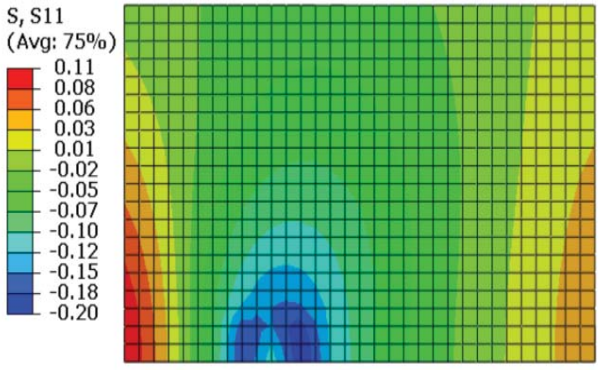

(d) Transversal normal stress σ_x

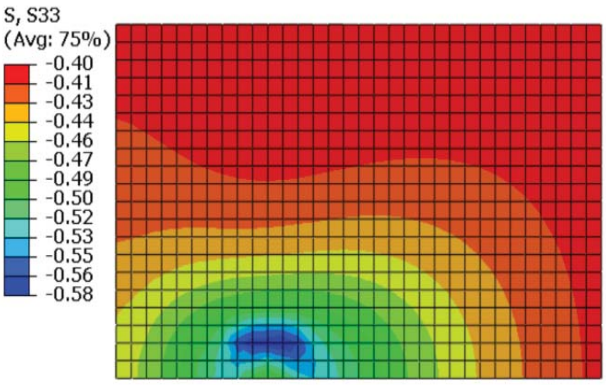

(e) Longitudinal normal stress σ_z

Figure 5.16: Stress contour in BD_9_9-7 (ksi)

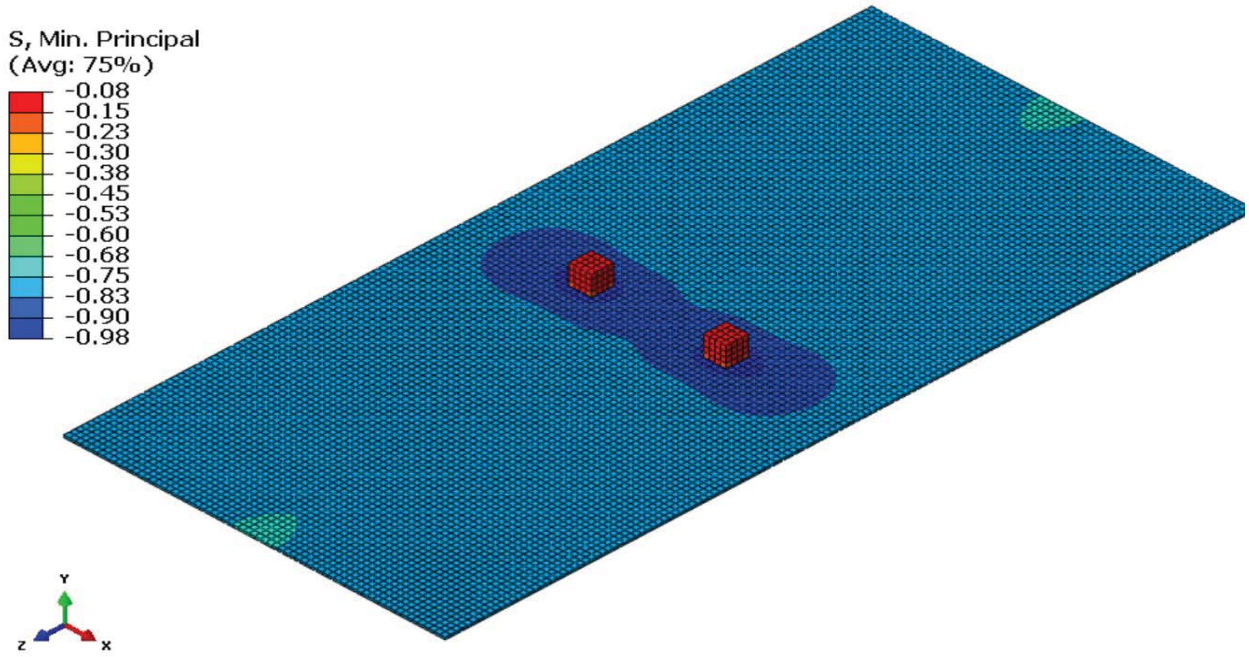

(a) 3rd principal stress

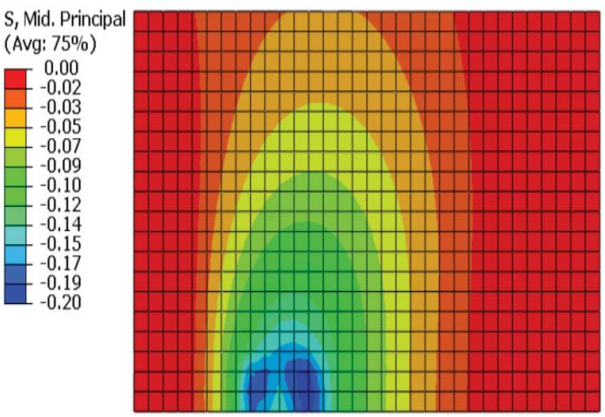

(b) 2nd principal stress

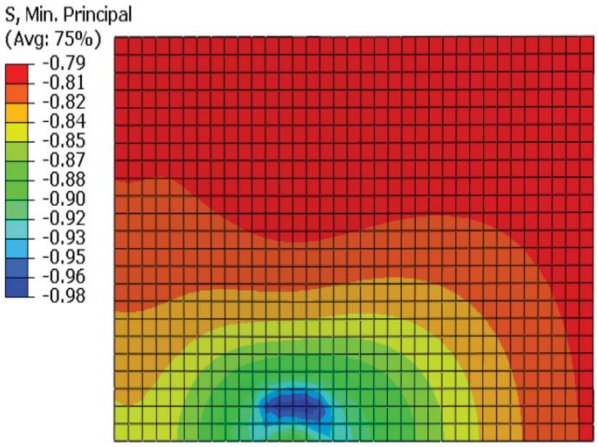

(c) 3rd principal stress

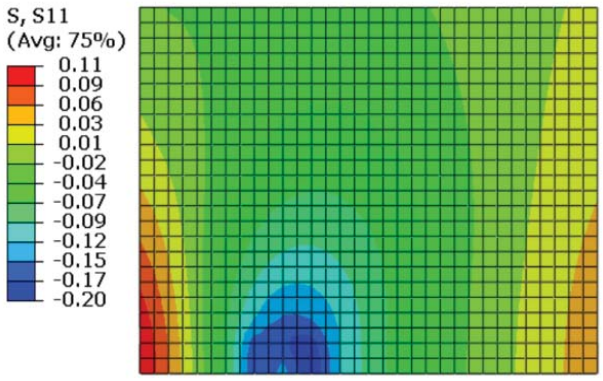

((d) Transversal normal stress σ_x

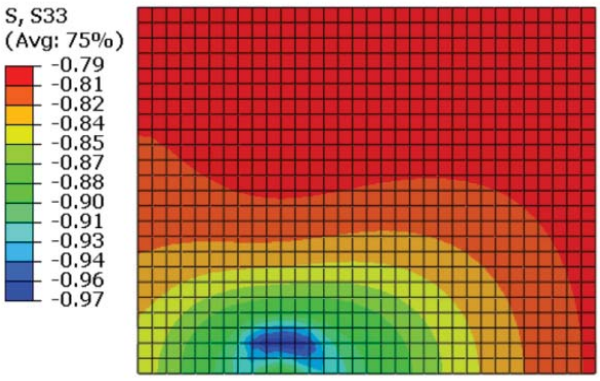

(e) Longitudinal normal stress σ_z

Figure 5.17: Stress contour in BD_9_9-8 (ksi)

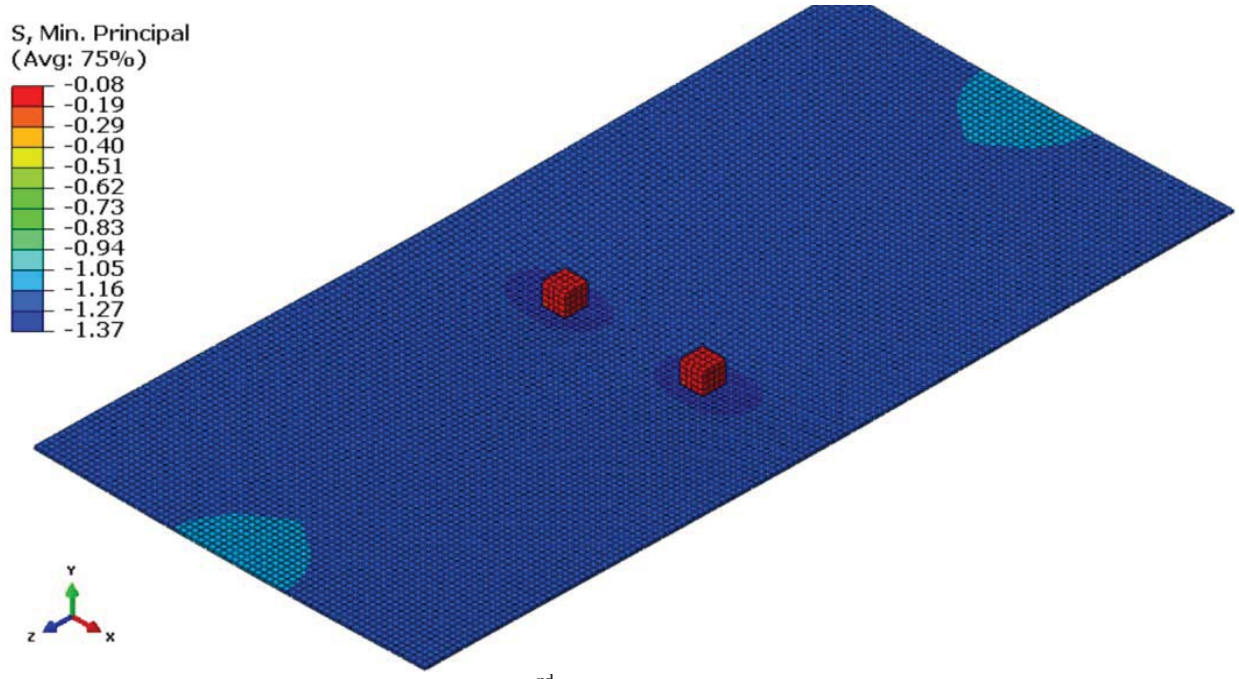

(a) 3rd principal stress

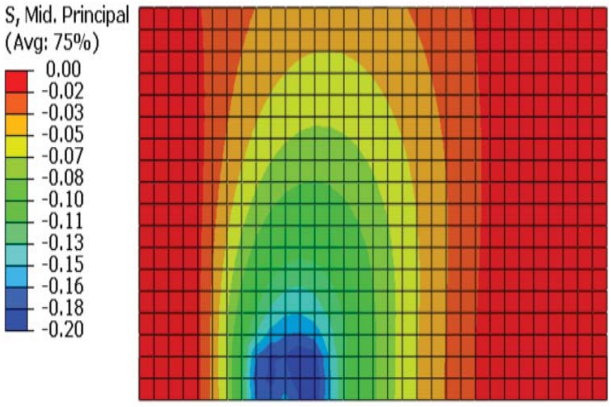

(b) 2nd principal stress

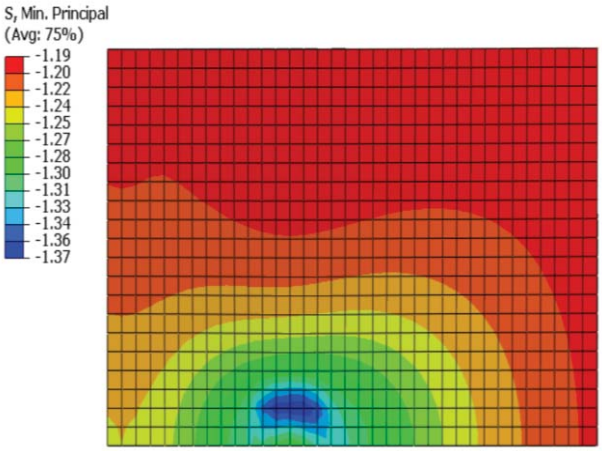

(c) 3rd principal stress

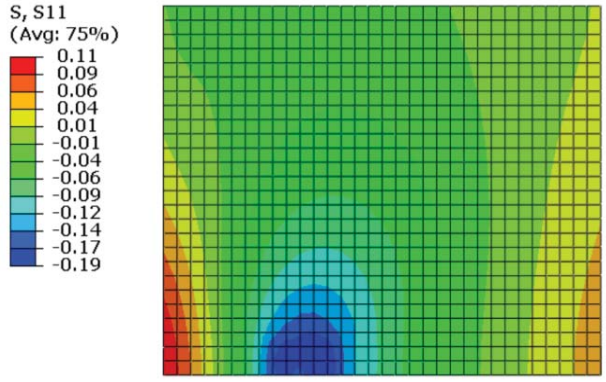

(d) Transversal normal stress σ_x

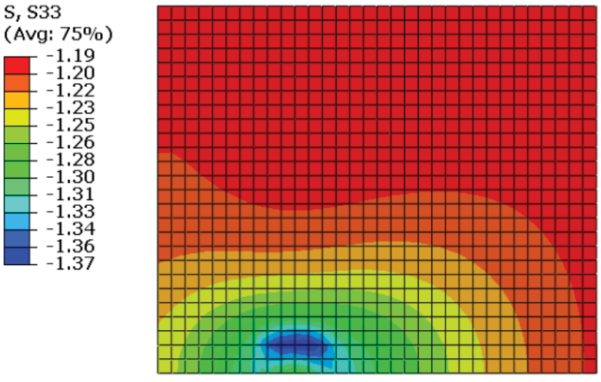

(e) Longitudinal normal stress σ_z

Figure 5.18: Stress contour in BD_9_9-9 (ksi)

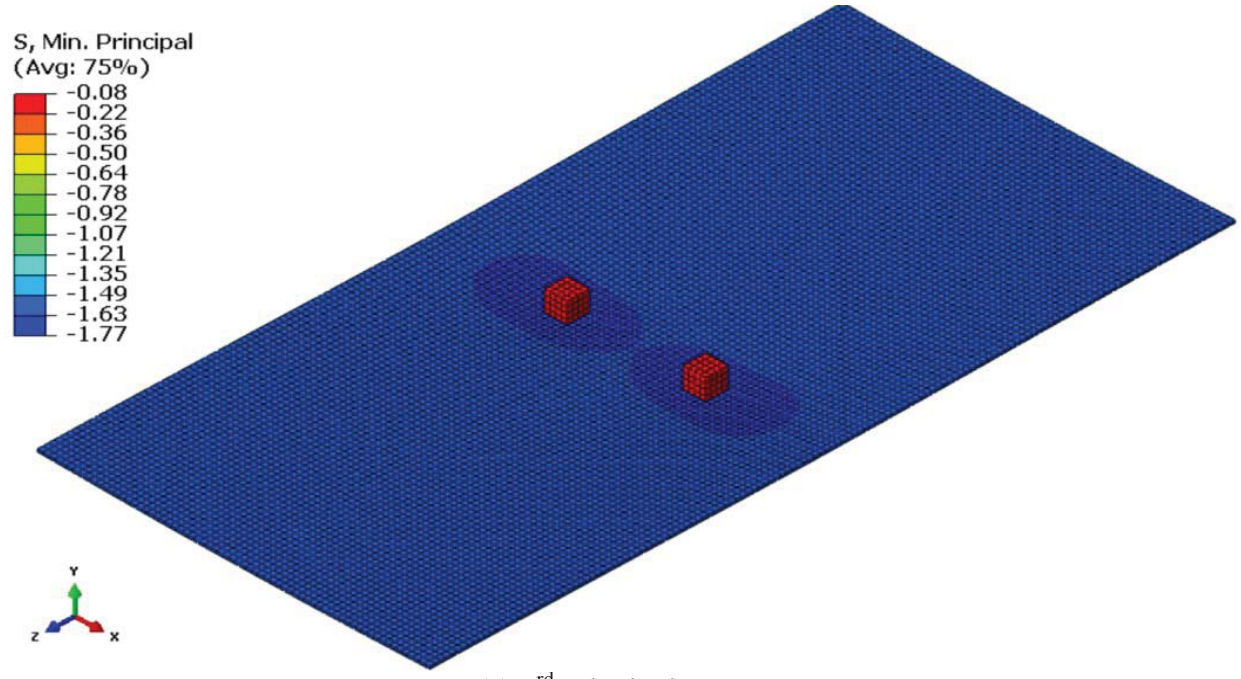

(a) 3rd principal stress

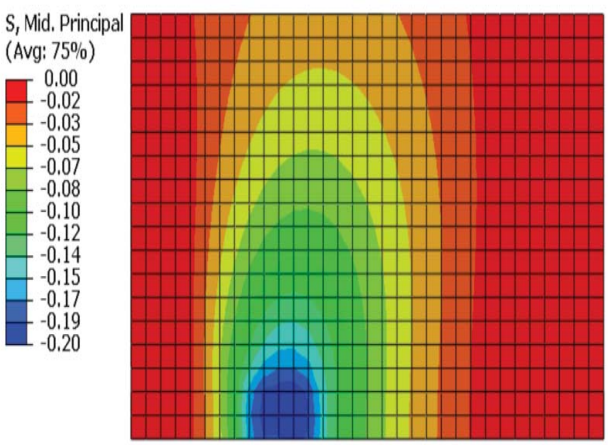

(b) 2nd principal stress

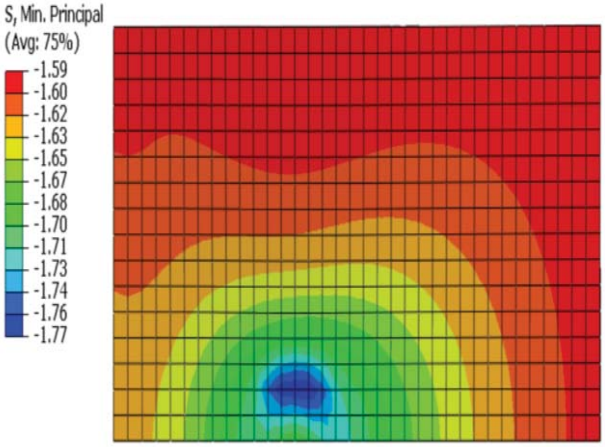

(c) 3rd principal stress

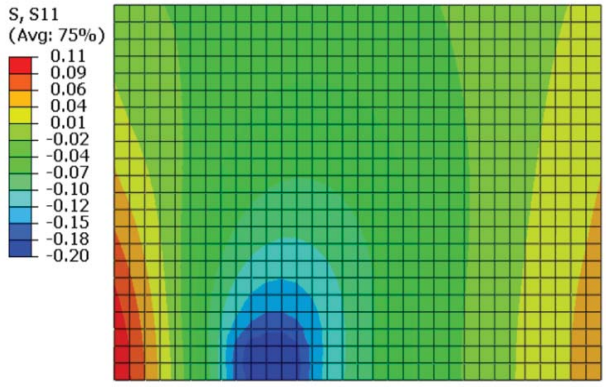

(d) Transversal normal stress σ_x

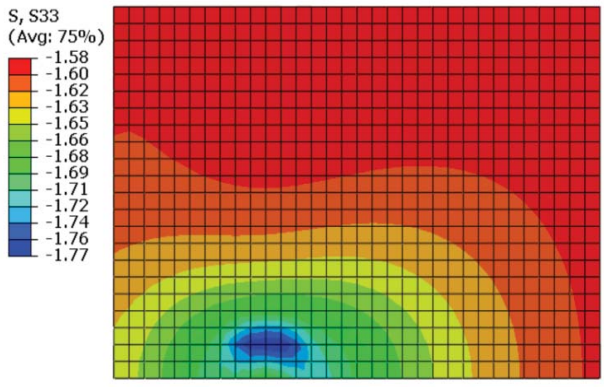

(e) Longitudinal normal stress σ_z

Figure 5.19: Stress contour in BD_9_9-10 (ksi)

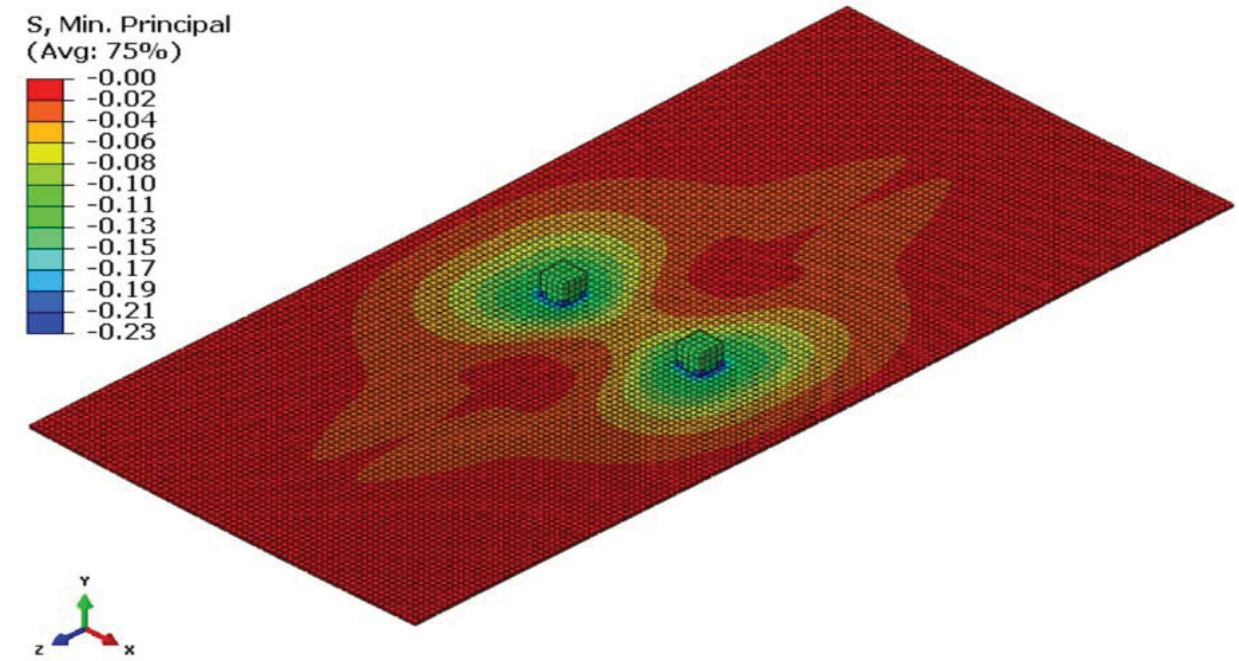

(a) 3rd principal stress

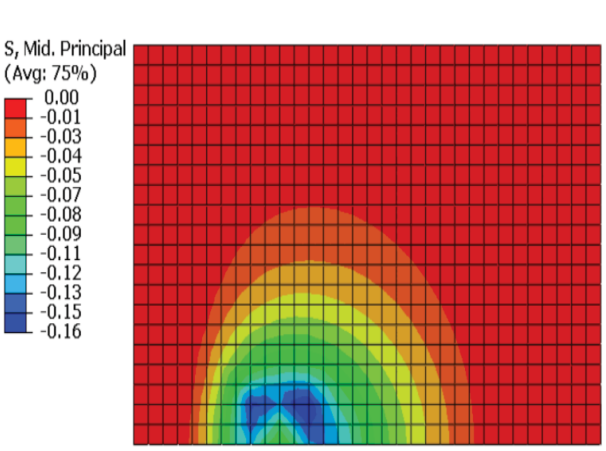

(b) 2nd principal stress

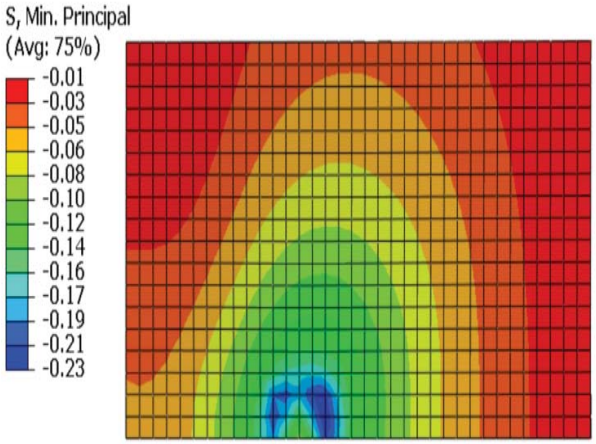

(c) 3rd principal stress

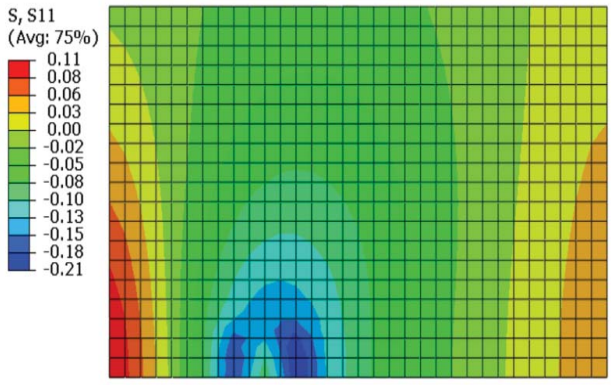

(d) Transversal normal stress σ_x

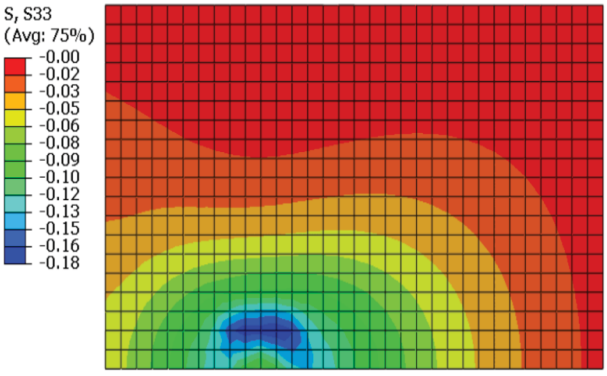

(e) Longitudinal normal stress σ_z

Figure 5.20: Stress contour in BD_9_9-6 (ksi)

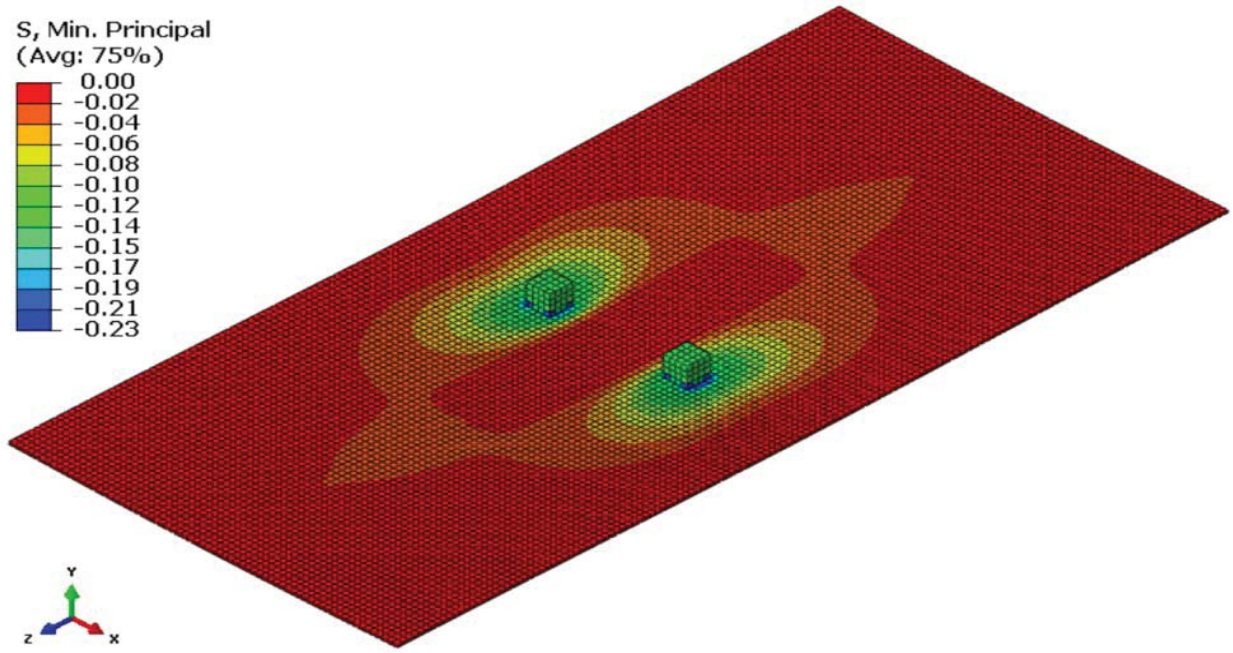

(a) 3rd principal stress

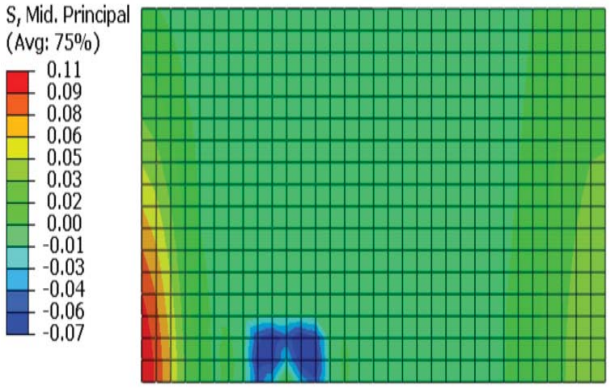

(b) 2nd principal stress

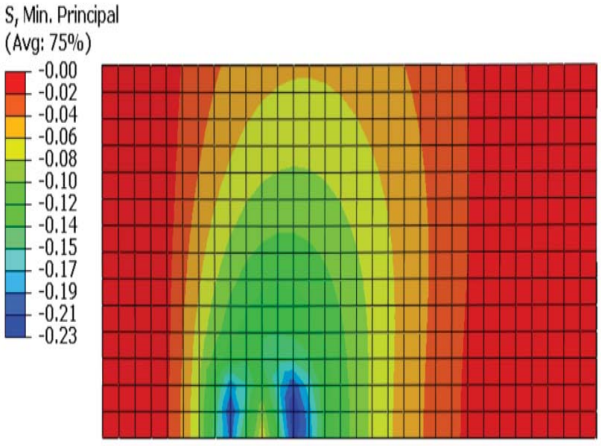

(c) 3rd principal stress

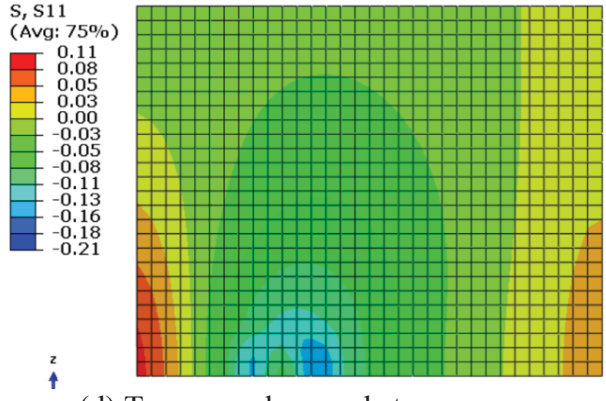

(d) Transversal normal stress σ_x

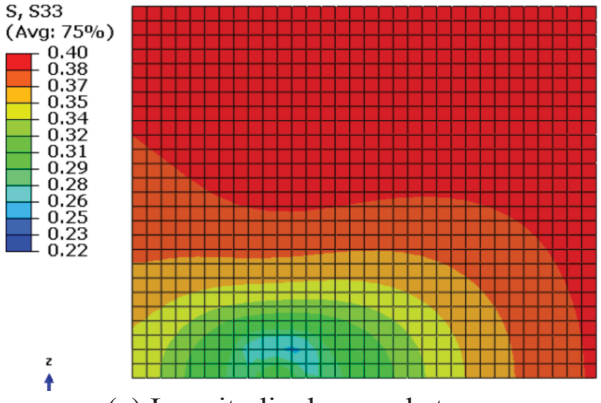

(e) Longitudinal normal stress σ_z

Figure 5.21: Stress contour in BD_9_9-5 (ksi)

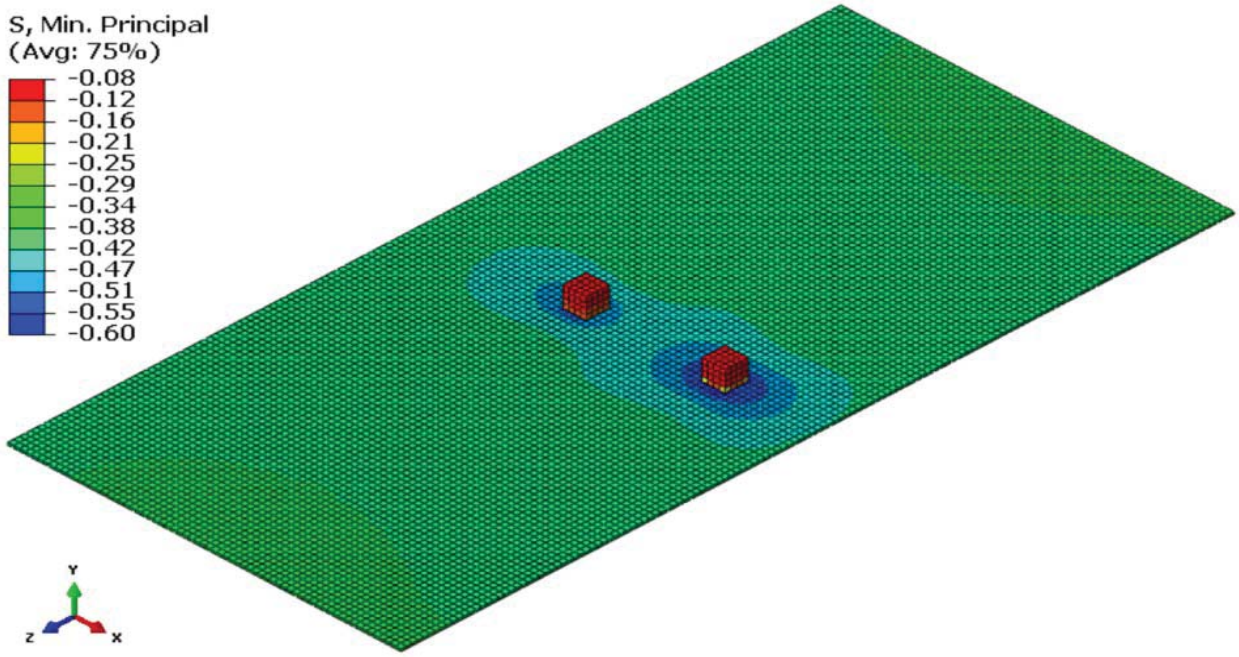

(a) 3rd principal stress

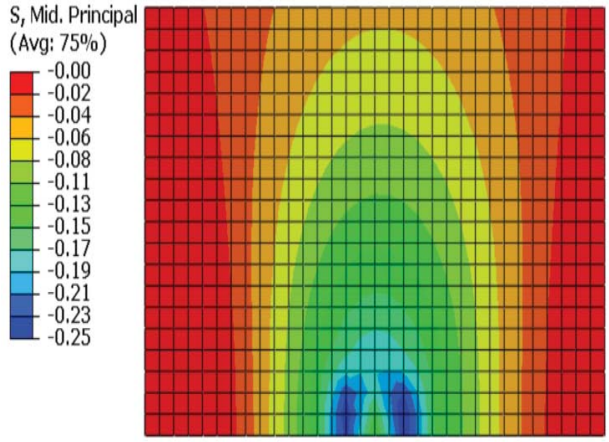

(b) 2nd principal stress

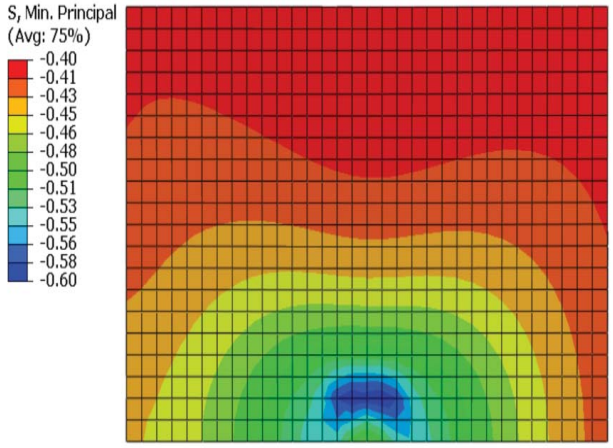

(c) 3rd principal stress

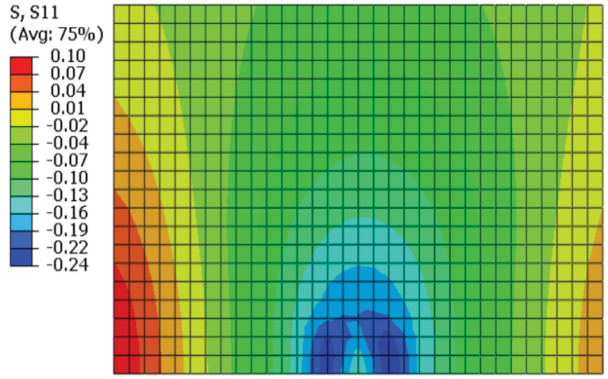

((d) Transversal normal stress σ_x

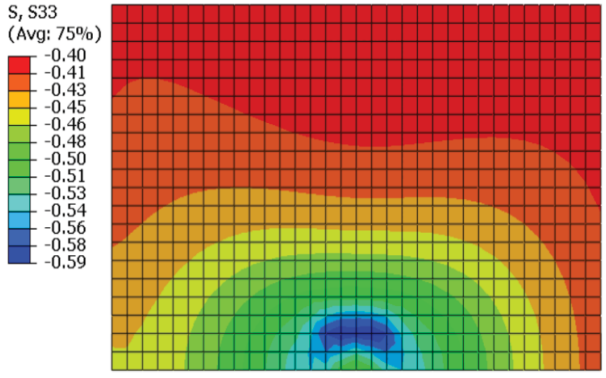

(e) Longitudinal normal stress σ_z

Figure 5.22: Stress contour in BD_9_9-3 (ksi)

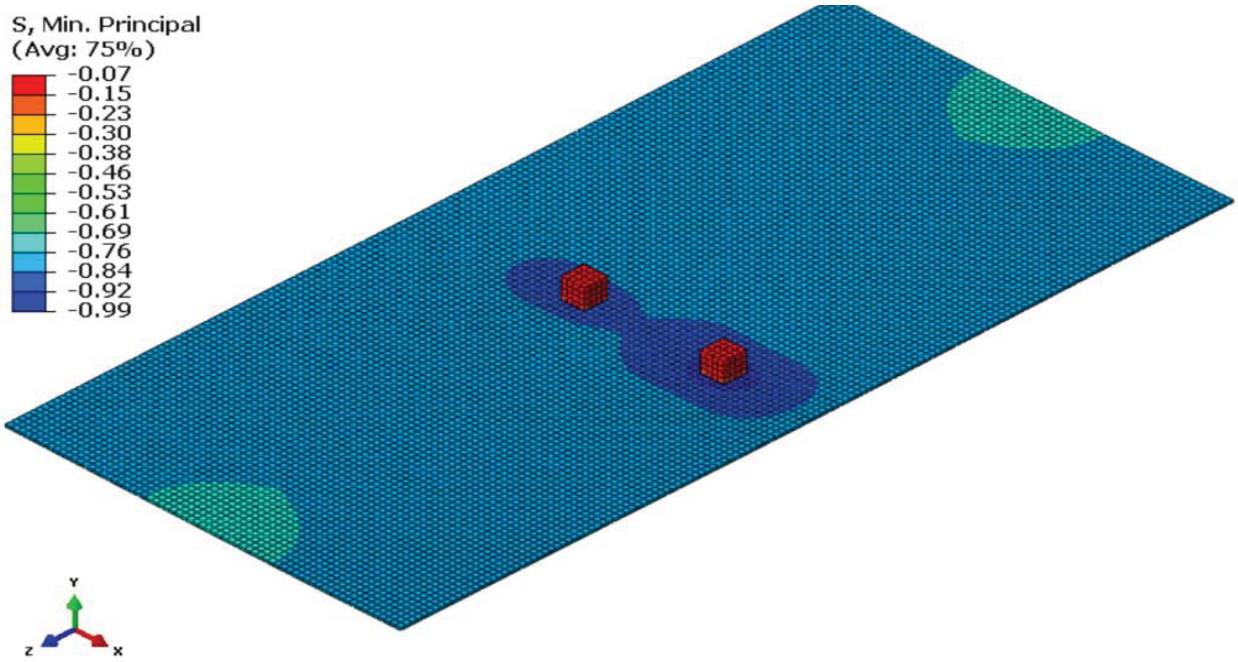

(a) 3rd principal stress

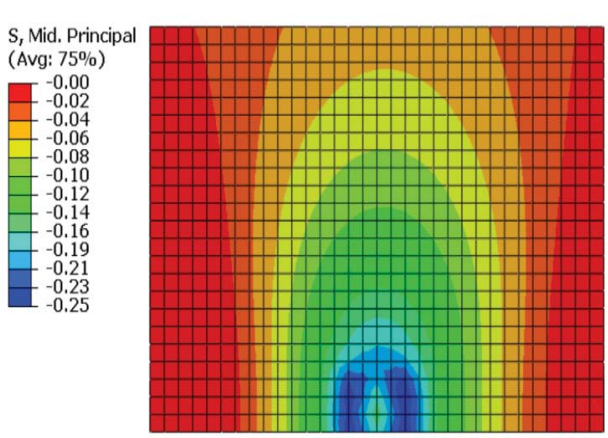

(b) 2nd principal stress

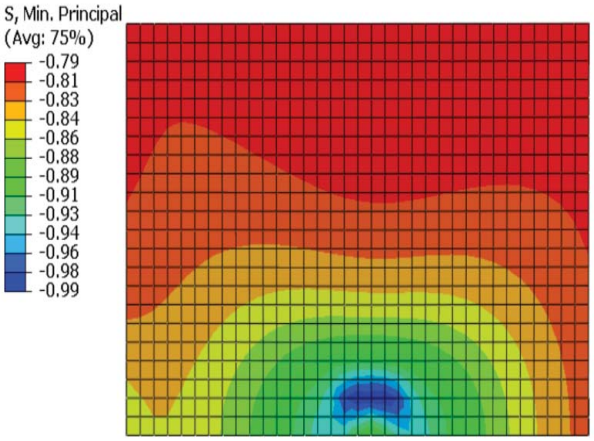

(c) 3rd principal stress

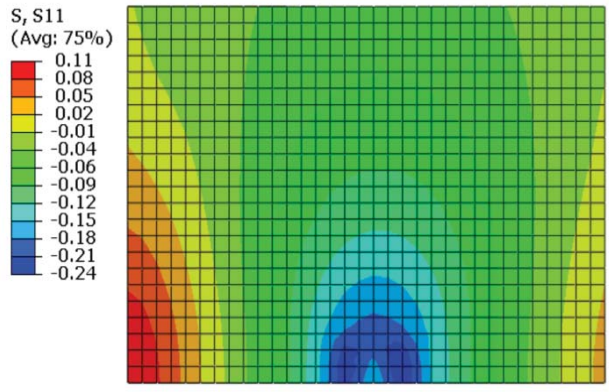

(d) Transversal normal stress σ_x

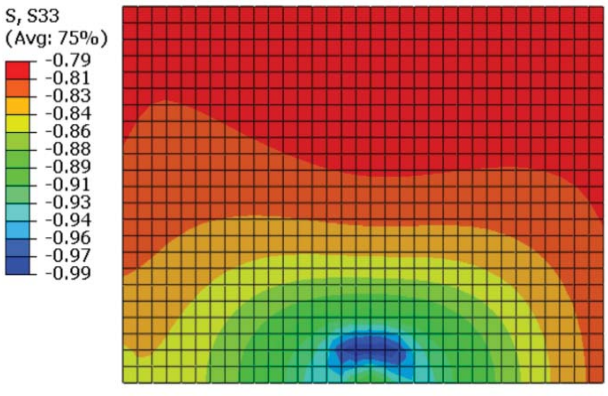

(e) Longitudinal normal stress σ_z

Figure 5.23: Stress contour in BD_9_9-13 (ksi)

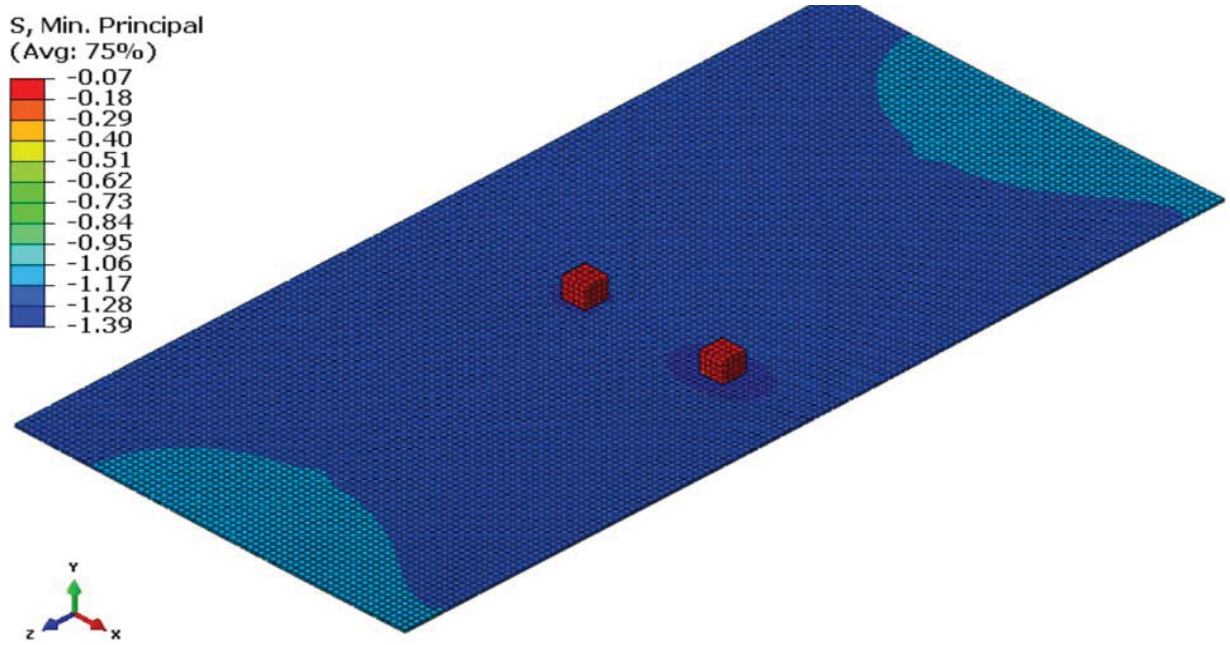

(a) 3rd principal stress

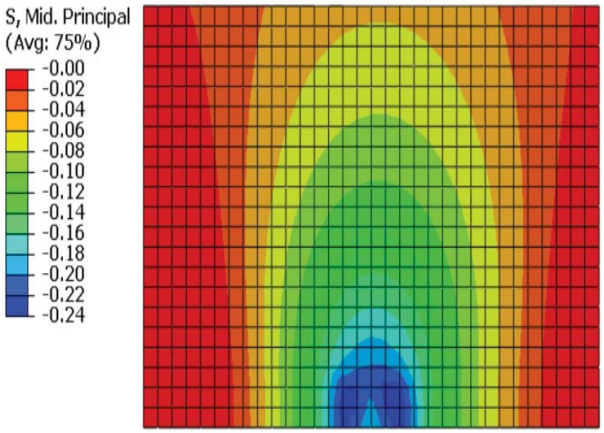

(b) 2nd principal stress

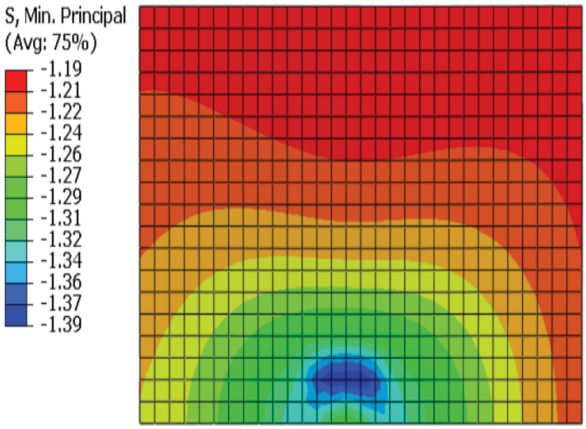

(c) 3rd principal stress

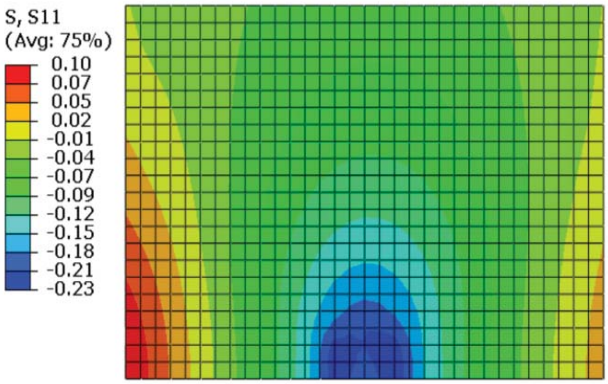

(d) Transversal normal stress σ_x

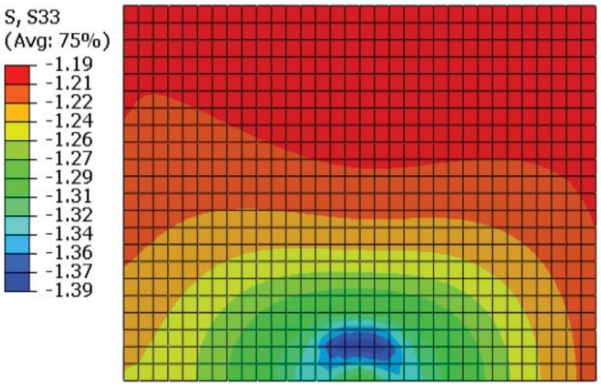

(e) Longitudinal normal stress σ_z

Figure 5.24: Stress contour in BD_9_9-14 (ksi)

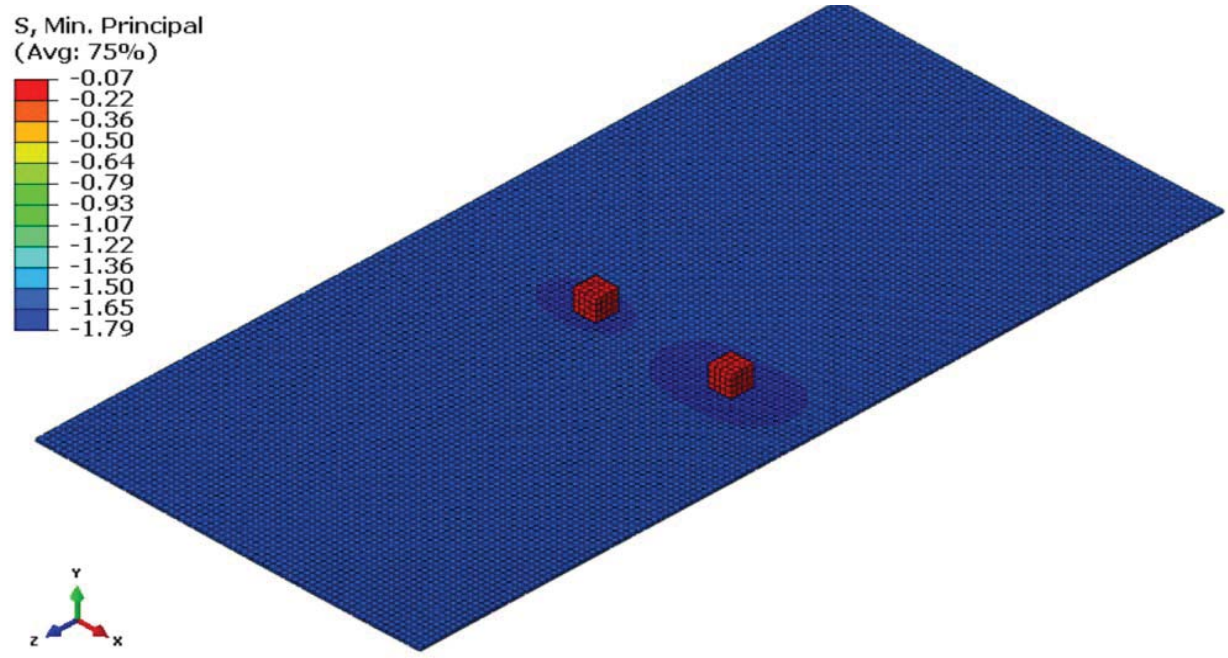

(a) 3rd principal stress

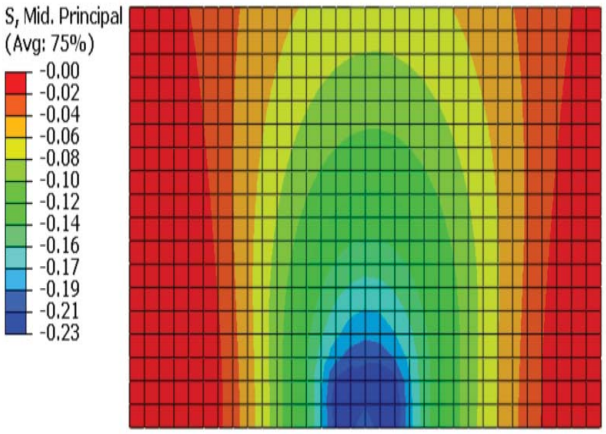

(b) 2nd principal stress

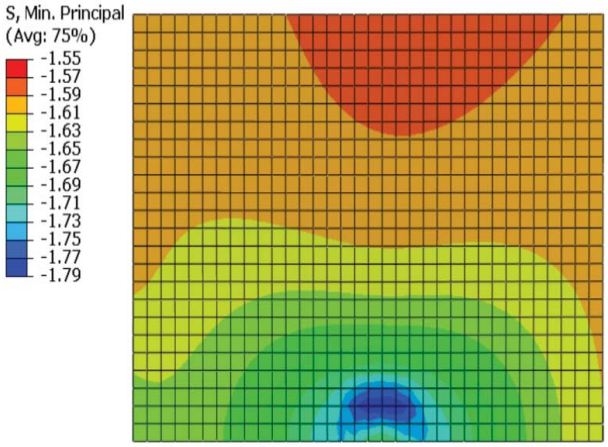

(c) 3rd principal stress

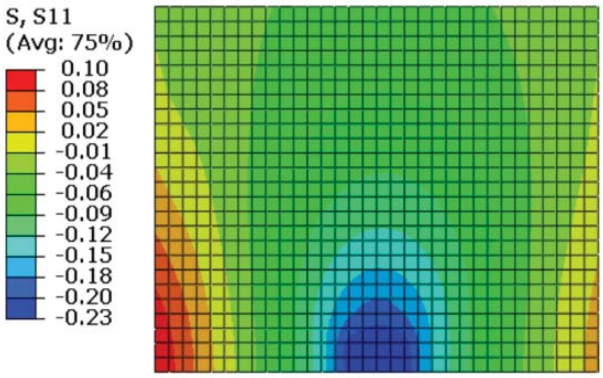

(d) Transversal normal stress σ_x

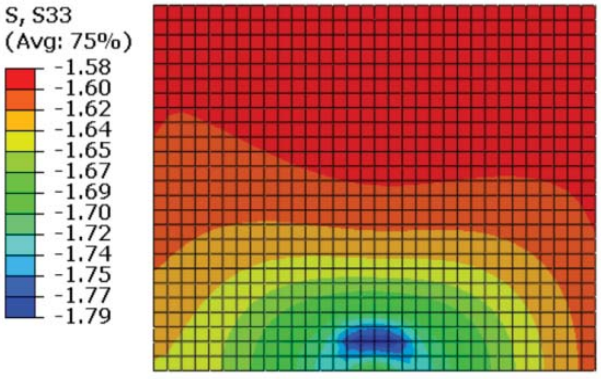

(e) Longitudinal normal stress σ_z

Figure 5.25: Stress contour in BD_9_9-15 (ksi)

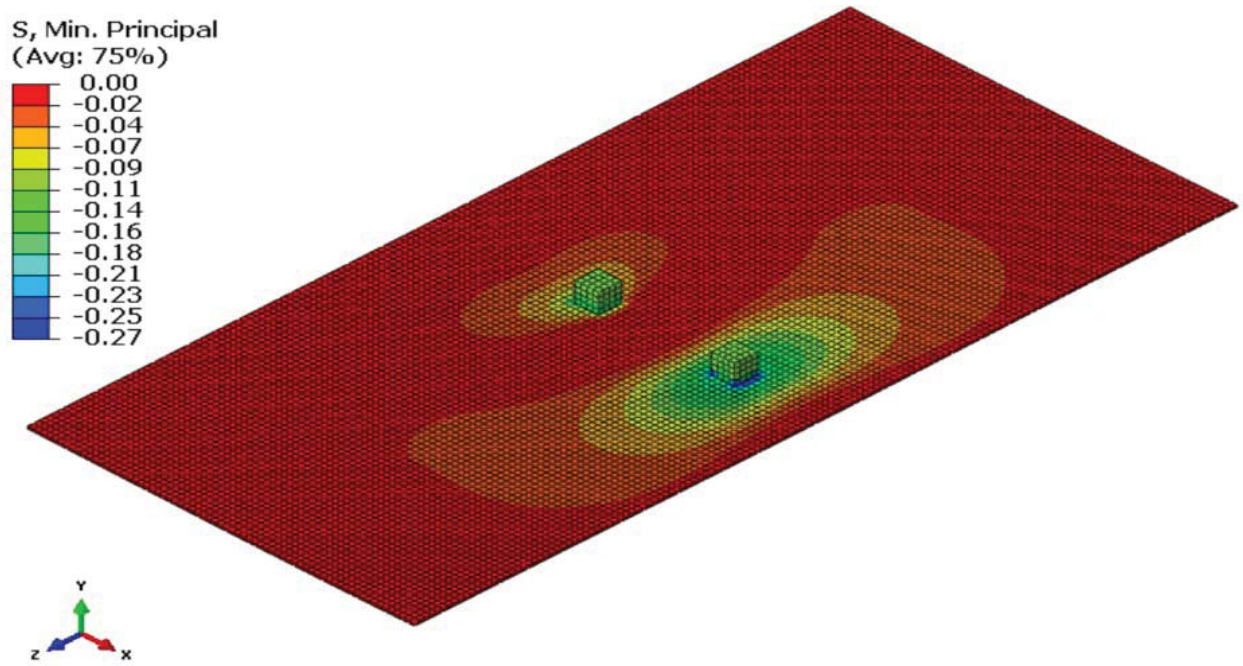

(a) 3rd principal stress

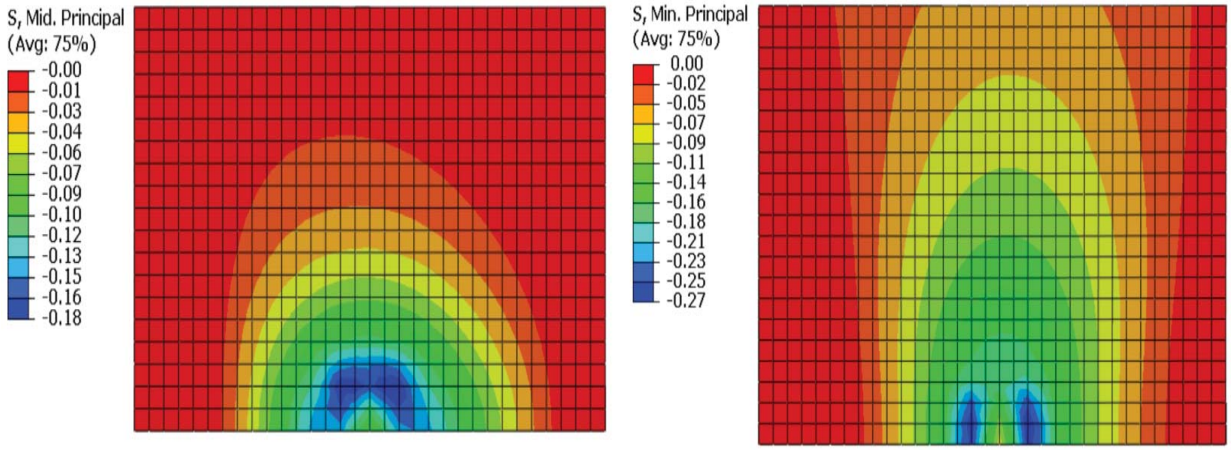

(b) 2nd principal stress

(c) 3rd principal stress

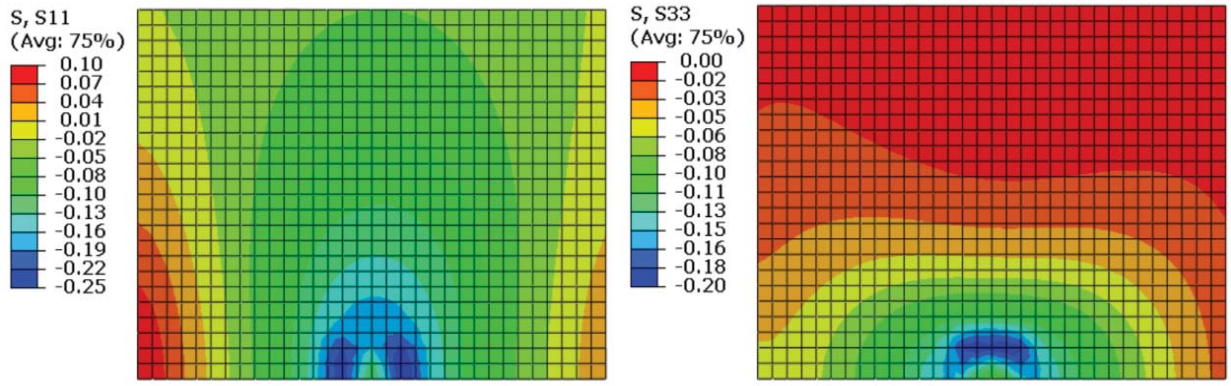

(d) Transversal normal stress σ_x

(e) Longitudinal normal stress σ_z

Figure 5.26: Stress contour in BD_9_9-12 (ksi)

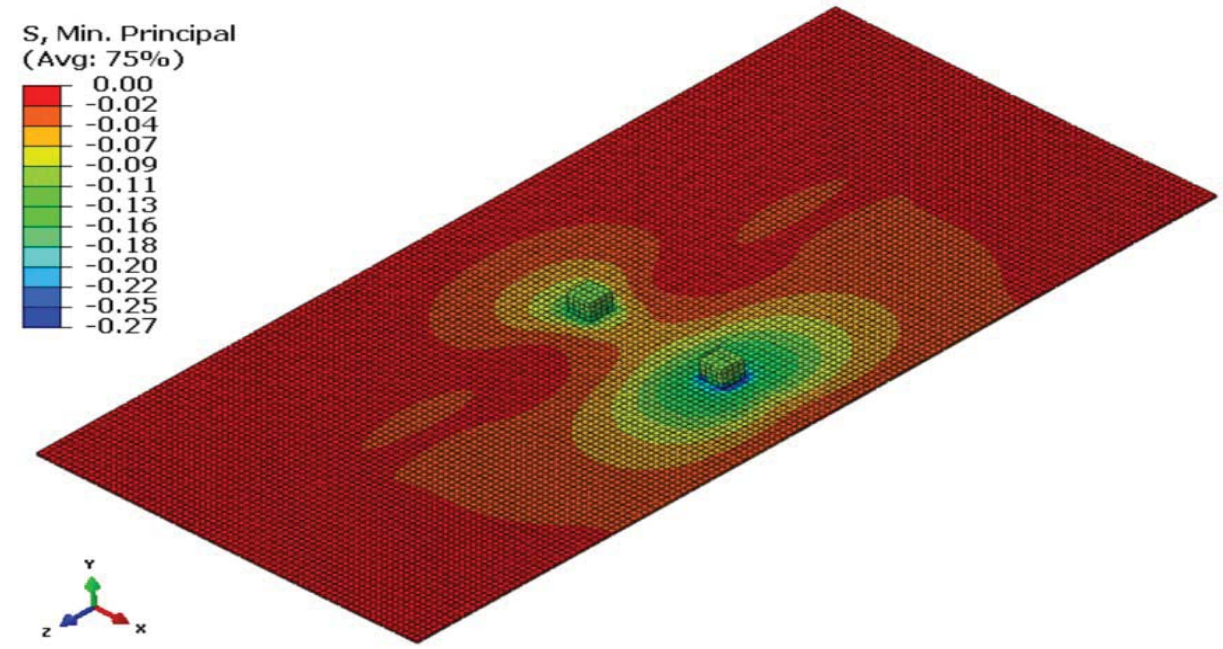

(a) 3rd principal stress

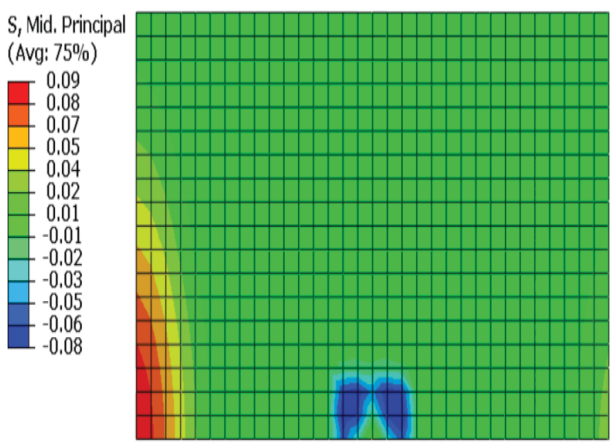

(b) 2nd principal stress

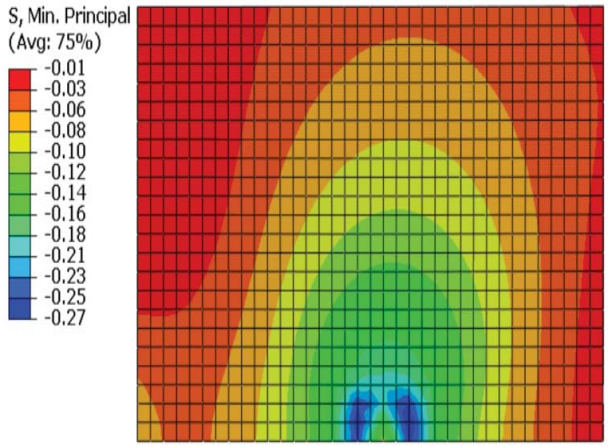

(c) 3rd principal stress

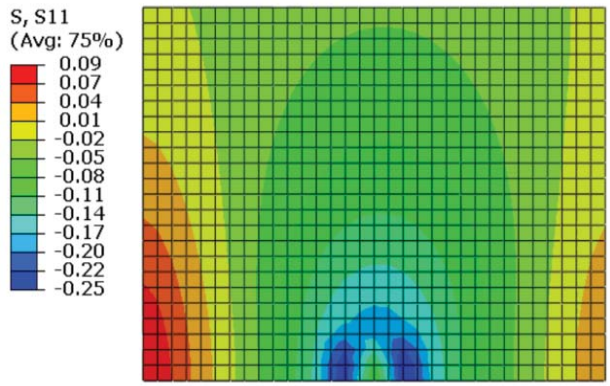

(d) Transversal normal stress σ_x

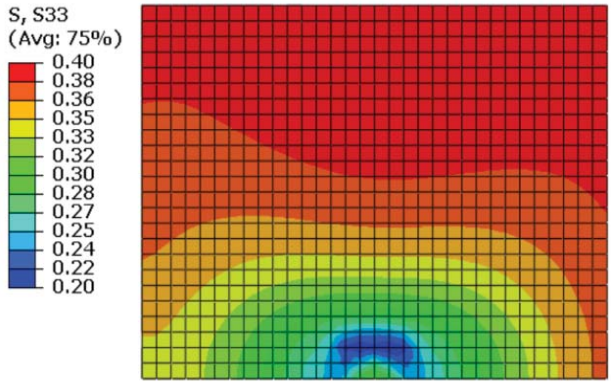

(e) Longitudinal normal stress σ_z

Figure 5.27: Stress contour in BD_9_9-11 (ksi)

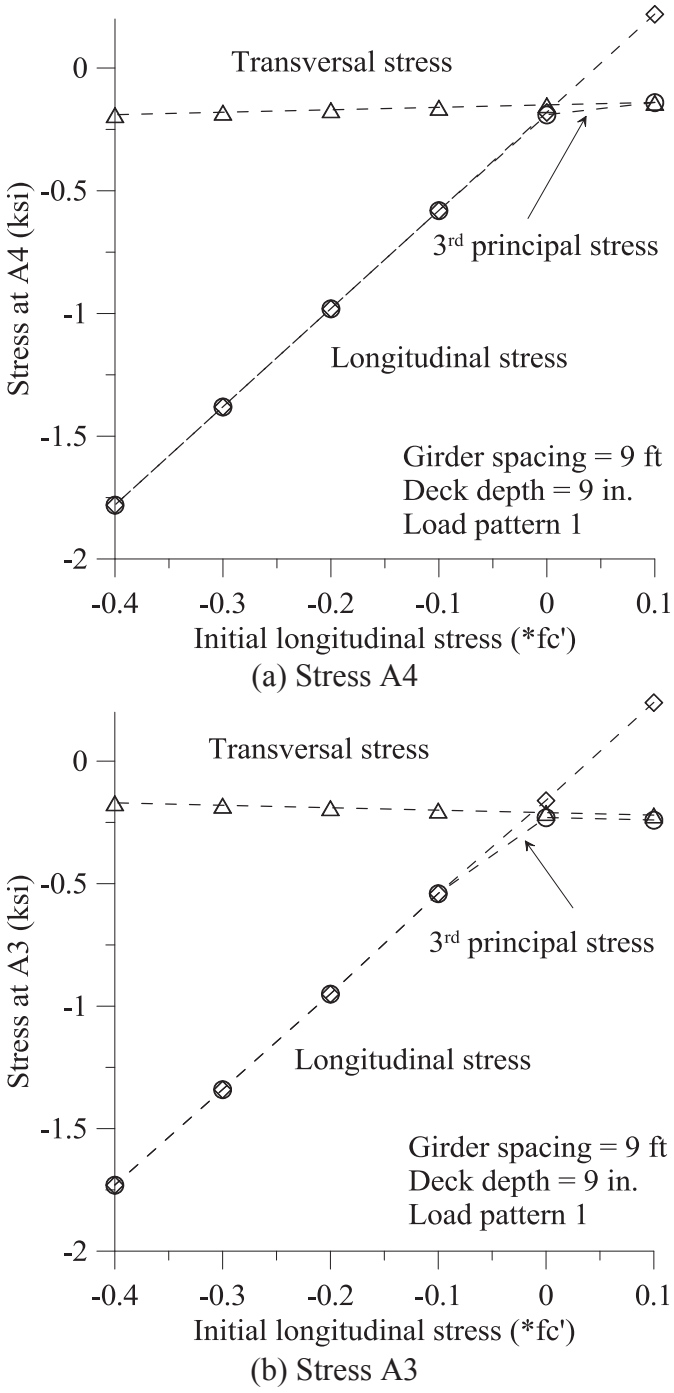

Figure 5.28: Effects of initial longitudinal stress on the final stresses

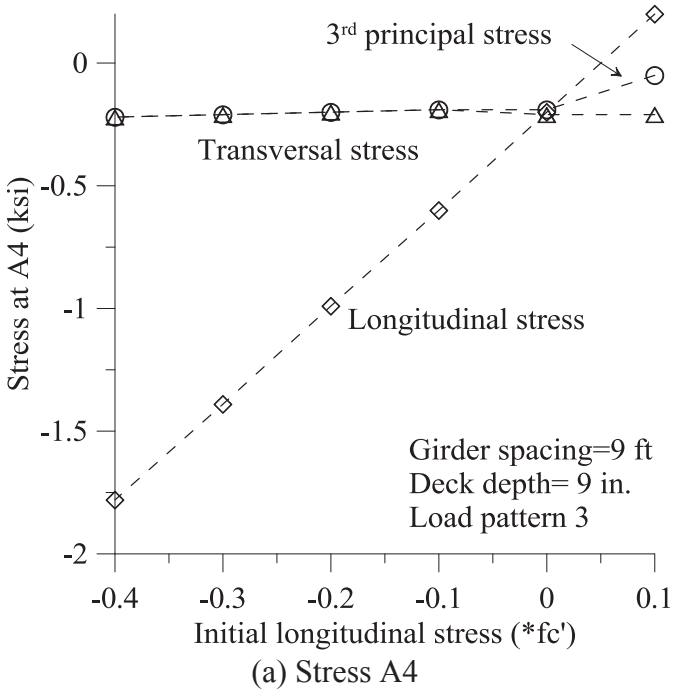

(a) Stress A4

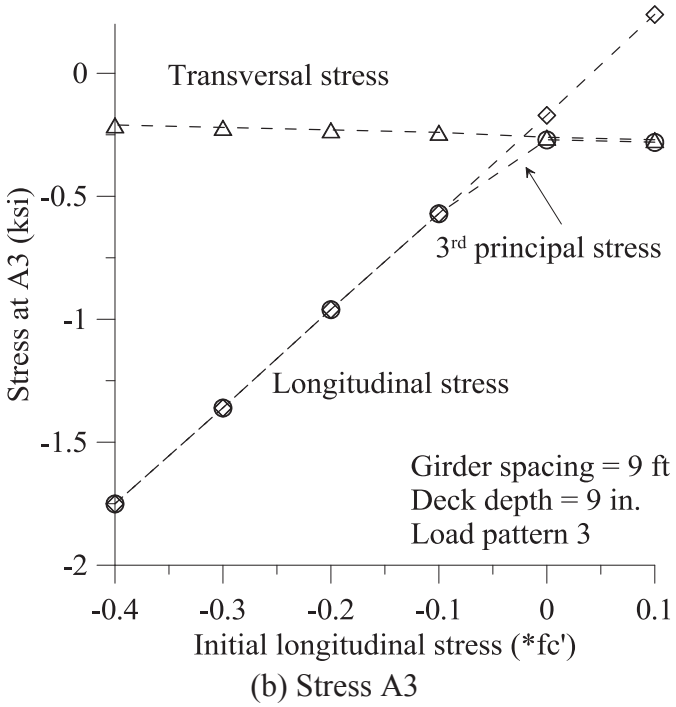

(b) Stress A3

Figure 5.29: Effects of initial longitudinal stress on the final stresses

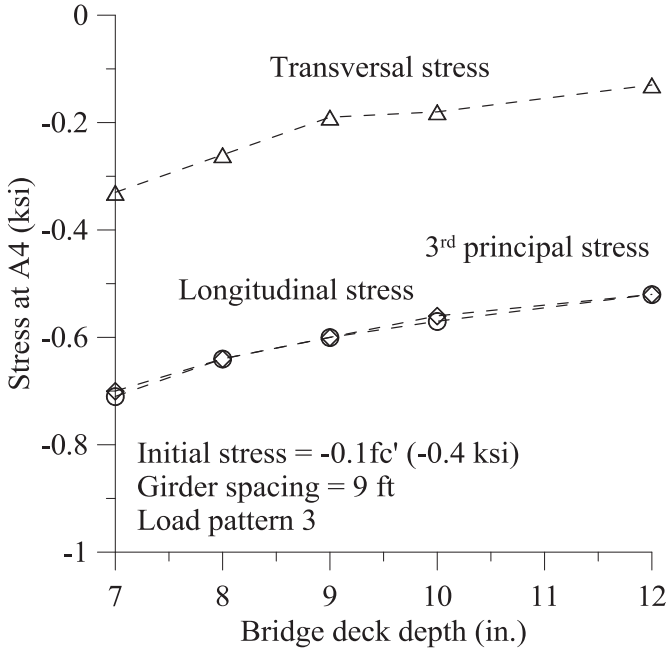

(a) Stress A4

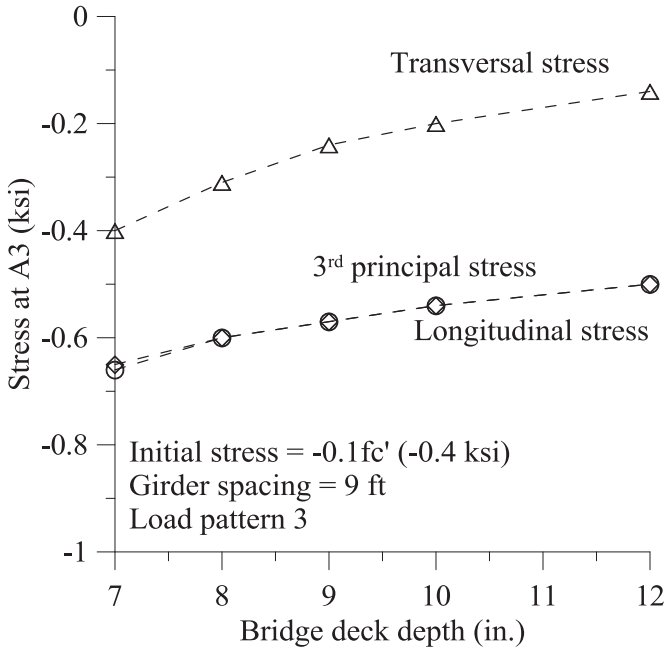

(b) Stress A3

Figure 5.30: Effects of varying bridge deck depth on stress

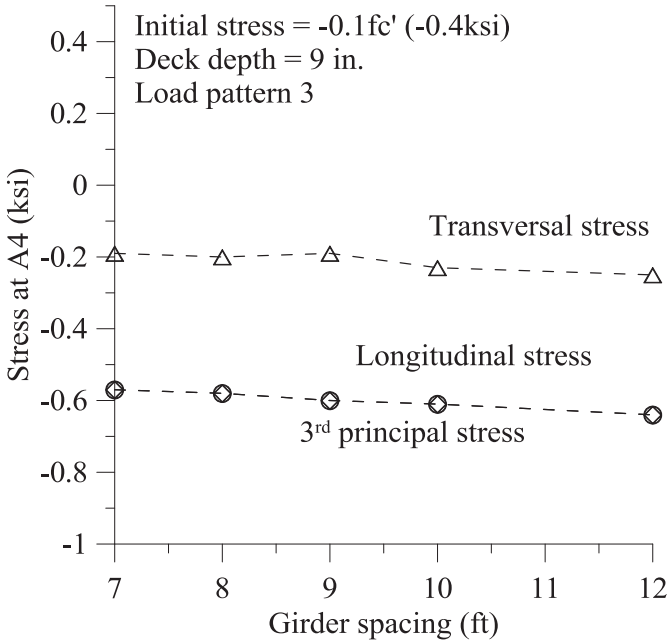

(a) Stress A4

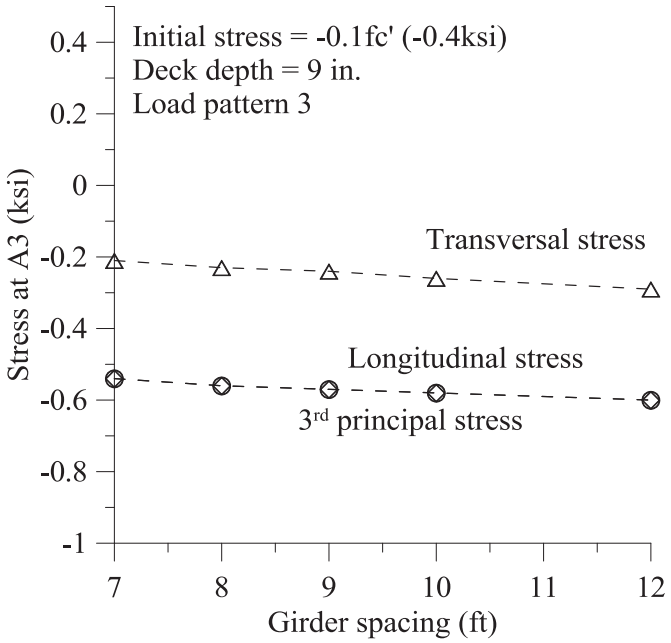

(b) Stress A3

Figure 5.31: Effects of varying spacing on stress

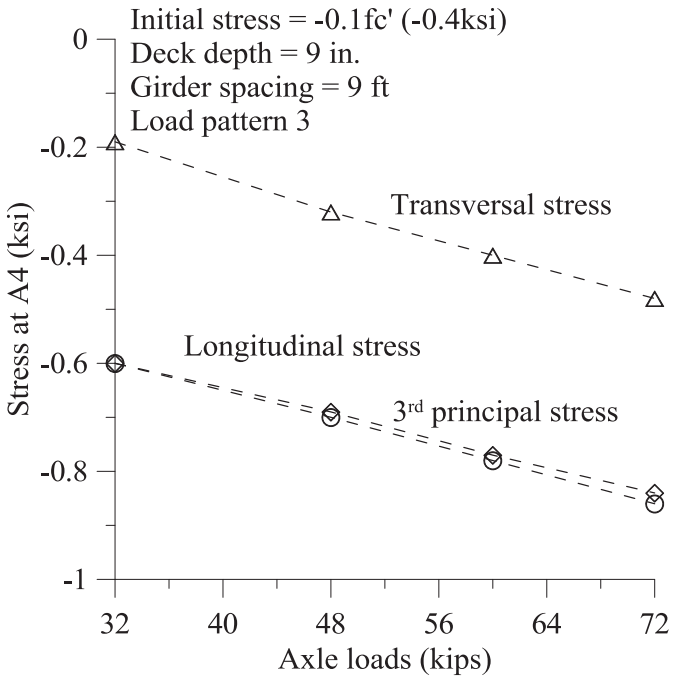

(a) Stress A4

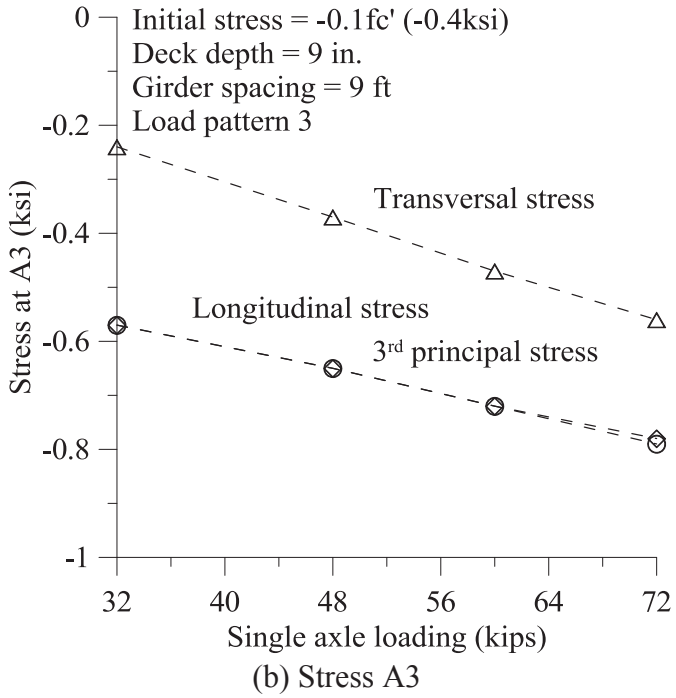

(b) Stress A3

Figure 5.32: Effects of overweight vehicle axles on stress levels

Chapter 6. Predictions of Stress Levels on Bridge Deck

6.1 Introduction

The parametric study described in Chapter 5 indicates that the longitudinal normal stresses in the deck of multi-girder bridges are mainly affected by the deck thickness and the axle loads. In addition to these two factors, the transverse normal stresses in deck are also affected by the girder spacing. It is reasonable to assume that the longitudinal normal stresses away from the axle loads in a bridge deck can be predicted during design checks, and the maximum longitudinal normal stresses near the wheel loads can be estimated with additional contribution from the stress concentration. In addition, the transverse normal stress can be estimated as flexural stresses in a continuous beam. Empirical equations for estimating these stresses in bridge decks caused by overweight vehicles are proposed in this section.

6.2 Bridge Deck Stress Prediction

The FE analyses of idealized bridge models shown in Chapter 5 indicate that the transverse stress in the deck of multi-girder bridges is not strongly coupled with the longitudinal stresses, which is caused by bending of the bridge superstructure. Therefore these two normal stresses may be estimated separately as shown below.

6.2.1 Transverse Stresses

The transverse stresses can be affected by deck depth, girder spacing, and the wheel load as shown in Table 5.10 through 5.13 and Figures 5.28 through 5.32. The transverse stresses may be derived using an "equivalent beam" formed by the continuous deck slab and its girders. In order to determine the normal stresses in the transverse direction, the width of the equivalent continuous beam is needed for estimating the section properties.

Westergaard (1930) derived a close-form equation of equivalent width, b, to determine the design moments in bridge slabs due to concentrated loads on one-way concrete slabs:

$$b = 0.6S + 2w, \tag{6.1}$$

where, S= girder spacing (*ft*) and w is the width of point load on slab. Based on Westergaard's solutions, a width of equivalent strip for positive bending moment used for bridge deck design moments due to wheel loads, as specified Table 4.6.2.1.3-1 in Section 4.6.2.1.3 (AASHTO, 2007), is defined as

$$b = 0.55S + 2.17. \tag{6.2}$$

Note that such equivalent width in Eq. (6.1) or (6.2) is derived to provide identical bending moment while the maximum transverse normal stresses that include the local stress concentration near the wheels due to high axle loads may not be accounted for.

The concept of equivalent width in this study was developed based on the results of the deck analyses as shown in Figures 6.1 and 6.2. The normal stresses in both longitudinal and transverse direction decreases significantly when the point of interest moves away from the wheel load. Unlike one dimensional stress distribution along one direction, the deck slab has a

highly non-uniform stress distribution in both transverse and longitudinal directions. The shear force transfer approximately with a 45 degree, as revealed in shear stress contour at x-z plane in Figure 6.3. Therefore an equivalent width deck width was developed similar to the effective width in solving shear lag (Timoshenko and Goodier, 1970; Moffat & Dowling, 1975; Lin and Zhao 2011) problems. Within the equivalent width, it is assumed that the deck develops a uniform normal stress that equals to the maximum normal stress under a bending moment. The normal transversal stress distribution through the longitudinal direction is approximately assumed as a cubic function through a length (identical to girder spacing length) while the distance from the center of a cubic function to the maximum point is one quarter of the length. As a result, an equivalent width may be used to replace the whole deck width:

$$b = 0.25S + c, \tag{6.3}$$

where, c is a constant. After a regress analysis was conducted based on the data under various girder spacing in Table 5.11, the equivalent width was estimated as,

$$b = 0.25S + 3. \tag{6.4}$$

Comparison of the proposed equivalent width in Eq. (6.4) to that in design specifications in Eq. (6.2) shows that the proposed equivalent width is about 20 to 30 percent smaller. This was because the purpose of the proposed equivalent width needs to account for the additional stress increase near the wheel due to local stress concentration. With the equivalent width and thickness of deck slab, t, the moment of inertia of the continuous beam was derived as $bt^3/12$.

The maximum bending moment in the deck slab with the equivalent width was estimated assuming the fixed boundary conditions for the span, on which the wheel load is applied. Therefore, the maximum bending moment that causes compression on the top deck surface is $PS/8$, where P is the wheel load (including the dynamic allowance factor) and S is the girder spacing or the length of the deck span in the transverse direction. With the bending moment and the equivalent cross section, the maximum normal stress in the deck, σ_x, can be estimated using,

$$\sigma_x = \frac{3PS}{t^2(S+12)}, \tag{6.5}$$

where P is the wheel load, S is the girder spacing, and t is the thickness of deck slab.

The predicted transverse stresses were compared with the observed stresses in the FE analyses in Figures 6.4. The maximum transverse stress predicted by the proposed empirical equation in Eq. (6.5) was plotted in solid lines while the results from the finite element analyses in circles (at Location A4) and triangles (at Location A3). The comparable results are also listed in Table 5.10. The prediction matched well with the calculated stresses. Similarly, the impacts of the girder spacing on transverse stress were well captured by the proposed equation as shown in Figure 6.5.

The impacts of various levels of axle loads from overweight vehicles on the transversal stresses in bridge deck were estimated using the proposed empirical equation in Eq. (6.5) and the results were plotted in Figure 6.6 against those observed in the finite element analyses. Again, the results predicted using the proposed empirical equations (in solid line) were in agreement well with the data predicted by finite element analysis demonstrated in Chapter 5.

6.2.2 Longitudinal Stress

The normal stresses in the longitudinal direction may be affected by the stiffness of the decks in the transverse direction due to lateral load distribution. It was thus assumed that the stress elevation in the longitudinal direction is related to the stresses in the transverse direction. The stress values obtained in the bridge analyses described in Chapter 5 were summarized in Table 6.1. The longitudinal stress elevations (σ_z - σ_{z0}, where σ_z is the calculated longitudinal normal stress and σ_{z0} is the assumed initial longitudinal stress in the deck) were compared to the transverse stress (σ_x) in Figure 6.7. A constant ratio ((σ_z - σ_{z0})/σ_x) of 0.8 may be observed from the data in Figure 6.7. Therefore, the maximum longitudinal stress can be estimated as the summation of the longitudinal stress from design/rating process (σ_{z0}) and the stress concentration,

$$\sigma_z = \sigma_{z0} + \frac{6PS}{5t^2(S+12)}. \tag{6.6}$$

With the introduction of the initial longitudinal stress into the equation, the longitudinal stresses can be estimated from the Eq. (6.6), as shown in Figure 6.8.

Table 6.1: Ratio of longitudinal stress increase over transversal stress

Sample No.	σ_x		σ_z		$(\sigma_z-\sigma_{z0})/\ \sigma_x$	
	A3	A4	A3	A4	A3	A4
1	-0.22	-0.14	0.24	0.22	0.73	1.29
2	-0.21	-0.15	-0.16	-0.18	0.76	1.20
3	-0.2	-0.16	-0.54	-0.58	0.70	1.13
4	-0.19	-0.17	-0.95	-0.98	0.79	1.06
5	-0.18	-0.18	-1.34	-1.38	0.78	1.00
6	-0.17	-0.19	-1.73	-1.78	0.76	0.95
7	-0.27	-0.21	0.24	0.2	0.59	0.95
8	-0.26	-0.21	-0.17	-0.2	0.65	0.95
9	-0.24	-0.19	-0.57	-0.6	0.71	1.05
10	-0.23	-0.2	-0.96	-0.99	0.70	0.95
11	-0.22	-0.21	-1.36	-1.39	0.73	0.90
12	-0.21	-0.22	-1.75	-1.78	0.71	0.82
13	-0.4	-0.33	-0.65	-0.7	0.63	0.91
14	-0.31	-0.26	-0.6	-0.64	0.65	0.92
15	-0.24	-0.19	-0.57	-0.6	0.71	1.05
16	-0.2	-0.18	-0.54	-0.56	0.70	0.89
17	-0.14	-0.13	-0.5	-0.52	0.71	0.92
18	-0.21	-0.19	-0.54	-0.57	0.67	0.89
19	-0.23	-0.2	-0.56	-0.58	0.70	0.90
20	-0.24	-0.19	-0.57	-0.6	0.71	1.05
21	-0.26	-0.23	-0.58	-0.61	0.69	0.91
22	-0.29	-0.25	-0.6	-0.64	0.69	0.96
23	-0.26	-0.22	-0.58	-0.61	0.69	0.95
24	-0.24	-0.19	-0.57	-0.6	0.71	1.05
25	-0.24	-0.21	-0.56	-0.58	0.67	0.86
26	-0.23	-0.2	-0.55	-0.57	0.65	0.85
27	-0.23	-0.2	-0.55	-0.57	0.65	0.85
28	-0.24	-0.19	-0.57	-0.6	0.71	1.05
29	-0.37	-0.32	-0.65	-0.69	0.68	0.91
30	-0.47	-0.4	-0.72	-0.77	0.68	0.93
31	-0.56	-0.48	-0.78	-0.84	0.68	0.92

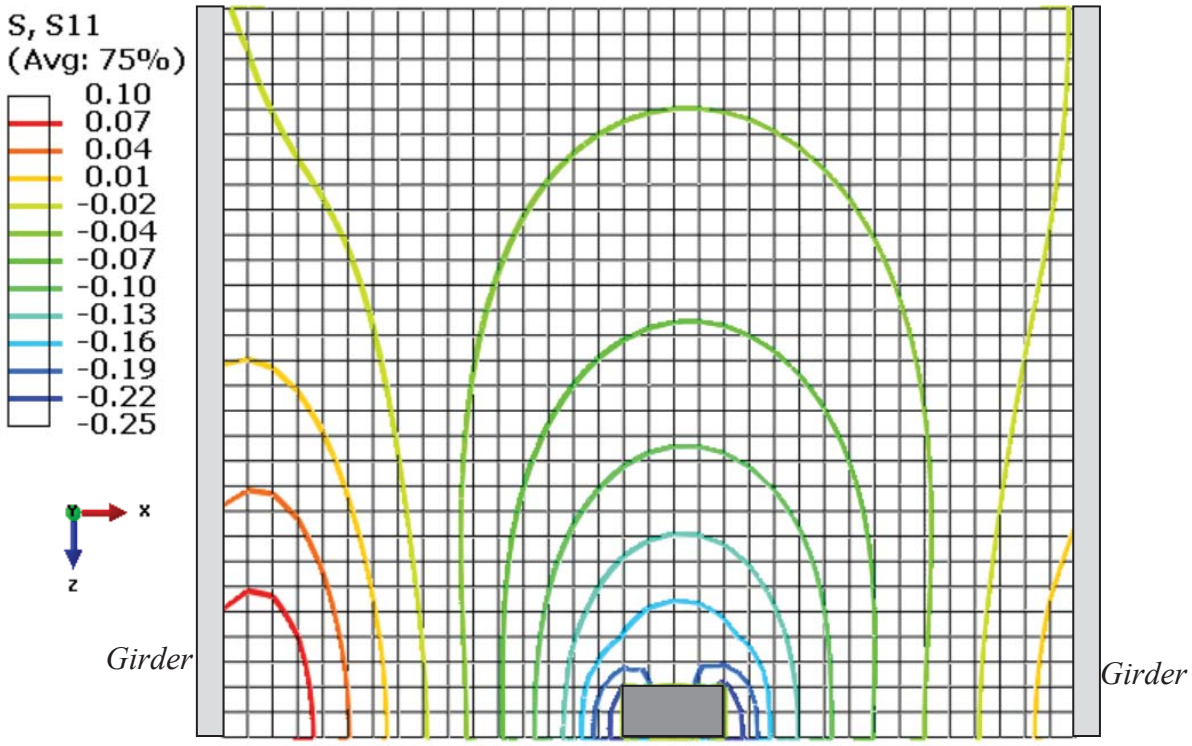

Figure 6.1: Transversal stress contour around the load (ksi)

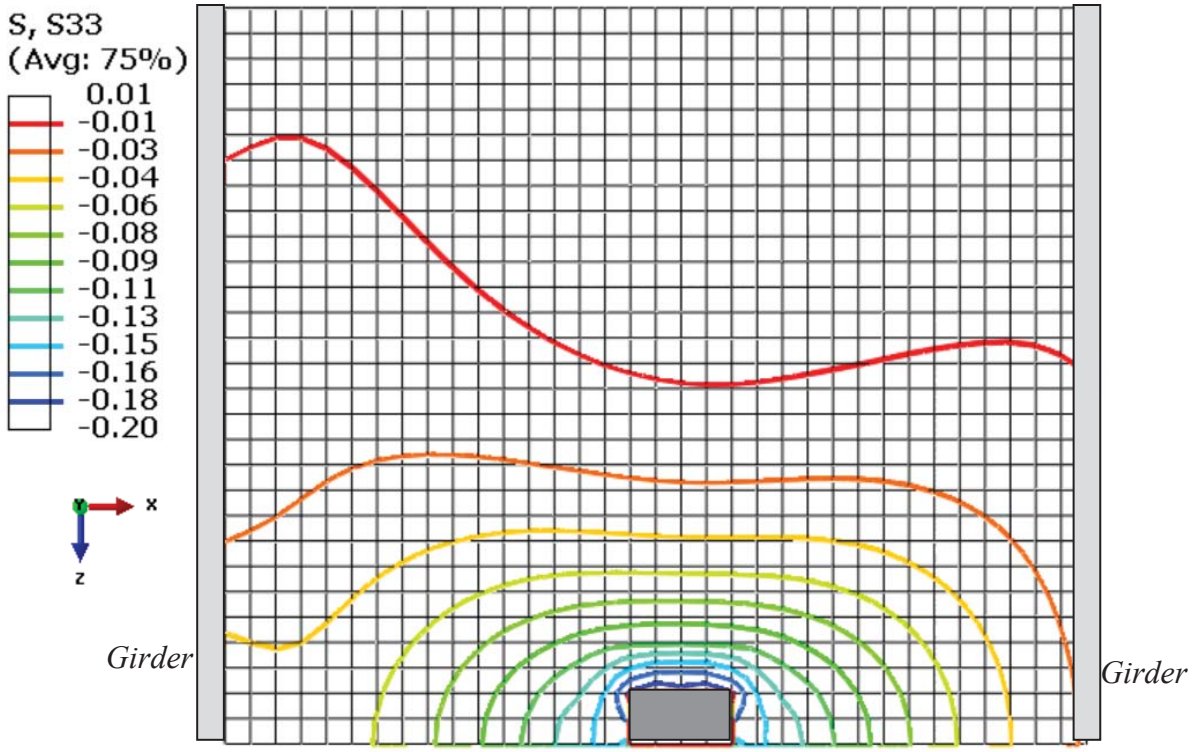

Figure 6.2: longitudinal stress contour around the load (ksi)

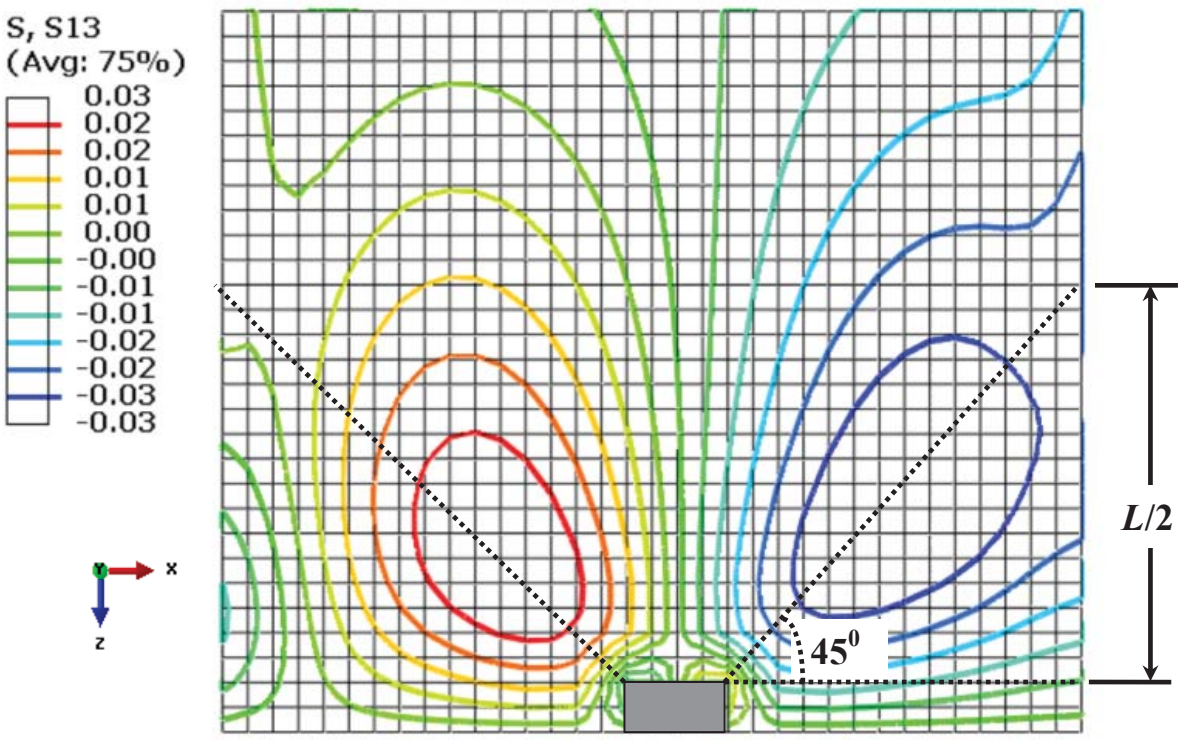

Figure 6.3: Shear stress contour at xz plane around the load (ksi)

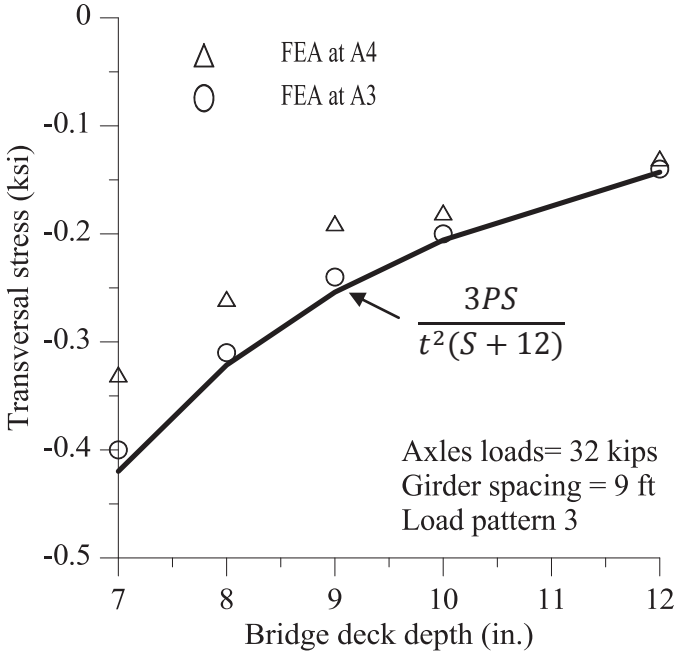

Figure 6.4: Comparison of transverse stresses (the impact of deck depth)

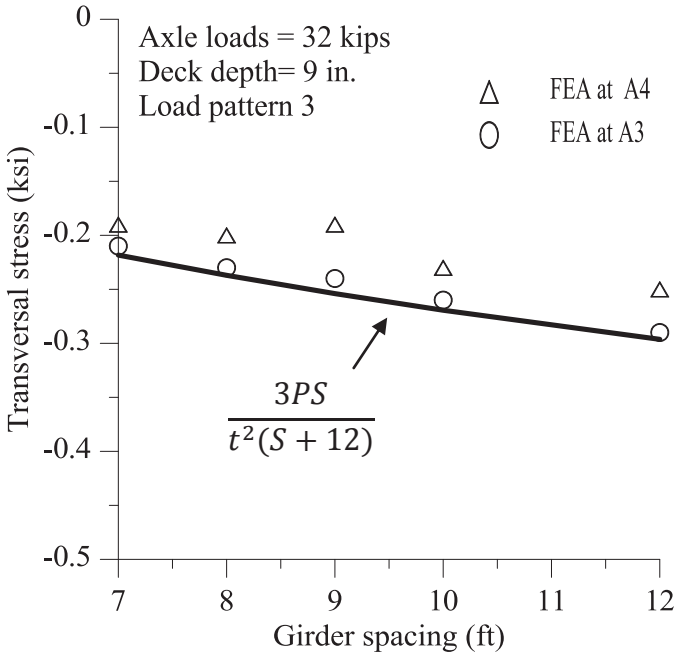

Figure 6.5: Comparison of transverse stress (the impact of girder spacing)

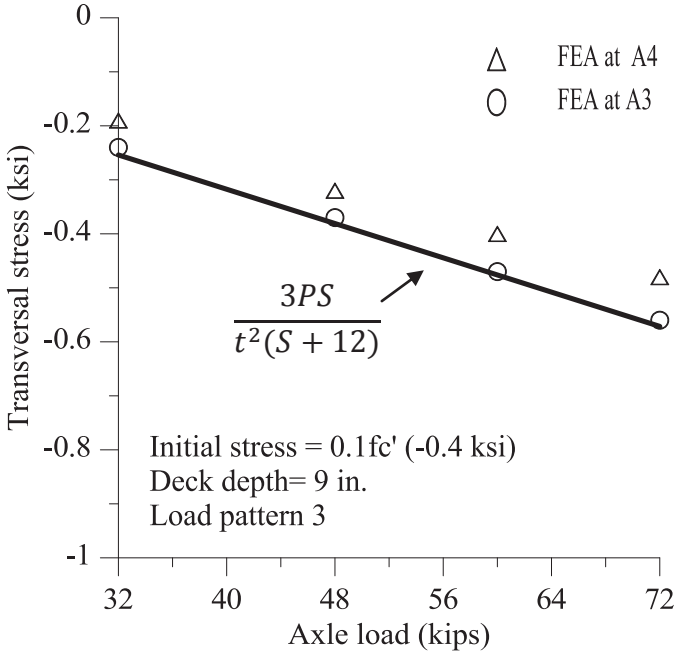

Figure 6.6: Comparison of transverse stress under varying overweight truck

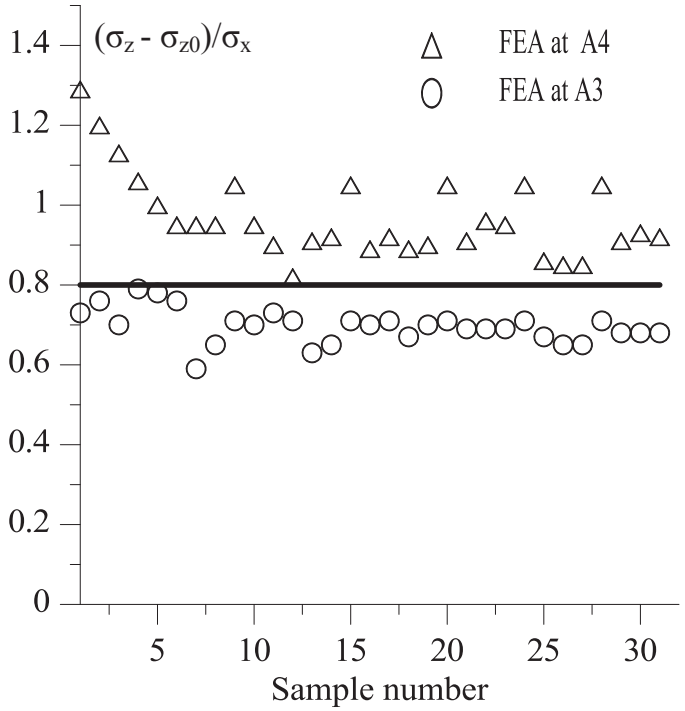

Figure 6.7: Ratio of longitudinal stress increase vs. transverse stress

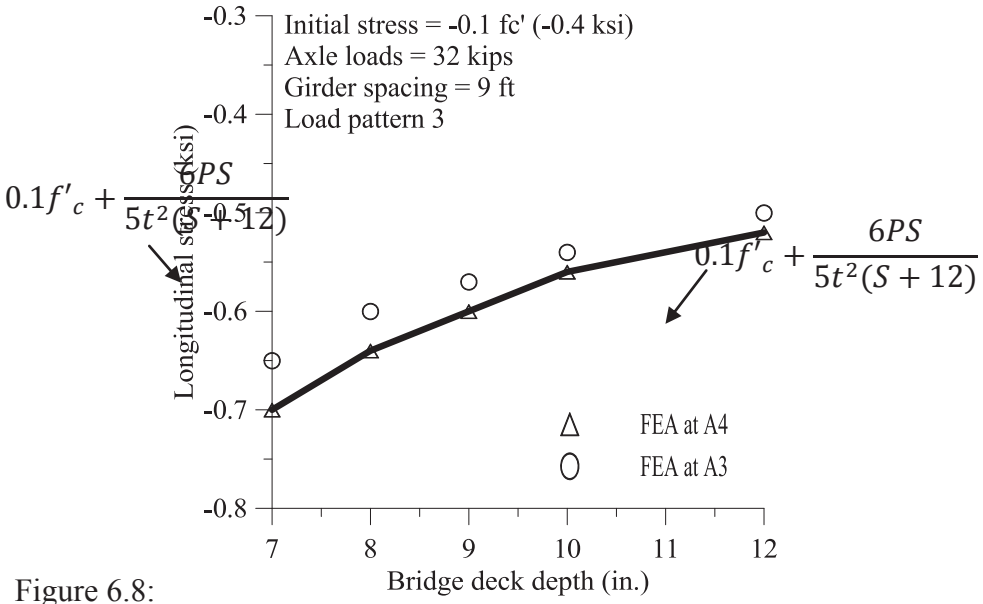

Figure 6.8:

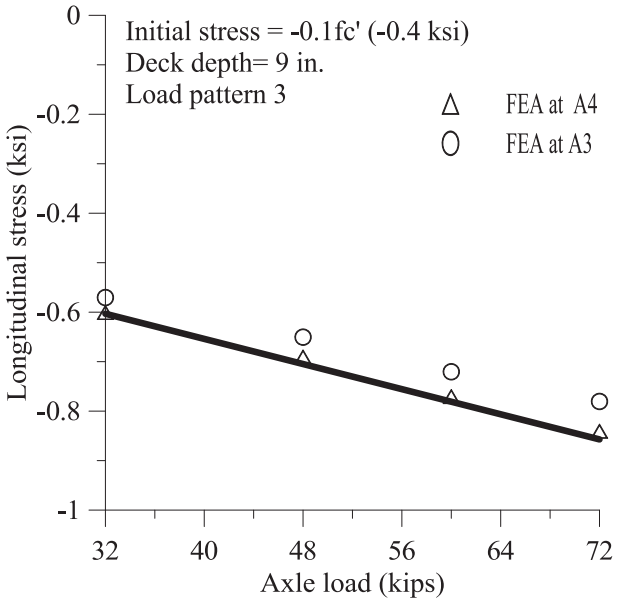

Figure 6.9: Comparison of longitudinal stress (the impact of deck depth and axle loads)

This page has been intentionally left blank.

Chapter 7. Summary, Conclusions and Future Research

7.1 Summary

Overweight vehicles can have heavy axle loads. The heavy axle loads, combined with a large gross weight may create micro-cracks in the concrete, and the accumulation of such damage along with environmental attacks can accelerate the deterioration of bridge decks. This study quantified the impact of overweight vehicles with heavy axle loads on bridge decks using laboratory tests and numerical simulations.

The laboratory tests focused on evaluating the impact of combined mechanical stresses and freeze-thaw cycles on the durability of air-entrained concrete. Eight groups of three 100×200 mm (4×8 in.) cylinders were cast using air-entrain concrete, which is widely used for bridge construction in Wisconsin. After being cured in saturated limewater for 28 days, the concrete cylinders were subjected to predefined compressive loads, equal to 40percent though 80percent of the measured compressive strength. The cylinders were then exposed to 300 freeze-thaw (F/T) cycles following a procedure similar to that described in ASTM C666. Concrete durability is closely related to its water and chloride permeability. Rather than measuring the dynamic moduli and weight losses, rapid chloride ion penetrability (RCIP) tests (ASTM C1202) were conducted to evaluate the chloride permeability of the concrete samples. Two 50-mm (2-in.) thick samples were sliced from each cylinder for the rapid chloride permeability tests. All RCIP tests were conducted within a week at roughly 120 days to minimize the impact of age to the test results. Samples sliced from cylinders without being subjected to loads and F/T cycles were also tested to provide reference performance. Selected samples were examined using an optical microscope and a scanning electronic microscope (SEM) to verify the hypotheses made during the explanation of the observed RCIP test results.

Concrete in bridge decks under a vehicular load is subjected to complex stresses. The actual complex stress states were not simulated in the laboratory tests on concrete permeability in this study. Instead, the bridge deck analyses were conducted to investigate stress distributions and stress levels in typical concrete bridge decks subjected to high axle loads. The numerical analyses focused on compressive stresses in both longitudinal and transverse directions and the resulted minimum principal stress developed on top of concrete deck slab. Deck slabs develop compressive stresses from global flexural deformation and locally from high-level wheel loads when it is subjected to overweight trucks. Linear elastic analysis was first conducted for a sample bridge documented in WisDOT Bridge Manual as a design example and the simulated stresses were compared with the calculated stress during the design process to validate the modeling technique used in the study. Instead of modeling bridges with numerous geometric configurations including bridge type, span length, girder spacing, deck thickness, the majority of the bridge deck analyses were conducted on idealized bridge models. The idealized bridge models contained a segment of multi-girder bridges near the wheel loads. In addition to the wheel loads that simulated the high axle weights, the bridge segments were subjected to initial longitudinal stresses ranging from 10 percent of the concrete compressive strength in tension to 40 percent of concrete compressive strength in compression. These initial longitudinal stresses were used to simulate the global flexural stresses in the deck slab of a variety of bridges subjected to many types of loads. The numerical analyses were then used to capture the true stress that included the global bending stresses and the local stress concentrations.

7.2 Conclusions

The laboratory test results indicated that the mechanical loading combined with freeze-thaw cycles significantly increased the permeability of air-entrained concrete and may accelerate the deterioration of concrete elements such as bridge decks. The reference samples made of air-entrained concrete allowed very small amount of passing charges (715 coulombs), indicating that the concrete used in the study can be classified as high performance concrete for northern States in US according to the high performance concrete (HPC) Lead State Team established by Federal Highway Administration (FHWA) in 1996. The chloride permeability of concrete samples increased significantly with an increase in the applied compressive loads. The highest increase in the total passing charge was 55 percent when compared with the samples from unloaded cylinders but subjected to F/T cycles. This increase became over 93 percent when the results are compared with the reference samples. The observed permeability increase was due to the fact that higher compressive loads caused more extensive microcracks in concrete. In addition, the initially damaged concrete further degrades under freeze-thaw cycles, which may have further opened and interconnected the microcracks.

The explanation for the test results was confirmed by the micrograph images of the loaded and unloaded specimens. The SEM images of concrete parallel to the applied compressive load revealed the through-thickness microcracks that were responsible for the observed increase in chloride permeability in loaded specimens. The amount of microcracks as well as air voids was indirectly measured using water absorption values. A strong relationship was identified between the chloride permeability and the water absorption, which outlined a new test method that can be used to evaluate the durability of concrete in the field.

The numerical analyses using the idealized bridge models indicated that the normal stress in bridge decks in the transverse direction can be significantly affected by the thickness of bridge deck, the girder spacing, and the magnitude of the wheel loads. The analyses results also indicated that the normal stresses in the longitudinal direction may be calculated as the summation of the stresses due to global bending of the bridge superstructure under the truck loads, which can estimated using typical design/rating procedures and the stress elevations near the wheel loads. The local stress increase in the longitudinal direction is about 80 percent of the transverse stress based on the limited number of analyses. In addition, the stress contours indicated that the normal stresses in the longitudinal and transverse directions are not highly coupled such that the minimum principle stress in the bridge decks is very close to the longitudinal stresses.

The analyses showed that the AASHTO design truck can cause low level stresses and therefore might not cause much internal damage to the bridge deck. Note that this conclusion did not include the impact of repeated loading. Meanwhile the overweight trucks may cause more than 50 percent increase in the minimum principal stress on the top of a deck slab. Specifically the local stress increase can be higher than $0.20f'_c$ when the thickness of deck is 7 in. In addition, the overweight truck also causes higher bending moments in bridge superstructure, thus leading to higher longitudinal normal stresses. The combined stresses in can be higher than $0.4f'_c$, which will cause internal micro-cracks in concrete as shown in the laboratory tests in this study. Empirical equations were proposed to capture the transverse stresses and the stress elevation in the longitudinal direction. The proposed equations can be used, in addition to the typical design/rating calculations, to capture the adverse stresses in bridge decks subjected to overweight trucks.

7.3 Future Research

The laboratory tests revealed important issues engineers may have ignored in the past regarding durable bridge construction. Specifically, the impact of combined mechanical loading and F/T cycles was found negligible when the weight loss and surface spalling were evaluated according to the existing standard such as ASTM C666. However, the impact of combined actions on concrete permeability was significant as it was represented by the results of rapid chloride permeability tests. Nevertheless, the idealized load levels and F/T exposures may not exactly represent the actual field situations. More tests that simulate more realistically the combined actions on field concrete are thus needed. In addition, the stresses applied to concrete samples were different from those in a typical bridge deck, and the actual complex stress states were not simulated in the laboratory tests on concrete permeability in this study. Therefore the impact of actual complex stresses on concrete durability should be studied in the future.

The concrete permeability was found closely related to its waster absorption capacity. Further study may be conducted in this direction to create a convenient means to evaluate the durability of concrete in the field. In addition, field samples with different ages and different history of truck loading should be tested to verify the test method.

Note that the material nonlinearity of concrete was not investigated in this study. Bridge deck may develop cracks with the actual concrete material included in the analyses. The moment of inertia of the deck slab reduces significantly when flexural cracks form in concrete, leading to higher stresses in bridge deck. Further studies that include material nonlinearity of concrete are required. In addition, laboratory tests and/or field tests of bridge decks are needed to verify the prediction of the stress levels.

This page has been intentionally left blank.

References

[1] AASHTO T277, Standard Method of Test for Rapid Determination of the Chloride Permeability of Concrete. American Association of State Highway and Transportation Officials, Washington, D.C.; 1983.

[2] AASHTO (2010) AASHTO LRFD Bridge Design Specifications, 5rd Edition, American Association of State Highway and Transportation Officials, Washington, DC, 1450 pp.

[3] ACI Committee 201. Guide to Durable Concrete (ACI 201.2R-1). American Concrete Institute, MI: Farmington Hills, 2001.

[4] Alexander M G, (1999) Engineering and transport properties of the interfacial transition zone in cementitious composites, Cachan : Rilem Publ. RILEM report, 20.

[5] American Association of State Highway and Transportation Officials. AASHTO Bridging the Gap: Restoring and Rebuilding the Nation's Bridges. See the web site http://www.transportation.org, 2008.

[6] Aldea C, Shah SP, and Karr A. Permeability of cracked concrete. Materials and Structures 1999; 32(5): 370-376.

[7] Aldea C, Shah SP, and Karr A. Effect of Cracking on Water and Chloride Permeability of Concrete. J Mater Civ Eng 1999; 11(3): 181-187.

[8] ASTM C 1585 (2010) "Standard Test Method for Measurement of Rate of Absorption of Water by Hydraulic-Cement Concretes," ASTM International, West Conshohocken, PA.

[9] ASTM C 1543-02 (2003): Standard Test Method for Determining the Penetration of Chloride Ion into Concrete by Ponding. In *Volume 04.02 Concrete and Aggregates, Standards on Disc.* West Conshohocken, PA.

[10] ASTM C 1152 (2004) "Standard Test Method for Acid-Soluble Chloride in Mortar and Concrete," ASTM International, West Conshohocken, PA.

[11] ASTM C 1156 (2010) "Standard Test Method for Determining the Apparent Chloride Diffusion Coefficient of Cementitious Mixtures by Bulk Diffusion," ASTM International, West Conshohocken, PA.

[12] ASTM C 666-3, Standard Test Method for Resistance of Concrete to Rapid Freezing and Thawing. ASTM International, West Conshohocken, PA; 2008.

[13] ASTM C 1202-10, Standard Test Method for Electrical Indication of Concrete's Ability to Resist Chloride Ion Penetration. ASTM International, West Conshohocken, PA; 2010.

[14] ASTM C 260-10a, Standard specification for air-entraining admixtures for concrete. ASTM International, West Conshohocken, PA, 2010.

[15] ASTM C 1231-10a. Standard practice for use of unbounded caps in determination of compressive strength of hardened concrete cylinders. ASTM International, West Conshohocken, PA, 2010.

[16] ASTM C215, Standard Test Method for Fundamental Transverse, Longitudinal, and Torsional Resonant Frequencies of Concrete Specimens. ASTM International, West Conshohocken, PA, 2002.

[17] Bae, Han-Ug; Oliva, M., (2009) "Bridge analysis and evaluation of effects under overload vehicles", National center for freight and infrastructure research and education, technical report, University of Wisconsin-Madison, WI USA.

[18] Basheer, P. A. M., McCauley. A., and Long, A. E., (1997). "Influence of Moisture Condition of Concrete on the Performance of Surface Treatments." Special Publication 170 (SP - 170), American Concrete Institute.

[19] Bentz D.P, (2007) A virtual rapid chloride permeability test. Cement and Concrete Composites, Vol. 29, pp.723-731.

[20] Bentz DP, Ehlen MA, Ferrais CF, and Garboczi EJ. (2001) Sorptivity-Based Service Life Predictions for Concrete Pavements, 7th International Conference on Concrete Pavements, Orlando, Florida; pp. 9-13.

[21] Bridges: Short Span Steel Bridge Plans and Software (1994), *American Iron and Steel Institute*, USA.

[22] Buenfeld,N., Newman,J., (1987) An examination of three methods for studying ion diffusion in cement pastes, mortars and concrete, Mats & Structs, Vol:20, Pages:3-10

[23] Cady P. and Weyers R. Deterioration Rates of Concrete Bridge Decks. Journal of Transportation Engineering. 1984; 110(1): 34-44.

[24] Cao L, Allen J, Shing P, and Woodham D, Behavior of RC Bridge Decks with Flexible Girders. Journal of Structural Engineering 1996; 122(1): 11-19.

[25] CEB. Durability concrete structures: CEB design guide, Bulletin d' information No. 182, Switzerland: Comite Euro-International du Beton;1992.

[26] Cemica JN, Geotechnical Engineering: Soil Mechanics. New York: John Wiley & Sons; 1995.

[27] Corps of Engineers Standards, Test method for water permeability of concrete using triaxial cell CRD-C 163-92, Handbook for Concrete and Cement, See the web site http://www.wes.army.mil/SL/MTC/handbook/handbook.htm, 1992.

[28] Elzafraney M, and Soroushian P, Quantitative Micro-structural Investigation of Deteriorated Reinforced Concrete Bridge Deck. Journal of Materials in Civil Engineering. 2005; 17(2): 150-167.

[29] Federal Highway Administration (2008) Deficient Bridges by State and Highway System, http://www.fhwa.dot.gov/BRIDGE/britab.htm.

[30] Federal Highway Administration (2006) Conditions and Performance Report. Chapter 11, http://www.fhwa. dot.gov/policy/2006cpr/es11.htm.

[31] Foley, C. (2009) personal communications.

[32] Freyermuth, C. (2001) "Life-Cycle Cost Analysis for Large Bridges," Concrete International, Vol. 23, No. 2, pp. 89-95.

[33] Gjørv, O., (2010) ”Durability Design and Quality Assurance of Concrete Infrastructure”, Concrete International, Vol. 32, No. 9, 2010, pp. 29-36.

[34] Hearn N. Effect of shrinkage and load induced cracking on water permeability of concrete. ACI Materials Journal 1999; 96(6): 234-241.

[35] Hooks, J. (2003) "Holding it together: FHWA Bridge Plan Part I," Roads & Bridges Magazine, Vol. 41, No.6.

[36] Hoseini M, Bindiganavile V, Banthia N. The effect of mechanical stress on permeability of concrete: a review. Cem Concr Compos 2009; 31(4): 213–20.

[37] Hsu TTC, Slate FO, Sturman GM, and Winter G. Microcracking of Plain Concrete and the Shape of the Stress-Strain Curve. Journal of the American Concrete Institute Proceedings 1963; 60(2): 209-224.

[38] Julio-Betancourt, G.A., Hooton, R.D., (2004) Study of the Joule effect on rapid chloride permeability values and evaluation of related electrical properties of concretes. Cement and Concrete Research, Vol. 34, No. 6, pp. 1007-1015.

[39] Kermani A. Permeability of stressed concrete. Building Research and Information 1991; 19(6): 360-366.

[40] Kim D, Shimura K, and Horiguchi T. Effect of tensile loading on chloride penetration of concrete mixed with granulated blast furnace slag. Journal of Advanced Concrete Technology 2010; 8(1): 27-34.

[41] Kostem CN, Overloading of Highway Bridges - Initiation of Deck Damage. Transportation Research Record 664 1978: 212-220.

[42] Kropp, J., Hilsdorf, H.K., (2005), Performance Criteria for Concrete Durability-State of the Art Report prepared by RILEM Technical Committee TC 116–PCD, Taylor and Francis(Spon Press).

[43] Lamond JF, Pielert JH, (2006) Significance of Tests and Properties of Concrete and Concrete-Making Materials, ASTM International.

[44] Lane, S., (2009) “Concrete permeability testing- part 1 & part 2. HPC Bridge Views, issue 58/59, http://www.hpcbridgeviews.com/i58/Article3.asp and http://www.hpcbridgeviews.com/i59/Article4.asp

[45] Lin, Z., and Zhao, J., (2011), "Least-work solutions of flange normal stresses in thin-walled flexural members with high-order polynomial", *Engineering Structures*, Vol. 33, NO.10, pp. 2754-2761.

[46] Liu, Z., Beaudoin, J.J, (2000) The permeability of cement systems to chloride ingress and related test methods. Cement, Concrete and Aggregates, Vo22. No. 1, pp.16-23.

[47] Liu, Z., Beaudoin, J.J., (1999) An assessment of the relative permeability of cement systems using AC impedance techniques, Cem. Concr. Res. 29, pp. 1085–1090.

[48] Ludirdja D, Berger RL, Young JF. Simple method for measuring water permeability of concrete. ACI Mater J 1989; 86 (5): 433-439.

[49] Luca Bertolini, Bernhard Elsener, Pietro Pedeferri, Rob B. Polder (2004), Corrosion of Steel in Concrete: Prevention, Diagnosis, Repair, Wiley-VCH

[50] Majumdar, P., Liu, Z., Lesko, J., Cousins, T., (2007) "Analysis of cellular FRP composite bridge deck utilizing conformable tire patch loading", *COMPOSITES & POLYCON 2007, American Composites Manufacturers Association,* October 17-19, 2007, Tampa, FL USA.

[51] Marchand J, Pigeon M, and Setzer M. Freeze-Thaw Durability of Concrete. London: E & FN Spon; 1997.

[52] Martys NS, and Ferraris CF. Capillary Transport in Mortars and Concrete. Cem Concr Res 1997; 27(5): 747-760.

[53] Mays, G., (1992). Durability of concrete structures. Investigation, repair, protection. E&FN Spon, London.

[54] Martys, N. S., and C. F. Ferraris, 1997, Capillary Transport in Mortars and Concrete, Cement and Concrete Research, Vol. 27, No. 5, pp. 747-760

[55] Moffatt, K., and Dowling, P., (1975) "Shear lag in steel box girder bridges," *The Structural Engineer*, Vol. 53 No.10, pp.439-448.

[56] McGrath, P. F. and Hooton, R. D., "Re-evaluation of the AASHTO T259 90-Day Ponding Test," Cement and Concrete Research, Vol. 29, 1999, pp. 239-248.

[57] Mehta, P.K. and Gerwick, B.C. (1982) Cracking-Corrosion Interaction in Concrete Exposed to Marine Environment, Concrete International, 4:45-51.

[58] Mehta P, and Monteiro P. Concrete Microstructure Properties and Materials. 3rd ed. Mc-Graw Hill Companies Inc., 2006.

[59] Mirza S. Durability and sustainability of infrastructure - a state-of-the-art report. Canadian Journal of Civil Engineering. 2006; 33(6): 639-649.

[60] McGrath, P.F., Hooton, R.D., (1999) Re-evaluation of the AASHTO T259 90 day salt ponding test, Cem. Concr. Res. 29, pp.1239– 1248.

[61] Martys, N. S., and C. F. Ferraris, 1997, Capillary Transport in Mortars and Concrete, Cement and Concrete Research, Vol. 27, No. 5, pp. 747-760

[62] Monteiro P. J. M., Bastacky, S. J. and Hayes, T. L. "Low-Temperature Scanning Electron Microscope Analysis of the Portland Cement Paste Early Hydration." Cement and Concrete Research, Vol. 15, no. 4, 1985, pp. 687-693.

[63] McGrath, P., (1996) Development of test methods for predicting chloride penetration into high performance concrete, PhD Thesis, University of Toronto.

[64] Pigeon, M., Prevost, J., and Simard, J. (1985) "Freeze-Thaw Durability versus Freezing Rate," *ACI Materials Journal*, Vol. 82, pp. 684-692.

[65] Nagi, MA, Okamoto, PA, Kozikowski RL, Hover, K. Evaluating air-entraining admixtures for highway concrete. Transportation Research Board of the national academies, NCHRP report 578; 2007,

[66] Nemati KM, Monteiro PJM, and Scrivener KL. Analysis of Compressive Stress-Induced Cracks in Concrete. ACI Mater J 1998; 95(5): 617-631.

[67] Nowak AS, Szerszen MM, and Juntunen DA, Michigan Deck Evaluation Guide. Michigan Department of Transportation. Technical report no. UMCEE 99-14; 2000.

[68] NT Build 492, Concrete, mortar and cement-based repair materials: chloride migration coefficient from non-state migration experiment. NORDTEST, Espoo; 1999.

[69] Oh, B. (1991) Cumulative Damage Theory of Concrete under Variable. Amplitude Fatigue Loading. ACI Materials Journal, Vol. 88, No. 1, pp. 41-48.

[70] Philleo RE, A method for analyzing void distribution in air entrained concretes. Cement concr Aggreg 1983; 5(2): 128-130.

[71] Pigeon M, and Pleau R, Durability of concrete in cold climates. London: Chapman & Hall; 1994.

[72] Powers TC, The air requirement of frost resistant concrete. Proc Highway Research Broad 1949; 29:184-211.

[73] Powers TC, Helmuth, RA, (1953), Theory of volume changes in hardened cement paste during freezing. Proc Highway Research Broad 1953; 32: 285-297.

[74] Rapoport J, Shah SP, and Karr A. Permeability of Cracked Steel Fiber–Reinforced Concrete. J Mater Civ Eng 2002; 14(4): 355–358.

[75] Reid, R. (2008) "Special report: the infrastructure crisis," Civil Engineering (ASCE), Vol. 78, No. 1, pp. 40-65.

[76] Robert Černý, Pavla Rovnaníková, 2002, Transport processes in concrete, Taylor & Francis Published Date: 2002

[77] Saito M, and Ishimori H. Chloride permeability of concrete under static and repeated compressive loading. Cem Concr Res 1995; 25(4): 803–808.

[78] Samaha HR, and Hover KC. Influence of Microcracking on the Mass Transport Properties of. Concrete. ACI Mater J 1992; 89(4): 416-424.

[79] Samir N. Shoukry, Gergis W. William, Brian Downie, Mourad Y. Riad, Effect of moisture and temperature on the mechanical properties of concrete, Construction and Building Materials 25 (2011) 688–696.

[80] Sapragonas, J., A. Dargužis, A., (2011) "Model of radial deformations of protector of vehicle tire", *ISSN 1392 - 1207. MECHANIKA*. Vol., 17. No.1, pp. 21-29.

[81] Sarja, A. and Vesikari, E. (Eds) (1996) Durability Design of Concrete Structures, RILEM Report 14, E&FN Spon, London, UK.

[82] Sengul, Ö. (2005) Effects of Pozzolanic Materials on Mechanical Properties and Chloride Diffusivity of Concrete, Ph.D. Thesis, Istanbul Technical University, Institute of Science and Technology, Istanbul.

[83] Shi C. Another look at the rapid chloride permeability test (ASTM C 1202 or ASSHTO T277). Baltimore: FHWA Resource Center; 2003.

[84] Stéphane Poyet, Sébastien Charles, Nicolas Honoré, Valérie L'hostis, Assessment of the unsaturated water transport properties of an old concrete:Determination of the pore-

interaction factor, Cement and Concrete Research, Volume 41, Issue 10, 2011, pp.1015-1023.

[85] Tabatabai H, Tabatabai M, and Lee CW. Reliability of Bridge Decks in Wisconsin. Journal of Bridge Engineering 2011; 16(1): 53-62.

[86] Timoshenko, S., and Goodier, J., (1970) "Theory of Elasticity", 3rd edition, McGraw-Hill, New York, NY.

[87] van Mier JGM. Strain-softening of concrete under multiaxial loading conditions. PhD thesis, Netherlands: Eindhoven University of Technology, The Netherlands, 1984.

[88] Wan, B., Foley, C.M. and Komp, J., (2010) *Concrete Cracking in New Bridge Decks and Overlays*, Technical Report WHRP 10-05, Wisconsin Highway Research Program (WHRP), WI USA.

[89] Wang K, Jansen D, Shah SP, and Karr A. Permeability study of cracked concrete. Cem Concr Res 1997; 27(3): 381-393.

[90] Wesche K. Fly Ash in Concrete: Properties and Performance. London: Spon Press; 1991.

[91] Westergaard, H., (1930) "Computation of Stresses in Bridge Slabs Due to Wheel Loads," *Public road*. Vol., 11. No.1, pp. 15-37.

[92] Whiting D, Rapid Determination of the Chloride Permeability of Concrete. Technical Report No. FHWA-RD-81/119; 1981.

[93] Whiting, D., and D. Stark. 1983. Control of air content in concrete. NCHRP report 258 (May). Washington: Transportation Research Board, National Research Council.

[94] Whittington, H.W., McCarter, J., and Forde, M.C., (1981) The conduction of electricity through concrete. Magazine of concrete research, Vol.33. No. 114, pp.48-60.

[95] Wilkinson, DS., (2000) Mass transport in solids and fluids, United Kindom at the University Press, Cambridge.

[96] Wisconsin Department of Transportation, Bridge Manual Part I and Part II; 2009.

[97] Yang Z, Weiss WJ, and Olek J. Interaction between micro-cracking, cracking, and reduced durability of concrete developing methods for quantifying life-cycle modeling. Technical report no.SPR-2474; 2005.

[98] Yang Z, Weiss WJ, and Olek J. Water Transport in Concrete Damaged by Tensile Loading and Freeze-Thaw Cycling. J Mater Civ Eng 2006; 18(3): 424-434.

[99] Zhao, J. and Tabatabai, T. (2009) Analysis of Permit Vehicle Loads in Wisconsin, Wisconsin Highway Research Program Project 0092-08-15.

[100] Zhao, J. and Tabatabai, H. (in print, online accessible) Evaluation of a permit vehicle model using weigh-in-motion truck records. Journal of Bridge Engineering.

Appendix A: Initial Stress in ABAQUS

The deformation by changing temperature:

$$\Delta=\alpha\times\Delta T\times L=\alpha\times(t_2-t_1)\times L$$

a) the **1st step**: define the material properties for thermal expansion when temperature changes-> Edit material-> Expansion -> type= orthotropic, reference temperature =0 (you can use absolute zero), and three coefficient of thermal expansion alpha11, alpha22, alpha33.

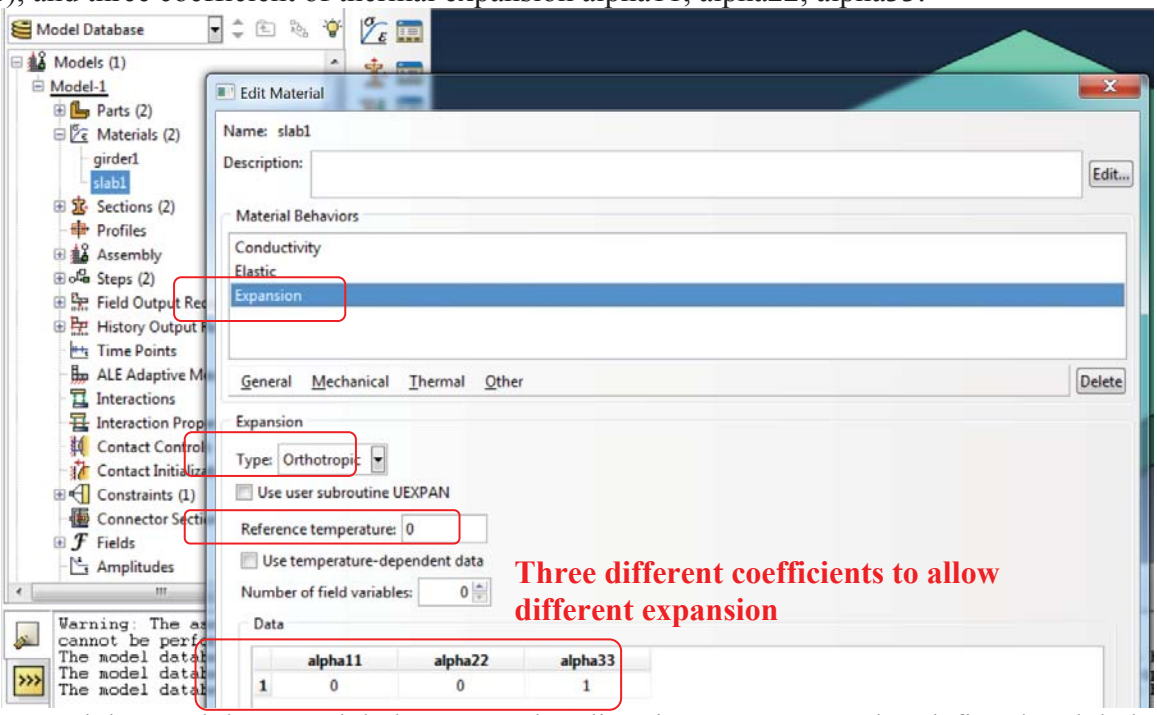

alpha11, alpha22, alpha33 = global x-, y-, and z- directions. So you need to define the global orientation in the models.

b) the **2nd step**: define global orientation in the models

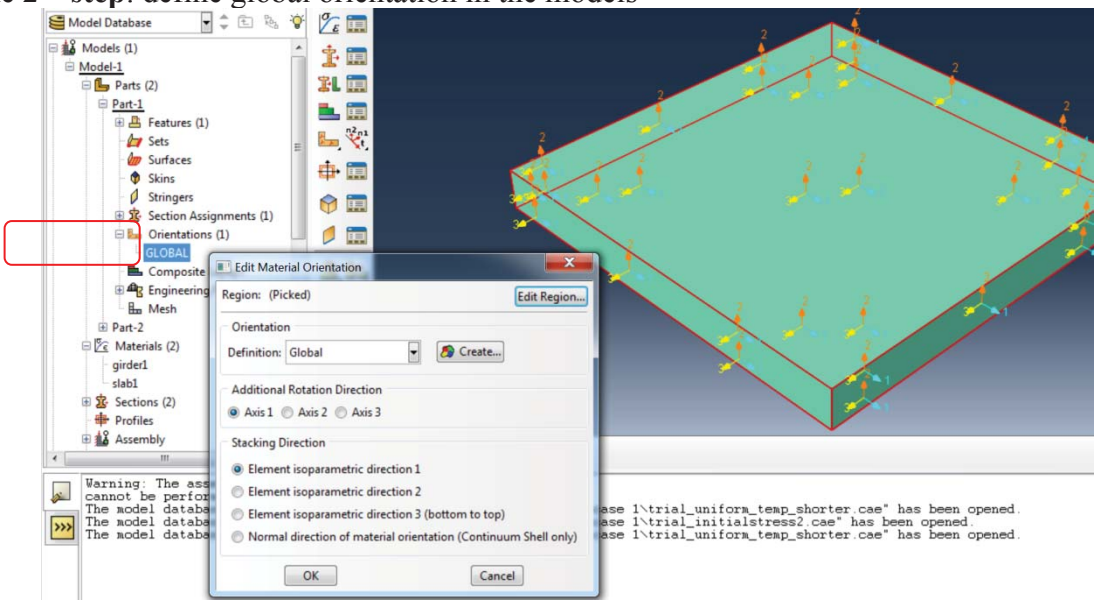

-> Model-1-> part -> orientation -> use default directions as the global one.

c) the **3rd step**: define the initial temperature and finial temperature

-> Steps-> initial -> predefined fields -> go back to screen toolbar at the top, predefined field -> manager -> create the initial and step temperature. -> define the region for the temperature change -> provide the values.

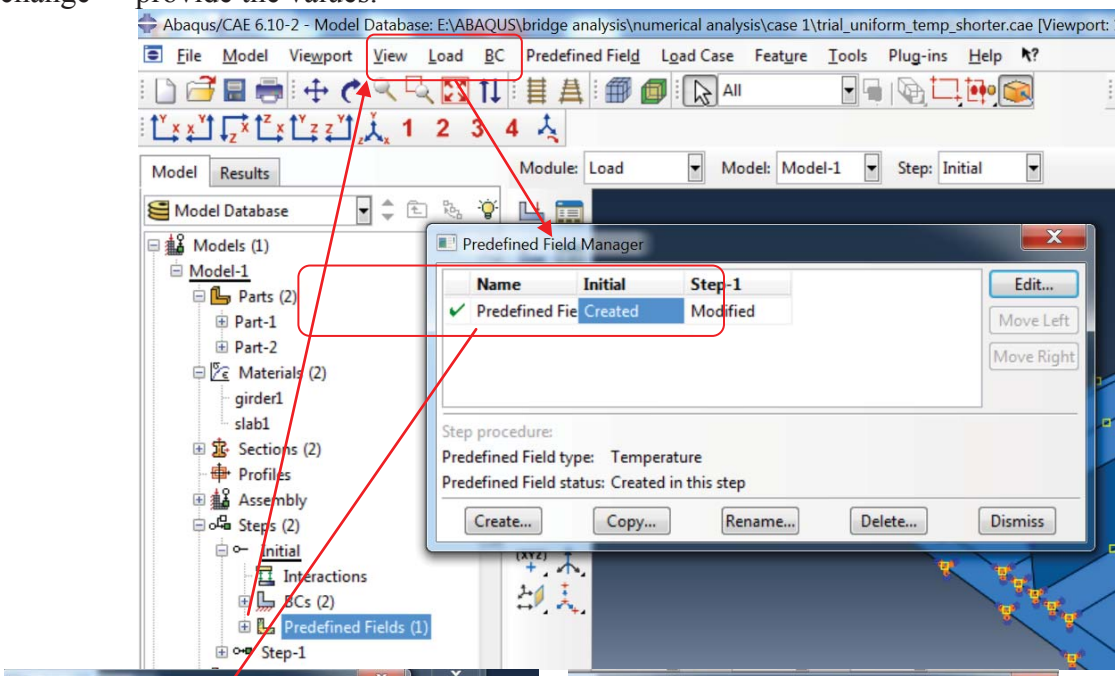

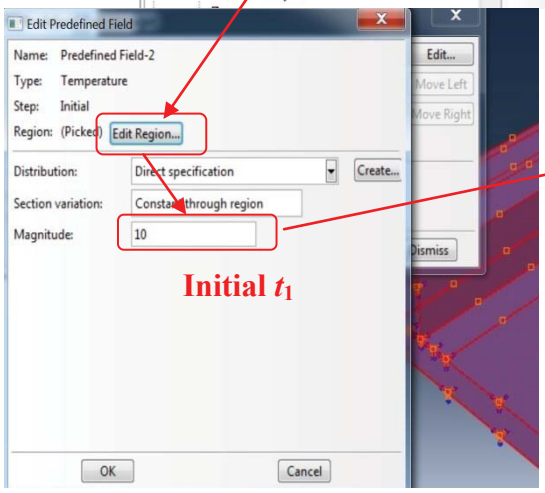

The initial value of temperature t_1

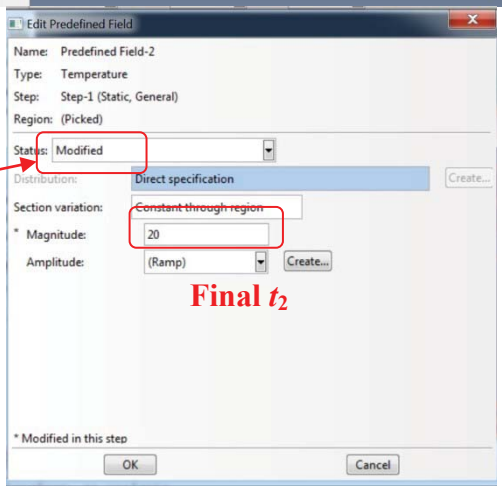

Modify the final value of temperature t_2

CFIRE

University of Wisconsin-Madison
Department of Civil and Environmental Engineering
1410 Engineering Drive, Room 270
Madison, WI 53706
Phone: 608-263-3175
Fax: 608-263-2512
cfire.wistrans.org